Imaging the (un)imaginable of the Barrier Immune system

Guo, N.

Imaging the (un)imaginable of the Barrier Immune System

Nannan Guo

Imaging the (un)imaginable of the Barrier Immune System

The work presented in this thesis was performed at the Department of Immunology of the Leiden University Medical Center in the Netherlands.

ISBN: 978-94-6419-748-8
Cover design by: Nannan Guo and Mette Schreurs
Layout by: Nannan Guo
Printed by: Gildeprint Drukkerijen

Financial support for the publication of this thesis was kindly provided by Standard Biotools.

Imaging the (un)imaginable of the Barrier Immune System

Proefschrift

ter verkrijging van
de graad van doctor aan de Universiteit Leiden,
op gezag van rector magnificus prof. dr.ir. H. Bijl,
volgens besluit van het college voor promoties
te verdedigen op dinsdag 18 april 2023
klokke 13:45 uur

door

Nannan Guo

geboren te Changchun, Jilin, China
in 1992

Promotor:	Prof. Dr. F. Koning
Co-promotor:	Dr. M. F. Pascutti Dr. K. D. Quint
Leden Promotiecommisie:	Prof. Dr. F. A. Ossendorp Prof. Dr. M. Yazdanbakhsh Prof. Dr. R.E. Mebius (Amsterdam UMC) Prof. Dr. M.R. van Dijk (UMC Utrecht)

Table of Contents

Chapter 1

General Introduction

Barrier Organs

Both the skin and intestinal tract have a large surface area that is constantly exposed to a large array of microorganisms. To protect the organism against invading pathogens multiple protective strategies are employed. In the intestine a mucous covered epithelial layer separates the lumen from the intestinal tissue, while in the skin the epidermis forms the first line defense barrier. In addition, the intestinal epithelium and lamina propria are home to numerous immune cells that together form the largest immune compartment in the body. Here, aberrant immune responses to the intestinal microbiota is thought to underly chronic intestinal disease like Crohn's disease and ulcerative colitis. In contrast, under homeostatic circumstances the skin contain relatively few immune cells but is characterized by the presence of Langerhans cells (LCs) in the epidermis and dermal dendritic cells (DCs) in the underlying dermis. Upon infection, however, many immune cells can be recruited to the skin leading to local inflammation and may result in chronic disease condition like psoriasis and atopic dermatitis (AD). Thus, while barrier immunity has developed to maintain local homeostasis by continual crosstalk between environmental signals and the immune system, disturbance of this crosstalk can result in a variety of chronic diseases. Therefore, to characterize the innate and adaptive immune cells that are present in the skin and intestine, the investigation of immune compositions and interactions need to be explored.

Immune system of human intestine

The intestine harbors the largest compartment of the human immune system. The intestinal epithelium and underlying lamina propria are the major effector sites of immune cell accumulation within the intestine. The lamina propria contains B cells, T cells, and numerous innate immune cell populations including innate lymphoid cells (ILCs), DCs, macrophages, whereas the epithelium primarily contains T cells[1]. While much is known about the organization and function of the intestinal immune system in adults, little is known about the population and development of the fetal intestinal immune compartment. As such we have a limited understanding of the molecular processes and cellular interactions that establish mucosal homeostasis and prepare the fetus for exposure to the invading microbiota right after birth. Given that disturbance of this homeostasis can lead to chronic inflammatory bowel diseases, more detailed information on how homeostasis is established and maintained will be required to better treat and prevent such diseases.

Immunohistochemistry analysis has shown that mature B cells were found in human fetal intestine at approximately 14 weeks of gestation[2, 3], of which around 10% express Ki-67 at gestational week 16 to 20[2]. By 19 weeks, distinct follicles of B cells with variable levels of expression of IgM, IgD, CD5 and CD23 are present and surrounded by T cells[3]. Mass cytometric analysis revealed that follicular and transitional B cells are enriched in fetal intestines from gestational weeks 16 to 23[4]. Moreover, single-cell RNA sequencing (scRNA-seq) analysis of fetal intestinal B cells from gestational week 8 to 17, identified common lymphoid progenitor, pro-B, pre-B and immature B cells. Also, a subpopulation of pro-B cells were frequently present till gestational week 15, after which there was an increase in the number of immature B cells[5].

Multiple single-cell cytometric technologies have been applied to investigate fetal intestinal T cells as well[4, 6, 7]. $CD3^+CD4^+CD8^-$ T cells were found to be present in both the epithelium and lamina propria of the human fetal intestine at gestational week 13, and their numbers increased with age[4]. Strikingly, tissue resident memory $CD4^+$ and $CD8^+$ T are abundant in human fetal intestines[4]. Here, multiple subsets of memory-like fetal intestinal $CD4^+$ T cells were identified in the second trimester and were found to display distinct TCR repertoire characteristics[7]. Moreover, TNF-α-expressing effector memory T cells have been observed in human the human fetal intestine[6]. Based on the expression patterns of the chemokine receptors CXCR3 and CCR6, the majority of fetal intestinal T cells were found to display a Th1 phenotype[4].

Innate lymphoid cells (ILCs) are a subset of innate immune cells that promote barrier immunity in the intestine and help to maintain immune homeostasis[8]. Recent analysis of the developmental pathways of the ILC family members indicates that natural killer (NK) cells, and non-cytotoxic helper ILCs, including ILC1s, ILC2s, ILC3s and lymphoid tissue inducer (LTi) cells are separate lineages[9, 10]. Single-cell mass cytometry data has shown that around 50% of human fetal intestinal ILCs are NK cells[4, 11]. In addition, ILC3s are also enriched with high expression of CD103[11] and CD69[4] in human fetal intestines, suggesting tissue resident subtypes. Moreover, RORC-expressing LTi, commonly recognized as the initiator of secondary lymphoid organ formation[12], were found in the developing fetal intestines and to express CXCR5 and CCR6[4, 5] to maintain the congregation of LTi there[13]. In addition, a unique population of the intermediate ILCs ($Lin^-CD7^+CD127^-CD45RO^+CD56^+$) has been identified in the human fetal intestine that can give rise to NK cells and ILC3[11].

Antigen presenting cells (APCs) are essential in maintaining homeostasis and are involved in the recruitment of T cells to the intestine by processing and presenting antigens to T cells. Single-cell cytometry analysis has shown that APCs are the most abundant intestinal innate cell in the fetal samples from the 2nd trimester[4]. scRNAseq data of the human fetal intestine have revealed that there is an increased abundance of myeloid cells, including monocytes, DCs, HLA-DR+ macrophages, mast cells and megakaryocyte in the 2nd trimester compared to the 1st trimester[5].

Thus, the fetal intestine already harbors a complex immune system that contains all major immune lineages long before birth. The presence of a sizable proportion of T cells expressing a memory phenotype in the second trimester suggests early exposure to exogenous antigens which may prepare the infant for the bacterial colonization upon birth. In the current thesis, we have explored novel approaches to map and follow the development of the human fetal intestinal immune system throughout the second trimester.

Immune system of skin

Historically, the skin is seen as an organ comprising an outermost layer, the epidermis, and a subjacent connective tissue, the dermis, that together provide a physical and biological barrier against chemical, physical and pathogenic insults. The skin is home to a variety of innate and adaptive immune cell populations that ensure protection against pathogens whilst maintaining tolerance to innocuous antigens, but can also contribute to the pathology of many inflammatory skin diseases[14] (**Figure 1**). Skin barrier dysfunction is critical in inducing cutaneous inflammatory diseases, such as psoriasis as a chronic inflammatory skin disease, but also mycosis fungoides (MF) as the most common type of cutaneous T cell lymphoma.

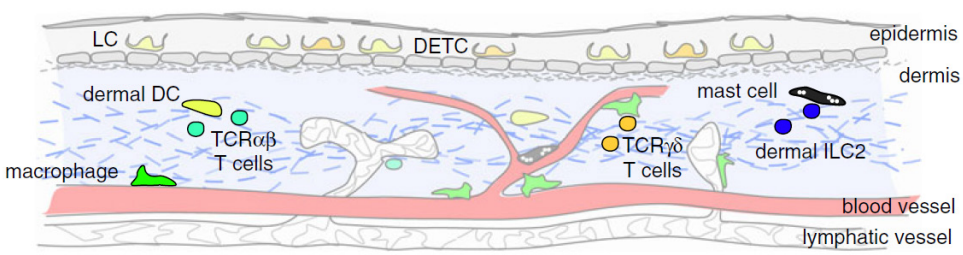

Figure 1. Schematic of skin resident immune cells. Dendritic epidermal T cell (DETC); Dendritic cell (DC); Group 2 innate lymphoid cells (ILC2); Langerhans cell (LC). Figure adapted from Tay et al. (2014)

Psoriasis

Psoriasis is an immune-mediated disorder primarily affecting the skin, in which T cell infiltration into epidermis and dermis is closely linked to disease pathogenesis and maintenance of inflammation[15]. Several T cells subsets, including central memory T cells, tissue-resident memory T cells, and exhausted and activated cytotoxic $CD8^+$ T cells were identified in psoriasis by single-cell RNA sequencing analysis[16, 17]. Psoriasis was considered to be a Th1-mediated skin disease for many years, because of the relative increase of circulating and skin-residing IFN-γ-producing T cells and upregulation expression genes involved in the IFN-γ immune response[18, 19, 20]. However, since IL-17A-producing $CD4^+$ T cells (Th17) were observed to be involved in the pathogenesis of psoriasis in mouse models[21], Th17 cells were described as main instigators of psoriasis[22, 23]. Moreover, Th17/Tc17 cytokines such as *IL17A*, *IL17F*, *IL26*, *IFNG*, and *CXCL13*[24] were predominantly produced by skin-resident memory T cells in proriasis[16].

Compared with uninflamed skin samples many myeloid subsets are increased in psoriasis. These include $CD68^+CD163^+$ macrophages, $CD14^+$ classical monocytes and an inflammatory monocyte population with expression of *IL1B* and *IL23A*, $HLA\text{-}DR^+CD301^+$ DCs and $CD207^+$ Langerhans cells, and mast cells[24]. Among these innate immune subsets, DCs play a critical role in the development of psoriasis in both of the initiation and maintenance phase[25]. LCs are a distinct immature DC subset that resides in the epidermis, and constitutes the first innate immune barrier against invading pathogens, but they have also been implicated in tolerance induction[26, 27]. While the density of LCs is decreased in psoriatic skin due to epidermal hyperplasia, their numbers and morphology are similar to normal skin[28]. However, mobilization and migration of LCs is profoundly impaired in psoriasis, even in non-lesional skin[29]. A mouse model of psoriasis has identified resident LCs and monocyte-derived LCs, and it was observed that monocyte-derived LCs produce higher level of IL-23 to induce differentiation/activation of Th17 cells[30]. For dermal DCs, a double immunofluorescence-based in *situ* study has shown that most $CD11c^+$ dermal DCs co-express CD1c[28, 31]. *In vitro* analysis of single-cell suspensions from psoriasis lesions increased numbers of both $CD11c^+CD1c^-$ resident DCs and $CD11c^+CD1c^-$ inflammatory DCs. Moreover, both DC types induced proliferation of T cells and the production of IL-17 and IFN-γ, while normal skin dermal DCs have no this ability[32]. In psoriatic lesions mature DCs present as dense cellular clusters, frequently aggregated with infiltrating T cells[33, 34, 35, 36]. Thus, interfering with DC/T cell interaction has been considered to be an effective therapeutic strategy for psoriasis. In addition, it has been confirmed

that macrophages enable to impact on the pathogenesis of psoriasis especially the initiation phase. Studies in mice have demonstrated that the depletion of macrophages improved psoriasis inflammation[37, 38], and reduced the production of Th1 cytokines like IL-23 and TNF-α in the psoriatic lesion[39, 40]. In human psoriatic plaques dermal macrophages expressed TNF-α[41]. Moreover, the number of $CD163^+$ macrophages was increased in psoriatic skin lesion in human, and decreased to non-lesional skin levels after treatment with TNF-α inhibitors[42]. So, next to DCs, it is worthwhile to study the contribution of T cells and macrophages to the development of psoriasis as well.

Mycosis fungoides

Mycosis fungoides (MF) is the most common type of cutaneous T cell lymphoma, which in the early stage presents with appearance of cutaneous patches or plaques covering a limited area of the skin[43]. In the early stages, MF typically exhibits an indolent clinical behavior and this has been considered to be points in a disease continuum for many years. However, at some point in time the skin lesions can progress from early stages to the advanced stage, while other patients diagnosed never progress to the advanced-stage disease. So many studies aim to understand why some patients progress and other not and to identify markers that can predict progression to the advanced stage.

Histopathological analysis of MF lesions has reported skin infiltration of both malignant $CD4^+$ and reactive $CD8^+$ T cells, which exacerbates as the disease progresses[44]. Here, MF with low numbers of $CD8^+$ tumor infiltrating lymphocytes could represent an early stage of the disease[45]. The analysis of scRNAseq and TCR sequencing for T cells from MF has showed that $CD4^+$ T cells with a dominant clonotype expressed CTLA4 and KI67, while $CD8^+$ T cells with a dominant clonotype exhibited the upregulation of markers associated with T-cell exhaustion and PD1/PDL1 signaling[46, 47]. Moreover, loss of the cell surface markers CD7, CD2, CD3, and CD26 have been observed in the advanced stage of MF[48, 49]. While early stage MF is characterized by a dominant Th1 cytokine pattern, there is a shift from a protective Th1 response to an immunosuppressive Th2 response during disease progression[50, 51].

Since 1976, the presence of $CD1a^+$ DCs has been well established in MF T cell infiltrates[52], and subsequent studies have investigated the role of DCs in MF progression[53, 54]. In early stage MF, immature DCs (LCs) of the epidermis migrate to the dermis to become highly efficient antigen presenting cells in areas of

epidermotropic invasion of tumor T cells[55]. The proportion of $CD1a^+$ LCs and dermal DCs with differential expression of CD1c and CD207 are increased through all stages of MF, however, most significantly in the tumor stage of the disease[47, 56]. Macrophages were previously designated to promote tumor growth by releasing many pro-angiogenic cytokines and growth factors[57, 58]. The number of $CD68^+$ and $CD163^+$ macrophages significantly increases as the MF disease progressed[47, 59]. Moreover, $CD163^+$ macrophages were located in the invasive margin of the tumor in MF patients[60], and the CD163/CD68 ratio was highest at the tumor stage of MF, indicating that alternatively activated macrophages (also called M2 macrophages) are associated with disease progression[59],which fits with other observations are associate M2 macrophages with tumor cell growth and metastasis through modulation of angiogenesis and tissue remodeling[57, 61]. Thus, ongoing interactions of T cells with DCs as well as macrophages in lesions of MF could lead to chronic T cell activation and inflammation associated with these lesions.

Although these immune subsets in the inflammation skin conditions has been explored, the investigation of composition and spatial characteristics of the cutaneous lymphocytes and myeloid cells infiltrate simultaneously has been incompletely characterized at single-cell level. Mass cytometry and spectral flow cytometry are novel tools to apply over 40 heavy metal or fluorochrome labelled markers as reporters for dissecting the immune composition in individual patients and diseases. Combined with imaging mass cytometry that enables the simultaneous spatial and phenotypic evaluation of up to 40 biomarkers in the tissue contexture. Therefore, these novel techniques can substantially contribute to a better understanding of the role of immune subsets in disease progression, knowledge that may be used for improved differential diagnosis and therapy of skin diseases.

High-dimensional single-cell cytometric technologies

Fluorescence-activated flow cytometry has been used for decades for the surface/intracellular protein expression single cell level. As such flow cytometry has been a key technology to unravel the complexity of the immune system. However, with conventional flow cytometry only a relatively limited number of antibodies can be applied simultaneously, prohibiting a detailed analysis of the ever expanding number of distinct immune subsets simultaneously. Novel single cell analysis technologies have emerged in the last decade that allow the incorporation of a far greater number of markers. Spectral flow cytometry, for example, can incorporate up to 40 antibodies can be measured at the single cell level in a single tube in a

single experiment[62, 63, 64, 65]. These antibodies are labelled with spectrally diverse fluorochromes that can be simultaneously detected by the use of multiple lasers in combination with detectors that capture the emitted fluorescence across the full-spectrum. Here, the application of algorithms based on the Least Squares Method enables separation of overlapping fluorescent spectra (**Figure 2**)[63]. Moreover, spectral flow cytometry can separate distinct autofluorescence signals, and the unmixing algorithm subtracts the autofluorescence signal to allow more accurate true fluorescence detection, thus improves signal-to-noise ratios and allows a more accurate phenotypic characterization of a large number of immune subsets in complex cellular mixtures[66]. Nevertheless, researchers applying spectral flow cytometry are frequently facing challenges when it comes to the distinction of the individual emission patterns of the applied fluorochromes. The development of suitable antibody panels, therefore, is often a laborious process. Nevertheless, spectral flow cytometry allows a more detailed analysis of immune system heterogeneity.

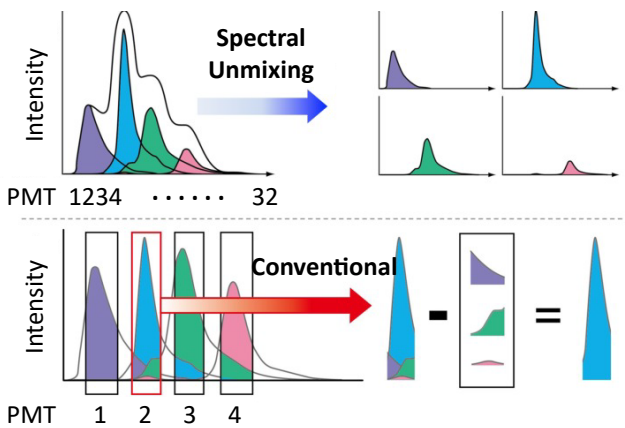

Figure 2. Principle of "Spectral Unmixing" and separation of fluoroprobes. The spectral flow cytometry unmixing algorithm uses all the emitted fluorescence as basic spectrum patterns to separate different spectrums (upper). In contrast, conventional flow cytometry utilizes only a narrow band of emitted light to remove overlapping fluorescence emissions (lower). Figure adapted from Koji et al. (2015)

Next to spectral flow cytometry, mass cytometry (CyTOF, also known as cytometry by time-of-fight) has been developed to utilize isotopically purified metal-tagged antibodies for the analysis single-cell suspensions. In mass cytometry, the antibody-stained cells are analyzed by breaking the individual antibody labelled cells to the atomic level followed by measurement of the cell bound metals with a time-of-flight mass spectrometer. A schematic overview of the mass cytometry

workflow[67] is shown in **Figure 4**. Currently, mass cytometry systems typically measure around 40 parameters per cell, but theoretically mass cytometry enables the detection of over 100 parameters simultaneously[68, 69]. An important advantage of mass cytometry or flow cytometry is that the distinct masses of the applied metal tags allows for baseline separation, minimizing the amount of signal spillover from one parameter to another, thus eliminating the problem of fluorochrome spectral overlap in flow cytometry **(Figure 3).** Moreover, there is no interference from autofluorescence in mass cytometry. However, throughput rates per second by mass cytometry are much lower than modern flow cytometers, and only around 60% stained-cell were acquired. Also, unlike flow cytometry, it is not possible to collect cells after measurement by mass cytometer, as they are nebulized during the analysis procedure. Despite these disadvantages, mass cytometry has in the past decade been widely utilized to study the composition of the immune system in both health and disease, providing novel insights into the potential role of distinct immune subsets in chronic diseases and cancer.

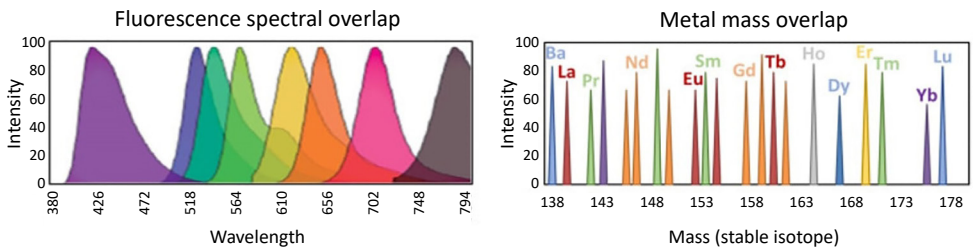

Figure 3. Overcoming spectral overlap via mass cytometry. Histograms demonstrating the emission spectra overlap that exists between different fluorophores by flow cytometry (left), and metal mass overlap that exists for heavy metals by mass cytometry (right). Figure adapted from Blair et al. (2019)

Single cell analysis with a 40-antibody panel simultaneously yields highly complex datasets that are difficult to interpret using the conventional gating strategies commonly used in flow cytometry. Since the inception of mass cytometry, t-distributed Stochastic Neighbor Embedding (t-SNE) has been widely used as a non-linear dimensionality reduction algorithm to obtain an unbiased overview of the immune subsets present in the dataset and visualize with the differential expression patterns of the various markers by which these subsets are defined[70, 71]. However, tSNE can only analyze a limited number of cells and requires long computing time. To overcome these problems, Hierarchical Stochastic Neighbor Embedding (HSNE)[72], optimized t-SNE (optSNE)[73], and Uniform Manifold Approximation and Projection (UMAP)[74] and have been developed to allow to analyze large high-

dimensional datasets on millions of cells rapidly. In addition, clustering-based algorithms are employed for the in-depth, including unsupervised Gaussian mean shift (GMS) clustering in Cytosplore[75], and FlowSOM in Cytobank[76]. Moreover, a data science platform, OMIQ (https://www.omiq.ai/) has been built, which contains stepwise operations to accomplish cytometric data analysis in a workflow.

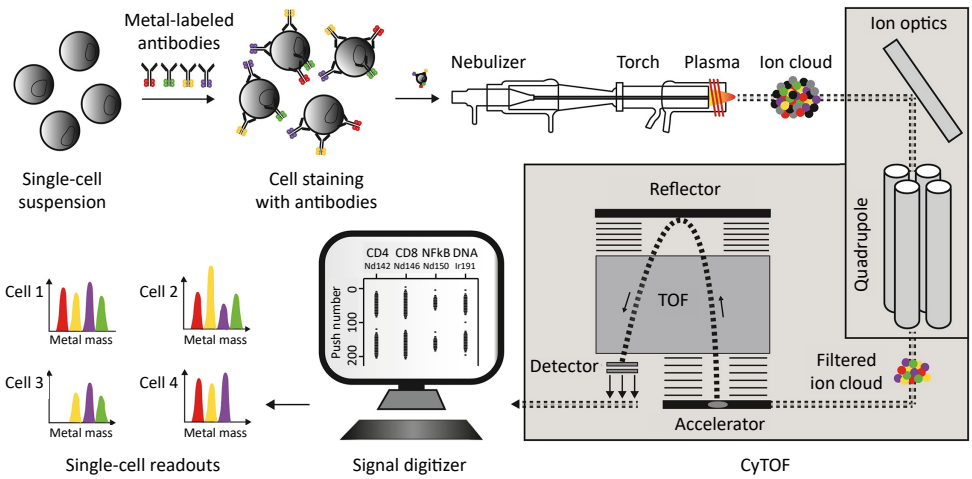

Figure 4. Sample preparation and analysis by mass cytometry. Adapted from Spitzer et al. (2016)

Imaging mass cytometry

Imaging mass cytometry (IMC) is an extension of mass cytometry, using metal-conjugated antibodies to label tissue samples, either formalin-fixed paraffin-embedded (FFPE) or snap-frozen samples that are subsequently ablated by a UV laser spot by spot with the use of the Hyperion[77]. The ablated tissue with a 1-µm resolution is then analyzed with the CyTOF instrument. Superior to conventional immunohistochemistry (IHC) and immunofluorescence (IF) techniques, IMC allows the simultaneous interrogation of over 40 markers in a single tissue section. **Figure 5** displays the workflow of imaging mass cytometry till the pre-analysis of data[78]. In general, MCD™ Viewer is used to examine the data quality during the optimization of the staining procedure[79, 80]. After validation of the full IMC antibody panel staining, computational approaches to visualize IMC data at the pixel-level and cell-level have been developed, like Cytosplore Imaging, Imacyte[81] and Histocat[82], which allow an analysis of the immune cell composition, their spatial organization, and cell-to-cell interactions in *situ*.

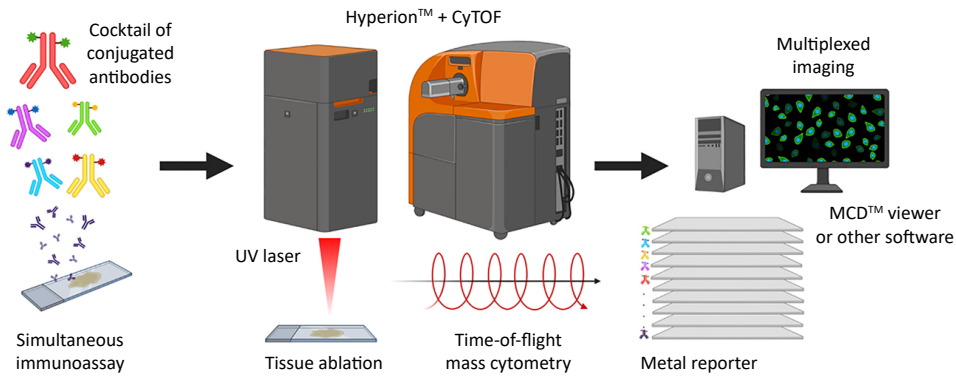

Figure 5. Imaging Mass Cytometry (IMC™) Workflow. Adapted from Cereceda et al. (2021)

Outline of the thesis

The novel high-dimensional cytometric techniques spectral flow cytometry and mass cytometry have provided an opportunities for high resolution comprehensive immune profiling of single-cell suspensions. Due to the dissociation of tissue materials by mechanical and enzymatic methods, however, spatial information on the distribution and interactions of immune cells is lacking. Therefore, imaging mass cytometry (IMC) complements the single cell technologies. In this thesis, I describe my work to characterize the intestinal and skin immune system by integration of single-cell immune profiles with their spatial distribution in the tissue contexture.

In **Chapter 2**, we provide an optimal IMC protocol for snap-frozen human fetal intestinal samples, which were also applied to snap-frozen human adult intestinal samples. Moreover, we present the tissue architecture and spatial distribution of the stromal cells and immune cells for both types of intestinal samples, revealing the colocalization of T cells, ILCs, and various myeloid cell subsets in the lamina propria of the human fetal intestine.

In **Chapter 3**, we further analyze a large number of human fetal intestinal samples from gestational week 14 through 22 by spectral flow cytometry and IMC. The spectral flow cytometry analysis identified stable clusters of Ki-67-expressing cells within all identified immune subsets that remain present in time. Moreover, with the use of the antibody panel developed in **Chapter** 2, IMC analysis revealed

formation of lymphoid follicles just below the epithelium in the developing intestine from week 16 onwards, harboring B, T, ILC and myeloid cells and confirmed the presence of Ki-67$^+$ cells in the various immune subsets in *situ*. Finally, we observe that a CD69$^+$CD117$^+$CD161$^+$CCR6$^+$CD127$^+$ phenotype is shared by subsets of fetal intestinal CD3$^-$CD7$^+$ ILCs and T cells and that these cells preferentially reside in the lymphoid structures, and harbor Ki-67$^+$ cells, indicating a role in the development of these follicles. Overall, these observations indicate the presence of immune subset-committed cells capable of local proliferation, contributing to the development and growth of organized immune structures throughout the 2nd trimester in the human fetal intestine, presumably preparing the infant for the microbial colonization right after birth.

In **Chapter 4**, we use single-cell mass cytometry and IMC to obtain a comprehensive analysis of the immune system in skin biopsies of early stage MF patients, with the goal to improve recognition of early stage MF faster and more accurately. We identified phenotypically distinct subsets in both the CD4$^+$ T cell and myeloid cell compartment that are shared by most MF patients. In addition, we find distinct CD4$^+$ T cell subsets that are exclusively present in particular patients, potentially representing more advanced stages of disease where phenotypically distinct CD4$^+$ T cells expand. Moreover, substantial numbers of CD4$^+$ T cells co-localized with both CD1a$^+$CD1c$^+$ HLA-DR$^+$ and CD1a$^-$CD1c$^+$HLA-DR$^+$ DCs in the dermis. Importantly, the identification of prominent cellular aggregates between CD4$^+$ T cells and myeloid cells in the dermis with a patient-unique cellular composition may provide a framework for improving mycosis fungoides diagnosis and development of treatment tailored to the characteristic features of these aggregates in individual patients.

In **Chapter 5,** we apply an updated IMC antibody panel to non-lesional and lesional skin from psoriasis patients to explore the complexity and organization of the immune compartment in *situ*. For this, we performed pixel-based analysis in *Cytosplore Imaging* for samples from nine psoriasis patients, by which the pixel-clusters associated with the major immune subset (CD3$^-$CD7$^+$ ILCs, B cells, CD4$^+$ T cells, CD8$^+$ T cells, DCs, macrophage and mast cells) were quantified and visualized in non-lesional and lesional skin from psoriasis patients. We demonstrate that clusters of pixels can be identified that have features of both T and myeloid cells and likely represent pixels at the interface between these cell types, allowing an unbiased quantification of cellular interactions in these tissue samples. The analysis of these "double feature" pixels revealed that T cells frequently colocalize with CD207$^-$CD1c$^+$ DCs in the dermis of lesion skin, and allow a classification of

these psoriasis patients in distinct groups. These data might guide more patient oriented treatment of psoriasis.

In **Chapter 6,** we discuss the main findings of this thesis and discuss potential future directions.

Reference

1. Mowat, A.M. & Agace, W.W. Regional specialization within the intestinal immune system. *Nat Rev Immunol* **14**, 667-685 (2014).
2. Golby, S. *et al.* B cell development and proliferation of mature B cells in human fetal intestine. *J Leukoc Biol* **72**, 279-284 (2002).
3. Spencer, J., MacDonald, T.T., Finn, T. & Isaacson, P.G. The development of gut associated lymphoid tissue in the terminal ileum of fetal human intestine. *Clin Exp Immunol* **64**, 536-543 (1986).
4. Stras, S.F. *et al.* Maturation of the Human Intestinal Immune System Occurs Early in Fetal Development. *Dev Cell* **51**, 357-373.e355 (2019).
5. Elmentaite, R. *et al.* Cells of the human intestinal tract mapped across space and time. *Nature* **597**, 250-255 (2021).
6. Schreurs, R. *et al.* Human Fetal TNF-α-Cytokine-Producing CD4(+) Effector Memory T Cells Promote Intestinal Development and Mediate Inflammation Early in Life. *Immunity* **50**, 462-476. e468 (2019).
7. Li, N. *et al.* Memory CD4(+) T cells are generated in the human fetal intestine. *Nat Immunol* **20**, 301-312 (2019).
8. Artis, D. & Spits, H. The biology of innate lymphoid cells. *Nature* **517**, 293-301 (2015).
9. Spits, H. *et al.* Innate lymphoid cells--a proposal for uniform nomenclature. *Nat Rev Immunol* **13**, 145-149 (2013).
10. Constantinides, M.G., McDonald, B.D., Verhoef, P.A. & Bendelac, A. A committed precursor to innate lymphoid cells. *Nature* **508**, 397-401 (2014).
11. Li, N. *et al.* Mass cytometry reveals innate lymphoid cell differentiation pathways in the human fetal intestine. *J Exp Med* **215**, 1383-1396 (2018).
12. Krishnamurty, A.T. & Turley, S.J. Lymph node stromal cells: cartographers of the immune system. *Nat Immunol* **21**, 369-380 (2020).
13. Sécca, C. *et al.* Spatial distribution of LTi-like cells in intestinal mucosa regulates type 3 innate immunity. *Proc Natl Acad Sci U S A* **118** (2021).
14. Tay, S.S., Roediger, B., Tong, P.L., Tikoo, S. & Weninger, W. The Skin-Resident Immune Network. *Curr Dermatol Rep* **3**, 13-22 (2014).
15. Conrad, C. *et al.* Alpha1beta1 integrin is crucial for accumulation of epidermal T cells and the development of psoriasis. *Nat Med* **13**, 836-842 (2007).
16. Cook, C.P. *et al.* A single-cell transcriptional gradient in human cutaneous memory T cells restricts Th17/Tc17 identity. *Cell Rep Med* **3**, 100715 (2022).
17. Liu, J. *et al.* Single-cell RNA sequencing of psoriatic skin identifies pathogenic Tc17 cell subsets and reveals distinctions between CD8(+) T cells in autoimmunity and cancer. *J Allergy Clin Immunol* **147**, 2370-2380 (2021).
18. Austin, L.M., Ozawa, M., Kikuchi, T., Walters, I.B. & Krueger, J.G. The majority of epidermal T cells in Psoriasis vulgaris lesions can produce type 1 cytokines, interferon-gamma, interleukin-2, and tumor necrosis factor-alpha, defining TC1 (cytotoxic T lymphocyte) and TH1 effector populations: a type 1 differentiation bias is also measured in circulating blood T cells in psoriatic patients. *J Invest Dermatol* **113**, 752-759 (1999).
19. Szabo, S.K., Hammerberg, C., Yoshida, Y., Bata-Csorgo, Z. & Cooper, K.D. Identification and quantitation of interferon-gamma producing T cells in psoriatic lesions: localization to both CD4+ and CD8+ subsets. *J Invest Dermatol* **111**, 1072-1078 (1998).
20. Zhou, X. *et al.* Novel mechanisms of T-cell and dendritic cell activation revealed by profiling of psoriasis on the 63,100-element oligonucleotide array. *Physiol Genomics* **13**, 69-78 (2003).
21. Langrish, C.L. *et al.* IL-23 drives a pathogenic T cell population that induces autoimmune inflammation. *J Exp Med* **201**, 233-240 (2005).
22. Lowes, M.A. *et al.* Psoriasis vulgaris lesions contain discrete populations of Th1 and Th17 T cells. *J Invest Dermatol* **128**, 1207-1211 (2008).
23. Cheuk, S. *et al.* Epidermal Th22 and Tc17 cells form a localized disease memory in clinically healed psoriasis. *J Immunol* **192**, 3111-3120 (2014).
24. Liu, Y. *et al.* Defining Patient-Level Molecular Heterogeneity in Psoriasis Vulgaris Based on Single-Cell Transcriptomics. *Front Immunol* **13**, 842651 (2022).

25. Glitzner, E. *et al.* Specific roles for dendritic cell subsets during initiation and progression of psoriasis. *EMBO Mol Med* **6**, 1312-1327 (2014).
26. Kissenpfennig, A. & Malissen, B. Langerhans cells--revisiting the paradigm using genetically engineered mice. *Trends Immunol* **27**, 132-139 (2006).
27. Romani, N., Holzmann, S., Tripp, C.H., Koch, F. & Stoitzner, P. Langerhans cells - dendritic cells of the epidermis. *Apmis* **111**, 725-740 (2003).
28. Zaba, L.C., Krueger, J.G. & Lowes, M.A. Resident and "inflammatory" dendritic cells in human skin. *J Invest Dermatol* **129**, 302-308 (2009).
29. Cumberbatch, M. *et al.* Impaired Langerhans cell migration in psoriasis. *J Exp Med* **203**, 953-960 (2006).
30. Lee, M. *et al.* Resident and monocyte-derived Langerhans cells are required for imiquimod-induced psoriasis-like dermatitis model. *J Dermatol Sci* **91**, 52-59 (2018).
31. Collin, M., McGovern, N. & Haniffa, M. Human dendritic cell subsets. *Immunology* **140**, 22-30 (2013).
32. Zaba, L.C. *et al.* Psoriasis is characterized by accumulation of immunostimulatory and Th1/Th17 cell-polarizing myeloid dendritic cells. *J Invest Dermatol* **129**, 79-88 (2009).
33. Lowes, M.A. *et al.* Increase in TNF-alpha and inducible nitric oxide synthase-expressing dendritic cells in psoriasis and reduction with efalizumab (anti-CD11a). *Proc Natl Acad Sci U S A* **102**, 19057-19062 (2005).
34. Nograles, K.E., Davidovici, B. & Krueger, J.G. New insights in the immunologic basis of psoriasis. *Semin Cutan Med Surg* **29**, 3-9 (2010).
35. Kim, T.G. *et al.* Dermal clusters of mature dendritic cells and T cells are associated with the CCL20/CCR6 chemokine system in chronic psoriasis. *J Invest Dermatol* **134**, 1462-1465 (2014).
36. Kim, T.G., Kim, D.S., Kim, H.P. & Lee, M.G. The pathophysiological role of dendritic cell subsets in psoriasis. *BMB Rep* **47**, 60-68 (2014).
37. Clark, R.A. & Kupper, T.S. Misbehaving macrophages in the pathogenesis of psoriasis. *J Clin Invest* **116**, 2084-2087 (2006).
38. Wang, H. *et al.* Activated macrophages are essential in a murine model for T cell-mediated chronic psoriasiform skin inflammation. *J Clin Invest* **116**, 2105-2114 (2006).
39. Ward, N.L. *et al.* Depletion of antigen-presenting cells by clodronate liposomes reverses the psoriatic skin phenotype in KC-Tie2 mice. *Br J Dermatol* **164**, 750-758 (2011).
40. Wang, Y. *et al.* Monocytes/Macrophages play a pathogenic role in IL-23 mediated psoriasis-like skin inflammation. *Sci Rep* **9**, 5310 (2019).
41. Marble, D.J., Gordon, K.B. & Nickoloff, B.J. Targeting TNFalpha rapidly reduces density of dendritic cells and macrophages in psoriatic plaques with restoration of epidermal keratinocyte differentiation. *J Dermatol Sci* **48**, 87-101 (2007).
42. Zaba, L.C. *et al.* Amelioration of epidermal hyperplasia by TNF inhibition is associated with reduced Th17 responses. *J Exp Med* **204**, 3183-3194 (2007).
43. Pimpinelli, N. *et al.* Defining early mycosis fungoides. *J Am Acad Dermatol* **53**, 1053-1063 (2005).
44. Wong, H.K., Mishra, A., Hake, T. & Porcu, P. Evolving insights in the pathogenesis and therapy of cutaneous T-cell lymphoma (mycosis fungoides and Sezary syndrome). *Br J Haematol* **155**, 150-166 (2011).
45. Goteri, G. *et al.* Density of neoplastic lymphoid infiltrate, CD8+ T cells, and CD1a+ dendritic cells in mycosis fungoides. *J Clin Pathol* **56**, 453-458 (2003).
46. Gaydosik, A.M., Stonesifer, C.J., Khaleel, A.E., Geskin, L.J. & Fuschiotti, P. Single-Cell RNA Sequencing Unveils the Clonal and Transcriptional Landscape of Cutaneous T-Cell Lymphomas. *Clin Cancer Res* **28**, 2610-2622 (2022).
47. Rindler, K. *et al.* Single-cell RNA sequencing reveals markers of disease progression in primary cutaneous T-cell lymphoma. *Mol Cancer* **20**, 124 (2021).
48. Ormsby, A., Bergfeld, W.F., Tubbs, R.R. & Hsi, E.D. Evaluation of a new paraffin-reactive CD7 T-cell deletion marker and a polymerase chain reaction-based T-cell receptor gene rearrangement assay: implications for diagnosis of mycosis fungoides in community clinical practice. *J Am Acad Dermatol* **45**, 405-413 (2001).
49. Zhang, Y. *et al.* Molecular markers of early-stage mycosis fungoides. *J Invest Dermatol* **132**, 1698-1706 (2012).
50. Campbell, J.J., Clark, R.A., Watanabe, R. & Kupper, T.S. Sezary syndrome and mycosis fungoides arise from distinct T-cell subsets: a biologic rationale for their distinct clinical behaviors. *Blood* **116**, 767-771 (2010).
51. Wilcox, R.A. Cutaneous T-cell lymphoma: 2017 update on diagnosis, risk-stratification, and management. *Am J Hematol* **92**, 1085-1102 (2017).
52. Goos, M., Kaiserling, E. & Lennert, K. Mycosis fungoides: model for T-lymphocyte homing to the skin? *Br J Dermatol* **94**, 221-222 (1976).
53. Nestle, F.O. & Nickoloff, B.J. Role of dendritic cells in benign and malignant lymphocytic infiltrates of the skin. *Dermatol Clin* **12**, 271-282 (1994).
54. Pimpinelli, N., Santucci, M., Romagnoli, P. & Giannotti, B. Dendritic cells in T- and B-cell proliferation in the skin. *Dermatol Clin* **12**, 255-270 (1994).
55. Lüftl, M., Feng, A., Licha, E. & Schuler, G. Dendritic cells and apoptosis in mycosis fungoides. *Br J Dermatol* **147**, 1171-1179 (2002).
56. Cioplea, M. *et al.* Dendritic cell distribution in mycosis fungoides vs. inflammatory dermatosis and

other T-cell skin lymphoma. *Oncol Lett* **17**, 4055-4059 (2019).
57. Qian, B.Z. & Pollard, J.W. Macrophage diversity enhances tumor progression and metastasis. *Cell* **141**, 39-51 (2010).
58. Sugaya, M. *et al.* Association of the numbers of CD163(+) cells in lesional skin and serum levels of soluble CD163 with disease progression of cutaneous T cell lymphoma. *J Dermatol Sci* **68**, 45-51 (2012).
59. El-Guindy, D.M., Elgarhy, L.H., Elkholy, R.A., Ali, D.A. & Helal, D.S. Potential role of tumor-associated macrophages and CD163/CD68 ratio in mycosis fungoides and Sézary syndrome in correlation with serum sCD163 and CCL22. *J Cutan Pathol* **49**, 261-273 (2022).
60. Günther, C. *et al.* Up-regulation of the chemokine CCL18 by macrophages is a potential immunomodulatory pathway in cutaneous T-cell lymphoma. *Am J Pathol* **179**, 1434-1442 (2011).
61. Gordon, S. & Martinez, F.O. Alternative activation of macrophages: mechanism and functions. *Immunity* **32**, 593-604 (2010).
62. Park, L.M., Lannigan, J. & Jaimes, M.C. OMIP-069: Forty-Color Full Spectrum Flow Cytometry Panel for Deep Immunophenotyping of Major Cell Subsets in Human Peripheral Blood. *Cytometry A* **97**, 1044-1051 (2020).
63. Futamura, K. *et al.* Novel full-spectral flow cytometry with multiple spectrally-adjacent fluorescent proteins and fluorochromes and visualization of in vivo cellular movement. *Cytometry A* **87**, 830-842 (2015).
64. Ferrer-Font, L. *et al.* Panel Optimization for High-Dimensional Immunophenotyping Assays Using Full-Spectrum Flow Cytometry. *Curr Protoc* **1**, e222 (2021).
65. Roederer, M. Multiparameter FACS analysis. *Curr Protoc Immunol* **Chapter 5**, Unit 5.8 (2002).
66. Peixoto, M.M. *et al.* Identification of fetal liver stroma in spectral cytometry using the parameter autofluorescence. *Cytometry A* (2022).
67. Spitzer, M.H. & Nolan, G.P. Mass Cytometry: Single Cells, Many Features. *Cell* **165**, 780-791 (2016).
68. Bendall, S.C., Nolan, G.P., Roederer, M. & Chattopadhyay, P.K. A deep profiler's guide to cytometry. *Trends Immunol* **33**, 323-332 (2012).
69. Chevrier, S. *et al.* Compensation of Signal Spillover in Suspension and Imaging Mass Cytometry. *Cell Syst* **6**, 612-620.e615 (2018).
70. Van der Maaten, L. & Hinton, G. Visualizing data using t-SNE. *Journal of machine learning research* **9** (2008).
71. Van Der Maaten, L. Accelerating t-SNE using tree-based algorithms. *The Journal of Machine Learning Research* **15**, 3221-3245 (2014).
72. van Unen, V. *et al.* Visual analysis of mass cytometry data by hierarchical stochastic neighbour embedding reveals rare cell types. *Nat Commun* **8**, 1740 (2017).
73. Belkina, A.C. *et al.* Automated optimized parameters for T-distributed stochastic neighbor embedding improve visualization and analysis of large datasets. *Nat Commun* **10**, 5415 (2019).
74. McInnes, L., Healy, J. & Melville, J. Umap: Uniform manifold approximation and projection for dimension reduction. *arXiv preprint arXiv:1802.03426* (2018).
75. Comaniciu, D. & Meer, P. Mean shift: a robust approach toward feature space analysis. *IEEE Transactions on Pattern Analysis and Machine Intelligence* **24**, 603-619 (2002).
76. Van Gassen, S. *et al.* FlowSOM: Using self-organizing maps for visualization and interpretation of cytometry data. *Cytometry A* **87**, 636-645 (2015).
77. Giesen, C. *et al.* Highly multiplexed imaging of tumor tissues with subcellular resolution by mass cytometry. *Nat Methods* **11**, 417-422 (2014).
78. Cereceda, K., Jorquera, R. & Villarroel-Espíndola, F. Advances in mass cytometry and its applicability to digital pathology in clinical-translational cancer research. *Advances in Laboratory Medicine / Avances en Medicina de Laboratorio* **3**, 5-16 (2022).
79. Ijsselsteijn, M.E., van der Breggen, R., Farina Sarasqueta, A., Koning, F. & de Miranda, N. A 40-Marker Panel for High Dimensional Characterization of Cancer Immune Microenvironments by Imaging Mass Cytometry. *Front Immunol* **10**, 2534 (2019).
80. Guo, N. *et al.* A 34-Marker Panel for Imaging Mass Cytometric Analysis of Human Snap-Frozen Tissue. *Front Immunol* **11**, 1466 (2020).
81. Somarakis, A., Unen, V.V., Koning, F., Lelieveldt, B. & Höllt, T. ImaCytE: Visual Exploration of Cellular Micro-Environments for Imaging Mass Cytometry Data. *IEEE Transactions on Visualization and Computer Graphics* **27**, 98-110 (2021).
82. Schapiro, D. *et al.* histoCAT: analysis of cell phenotypes and interactions in multiplex image cytometry data. *Nat Methods* **14**, 873-876 (2017).

Chapter 2

A 34-marker panel for Imaging Mass Cytometric analysis of human snap-frozen tissue

Nannan Guo[1], Vincent van Unen[1], Marieke E. Ijsselsteijn[2], Laura F. Ouboter[3], Andrea E. van der Meulen[3], Susana M. Chuva de Sousa Lopes[4], Noel F. C. C. de Miranda[2], Frits Koning[1,*], Na Li[1, 5 *]

[1]Immunohematology and Blood Transfusion, Leiden University Medical Center, Leiden, The Netherlands
[2]Pathology, Leiden University Medical Center, Leiden, The Netherlands
[3]Gastroenterology, Leiden University Medical Center, The Netherlands
[4]Anatomy, Leiden University Medical Center, Leiden, The Netherlands
[5]Key Laboratory of Zoonoses Research, Ministry of Education Institute of Zoonoses, College of Veterinary Medicine, Jilin University

[*]Equal contribution

Frontiers in Immunology 2020; 11: 1466.

Abstract

Imaging mass cytometry (IMC) is able to quantify the expression of dozens of markers at sub-cellular resolution on a single tissue section by combining a novel laser ablation system with mass cytometry. As such, it allows us to gain spatial information and antigen quantification *in situ*, and can be applied to both snap-frozen and formalin-fixed, paraffin-embedded (FFPE) tissue sections. Herein, we have developed and optimized the immunodetection conditions for a 34-antibody panel for use on human snap-frozen tissue sections. For this, we tested the performance of 80 antibodies. Moreover, we compared tissue drying times, fixation procedures and antibody incubation conditions. We observed that variations in the drying times of tissue sections had little impact on the quality of the images. Fixation with methanol for 5 min at -20° C or 1% paraformaldehyde (PFA) for 5 min at room temperature followed by methanol for 5 min at -20° C were superior to fixation with acetone or PFA only. Finally, we observed that antibody incubation overnight at 4° C yielded more consistent results as compared to staining at room temperature for 5 hours. Finally, we used the optimized method for staining of human fetal and adult intestinal tissue samples. We present the tissue architecture and spatial distribution of the stromal cells and immune cells in these samples visualizing blood vessels, the epithelium and lamina propria based on the expression of α-smooth muscle actin (α-SMA), E-Cadherin and Vimentin, while simultaneously revealing the colocalization of T cells, innate lymphoid cells (ILCs), and various myeloid cell subsets in the lamina propria of the human fetal intestine. We expect that this work can aid the scientific community who wish to improve IMC data quality.

Key terms: Imaging mass cytometry, IMC, Snap-frozen tissue sections, Human intestine, Mass cytometry

Introduction

In recent years, the development of a variety of single-cell technologies increased recognition of cellular heterogeneity both in physiological and pathological contexts. Single-cell technologies based on RNA sequencing and mass cytometry (CyTOF) have been utilized to investigate cellular heterogeneity and identify novel cellular subsets[1, 2], and to discover biomarkers with clinical value[3]. Single-cell mass cytometry employs antibodies conjugated to stable metal isotopes, mostly from the lanthanide series, and is currently able to analyze over 40 different markers simultaneously, allowing an in-depth analysis of immune subsets. However, when analyzing cells isolated from tissue, no spatial information on cell-cell interactions within the tissue is obtained. Imaging mass cytometry (IMC) is an extension of mass cytometry, which couples a laser ablation system with a mass cytometer[4] and therefore has the ability to analyze up to 40 markers in a single tissue section. As such, IMC has the potential to simultaneously characterize the composition of the immune compartment, the spatial relationship between immune cells and stromal cells, and the interactions among immune subsets in tissue sections of choice.

Classical immunohistochemistry or immunofluorescence techniques for cell and tissue imaging provide high spatial resolution at subcellular resolution[5], however, these suffer from limitations including the limited number of markers that can be used simultaneously and tissue auto-fluorescence[6]. IMC does not suffer from background interference as the read-out is provided by the presence of rare earth metals conjugated to antibodies which considerably increase the multiplexing capacity. The IMC laser system ablates the tissue in segments of one by one micrometer which are directed into the mass cytometer using a gas stream, then atomized and ionized followed by determination of the metal-isotope ion content in the on-line time-of-flight mass analyzer[7]. IMC thus offers significant advantages over the current imaging standards. However, care should be taken with the design of the antibody panels as there can be spillover detectable from one mass channel into other channels due to isotopic impurities of the rare metals, usually below 3%[8], and a method has been developed to reduce spillover artifacts and improve the generation of high-quality data[9]. IMC is rapidly becoming widespread as it can aid both basic research and clinical practice[10, 11].

However, the use of IMC is still challenging due to the limited experience with the design and validation of antibody panels and the best tissue processing procedures and staining procedures compatible with the dozens of antibodies that are applied

simultaneously, especially with respect to snap-frozen tissue as most experience to date is with formalin-fixed paraffin-embedded (FFPE) tissue.

Here, we developed a 34 antibody panel for the analysis of snap-frozen tissues by IMC, which contains immune lineage and additional markers to distinguish immune cell subsets in addition to structural markers to reveal tissue organization. This panel can be used to obtain comprehensive spatial information on interactions both between immune cell subsets and between immune cell subsets and stromal components. Furthermore, we developed an optimized fixation and antibody incubation protocol to improve the IMC data quality. We anticipate that this optimized methodology will give guidance to the scientific community in using IMC on snap-frozen tissue to generate high-quality images.

Material and methods

Tissue samples

Fetal tissues were obtained from elective abortions with informed consent. The adult intestinal samples were collected from patients undergoing routine diagnostic endoscopies. Approval by the medical ethical commission of the Leiden University Medical Center (protocol P08.087) was obtained in accordance with the local ethical guidelines and the Declaration of Helsinki. The adult and fetal intestinal samples were embedded in optimal cutting temperature compound, snap-frozen in isopentane (VWR) and stored at -80° C.

Antibody validation and conjugation

Antigens were selected based on previously published single-cell mass cytometry and single-cell RNA sequencing data on the human fetal intestinal samples[1, 12, 13]. Antibodies used for IMC are listed in Table 1. 16 of the 34 antibodies used in the current panel were directly purchased from Fluidigm, which were already conjugated with metals. For the remaining 18 antibodies, BSA-free and carrier-free formulations of antibodies were purchased from different suppliers and initially tested for performance by immunohistochemical staining (IHC) on human fetal intestine and tonsil. Subsequently, antibodies with an appropriate signal intensity were conjugated to lanthanide metals using the MaxPar Antibody Labeling Kit (Fluidigm) following the manufacturer's instructions. Post-conjugation, all antibodies were eluted in 100 µl W-buffer (Fluidigm) and 100 µl antibody stabilizer buffer (Candor Bioscience, Wangen im Allgäu, Germany) supplemented with 0.05% sodium azide.

Optimization of IMC Immunostaining protocol

Here, three variables were tested: 1) Drying condition of freshly prepared snap-frozen tissue sections; 2) Fixation procedures; and 3) Antibody staining conditions. For drying we compared 3 min at room temperature (RT) with 30 min at RT, and 1 hr at 60° C. For fixation we compared methanol for 5 min at -20° C, with 1% PFA for 5 min at RT, 1% PFA for 5 min at RT followed by methanol for 5 min at -20° C, acetone for 10 min at RT, and 4% PFA for 5 min at RT. For antibody incubation we compared 5 hr at RT with overnight at 4° C. We utilized one frozen sample to test each condition and a single antibody mix to stain all section slides. An overview of the experimental set up for the testing of the various conditions is provided in Table 2. All comparisons were performed simultaneously. The following is a step-by-step staining procedure of the IMC procedure utilizing snap-frozen tissue.

Material

- 5 µm fresh snap-frozen sections on silane-coated glass slides (VWR)
- Paraformaldehyde (1%, 4%)
- Methanol
- Acetone
- Superblock solution (Thermo Fisher Scientific)
- DPBS (Gibco)
- Wash buffer (DPBS supplemented with 0.05% Tween and 1% BSA)
- Metal-conjugated antibodies (Table 1)
- Intercalator-Ir (500 µM, Fluidigm)
- Milli-Q water
- Dako Pen (Thermo Fisher Scientific)
- Slide container, 5 slide capacity (VWR)
- Incubation chamber (humid, 4° C and RT)

Stepwise procedure for immunodetection

1. Cut the fresh frozen sections at 5 µm and mount them on silane-coated glass slides
2. Dry the tissue sections for 3 min at RT, 30 min at RT or 1 hr at 60° C
3. Fix the tissue slides without shaking as mentioned above
4. Rinse the slides once, followed by washing the slides twice for 5 min in a container of 5 slide capacity with 25 ml wash buffer
5. Rehydrate the slides for 5 min in container of 5 slide capacity with 25 ml DPBS
6. Wash the slides for 5 min in container of 5 slide capacity with 25 ml wash buffer

7. Use the Dako Pen to draw a circle around the tissue sections to create a barrier to contain the antibody solutions on the tissue sections
8. Apply 100 µl superblock solution to each slide for 30 min at RT
9. Remove excess superblock solution by tapping on a tissue
10. Prepare the antibody cocktail by diluting the antibodies in wash buffer as described in Table 1
11. Add 100 µl of the antibody cocktail to each section and incubate for 5 hr at RT or overnight at 4° C in a humid chamber
12. After the incubation, wash the sections three times for 5 min in container of 5 slide capacity with 25 ml wash buffer
13. Incubate the slides with 100 µl 1:400 dilution of Intercalator-Ir in DPBS for 30 min at RT
14. Rinse the slides once, wash the slides for 5 min in container of 5 slide capacity with 25 ml wash buffer twice
15. Wash the slides for 1 min in container of 5 slide capacity with 25 ml Milli-Q water
16. Dry the slides with an air flow
17. Store the slides at 4° C until ablation on Hyperion

Imaging mass cytometry acquisition

Tissue acquisition was performed on a Helios time-of-flight mass cytometer coupled to a Hyperion Imaging System (Fluidigm). All IMC operation was performed as described using the Hyperion Imaging System (Fluidigm). Briefly, after flushing the ablation chamber with helium, tissues were ablated by a UV-laser spot-by-spot at a resolution of 1 µm and a frequency of 200 Hz. Regions of interest (ROIs) with 1,000 µm x 1,000 µm were selected. We ablated 5~8 ROIs for each tissue section. All raw data were analyzed for marker intensity based on the maximum signal threshold, defines at the 98th percentile of all pixels in a single ROI using the Fluidigm MCD™ viewer (v1.0.560.2). To distinguish the signal from background, we used the Fluidigm MCD™ viewer to visualize our data, based upon which we determined the threshold for each marker individually (between 1 and 2 for majority of immune markers and between 1 and 3 for structural markers) to eliminate background.

Results

To develop the IMC antibody panel, we first evaluated the performance of an antibody panel previously developed for cell suspension mass cytometry[1]. This revealed that 18 out of the 36 antibodies were suitable for IMC on snap-frozen

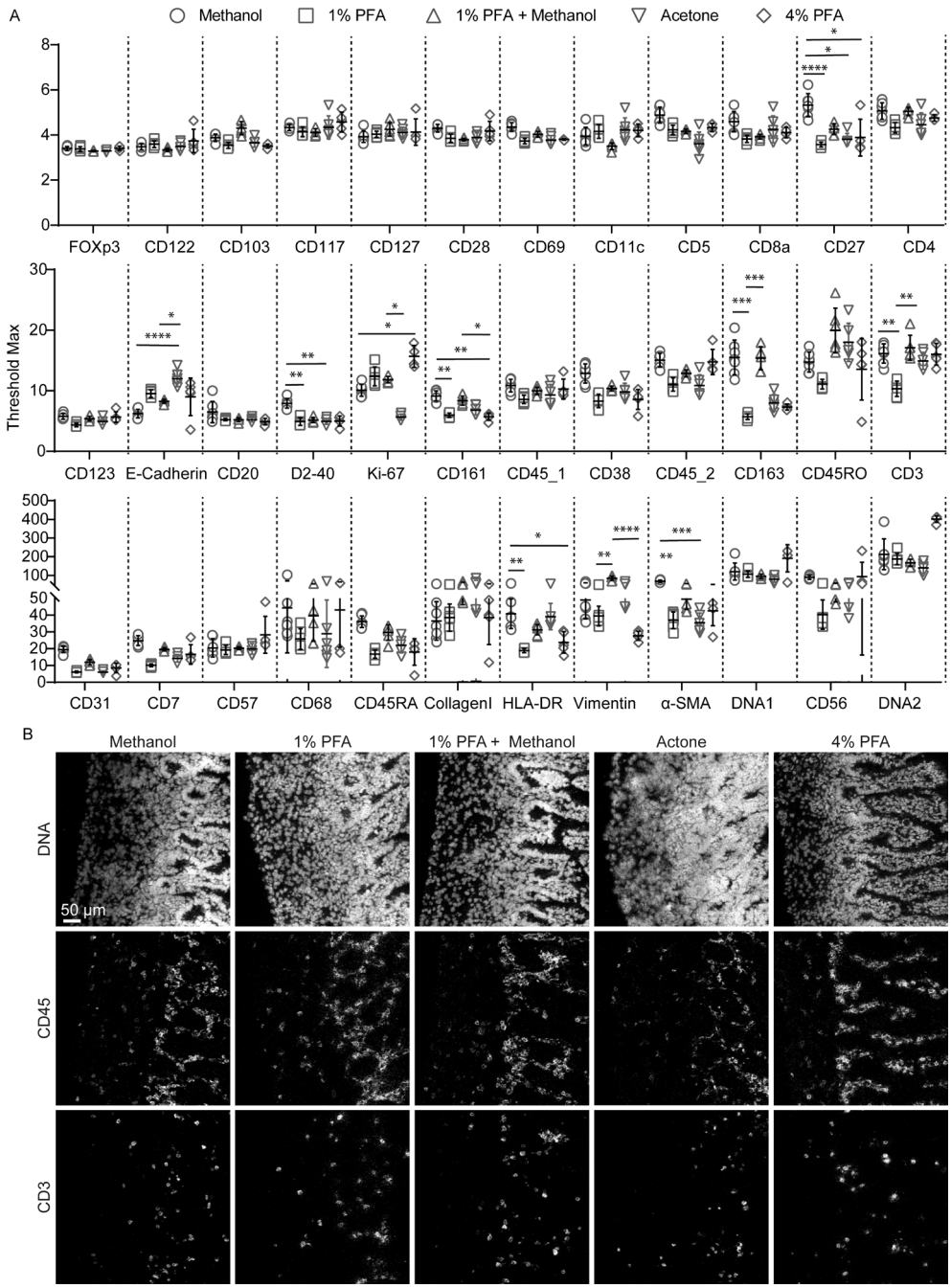

(Figure legend in next page)

Figure 1 Comparison of antibody and nuclear staining between different fixation procedures for IMC within a single tissue block. (A) Comparison of the staining intensity of each antibody depending on the fixation conditions, based on the maximum signal threshold in MCDTM viewer. Black bars indicate median±IQR. Each gray dot represents an individual ROI. *P<0.05 by Kruskal-Wallis test with Dunn's test for multiple comparisons. (B) The markers CD45 and CD3 are representative for the variations observed with the tested incubation conditions. The minimum signal threshold of 2 dual count was set for the nuclear staining, while that was 1.5 for the immune markers.

tissue. Subsequently we continued to select additional antibodies to phenotype immune cells and visualize the tissue structure. All candidate antibodies which required in-house conjugation with metals were initially tested for performance by conventional immunohistochemistry (not shown). Based on this we selected antibodies that displayed a clear signal-to-noise ratio for potential inclusion in the final IMC antibody panel. In total, 80 antibodies were tested, 43 of which performed well on frozen sections. Table 2 lists the 34 antibodies that were finally chosen for inclusion into the IMC antibody panel. Supplementary Table 1 provides information on the performance of the 46 antibodies that were not included in the panel. In order to ensure proper tissue adherence, we determined the influence of the time of drying for the freshly prepared tissue sections. We evaluated the staining obtained with each of the 34 antibodies on tissue sections that were either dried for 3 or 30 min at RT, or for 1 hr at 60 °C. Both visual inspection of the obtained images and comparison of the maximum signal threshold values for each antibody indicated that the staining intensity was comparable with all three drying conditions (Supplementary Figure 1A). We also observed that the signal-to-noise ratio was highly similar with the three tested conditions (Supplementary Figure 1B). Therefore, we conclude that the drying conditions tested are in principle all suitable for IMC on snap-frozen tissue sections.

As tissue fixation is required to preserve antigenic determinants in tissues we first evaluated the protocol provided by Fluidigm[14]. However, we observed that acetone fixation did not yield satisfactory results with respect to the quality of both the nuclear staining and the antibody staining (not shown). Therefore, we proceeded to test additional fixation procedures to optimize signal intensity and signal-to-noise ratio. We tested 5 conditions, using serial sections from a single tissue sample: methanol, 1% PFA, 1% PFA followed by methanol, acetone and 4% PFA and evaluated the staining obtained with the 34 antibodies individually (Figure 1A, B). We observed that none of the tested fixation conditions yielded optimal results for all antibodies in the panel. As expected, we observed inadequate nuclear staining with acetone, incompatible with proper cell identification and cell segmentation analysis (Figure 1B). Moreover, comparison of the maximum signal threshold

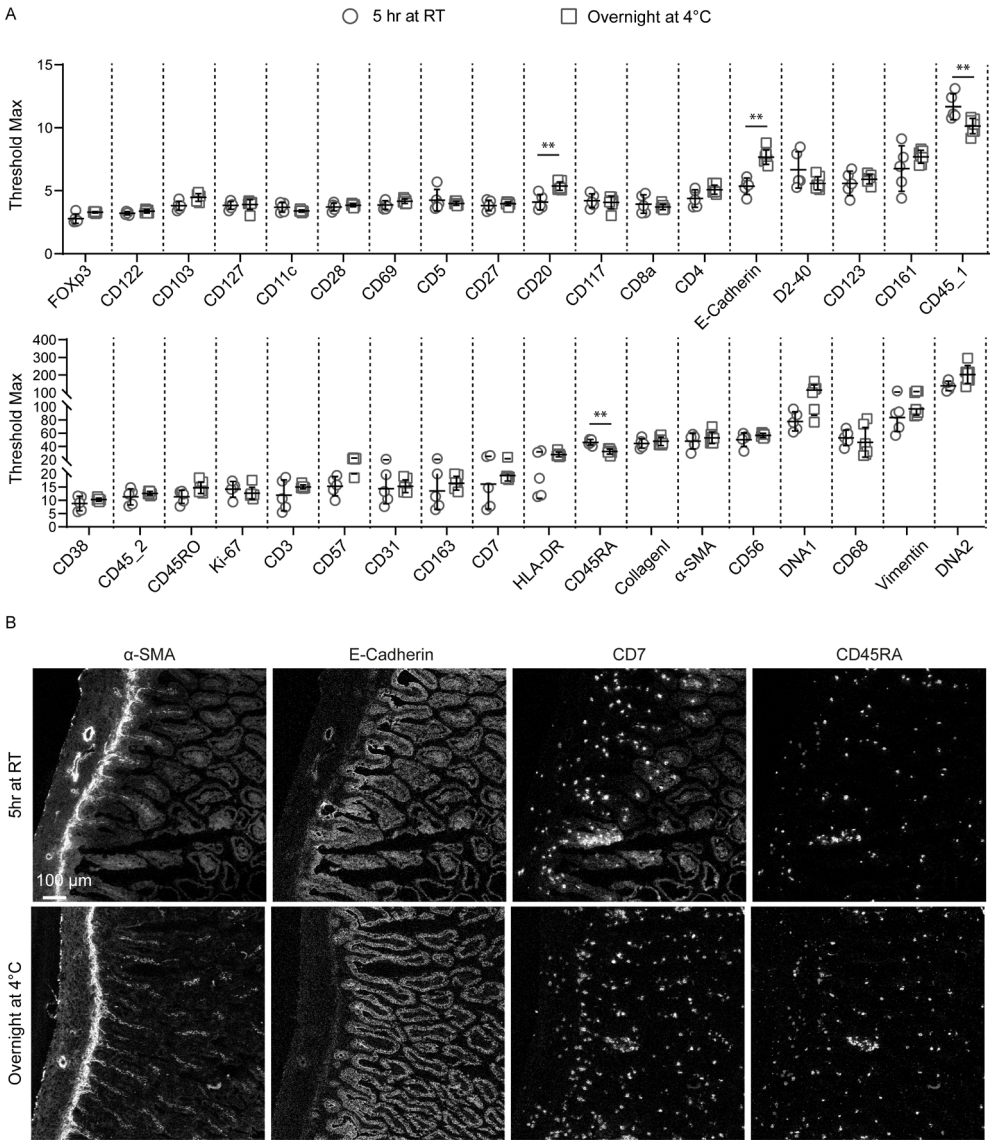

Figure 2 Comparison of antibody performance between two immunodetection conditions for IMC. (A) The staining intensity of each antibody at either 5 hr at room temperature or overnight at 4° C is shown, based on the maximum signal threshold in MCDTM viewer. Black bars indicate median±IQR. Each gray dot represents an individual ROI. **P < 0.01 by Kruskal-Wallis test with Dunn's test for multiple comparisons. (B) The structural markers E-Cadherin, α-SMA and the immune markers CD7, CD45RA are representative for the variations observed with the tested conditions.

values for each antibody indicated that several markers performed relatively poor when either 1% or 4% PFA were used for fixation (e.g. CD161, CD163, CD3, CD7, CD68, HLA-DR, Vimentin, α-SMA) while fixation with methanol or 1% PFA followed by methanol yielded stronger signals. In addition, we observed higher background staining for immune markers (e.g. anti-CD45, clone HI30 and anti-CD3, Figure 1B) in both the acetone and PFA-only samples while the methanol and 1% PFA followed by methanol fixed samples provided superior antibody staining results (Figure 1B). However, the nuclear staining in the lamina propria of the intestine was slightly better in the PFA + methanol samples. Based on these observation, we conclude that fixation with methanol or with the combination of 1% PFA followed by methanol are both preferred for IMC immunodetection of snap-frozen samples.

As staining quality is strongly influenced by duration of and temperature during antibody incubation[15], we tested two different incubation conditions for the individual antibodies in the 34-marker panel: 5 hr at RT or overnight at 4° C, after which the signal intensity and specificity were assessed by IMC for each antibody. We also determined the maximum signal threshold for all antibodies within several ROIs to compare the staining intensity between the two conditions. We found that the staining intensity of many antibodies were similar under both conditions, while a number of markers performed better either at 4° C (anti-CD20 and anti-E-Cadherin) or at RT (anti-CD45_1, and anti-CD45RA) (Figure 2A). However, we observed more variation in the maximum threshold values for the evaluated ROIs stained at RT compared to 4° C and for many antibodies higher background was observed at RT. For example, anti-α-SMA, anti-E-Cadherin and anti-CD7 yielded higher specific staining and lower background after overnight incubation at 4°C compared to a 5 h incubation at RT while several other antibodies performed equally well at both test conditions as observed with anti-CD45RA (Figure 2B). As incubation at 4°C yielded generally better results we decided to use this condition for validation of the full antibody panel.

We next applied the optimized protocol in which the tissue section was dried for 1 hr at 60 °C, followed by fixation with PFA + methanol and antibody panel incubation overnight at 4°C to stain a human fetal intestinal sample with the full 34-antibody panel which included structural tissue markers (Collagen I, E-Cadherin, α-SMA, Vimentin and D2-40) as well as markers to identify various cell types within the lymphoid and myeloid compartments (Table 1). Moreover, the panel allows for the visualization of additional features such as naïve and memory states (CD45RA/RO), cell division (Ki-67), tissue-residency (CD103 and CD69) and expression of cytokine receptors (e.g.,CD122 and CD127) (Figure 3A, B, C).

A

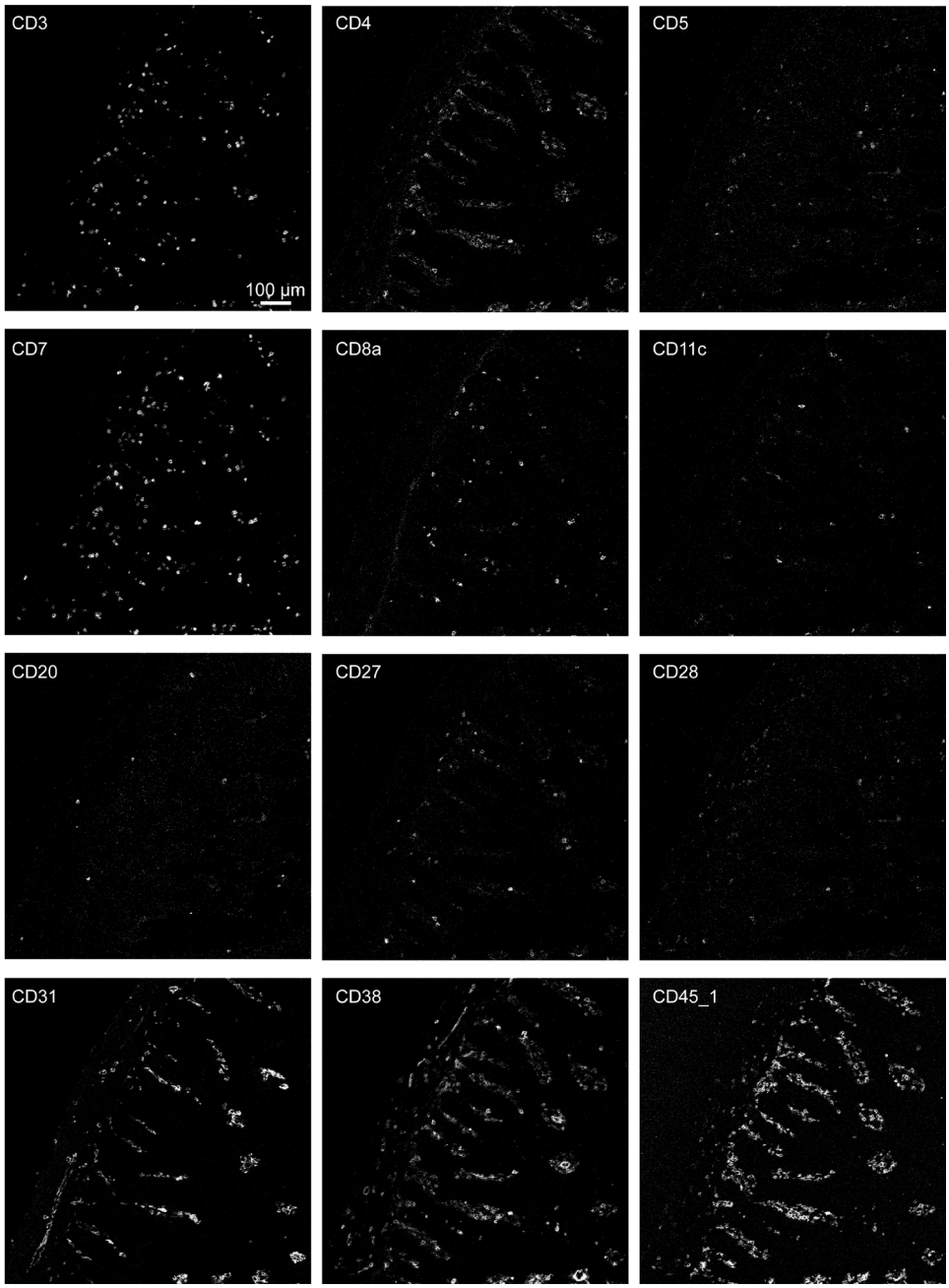

(B in next page)

B

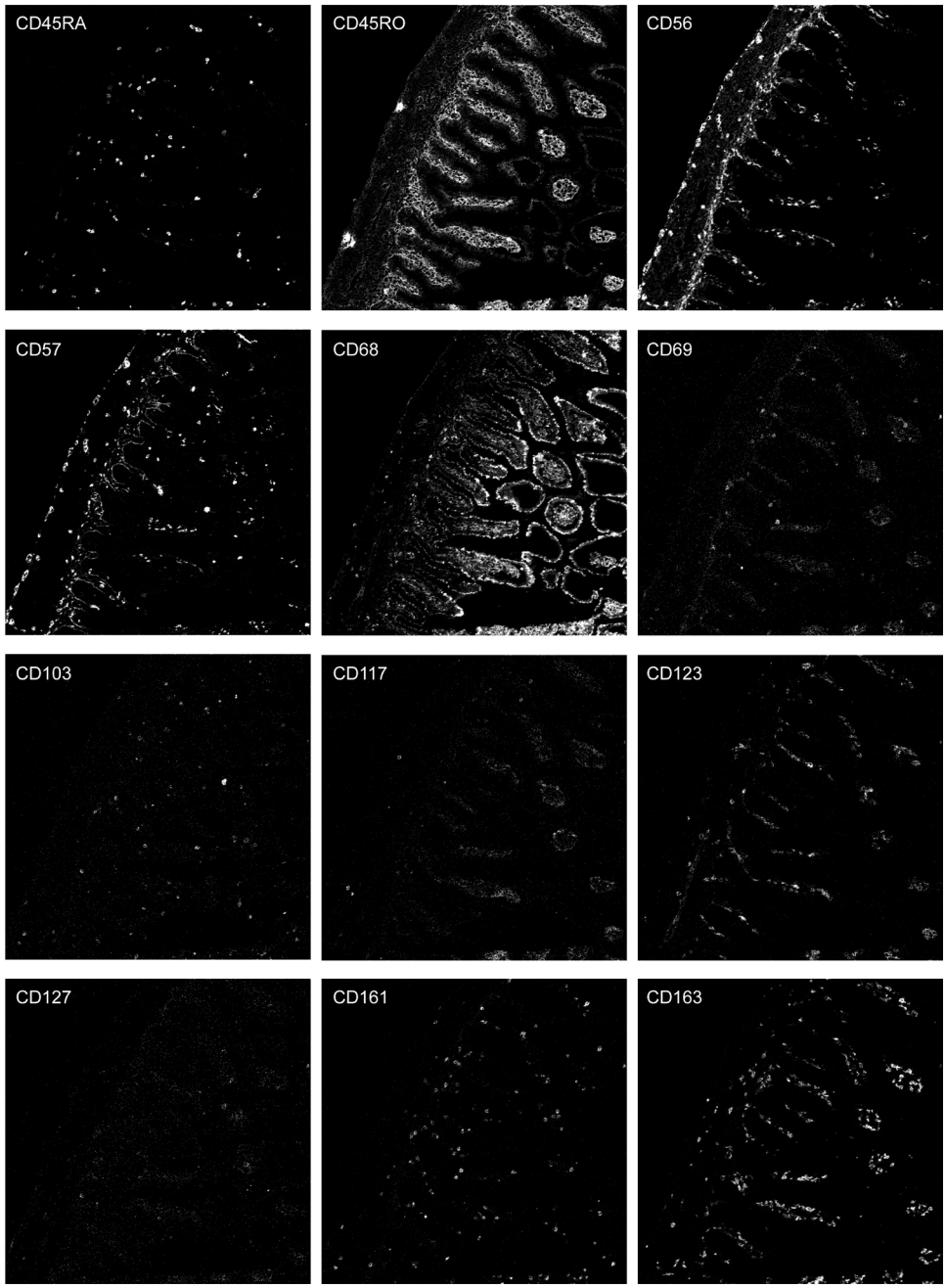

(C in next page)

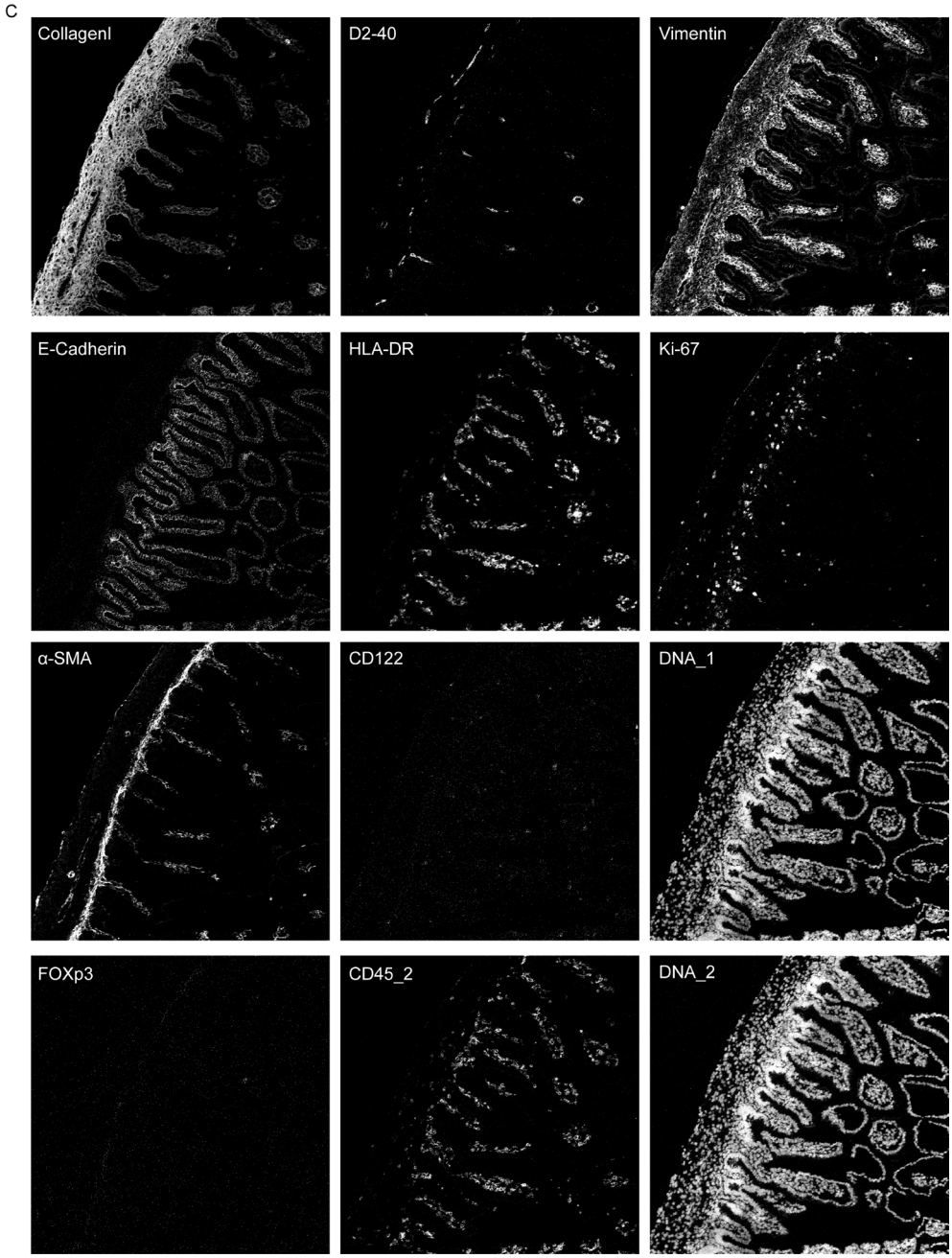

Figure 3 The optimized immunodetection of the 34-marker panel and cell nuclear staining in a single representative ROI for IMC on the human fetal intestine.

Based on the adjusted Threshold Min and Threshold Max in the MCDTM viewer (Table 3), the resulting images were analyzed. Collagen I immunodetection was used to delineate the extracellular matrix of the basement membrane which exhibited the highest staining intensity (Figure 3C). Vessels with smooth muscle lining were detected by the presence of α-smooth muscle actin (α-SMA, Figure 3C and Figure 4A), and CD31 and D2-40 staining (Figure 3A, C). The epithelium and lamina propria were distinguished as Vimentin–E-Cadherin+ and Vimentin+E-Cadherin–, respectively (Figure 4A). Cells of hematopoietic origin were identified with an anti-CD45 specific antibody, revealing that the majority of the immune cells were localized in the lamina propria (Figure 3). To define the spatial distribution of different immune subsets in the human fetal intestine, T cells ($CD3^+CD7^+$), innate lymphoid cells (ILCs, $CD3^-CD7^+$), B cells ($CD20^+$), $CD11c^+$HLA-DR^+ myeloid cells, and macrophages (HLA-DR^+CD163^+), were identified and visualized in a single region of interest (Figure 4B,C). For comparison, the individual stains for DNA, the structural markers E-Cadherin, α-SMA, and Vimentin, as well as the immune markers CD3, CD7, CD20, CD11c, HLA-DR and CD163 are shown in Figure 4D. In Figure 4B a single $CD20^+$ B cells is identified (cyan) while $CD3^+CD7^+$ T cells (yellow) and $CD3^-CD7^+$ ILCs (green) are present both as isolated cells and adjacent to each other (two boxed areas on the left side of the image, Figure 4B). In addition, a white $CD11c^+$ myeloid cells was detected colocalized with a T cell (boxed area on the right side of the image, Figure 4B). Moreover, the visualization of HLA-DR and CD163 reveals the close association of HLA-DR^+CD163^+ macrophages (blue/cyan) with adjacent T cells and ILCs (two boxed area's on the left side of the image, Figure 4C), and several clusters of T cells and HLA-DR+ myeloid cells (Figure 4C). Thus, the optimized approach for snap-frozen tissue analysis with IMC presented here facilitates the simultaneous identification of multiple distinct cells types and distinct colocalization patterns thereof in a single image. In addition we applied the optimized staining protocol with the full antibody panel to two adult intestinal samples, one from a healthy control (Figure 5A) and another from a patient with inflammatory bowel disease (Figure 5B). Here we observed clear tissue structures based on E-Cadherin, α-SMA, Vimentin and DNA staining (Figure 5). Moreover, visualization of the immune lineage markers CD3, CD7, CD20, HLA-DR, CD163 and CD11c revealed the presence and distribution of lymphoid and myeloid immune cell subsets within the tissue context in a single section (Figure 5).

Discussion

We report the development of a 34-antibody panel and an optimized staining protocol for snap-frozen tissue sections for analysis with IMC. Based on staining

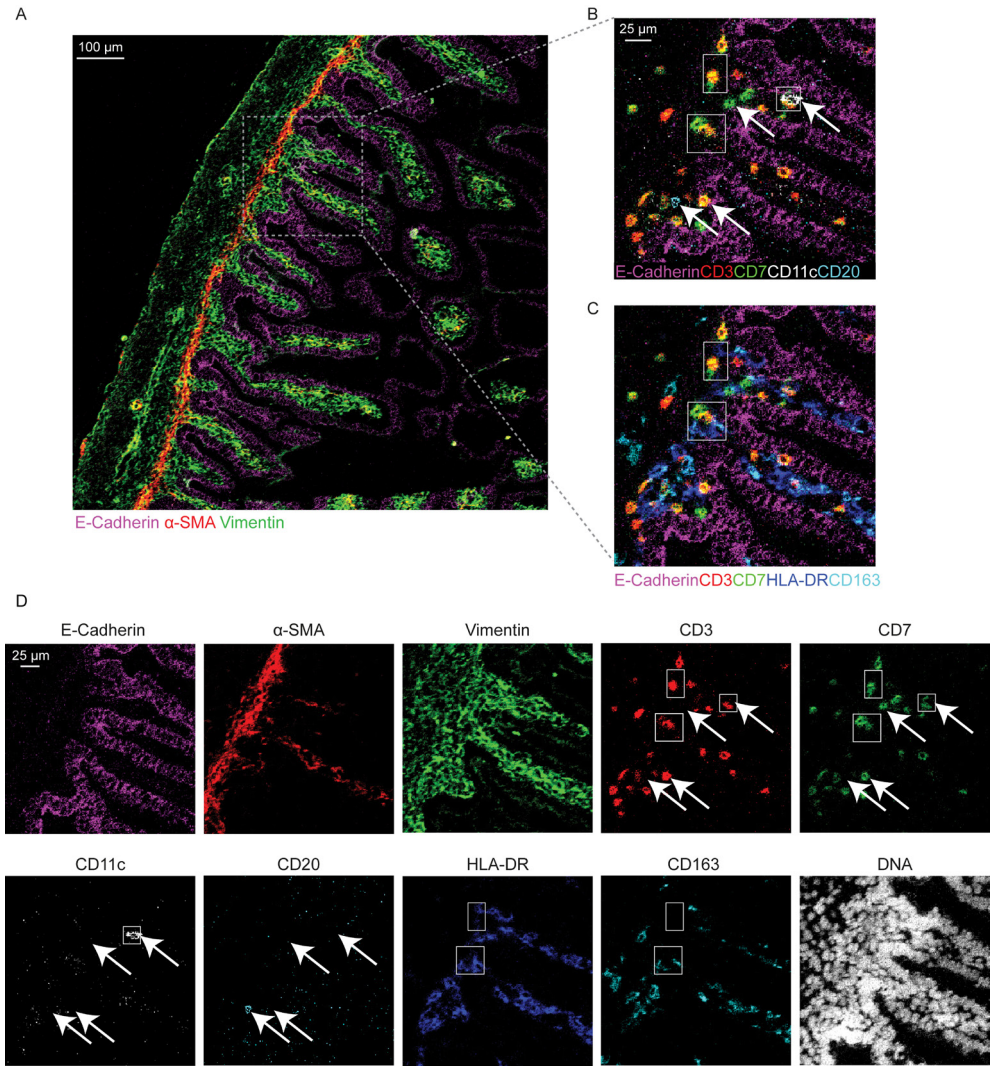

Figure 4 Visualization of the tissue structure and detection of immune cell types in a single region of interest in the human fetal intestine by IMC. (A) Representative mass cytometry image of the fetal intestine showing the overlay of E-Cadherin (magenta), Vimentin (green) and α-SMA (red). (B-D) Identification of immune cell subsets: (B) T cells ($CD3^+CD7^+$), innate lymphoid cells (ILCs, $CD3^-CD7^+$) and B cells ($CD20^+$); (C) myeloid cell ($CD11c^+$) and macrophages ($HLA\text{-}DR^+CD163^+$). The arrows indicate different immune cell types, while the boxes indicate the interaction between ILCs, T cells, and myeloid cells. (D) Individual antibody stains.

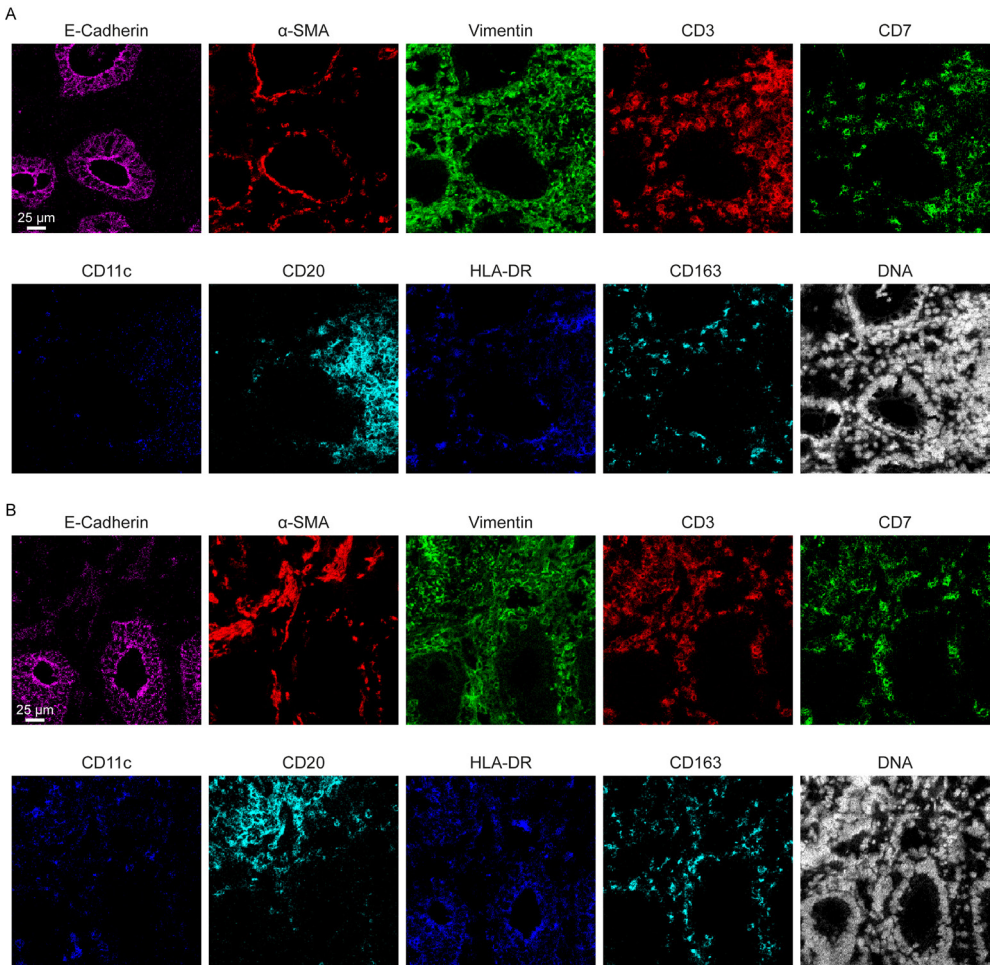

Figure 5 Representative mass cytometry images of 2 adult intestines. (A) The adult intestinal sample from a healthy control. (B) The adult intestinal sample from a patient with inflammatory bowel disease.

intensity and signal-to-noise ratio, we compared different fixation procedures, drying time of the tissue sections and the impact of duration and temperature during the antibody incubation. In principle, IMC is applicable to both FFPE and snap-frozen tissue but most studies so far have used FFPE tissue. In contrast to FFPE, snap-frozen tissue samples do not require antigen retrieval, thus simplifying the immunodetection protocol. Moreover, antibodies that can be used with frozen tissue cannot always be employed with FFPE tissue and vice versa. Thus, it is useful to have both options available. Previously, Chang *et al*. have shown that acetone can be used for the fixation of frozen and FFPE tissue for IMC[14]. However, while we also observed that acetone fixation can be used, the low quality DNA

staining did not allow an optimal cell segmentation analysis. Therefore we compared several fixation procedures that identified methanol or a combination of 1% PFA and methanol as appropriate for snap-frozen samples. While the tested variations in drying condition of the tissue samples did not influence the outcome of the staining procedure, we observed that antibody incubation overnight at 4° C yielded optimal results.

We applied the 34-antibody panel to identify various stromal elements and a variety of immune cell subsets in the human fetal intestine. The localization of collagen I, Vimentin, E-Cadherin and α-SMA allowed the visualization of the major architecture of the tissue sample and distinction of the villi, crypts, basal membrane and lamina propria. Simultaneously, T cells, ILCs and various myeloid cell subsets could be identified as well as interactions between these cell types individually and in clusters of lymphoid and myeloid cells. Here, the specific co-localization of ILCs, T cells and myeloid cells in the lamina propria suggests that the ILCs may somehow modulate the interaction between the T cells and myeloid cells directly. Moreover, recent findings have shown that memory T cells are generated in the human fetal intestine and the specific co-localization of T cells and myeloid cells may ultimately reveal where such memory responses are initiated[16]. Here, additional markers in the antibody panel, like HLA-DR and Ki-67, will likely aid in the identification of activated T cells in *situ*.

In the present study we have used the MCD™ viewer software to visualize the images of the tissue sections. In addition cell segmentation approaches based on the identification of nuclei have been developed to aid in the visualization of IMC data[17, 18] as well as computational approaches to identify and quantify cell-cell interactions like Imacyte and Histocat[19, 20]. Together this allows for an in depth investigation of cellular interactions in a variety of tissues. Thus, IMC offers a major advantage over classical immunohistochemistry techniques which are limited by the numbers of markers that can be included simultaneously. Together with other studies that have developed antibody panels for FFPE tissue[15, 21, 22] this sets the stage for detailed studies to determine immune heterogeneity and cell-cell interactions *in situ*, providing a novel layer of understanding of functioning of the immune system on tissues. We anticipate that our study will guide other researchers that wish to use IMC for analysis of tissue of choice. Here the conditions defined in the present study can be used as a starting point, however, we like to emphasize that every tissue has its own characteristics that may require further optimization for the tissue under investigation.

Ethics Statement

The studies involving human participants were reviewed and approved by Leiden University Medical Center_LUMC (Protocol P08.087). The patients/participants provided their written informed consent to participate in this study. Written informed consent was obtained from the individual(s) for the publication of any potentially identifiable images or data included in this article.

Author contributions

NG, NL and FK conceived the study and wrote the manuscript. NG performed most experiments with the help of VvU. NG performed most of the analyses with the help of VvU, MEI, LFO, AEvdM and NFCCdM. SMCdSL provided human fetal tissues. All authors discussed the results and commented on the manuscript.

Funding

This research was supported by Leiden University Medical Center (NG, VU, MI, LO, AM, SC, NM, FK, and NL), and the China Scholarship Council (NG and NL). FK was supported by the collaboration project TIMID (LSHM18057-SGF) financed by the PPP allowance made available by Top Sector Life Sciences & Health to Samenwerkende Gezondheidsfondsen (SGF) to stimulate public-private partnerships and co-financing by health foundations that are part of the SGF.

Acknowledgments

We thank the Center for Contraception, Abortion and Sexuality (Leiden and The Hague) for collection and provision of fetal material, K. Lodder, T. van Herwaarden, M. Bialecka, and F. Wang for dissection of fetal tissues.

Reference

1. Li, N. et al. Mass cytometry reveals innate lymphoid cell differentiation pathways in the human fetal intestine. J Exp Med 215, 1383-1396 (2018).
2. de Vries, N.L. et al. High-dimensional cytometric analysis of colorectal cancer reveals novel mediators of antitumour immunity. Gut 69, 691-703 (2020).
3. Havel, J.J., Chowell, D. & Chan, T.A. The evolving landscape of biomarkers for checkpoint inhibitor immunotherapy. Nat Rev Cancer 19, 133-150 (2019).
4. Chang, Q. et al. Imaging Mass Cytometry. Cytometry A 91, 160-169 (2017).
5. Lichtman, J.W. & Conchello, J.A. Fluorescence microscopy. Nat Methods 2, 910-919 (2005).
6. Davis, A.S. et al. Characterizing and Diminishing Autofluorescence in Formalin-fixed Paraffin-embedded Human Respiratory Tissue. J Histochem Cytochem 62, 405-423 (2014).
7. Giesen, C. et al. Highly multiplexed imaging of tumor tissues with subcellular resolution by mass cytometry. Nat Methods 11, 417-422 (2014).
8. Bandura, D.R. et al. Mass Cytometry: Technique for Real Time Single Cell Multitarget Immunoassay Based on Inductively Coupled Plasma Time-of-Flight Mass Spectrometry. Anal Chem 81, 6813-6822 (2009).
9. Chevrier, S. et al. Compensation of Signal Spillover in Suspension and Imaging Mass Cytometry. Cell Syst 6, 612-+ (2018).
10. Damond, N. et al. A Map of Human Type 1 Diabetes Progression by Imaging Mass Cytometry. Cell Metab 29, 755-+ (2019).
11. Wang, Y.J. et al. Multiplexed In Situ Imaging Mass Cytometry Analysis of the Human Endocrine Pancreas and Immune System in Type 1 Diabetes. Cell Metab 29, 769-+ (2019).
12. Li, N. et al. Memory CD4(+) T cells are generated in the human fetal intestine. Nat Immunol 20, 301-312 (2019).
13. Li, N. et al. Early-Life Compartmentalization of Immune Cells in Human Fetal Tissues Revealed by High-Dimensional Mass Cytometry. Front Immunol 10, 1932 (2019).
14. Chang, Q., Ornatsky, O. & Hedley, D. Staining of Frozen and Formalin-Fixed, Paraffin-Embedded Tissues with Metal-Labeled Antibodies for Imaging Mass Cytometry Analysis. Curr Protoc Cytom 82, 12 47 11-12 47 18 (2017).
15. Ijsselsteijn, M.E., van der Breggen, R., Sarasqueta, A.F., Koning, F. & de Miranda, N.F.C.C. A 40-Marker Panel for High Dimensional Characterization of Cancer Immune Microenvironments by Imaging Mass Cytometry. Front Immunol 10 (2019).
16. Li, N. et al. Memory CD4(+) T cells are generated in the human fetal intestine. Nat Immunol 20, 301-+ (2019).
17. Sommer, C., Straehle, C., Kothe, U., Hamprecht, F.A. & th Ieee International Symposium on Biomedical Imaging: From Nano to Macro, I. Ilastik: Interactive learning and segmentation toolkit. IEEE Comput. Soc. Conf. Comput. Vis. Pattern Recogn. Proceedings - International Symposium on Biomedical Imaging, 230-233 (2011).
18. Jones, T.R. et al. CellProfiler Analyst: data exploration and analysis software for complex image-based screens. Bmc Bioinformatics 9 (2008).
19. Somarakis, A., Van Unen, V., Koning, F., Lelieveldt, B.P.F. & Hollt, T. ImaCytE: Visual Exploration of Cellular Microenvironments for Imaging Mass Cytometry Data. IEEE Trans Vis Comput Graph (2019).
20. Schapiro, D. et al. histoCAT: analysis of cell phenotypes and interactions in multiplex image cytometry data. Nat Methods 14, 873-876 (2017).
21. Carvajal-Hausdorf, D.E. et al. Multiplexed (18-Plex) Measurement of Signaling Targets and Cytotoxic T Cells in Trastuzumab-Treated Patients using Imaging Mass Cytometry. Clin Cancer Res 25, 3054-3062 (2019).
22. Singh, N. et al. Development of a 2-dimensional atlas of the human kidney with imaging mass cytometry. Jci Insight 4 (2019).

Supplementary Information

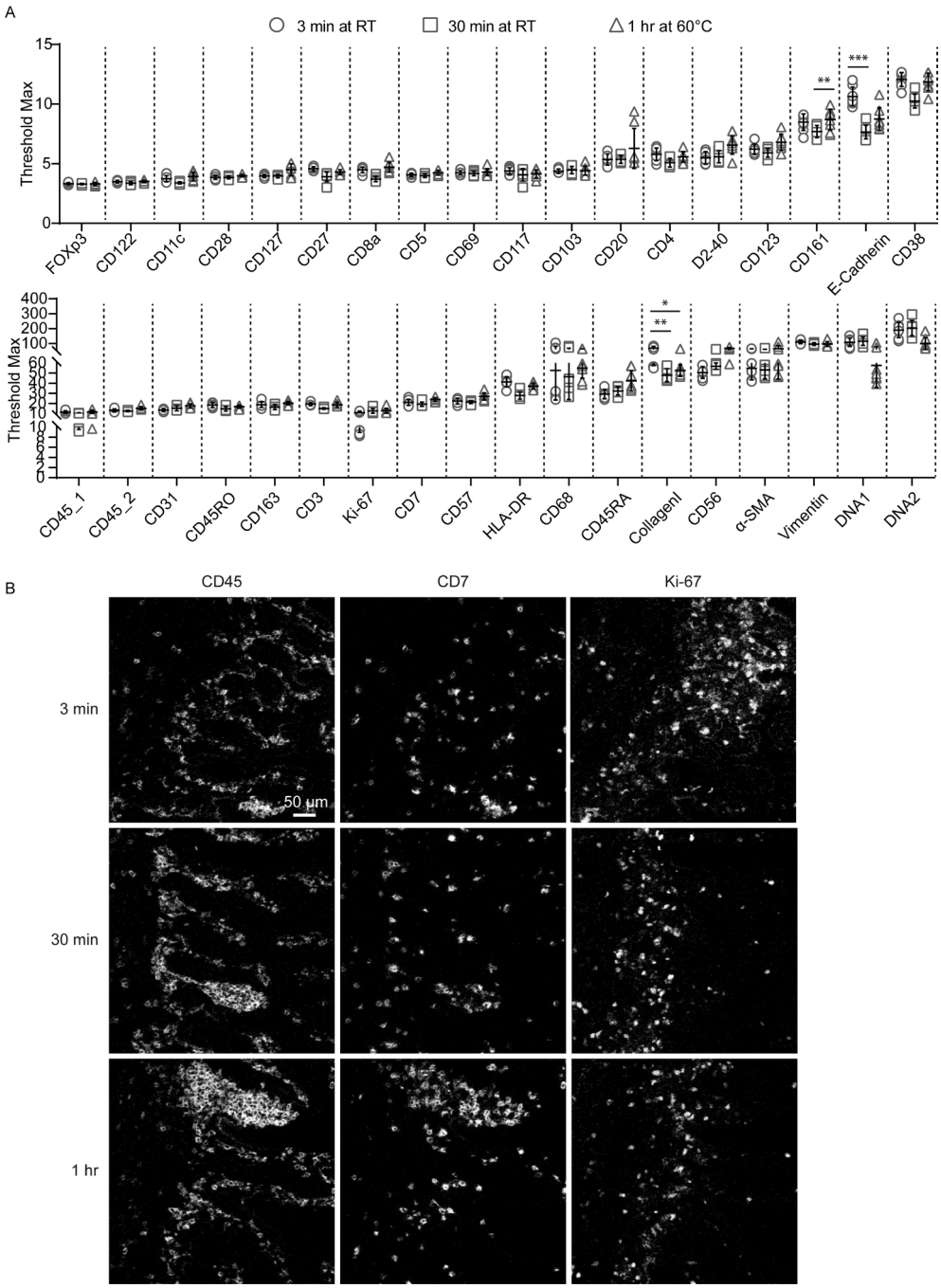

(Figure legend in next page)

Supplementary Figure 1 Comparison of the impact of the drying time of tissue sections on immune marker performance. (A) The staining intensity of each antibody for different drying tissue conditions was determined, based on the maximum signal threshold in MCDTM viewer. Black bars indicate median±IQR. Each gray dot represents an individual ROI. *P<0.05 by Kruskal-Wallis test with Dunn's test for multiple comparisons. (B) The surface markers CD45 and CD3, and the intracellular marker Ki-67 are representative for the variations observed by changing drying time. The minimum signal threshold of 1~2 dual count was set for the immune markers.

Supplementary table 1 Antibody validation for exclusion in the 34-antibody panel for IMC on snap-frozen tissue sections.

	Antigen	Tag	Clone	Supplier	Cat. No	Suitable for IMC
1	CD1a	115In	010	Dako	M357101-2	Yes
2	CD24	198Pt	ML5	BD	555426	Yes
3	CD26	157Gd	BA5b	Biolegend	302702	Yes
4	CD30	158Gd	Ber-H2	Dako	M075101-2	Yes
5	FcεRIα	143Nd	AER-37 (CRA-1)	Biolegend	334602	Yes
6	FOXp3	142Nd	D608R	CST	12653BF	Yes
7	ICOS	143Nd	D6N8TYM	CST	CST89601BF	Yes
8	SOX6	158Gd	polyclonal	Abcam	ab30455	Yes
9	TCRαβ	141Pr	8A3	Thermo Fisher	TCR1151	Yes
10	CCR6	141Pr	G034E3	Fluidigm	3141003A	No
11	CCR7	115In	Y59	Abcam	ab221209	No
12	CCR7	159Tb	G043H7	Fluidigm	3159003A	No
13	CD103	155Gd	Ber-ACT8	Biolegend	350202	No
14	CD11b	209Bi	ICRF44	Fluidigm	3209003B	No
15	CD127	165Ho	AO19D5	Fluidigm	3165008B	No
16	CD127	168Er	EPR2955(2)	Abcam	ab180521	No
17	CD14	160Gd	M5E2	Fluidigm	3160001B	No
18	CD14	Qdot800	TüK4	Thermo Fisher	Q10064	No
19	CD142	194Pt	TF9-10H10	Thermo Fisher	MA1-83495	No
20	CD15	115In	W6D3	Biolegend	323035	No
21	CD16	148Nd	3G8	Fluidigm	3148004B	No
22	CD1a	142Nd	HI149	Sony Biotech	2100510	No
23	CD20	163Dy	2H7	Biolegend	302343	No
24	CD25	149Sm	2A3	Fluidigm	3149010B	No
25	CD34	142Nd	581	Biolegend	343531	No
26	CD74	157Gd	LN2	BD	555612	No
27	CD8b	166Er	SIDI8BEE	BD	14-5273	No
28	CD90	104Pt	5E10	BD	14-0909-82	No
29	C-Kit	143Nd	104D2	Fluidigm	3143001B	No
30	C-Kit	143Nd	D3W6Y	Fluidigm	37805BF	No
31	CRTH2	156Gd	BM16	Biolegend	350102	No
32	Eomes	165Ho	21Mags8	BD	14-4876-82	No
33	Granzyme B	141Pr	EPR20129-217	Abcam	ab219803	No
34	IgM	150Nd	MHM88	Biolegend	314527	No
35	KLRG-1	161Dy	REA261	MACS	120-014-229	No
36	NKp44	147Sm	P44-8	Biolegend	325102	No
37	NKp44	147Sm	253415	R&D System	MAB22491	No
38	NKp46	174Yb	n1D9	Abcam	ab14823	No
39	NKp46	174Yb	9E 2	Biolegend	331902	No
40	PD-1	175Lu	EH 12.2H7	Fluidigm	3175008B	No
41	RORγt	156Gd	AFKJS-9	BD	14-6988-82	No
42	SLPI	110Pd	31	Abcam	ab17157	No
43	Tbet	149Sm	D6N88	Fluidigm	13232BF	No
44	TCRγδ	152Sm	B1	Biolegend	331202	No
45	TCRγδ	152Sm	11F2	Fluidigm	3152008B	No
46	TIGIT	143Nd	MBSA430	BD	16-9500-82	No
Cell Signaling Technology (CST), Sony Biotechnology (Sony Biotech)						

Tables

Table 1 The 34-marker panel on the snap-frozen section for imaging mass cytometry.

	Antigen	Tag	Clone	Supplier	Cat. No	Dilution
1	CD45	89Y	HI30	Flui	3089003B	1/50
2	D2-40	115In	D2-40	BioL	916606	1/50
3	FOXp3	142Nd	D608R	CST	12653BF	1/50
4	CD69	144Nd	FN50	Flui	3144018B	1/50
5	CD4	145Nd	RPA-T4	Flui	3145001B	1/50
6	CD8a	146Nd	RPA-T8	Flui	3146001B	1/50
7	Collagen I	147Sm	Polyclonal	Millipore	AB758	1/100
8	αSMA	148Nd	1A4	CST	CST5685BF	1/200
9	CD31	149Sm	8 9C2	CST	CST3528BF	1/100
10	E-cadherin	150Nd	24 E 10	CST	CST3195BF	1/50
11	CD123	151Eu	6H6	Flui	3151001B	1/50
12	CD7	153Eu	CD7-6B7	Flui	3153014B	1/100
13	CD163	154Sm	GHI/61	Flui	3154007B	1/100
14	CD103	155Gd	EPR4166	Abcam	ab221210	1/50
15	CD127	156Gd	R34.34	Beckman	18LIQ494	1/50
16	CD122	158Gd	TU27	BioL	339015	1/25
17	CD68	159Tb	KP1	Flui	3159035D	1/200
18	CD5	160Gd	UCHT2	BioL	300627	1/25
19	CD20	161Dy	H1	Flui	3161029D	1/50
20	CD11c	162Dy	Bu15	Flui	3162005B	1/50
21	CD45	163Dy	D9M81	CST	13917BF	1/200
22	CD161	164Dy	HP-3G10	Flui	3164009B	1/50
23	CD117	165Ho	104D2	BioL	313202	1/50
24	Ki-67	166Er	D3B5	CST	CST 9129BF	1/200
25	CD27	167Er	O323	Flui	3167002B	1/50
26	HLA-DR	168Er	L243	BIoL	307651	1/800
27	CD45RA	169Tm	HI100	Flui	3169008B	1/100
28	CD3	170Er	UCHT1	Flui	3170001B	1/100
29	CD28	171Yb	CD28.2	BioL	302937	1/50
30	CD38	172Yb	HIT2	Flui	3172007B	1/100
31	CD45RO	173Yb	UCHL1	BioL	304239	1/50
32	CD57	174Yb	HNK-1/Leu-7	Abcam	Ab212403	1/100
33	Vimentin	175Lu	D21H3	CST	CST5741BF	1/200
34	CD56	176Yb	NCAM16.2	Flui	3176008B	1/50
Fluidigm (Flui), Cell Signaling Technology (CST) and Biolegend (BioL)						

Table 2 The experimental set up of the testing of the various conditions.

Slide Nr	Slide Drying			Fixation					Panel Incubation	
	3 min	30 min	1 hr	Methanol	1% PFA	1% PFA + methanol	Acetone	4% PFA	5 hr at RT	Over-night at 4° C
1	+	-	-	-	-	+	-	-	-	+
2	-	+	-	+	-	-	-	-	-	+
3	-	+	-	-	+	-	-	-	-	+
4	-	+	-	-	-	+	-	-	-	+
5	-	+	-	-	-	-	+	-	-	+
6	-	+	-	-	-	-	-	+	-	+
7	-	+	-	-	-	+	-	-	+	-
8*	-	-	+	-	-	+	-	-	-	+

***** Conditions applied to slide #8 represent the optimal staining protocol.

Table 3 The signal-to-noise ratio of individual antibody under optimal staining protocol.

Antigen	Channel	Threshold Min	Threshold Max	Signal-to-noise ratio
CD3	170Er	1.00	17.94	17.94
CD4	145Nd	1.50	5.41	3.61
CD5	160Gd	1.50	4.17	2.78
CD7	153Eu	1.50	21.97	14.65
CD8a	146Nd	1.50	4.60	3.07
CD11c	162Dy	1.00	4.42	4.42
CD20	161Dy	2.00	5.08	2.54
CD27	167Er	1.00	4.93	4.93
CD28	171Yb	1.00	3.99	3.99
CD31	149Sm	2.00	18.62	9.31
CD38	172Yb	1.50	12.01	8.01
CD45_1	89Y	1.50	9.66	6.44
CD45RA	169Tm	2.00	32.74	16.37
CD45RO	173Yb	3.00	17.60	5.87
CD56	176Yb	5.00	61.80	12.36
CD57	174Yb	5.00	22.25	4.45
CD68	159Tb	5.00	66.47	13.29
CD69	144Nd	1.50	4.20	2.80
CD103	155Gd	1.50	4.16	2.77
CD117	165Ho	1.00	4.58	4.58
CD123	151Eu	1.50	6.46	4.31
CD127	156Gd	2.00	4.32	2.16
CD161	164Dy	1.50	7.42	4.95
CD163	154Sm	2.00	23.10	11.55
Collagen I	147Sm	3.00	46.60	15.53
D2-40	115In	3.00	6.56	2.19
Vimentin	175Lu	5.00	94.23	18.85
E-cadherin	150Nd	1.50	7.89	5.26
HLA-DR	168Er	3.00	41.36	13.79
Ki-67	166Er	2.00	11.69	5.85
α-SMA	148Nd	3.00	46.20	15.40
CD122	158Gd	1.00	3.48	3.48
DNA1	191Ir	3.00	44.85	14.95
FOXp3	142Nd	2.00	3.10	1.55
CD45_2	163Dy	2.00	14.10	7.05
DNA2	193Ir	3.00	76.37	25.46

*The Threshold Max represents signal energy, while the Threshold Min represents noise energy for per marker in MCD™ Viewer. So Signal-to-noise ratio = Threshold Max / Threshold Min

Chapter 3

Immune subset-committed proliferating cells populate the human foetal intestine throughout the second trimester of gestation

Nannan Guo[1], Na Li[1,2], Li Jia[1], Qinyue Jiang[1], Mette Schreurs[1], Vincent van Unen[1,3], Susana M. Chuva de Sousa Lopes[4], Alexandra A. Vloemans[1], Jeroen Eggermont[5], Boudewijn Lelieveldt[5], Frank J.T. Staal[1], Noel F. C. C. de Miranda[6], M. Fernanda Pascutti[1 *], Frits Koning[1 *]

[1]Department of Immunology, Leiden University Medical Center, Leiden, The Netherlands
[2]State Key Laboratory of Zoonotic Diseases, Institute of Zoonoses, College of Veterinary Medicine, Jilin University, Changchun, China
[3]Institute for Immunity, Transplantation and Infection, Stanford University, Stanford, CA, United States
[4]Department of Anatomy, Leiden University Medical Center, Leiden, The Netherlands
[5]Department of Radiology, Leiden University Medical Center, Leiden, The Netherlands
[6]Department of Pathology, Leiden University Medical Center, Leiden, The Netherlands

[*] Equal contribution

Nature Communications 2023, 10;14(1):1318

Summary

The intestine harbors the largest immune compartment in the human body, yet how it is formed and organized during human fetal development is largely unknown. Here, we have analyzed a large number of human fetal intestinal samples from week 14 through week 22 of gestation. Spectral flow cytometry indicated that at week 14 of gestation, the fetal intestine was mainly populated by myeloid cells and three distinct $CD3^{-}CD7^{+}$ ILCs subsets, followed by rapid appearance of adaptive CD4, CD8 T and B cell subsets in time. Ki-67^{+} cells were observed in all identified immune subsets as early as week 14 and up to week 22. Imaging mass cytometry (IMC) confirmed the presence of Ki-67^{+} cells in *situ* and identified lymphoid follicles (LFs) from week 16 onwards, which contained $CD3^{-}CD7^{+}$ ILCs, T, B and myeloid cells in a villus-like structure covered by epithelium. Moreover, a proportion of $CD3^{-}CD7^{+}$ ILC and T cells shared a $CD69^{+}CD117^{+}CD161^{+}CCR6^{+}CD127^{+}$ phenotype, resided within the LFs, and harbored Ki-67^{+} cells. *In vitro* proliferation of fetal intestinal lymphoid subsets was observed both in unstimulated conditions and with IL-7. Overall, these observations demonstrate the presence of immune subset-committed cells capable of local proliferation in the developing human fetal intestine, likely contributing to the development and growth of organized immune structures throughout most of the 2^{nd} trimester, and preparing the infant for the microbial colonization right after birth.

Key terms: Imaging mass cytometry, IMC, mass cytometry, CyTOF, spectral flow cytometry, human fetal intestine, proliferating cells

Introduction

The developing human fetus generates tolerogenic and protective immune responses, in preparation for antigen exposure during pregnancy and after birth[1]. Multiple immune cell types develop and mature at different gestational stages, and diverse immune cells seed lymphoid and peripheral organs, including lymph nodes, skin, intestine, kidney and lung[1, 2, 3]. The intestine represents the largest compartment of the immune system. Immunohistochemistry (IHC) analysis of human fetal intestinal samples has shown that T cells are detectable in the lamina propria and epithelium from 12-14 weeks of gestation and T cells increase in abundance afterwards[4]. Moreover, evidence for co-localization of T and B cells has been presented[5, 6]. Nevertheless, the development and complexity of the immune compartment during human fetal life is understudied for reasons of scarcity of material and ethical concerns.

Lymphoid tissues are important locations for the initiation of adaptive immune responses[7], and their formation requires interaction between lymphoid-tissue inducer cells (LTi) and stromal cells[8, 9, 10]. B cells also contribute to the maturation of gut-associated lymphoid tissues (GALT), including Peyer's patches (PP) and isolated lymphoid follicles (ILFs)[11]. In the intestinal mucosa, antigen-presenting cells (APCs) and in particular dendritic cells (DCs) are located throughout the intestinal lamina propria, and can recruit naive T cells to the different lymphoid tissues[12, 13]. In addition, memory $CD4^+$ T cells were frequently observed in the human fetal intestine[14], and fetal intestinal $TNF\text{-}\alpha^+CD4^+$ T cells promote mucosal development[15, 16].

Improvements in high-dimensional imaging and flow cytometry techniques provide new opportunities to map the niche and development of the human fetal intestinal immune compartment with higher resolution than ever before. Here we used multi-parametric spectral flow cytometry to determine the composition of the fetal immune system throughout a major part of the 2^{nd} trimester. Furthermore, we have combined this with an imaging mass cytometry (IMC)-based approach to gain detailed insight into the spatial localization of the fetal intestinal immune system in the tissue context in time[17, 18]. The results indicate dynamic changes in the composition of the fetal intestinal immune system, the continuous presence of proliferation-associated $Ki\text{-}67^+$cells in all detected immune subsets and the early formation of lymphoid follicles (LFs) harboring B cells, as well as various types of innate lymphoid cells (ILCs), T cells and myeloid cells. In addition, $Ki\text{-}67^+$ cells were frequently observed in such LFs. Moreover, we observed that subsets of $CD3^-$

$CD7^+$ ILCs, $CD4^-CD8a^-$, $CD4^+$ and $CD8a^+$ T cells displayed a shared phenotype characterized by the expression of CD69, CD117, CD161 and CCR6 and that these cells were preferentially found in the LFs.

Together these results point very early formation of complex lymphoid structures in the human fetal intestine and suggest that local proliferation of immune subset-committed cells contributes to the development and growth of organized immune structures throughout most of 2^{nd} trimester.

Methods

Sample processing and cell isolation

The human fetal material used in this work was obtained from elective abortions (without medical indication) with signed informed consent from all donors. The work described here was reviewed and approved by the Medical Ethical Committee of Leiden University Medical Centre (P08.087). The gestational age ranged from 14 to 22 weeks. The small intestine and colon were separated from mesentery, cut into small pieces, embedded in optimal cutting temperature compound, snap-frozen in isopentane and stored at -80 °C. The remainder of the material was used for single-cell isolation as described previously[19]. Briefly, after clearing of meconium, fetal intestines were cut into small fragments in a petri dish, then incubated in 15 mL 1 mM dithiothreitol (Fluka) for 10 min twice at room temperature, and then incubated with 1 mM ethylenediaminetetraacetic acid (Merck) for 1 hour twice at 37 °C under rotation to acquire intraepithelial lymphocytes (IELs). To obtain single-cell suspensions from the lamina propria, the intestines fragments were enzymatically digested with 10 U/mL collagenase IV (Worthington) and 200 µl/mL DNAseI grade II (Roche Diagnostics) in 15 mL of Hank's balanced salt solution (ThermoFisher Scientific) overnight at 37 °C. After incubation, the cell preparations were filtered through a 70 µm cell strainer (Corning) followed by washing of the cells with Iscove's Modified Dulbecco's Medium (IMDM, Lonza). Isolated cells were then purified with a Percoll gradient (GE Healthcare). Purified cells were cryopreserved in liquid nitrogen until time of analysis in 90% FCS and 10% dimethyl sulfoxide (DMSO) (Merck). All experiments were conducted in accordance with local ethical guidelines and the principles of the Declaration of Helsinki.

Spectral Flow cytometry immunophenotypic studies

The 26-antibody flow cytometry-based panel was developed for in-depth immunophenotyping of the major cell subsets present in the human fetal intestine

through time. In total, 3 experiments were performed for immunophenotypic studies of 28 human fetal intestinal samples. Antibodies used for spectral flow cytometry with a 5-laser Cytek® Aurora are listed in Supplementary Table 1. For surface staining, single-cell suspensions of fetal intestinal samples were incubated with fluorochrome-conjugated antibodies and human Fc block (BioLegend) for 30 min at 4 °C. After washing, cells of samples were then fixed/permeabilized using Foxp3 Staining Buffer Set, according to manufacturer's instructions (ThermoFisher). For intracellular staining, the fixed/permeabilized cells were incubated with the antibodies for 45 min at 4 °C, followed by washing of the cells with permeabilization buffer. Then the stained cells were resuspended. Reference samples were incorporated and individually stained by UltraComp eBeads™ Compensation Beads (ThermoFisher), PBMCs or cells from human tonsils. After the completion of the sample preparation, the samples were immediately acquired using a 5-laser Cytek® Aurora (BD Biosciences). Data were analyzed to check quality with FlowJo software version 10.6 (Tree Star Inc). We utilized OMIQ to perform the high-dimensional analysis for human fetal intestinal samples (https://www.omiq.ai/).

Imaging Mass Cytometric Immunostaining, Acquisition and Analysis

Antibodies and staining procedures used on the human fetal intestine for IMC were optimized from the antibody panel and protocol developed in a previous publication[18]. IMC immunostaining was performed on frozen human fetal intestine samples in three independent experiments, and antibodies used for each IMC are listed in Supplementary Table 2-4. The carrier-free formulations of antibodies were conjugated to lanthanide metals using the MaxPar Antibody Labeling Kit (Fluidigm) following the manufacturer's instructions. We dried the tissue section for 1 h at 60 ° C, followed by fixation with paraformaldehyde (PFA) for 5 min at RT, then cold methanol for 5 min at -20° C. Then, the samples were incubated with the antibody panel at 4°C overnight. Next, tissue acquisition was performed on a Helios time-of-flight mass cytometer coupled to a Hyperion Imaging System (Fluidigm). All IMC operations were performed as described using the Hyperion Imaging System (Fluidigm). All raw data were analyzed for marker intensity based on the maximum signal threshold, defined at the 98th percentile of all pixels in a single ROI using Fluidigm MCD™ viewer (v1.0.560.2).

We developed the computational tool "Cytosplore Imaging" to analyze multiple markers simultaneously to perform pixel analysis for IMC data. Cytosplore Imaging facilitates the complete exploration pipeline in an integrated manner in a ROI (Supplementary Fig. 5). Data analysis in Cytosplore Imaging included the

following steps: We applied the arcsin transformation with a cofactor of five upon loading the data sets (ome.TIFF files) exported from Fluidigm MCD™ viewer. Next, we applied an HSNE analysis[20] on 2.5 × 10^5 pixels from an ROI and defined the markers used for the similarity computation: CD45, D2-40, Collagen I, αSMA, CD31, E-cadherin, CD123, CD7, CD163, CD20, CD11c, CD161, Ki-67, HLA-DR, CD45RA, CD3, CD57, vimentin and CD56. Based on marker expression (Supplementary Fig. 5a), we could distinguish tissue pixels from background pixels and projected each population on the imaging viewer (Supplementary Fig. 5b). Next, we selected tissue pixels and zoomed in on these through a new HSNE analysis to visualize the structural components and identify immune cells located in the human fetal intestine (Supplementary Fig. 5c, d). Finally, we focused on $CD45^{+/dim}$ pixels and performed a t-SNE analysis clustering for the immune markers: CD45, CD3, CD7, CD20, HLA-DR, CD163, CD11c, CD161, CD45RA (Supplementary Fig. 75e). Using this approach, we could visualize T cells, $CD3^{-}CD7^{+}$ cells, B cells, $CD163^{+}$ macrophages, Lin^{-}HLA-DR^{+} myeloid cells and E-$cadherin^{+}$ epithelial cells simultaneously in a single region (Fig. 3f, g).

Cell Proliferation Assays by spectral flow cytometry

After thawing, single-cell suspensions of fetal intestinal samples were kept in a pre-warmed PBS buffer. We prepared CellTrace™ Violet stock solution in 5 mM by DMSO (ThermoFisher). Cells were incubated with 2 mL of 1250 nM CellTrace™ Violet dye in PBS buffer for 8 min at 37° C. Then 10 mL IMDM (Lonza) supplemented with 10% FCS was added and incubated at RT for 5 min. Next, cells were spun down at 1500 rpm for 10 min, and cells were resuspended in 6 mL pre-warmed IMDM (Lonza) supplemented with 10% FCS medium at RT for 10 min before seeding in a 96-well cell culture plate. Cells were maintained in culture medium (IMDM supplemented with 10% human serum) or in culture medium containing 25 ng/mL IL-7 (Peprotech) for 4 days. The phenotype of generated progeny as well as proliferation were determined by flow cytometry. Details on antibodies used are listed in Supplementary Table 5. After the cell surface and intracellular staining as described before, cells were acquired on a 5-laser Cytek® Aurora (BD Biosciences). Four independent experiments were performed for four fetal intestinal samples, and PBMC samples were included as a control. Data was analyzed with FlowJo software version 10.6 (Tree Star Inc).

TREC analysis

DNA was extracted from fetal cells and used in a the δREC-ψJα TREC analysis. 50 ng total DNA was used in qPCR experiments as described by van der Weerd et al[21], using the following primers and probes on a

TaqMan lightcycler: sj TREC ψJα-δREC_F:CCATGCTGACACCTCTGGTT; sjψJα-δREC_R: TCGTGAGAACGGTGAATGAAG; sj TRECψJαδREC_T:[FAM] CACGGTGATGCATAGGCACCTGC[TAM]probe; cjψJαδREC_F:AAGCAACATCAC TCTGTGTCTAGCAC;cjψJα-δREC_R: AATTCTGCCAAATATTACTTACTTGCTGAG; cjψJα-δREC_T [FAM]CCAGAGGTGCGGGCCCCA[TAM] probe and genomic albumin primers/probe ALB_F: TGAAACATACGTTCCCAAAGAGTTT ALB_R: CTCTCCTTCTCAGAAAGTGTGCATAT; ALB_T [FAM] TGCTGAAACATTCACCTTCCATGCAGA[TAM]. Data were calculated as Ct and number of divisions reported as described[22].

Cytokine production analysis by spectral Flow cytometry

After staining with CellTrace™ Violet dye as described before, single-cell suspensions of fetal intestinal samples and PBMCs samples were seeded into 96-well round-bottom plates in IMDM/L-glutamine medium (Lonza) complemented with 10% human serum with or without 25 ng/mL IL-7 for 2 days at 37°C. Brefeldin A solution (10 ng/mL, Sigma-Aldrich) was added for the final 5 hours. PBMCs stimulated with anti-CD3 antiCD28 agonist antibodies (2.5 µg/ml each, BioLegend) for the final 6 hours were included as a control. The flow cytometry antibody panels were designed to detect granzyme B, IL-2, IL-17A, CD40L, IFNγ and TNF-α production in identified immune subsets at day 2 by the Cytek® Aurora (BD Biosciences). Four independent experiments were performed. Details on the flow cytometry antibodies are available in Supplementary Table 6. Data was analyzed with FlowJo software version 10.6 (Tree Star Inc). All statistics were analyzed using GraphPad Prism8 software.

Results

Identification of Ki-67-positive cells within all immune subsets in the developing human fetal intestine

To investigate the development of the human fetal intestinal immune compartment in time, we applied a 26-antibody flow cytometry panel to single-cell suspensions of intestinal samples from gestational weeks 14 to 22 (antibodies listed in Supplementary Table 1). We pooled the spectral flow cytometer-acquired data on $CD45^+$ immune cells of all samples (2.6 million cells) in a single analysis with optSNE.

Based on marker expression profiles (Fig. 1a), seven major immune cell populations were identified, corresponding to $CD3^+CD4^+$ T cells, $CD4^+CD25^+CD127^-FoxP3^+$ T regulatory cells (Tregs), $CD3^+CD8^+$ T cells, $CD3^+CD4^-CD8^-$ double-negative (DN)

T cells, $CD20^+HLA\text{-}DR^+$ B cells, $CD3^-CD7^+$ ILCs and $CD11c^+$ myeloid cells (Fig. 1b, Supplementary Fig. 1-2). As we have reported previously[14], we observed a dominant presence of $CD4^+FOXP3^-$ conventional T cells in the fetal intestine, approximately 50% of which expressed CD161 and CD45RO while lacking CCR7 and CD45RA, indicative of a $CD161^+$ effector memory T cell type (T_{EM}) (Fig. 1a). All $CCR7^-CD45RA^-$ T_{EM} cells were $CD127^+$ and $CD69^+$, and differential expression of CD117 and CCR6 was observed (Fig. 1a), reflecting additional phenotypic diversity. The remainder of the $CD4^+$ conventional T cell population expressed CCR7, implying a $CD45RA^+$ naive T cell (T_N) or central $CD45RO^+$ memory T cell (T_{CM}) phenotype (Fig. 1a).

Moreover, three clusters of $CD8^+$ T cells (a. $CCR7^+CD8\alpha^+CD8\beta^+$, b. $CCR7^-CD8\alpha^+CD8\beta^+$ and c. $CD8\alpha^+CD8\beta^-$), and a single DN T cell cluster were observed (Fig. 1a, b). Also, the differential expression of CD8α, CD25, CD45RA, CD117, CD127, RORγt and CCR6 revealed the presence of three distinct subpopulations of $CD3^-CD7^+$ ILCs, one of which expressed CD117, CD127 and RORγt, compatible with LTi cells (Fig. 1a, b). Two B cell clusters were present, one of which was $HLA\text{-}DR^+CD1c^+CD45RA^+CCR6^+$, while another was $HLA\text{-}DR^{low}CD1c^-CD45RA^{low}CCR6^-$ (Fig. 1a, b). Finally, a single cluster of myeloid cells was observed, but differential expression of CD11c, CD163, HLA-DR, and CD1c points towards heterogeneity within this myeloid subset (Fig. 1a, b). Strikingly, we observed clusters of Ki-67-positive cells within all identified cell subsets, indicative of cell proliferation (Fig. 1b, c). Similar results were obtained in two additional independent experiments (Supplementary Fig. 1-2).

Together, these results indicated substantial heterogeneity in the developing fetal intestinal immune compartment and revealed Ki-67-positive cells in all adaptive and innate cell subsets detected.

Stable presence of Ki-67 positive cells throughout gestational week 14 to 22

To obtain further information on the development of the fetal intestinal immune system and the presence of Ki-67 positive cells in time, we analyzed the tSNE-plots of the individual human fetal samples from gestational weeks 14 to 22 (Fig. 2a, cluster partition as shown in Fig. 1a, Supplementary Fig. 3a, b). The absolute number of $CD45^+$ cells acquired from each sample is summarized in Fig 2b while the absolute number of cells acquired for the major immune subsets in all samples is summarized in supplementary Fig. 4. At week 14, the intestinal immune compartment was primarily composed of one B cell subset, $CD3^-CD7^+$ ILC subsets

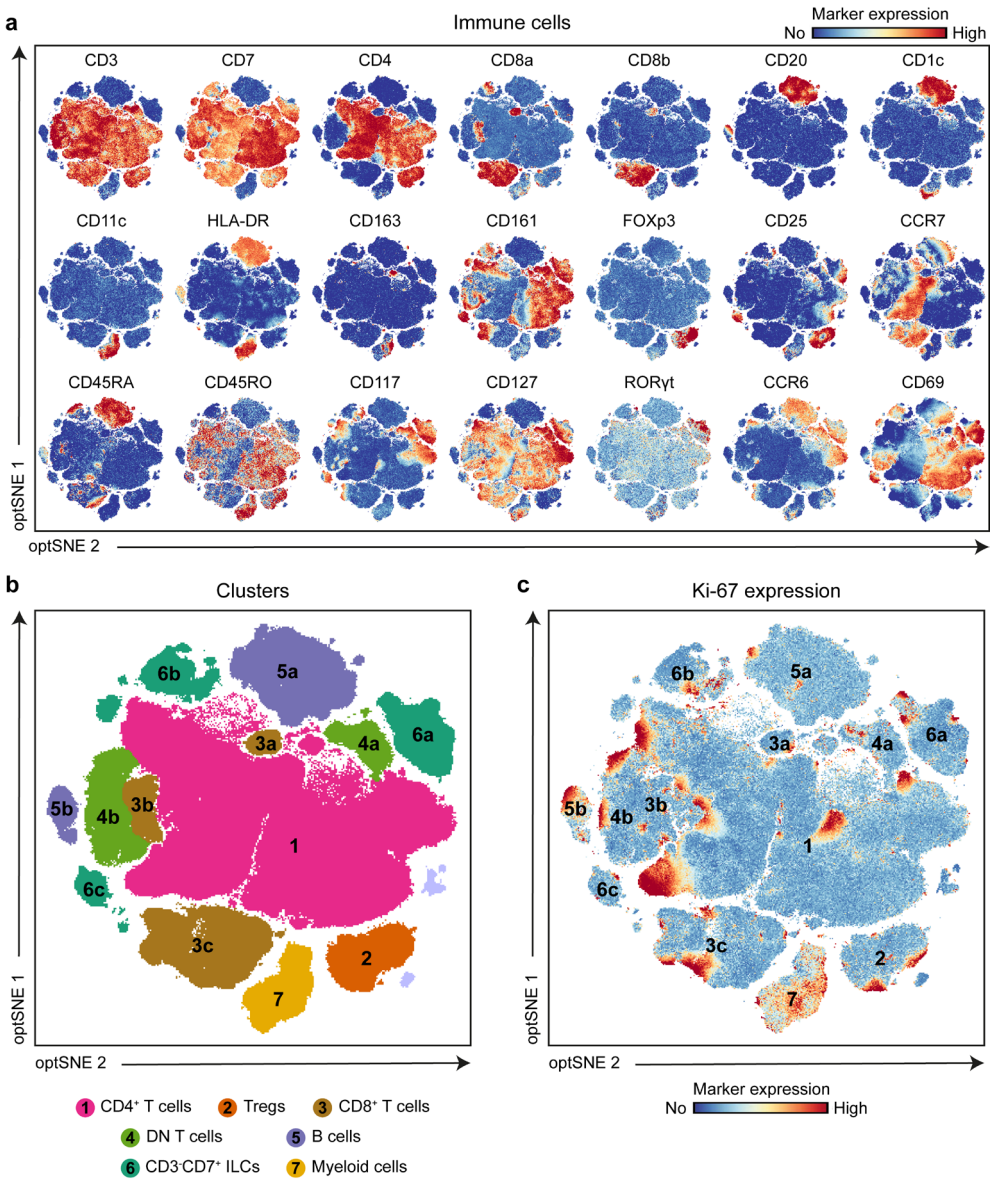

Figure 1. Identification of Ki-67⁺ cells within all immune subsets in the human fetal intestine. (a) A collective optSNE was performed on CD45⁺ immune cells from 12 human fetal intestinal samples. Each dot represents a single cell. In total, 2.7×10⁶ CD45⁺ immune cells were analyzed by OMIQ. Colors represent relative expression of indicated immune markers. **(b)** Based on the relative marker expression profile, each immune lineage was identified and color-coded. **(c)** Display of the Ki-67 expression within the CD45⁺ immune cells. Colors represent relative expression of Ki-67. Data represent three independent experiments.

and myeloid cells, followed by the rapid emergence of the other immune subsets in the weeks thereafter (Fig. 2a). The frequencies of myeloid cells and $CD3^{-}$ $CD7^{+}$ ILC steadily decreased in time (Fig. 2c, d), while the percentage of B cells, $CD4^{+}$ T cells, and Tregs increased in time (Fig. 2e-g), and $CD8^{+}$ and DN T cells remained more constant (Fig. 2h, i). From week 15 onwards, $CD4^{+}$ T cells were the dominant immune lineage in the intestine samples (Fig. 2f). Remarkably, we identified Ki-67^{+} cells within all detected immune subsets at all time points (Fig. 2j, Supplementary Fig. 4c-k), while the actual percentage of Ki-67^{+} cells within the $CD45^{+}$ cells remained stable in time (Fig. 2k).

Thus, while at week 14, $CD3^{-}CD7^{+}$ ILC, B cells and myeloid cells are abundant in the fetal intestine, from week 15 onwards, adaptive T and B cell populations dominate the immune compartment. Moreover, stable clusters of Ki-67^{+} cells are present in all immune lineages throughout a major part of the second trimester.

Molecular analysis confirms peripheral expansion of intestinal T cells

T cell receptor excision circles (TREC) provide a molecular means to quantitively assess the replication history of T lymphocytes. Different TREC assays exist, which allow the measurement of extensive proliferation in the thymus (Vg-Jg TREC) or mostly peripheral expansion after thymic egress (δREC-ψJα TREC). We applied the δREC-ψJα TREC to fetal intestinal samples, because of its greater sensitivity to measure post thymic proliferation. Similar to earlier results in purified cord blood naive T cells, the T cells in the fetal intestine had undergone 3-4 cell divisions at week 20 and this number increased to 6.5 divisions at week 22 (Fig. 3a).

In addition we re-analyzed a previously generated single cell RNAseq dataset on purified fetal intestinal $CD4^{+}$ T cells[14]. tSNE analysis revealed a distinct cluster of $CD4^{+}$ T cells expressing *MKI67*, *CCNB2* and *CDK1*, in line with active proliferation (Fig. 3b). In addition these cells co-expressed *IL7R* and *CD69*, indicative of responsiveness to stimulation with IL-7 and tissue residency, respectively. Integrated analysis of the cell cycle gene expression patterns placed the *MKI67*

Figure 2. Presence of Ki-67^{+} cells throughout gestational week 14 to 22. (a) Display of the Ki-67 expression in the optSNE plots of the individual fetal intestinal samples from week 14 through 22. Colors represent relative expression of Ki-67. Data are representative of three independent experiments. **(b)** The frequency of $CD45^{+}$ immune cells within all human fetal intestine samples analyzed (n = 28)**. (c-i)** Overview of the frequency of each immune lineage within the $CD45^{+}$ immune cells of all human fetal intestine samples analyzed (n = 28). **(j)** Overview of the distribution of Ki-67^{+} cells in the indicated immune lineages from gestational week 14 through 22, the results shown are from the samples shown in panel **(a). (k)** The percentage of Ki-67^{+} cells within the $CD45^{+}$ immune cells of all human fetal intestine samples analyzed (n = 28)**.**

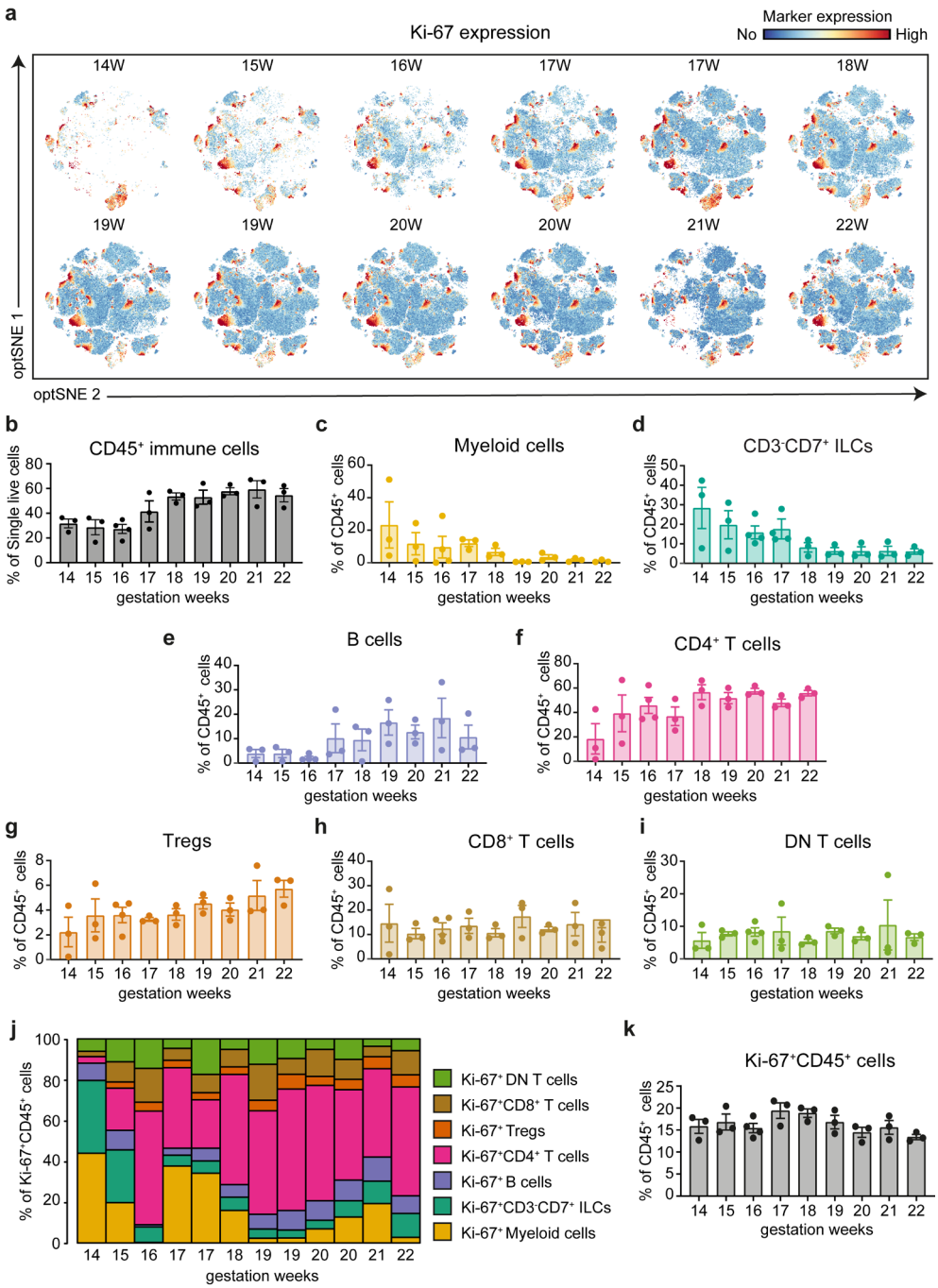

(Figure legend in previous page)

positive cells in the G2M phase (Fig. 3c), indicative of active proliferation. Finally, we analyzed the expression of genes associated with T cell receptor rearrangements. Expression of *RAG1* and *LIG4* were only detected in few cells while no expression of *RAG2* and *DNTT* was found (Fig. 3d), arguing against T cell receptor rearrangements taking place in the fetal intestinal compartment.

Altogether, these results point to recent or active proliferation in the intestinal T cell compartment.

Lymphoid Follicles form early in the development of the human fetal intestine

To explore the development and spatial organization of the fetal intestinal immune system *in situ*, we employed imaging mass cytometry (IMC) on tissue sections of human fetal intestinal samples from different gestational ages (Fig. 4). For this we developed and optimized antibody panels that incorporated markers to distinguish tissue structure, and innate and adaptive immune subsets (Supplementary Table 2-4). Based on E-cadherin and CD45 expression patterns, the epithelium and immune cells could be readily identified (Fig. 4a). Most $CD45^+$ immune cells were localized in the lamina propria in all fetal intestine samples (Fig. 4a). Strikingly, aggregates of immune cells were present in all samples in villus-like structures covered by epithelium, termed lymphoid follicles (LFs) hereafter, which presented with a higher density of $CD45^+$ immune cells in time (Fig. 4a, encircled by boxes). Analysis of the expression of the immune lineage markers CD3, CD7, CD20, HLA-DR and CD163 revealed the presence of T cells, $CD3^-CD7^+$ ILCs, B cells and two subsets of myeloid cells within the LFs (Fig. 4b-f). At week 16 of gestation, HLA-DR^+ myeloid cells were the primary immune cell population in the LFs, while $CD3^-CD7^+$ ILCs, B cells and a few T cells were also detected. At later time points in gestation, increased numbers of B and T cells were detected.

Further analysis indicated the expression of CD127 and CD117 by the $CD3^-CD7^+$ ILCs, suggestive of an LTi-like phenotype (Supplementary Fig. 5a). Moreover, most B cells within the LFs displayed expression of CD1c (Supplementary Fig. 5b,c), while both $CD11c^+$HLA-DR^+ and $CD163^+$ myeloid cells could be identified at all gestational ages investigated (Fig. 4d, e, Supplementary Fig. 5d). Together, this global analysis revealed the presence of similar immune subsets in LFs through gestational week 16 to 21, with a gradual increase in adaptive immune cells in time.

We next aimed to obtain a comprehensive overview of the organization of all

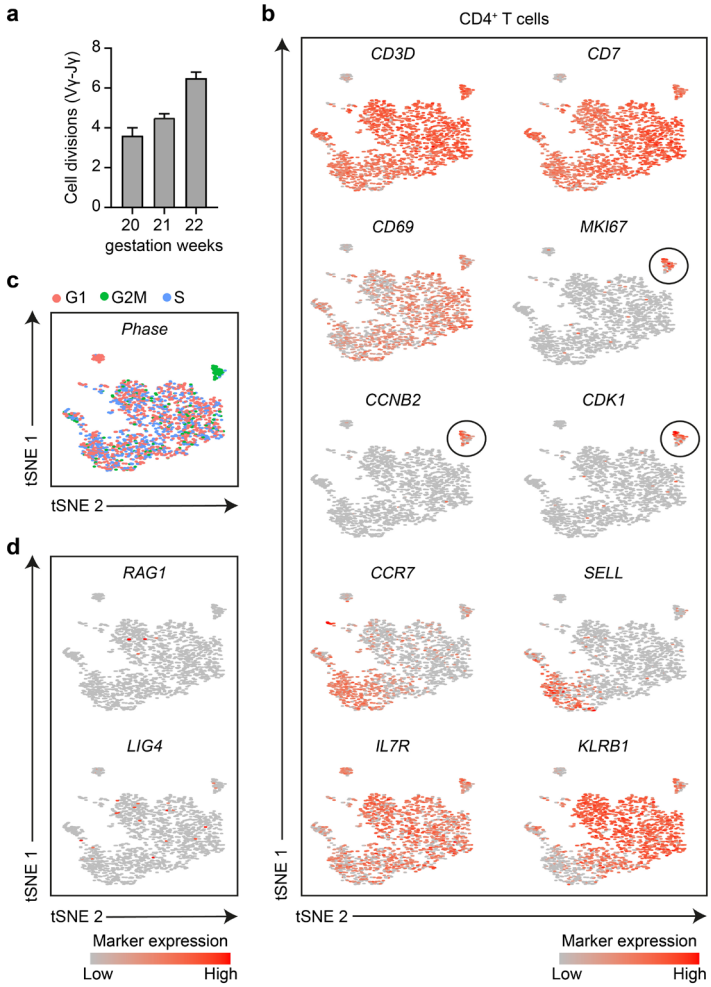

Figure 3. T cell receptor excisions circle (TREC) and single cell RNA-seq analysis confirms peripheral expansion of intestinal T cells. (a) Proliferative history in human fetal intestinal samples. **(b-d)** t-SNE embedding showing 1804 CD4⁺ T cells from a human fetal intestine analyzed by single-cell RNA-sequencing. The log-transformed expression levels of indicated immune markers **(b)**, the phase of the cell-division cycle **(c)** and genes involved in TCR rearrangement **(d)** are shown. Each dot represents a single cell. The proliferative CD4⁺ T cells are encircled **(b)**.

detected immune subsets in a single image from a 21-week sample where a large LF was visible. For this we made use of "*Cytosplore Imaging*", which was adapted from *Cytosplore*$^{+HSNE\ 20}$, to allow analysis of the IMC data at the single-pixel level. Supplementary Fig. 6 provides an exploration workflow of "*Cytosplore Imaging"*, indicating how the tissue-specific pixels are extracted from the original

IMC dataset, where pixels representing a single cell type are assigned a color and projected back onto the original image. The approach allows the simultaneous visualization of up to 9 cell types with unique colors in a single image at 1 μM pixel resolution (Supplementary Fig. 6a-d).

We applied this approach to visualize the composition and organization of immune cells in the 21-week LF. For this, we embedded the $CD45^{+/dim}$ pixels at the data level and projected the immune subset-related pixels back onto the image. The resulting image revealed the distribution of T cells ($CD3^{+}CD7^{+}$), $CD3^{-}CD7^{+}$ ILCs ($CD3^{-}CD7^{+}$), B cells ($CD20^{+}$HLA-DR^{+}), Lin^{-}HLA-DR^{+} myeloid cells ($CD3^{-}CD7^{-}$ $CD20^{-}CD163^{-}$HLA-DR^{+}) and $CD163^{+}$ macrophages ($CD163^{+}$HLA-DR^{+}) in *situ* in a single region (Fig. 4f, Supplementary Fig. 6e) while the individual cell types in the LF are shown in Fig. 4g. The overview of the image indicates the presence of a B cell follicle in close contact with $CD3^{-}CD7^{+}$ ILCs and T cells in the top of the villus-like structure, while underneath a cluster of HLA-DR^{+} and $CD163^{+}$ myeloid cells with T cells was present. Moreover, the HLA-DR^{+} myeloid cells appeared to be present in the LF, while the $CD163^{+}$ myeloid cells were abundant in the lamina propria.

Together these results indicated a dynamic and distinct spatial organization of the immune compartment in LFs in the developing fetal intestine.

A $CD69^{+}CD117^{+}CD161^{+}CCR6^{+}CD127^{+}$ phenotype is shared by subsets of fetal intestinal $CD3^{-}CD7^{+}$ ILCs and T cells

Next we focused our analysis on $CD3^{-}CD7^{+}$ ILCs, DN T cells, $CD4^{+}$ T and $CD8^{+}$ T cells in the human fetal intestine. tSNE analysis of the single-cell data revealed substantial heterogeneity in all four lymphoid cell subsets (Fig. 5a-d). As expected, a sizable proportion of $CD3^{-}CD7^{+}$ ILCs expressed CD117 (Fig. 5a). In addition, CD117 expressing cells were present in all T cell subsets (DN, CD8 and CD4) (Fig. 5b-d). Moreover, most $CD117^{+}$ lymphoid cells were $CD161^{+}$, $CCR6^{+}$ and $CD127^{+}$, while the tissue-residency marker CD69 was only present on a subset of these cells (encircled in Fig. 5b-d). Finally, small pockets of Ki-67^{+} cells were detectable in both $CD69^{+}$ (encircled in Fig. 5b-d) and $CD69^{-}$ (indicated by the arrow in Fig. 5b-d) counterparts of the four $CD117^{+}$ lymphoid cell clusters, indicative of cell proliferation.

We next determined the spatial location of $CD69^{+}CD117^{+}CD161^{+}CD127^{+}$ ILCs and T cells within the fetal intestine by IMC. First we performed pixel analysis to specifically detect and quantify co-expression of CD161 and CD69 inside and

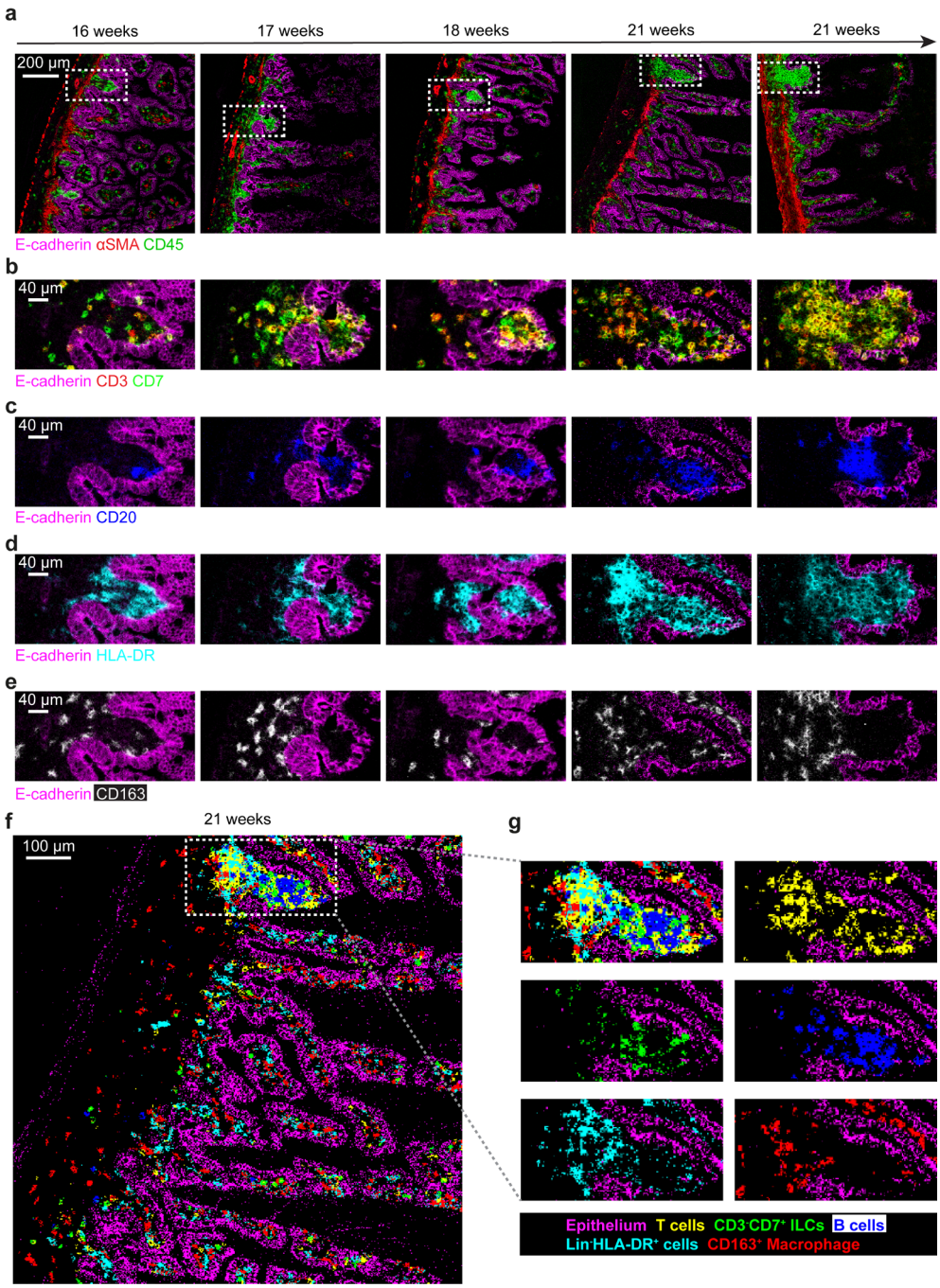

(Figure legend in next page)

Figure 4. Identification and visualization of the immune cell composition of LFs in human fetal intestinal samples by imaging mass cytometry. (a) Visualization of E-cadherin, αSMA, and the immune cell marker CD45 reveals the overall structure of the fetal intestinal samples from week 16 through 21 and the location of LF (indicated by boxes) within those samples. Scale bar, 200 μm. Identification of $CD3^+CD7^+$ T cells (yellow) and $CD3^-CD7^+$ ILCs (green) by the overlay of CD3 (red) and CD7 (green) **(b);** $CD20^+$ B cells (blue) **(c);** $Lin^-HLA\text{-}DR^+$ myeloid cells (magenta) **(d);** $CD163^+$ macrophages (white) **(e).** Scale bar, 40 μm. **(f)** Visualization of the location of the immune subsets in a representative human fetal intestine sample from gestational week 21 by pixel analysis in *"Cytosplore imaging"*. Scale bar, 100 μm. The image is representative of three independent experiments. **(g)** Overview of the individual immune cell populations in the LF by pixel analysis. Scale bar, 40 μm.

outside the LFs (Fig. 5e, f). Here a significantly higher proportion of $CD161^+CD69^+$ double-positive pixels was present in LFs compared to a similar surface area outside the LFs (Fig. 5e, f). Moreover, simultaneous visualization of CD3, CD7, CD4, CD8a, CD161, CD69, CD117 and CD127 in a single tissue slide revealed the presence of both $CD3^-CD7^+$ ILC, $CD4^-CD8^-$ T cells, $CD4^+$ T cells and $CD8^+$ T cells displaying a $CD69^+CD117^+CD161^+CD127^+$ phenotype within the lymphoid follicles (Fig. 5g).

Thus, a subset of $CD3^-CD7^+$ ILC and T cells share a $CD69^+CD117^+CD161^+$ $CCR6^+CD127^+$ phenotype, harbor cells with proliferative capacity and reside within the LFs.

Multiple types of Ki-67$^+$ proliferating cells are identified in *situ*

To verify the presence of $Ki\text{-}67^+$ proliferating cells in each immune lineage in *situ*, we included a Ki-67-specific antibody in the IMC panel and applied it to frozen sections of human fetal intestinal samples (Supplementary Table 2-4). We observed $Ki\text{-}67^+$ cells in all human fetal intestinal samples, in both the epithelium and the lamina propria (Fig. 6a, b). Moreover, within the LFs, $Ki\text{-}67^+$ cells were also detected (Fig. 6b). Within the lamina propria, we also defined the phenotype of the $Ki\text{-}67^+CD45^+$ cells by simultaneous visualization of immune lineage markers (Fig. 6b, c). This revealed the presence of $Ki\text{-}67^+CD4^+$ T cells, $Ki\text{-}67^+CD8^+$ T cells, $Ki\text{-}67^+CD3^-CD7^+$ ILCs, $Ki\text{-}67^+CD20^+$ B cells, $Ki\text{-}67^+CD163^+$ macrophages, and $Ki\text{-}67^+Lin^-HLA\text{-}DR^+$ myeloid cells in the human fetal intestine (Fig. 6c and Supplementary Fig. 7). Thus, $Ki\text{-}67^+$ cells were identified in all major immune lineages in the developing fetal intestine *in situ*.

Fetal intestinal immune subsets display proliferation potential *ex vivo*

Since we identified proliferation-associated $Ki\text{-}67^+$ cells across all immune cell types, we next aimed to determine if spontaneous proliferation could be detected

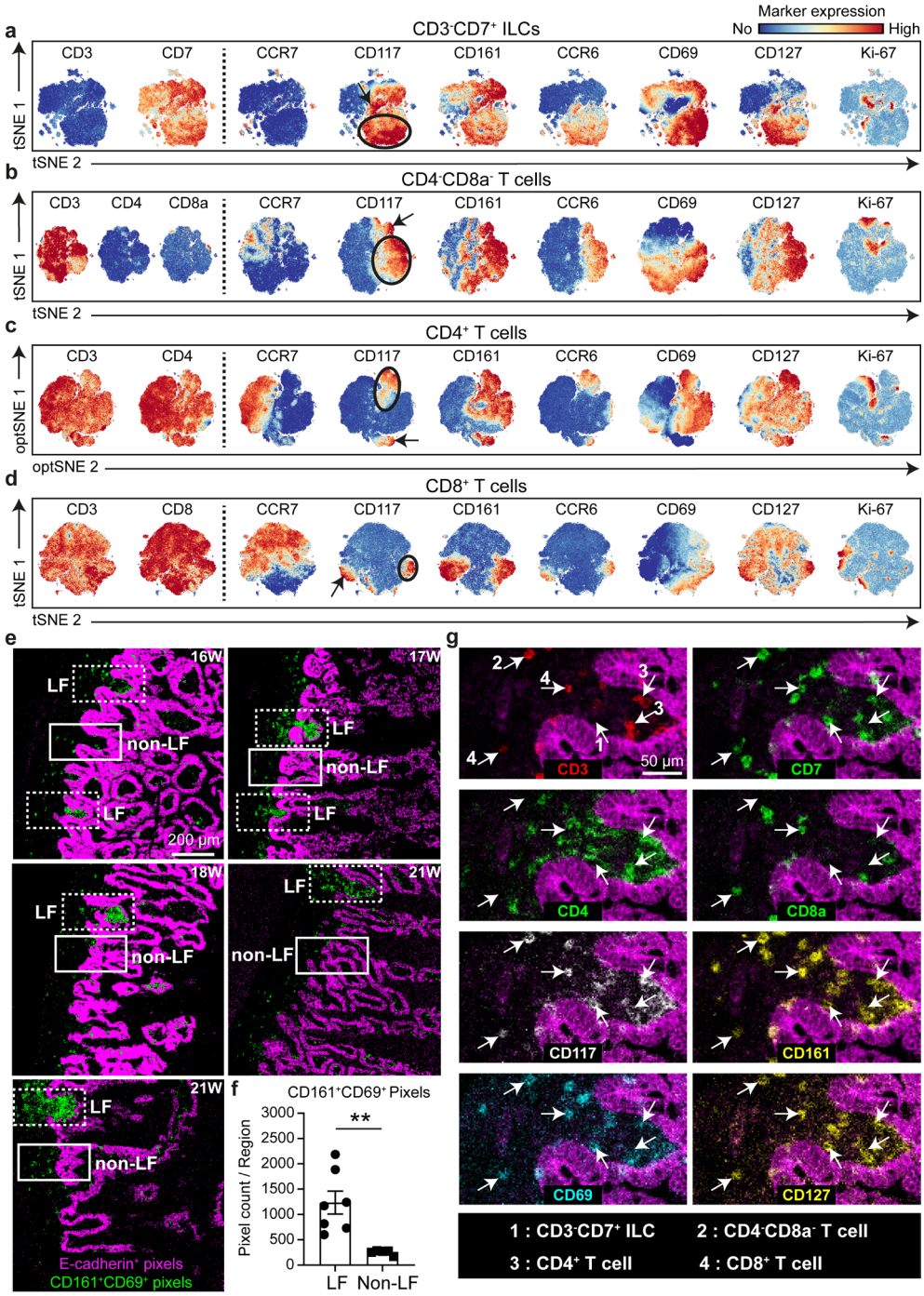

(Figure legend in next page)

Figure 5. Subsets of T cells and ILCs display a highly similar CD69$^+$CD161$^+$CD117$^+$CCR6$^+$CD127$^+$ phenotype. (a-d) tSNE analysis of the CD3$^-$CD7$^+$ ILCs cells (2.4 × 10^5 cells), CD4$^-$CD8$^-$ T cells (1.9 × 10^5 cells), CD4$^+$ T cells (1.2 × 10^6) and CD8$^+$ T cells (3.1 × 10^5 cells) from 12 human fetal intestinal samples from gestational week 14 through 22. Colors represent the relative expression of the indicated immune markers. CD69$^+$CD161$^+$CD117$^+$CCR6$^+$CD127$^+$ cells are encircled, while their CD69$^-$ counterparts are indicated by arrows. **(e)** CD161$^+$CD69$^+$ immune cells (green) and epithelium (pink) were visualized by pixel analysis in the human fetal intestine from different gestational ages. LFs are boxed by dashed lines, while similar area's devoid of LFs (non-LFs) are boxed by solid line. Scale bar, 200 μm. **(f)** CD161$^+$CD69$^+$ pixels were quantified within LFs (n = 7) and non-LF (n = 5). Error bars indicate mean ± s.e.m. ** P < 0.01, Mann-Whitney test for comparisons. **(g)** The combination of the immune cell markers indicated was used to visualize CD69$^+$CD161$^+$CD117$^+$CD127$^+$ CD3$^-$CD7$^+$ ILC (indicated by arrow 1), CD69$^+$CD161$^+$CD117$^+$CD127$^+$ CD4$^-$CD8$^-$ T cell (arrow 2), CD69$^+$CD161$^+$CD117$^+$CD127$^+$ CD4$^+$ T cell (arrow 3) and CD69$^+$CD161$^+$CD117$^+$CD127$^+$ CD8$^+$ T cell (arrow 4) in the LF of a human fetal intestinal sample *in situ*. Scale bar, 50 μm.

in fetal intestinal cells when cultured *in vitro*. For this purpose, proliferation assays were performed based on CellTrace™ Violet dye dilution by culturing immune cells isolated from a fetal intestinal sample in medium alone.

In addition, as we observed the prominent expression of the IL-7 receptor (CD127) by most fetal immune cell subsets (Fig. 1a), we also assessed proliferation in the presence of IL-7 for four days. Adult peripheral blood mononuclear cells (PBMCs) were used as a control. To analyze the cell cultures, we used a spectral flow cytometry antibody panel designed to discriminate B cells, CD3$^-$CD7$^+$ ILCs, DN T cells, CD8$^+$ T cells, and CD4$^+$ T cells (including CD25$^+$ Treg-like, CD117$^-$CD161$^+$ and CD117$^+$CD161$^+$ subsets).

All subsets were identified in both culture conditions (Fig. 7a), indicating the presence of stable immune phenotypes in time. In the absence of IL-7, the dilution of CellTrace™ Violet dye revealed cellular division accompanied by the expression of Ki-67 in all fetal intestinal immune subsets that was significantly enhanced by the addition of IL-7 (Fig. 7b). In contrast, proliferation was hardly observed in the cultures of the PBMC sample (Fig. 7c, Supplementary Fig. 8). Similar analysis

Figure 6. Visualization of Ki-67 expression *in situ.* (a) Visualization of Ki-67$^+$CD45$^+$ cells in a LF by overlay of Ki-67 and CD45 on a representative human fetal intestinal sample from gestational week 21. Scale bar, 200 μm. **(b)** Visualization of Ki-67$^+$CD45$^+$ cells in the lamina propria by overlay of Ki-67 and CD45 on an additional human fetal intestinal sample from gestational week 21. Scale bar, 200 μm. **(c)** The combination of Ki-67 and immune cell markers was used to visualize **(a1 and b1)** Ki-67$^+$CD4$^+$ T cells, **(a2 and b2)** Ki-67$^+$CD8$^+$ T cells, **(b3)** Ki-67$^+$CD3$^-$CD7$^+$ ILCs, **(b4)** Ki-67$^+$CD20$^+$ B cells, **(b5)** Ki-67$^+$CD163$^+$ macrophage, and **(b6)** Ki-67$^+$Lin$^-$HLA-DR$^+$ myeloid cells in human fetal intestinal samples as indicated by white arrows. Scale bar, 20 μm.

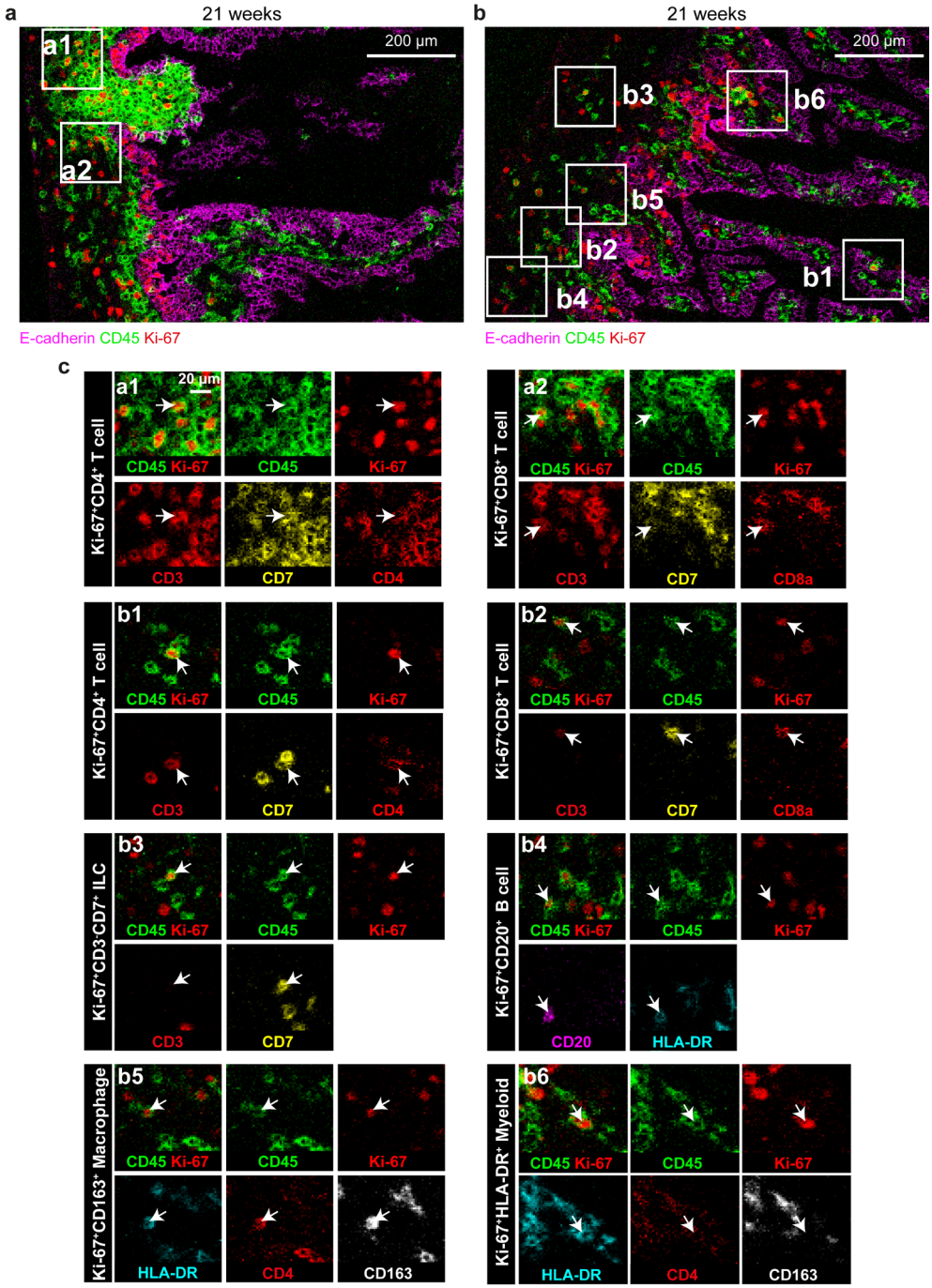

(Figure legend in previous page)

of fetal immune cells from samples of gestational weeks 18, 20 and 21 likewise revealed spontaneous proliferation of fetal intestinal immune subsets that was enhanced in the presence of IL-7 (Fig. 7d).

To determine functional characteristics of the cultured fetal intestinal immune cells, we analyzed the expression of CD40L, granzyme B, TNF-α, IFNγ, IL-2 and IL-17A by flow cytometry (Supplementary Fig. 9). In both the presence and absence of IL-7, a substantial proportion of $CD3^{-}CD7^{+}$ ILCs, DN T cells and $CD4^{+}$ T cells expressed CD40L after 48 hours of culture, while this was much lower on $CD8^{+}$ T cells (Supplementary Fig. 9). Granzyme B was detected in $CD3^{-}CD7^{+}$ ILCs, DN T cells and $CD8^{+}$ T cells, while intracellular levels of TNF-α, IFNγ, IL-2 and IL-17A were low in all cell populations in both culture conditions (Supplementary Fig. 9). Furthermore, in the presence of IL-7 the median fluorescence intensities (MFI) of CD40L expression increased substantially in $CD3^{-}CD7^{+}$ ILCs, DN T cells and $CD4^{+}$ T cells (Fig. 7e). Moreover, higher frequencies of $CD40L^{+}$granzyme B^{+} ILCs and T cells were detected after 48 hours of culture in the presence of IL-7 (Fig. 7f).

Thus, all immune subsets in the fetal intestine contain cells that give rise to progeny *in vitro*, in particular in the presence of IL-7, which is accompanied by upregulation of CD40L and granzyme B expression.

Discussion

The human intestine harbors a significant fraction of the body's immune cells[23, 24, 25] that controls local responses to the microbiota and food antigens to maintain homeostasis[26]. We and others have described the presence of both innate and

Figure 7. Fetal intestinal samples harbor cells with proliferative capacity *in vitro.* **(a)** Biaxial plots showing the gating strategy to identify immune subsets in a human fetal intestinal sample from gestational week 16 cultured in medium alone or medium with IL-7 for 4 days. The colored gates indicate the identified immune subsets. Data represent four independent experiments. **(b)** Histogram showing CellTrace™ Violet dye dilution in the indicated immune subsets from the human fetal intestine. Dashed lines represent the fetal intestinal sample cultured in medium, while solid lines represents the fetal intestinal sample cultured in medium with IL-7. **(c)** Histogram showing CellTrace™ Violet dye dilution by the indicated immune subsets from a PBMCs sample. Dashed lines represent the PBMCs cultured in medium, while solid lines represents the PBMCs cultured in medium with IL-7. **(d)** $CTV^{diluted}$ cells of the immune subset indicated from human fetal intestinal samples in both culture conditions. Data were from four independent experiments. *P < 0.05, Mann-Whitney test for comparisons. **(e)** Comparison of the mean MFI values of CD40L expression between culture in medium alone and in the presence of IL-7. **(f)** Comparison of the percentages of $CD40L^{+}$granzyme B^{+} expressing cells within $CD3^{-}CD7^{+}$ ILCs, $CD4^{-}CD8^{-}$ T cells, $CD4^{+}$ T cells and $CD8^{+}$ cells in both culture conditions. Error bars indicate mean ± s.e.m. *P < 0.05, Wilcoxon signed-rank test for comparisons.

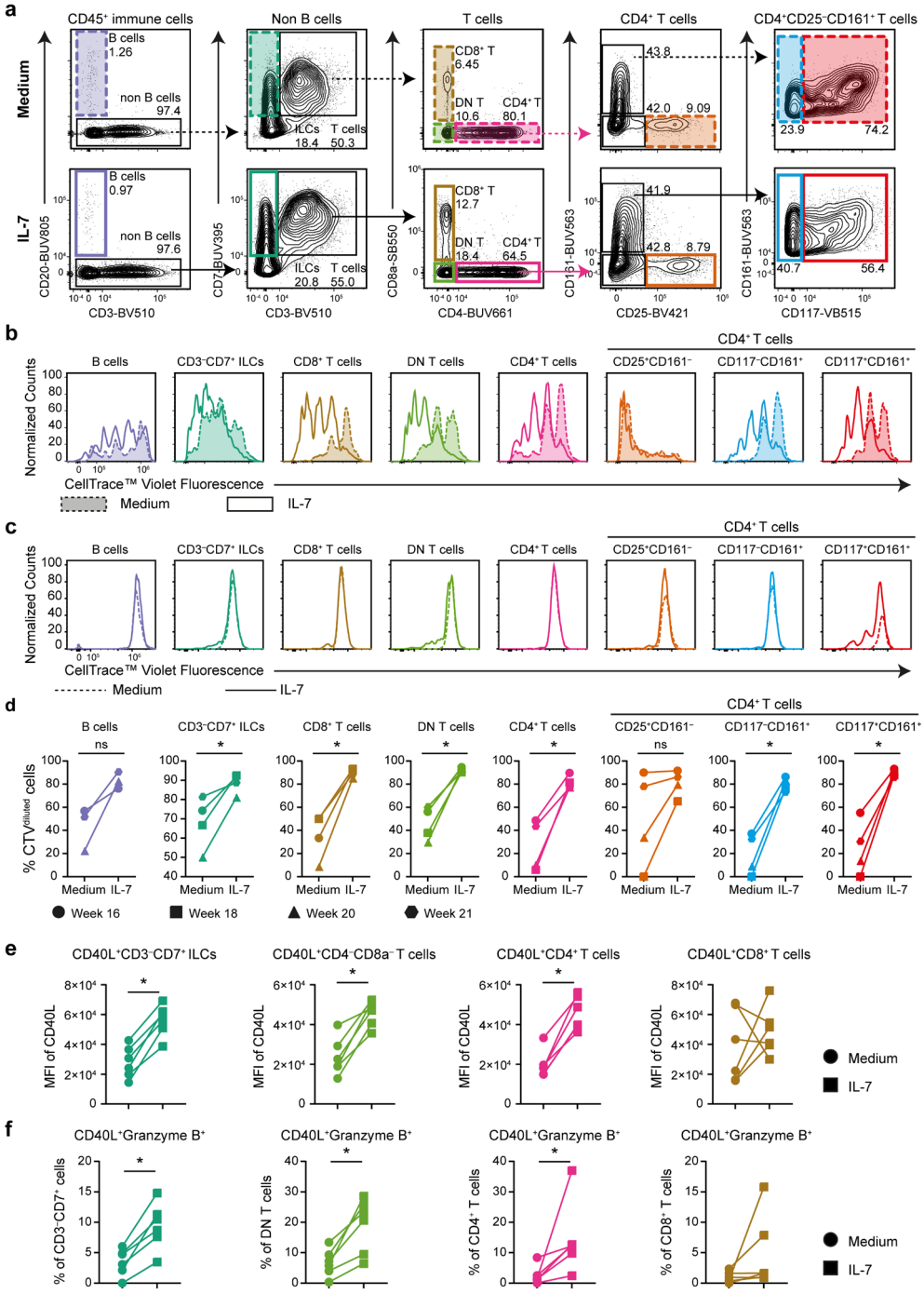

(Figure legend in previous page)

adaptive cells with complex immune phenotypes in the human fetal intestine[14, 15, 19, 27]. Moreover, direct comparison of fetal and infantile samples has revealed substantial differences in immune composition in both the adaptive and innate compartment[16]. Yet little is known about the temporospatial development of the fetal intestinal immune system.

Here, we have used spectral cytometry and imaging mass cytometry (IMC) to explore the composition and distribution of immune cells in the human fetal intestine across the second trimester (14 to 22 weeks of gestation). At gestational weeks 14-15, the immune compartment was mostly composed of myeloid cells and $CD3^{-}CD7^{+}$ ILCs (Fig. 1 and 2), which corresponds with observations in other fetal tissues, where these innate cell subsets appear earlier than their adaptive counterparts[15]. In suspension, most myeloid cells co-expressed CD11c, HLA-DR and CD45RO, with some cells expressing CD1c or CD163. IMC confirmed the abundant presence of $Lin^{-}HLA\text{-}DR^{+}$ and $CD163^{+}HLA\text{-}DR^{-}$ cells in different anatomical locations. While $Lin^{-}HLA\text{-}DR^{+}$ cells were close to the epithelium in the lamina propria, $CD163^{+}HLA\text{-}DR^{-}$ cells were found both in the LP as well as in the submucosa (Fig. 4). Previously we have provided evidence for the presence of several $CD3^{-}CD7^{+}$ ILC subsets in the fetal intestine, including ILC3[19]. In agreement, we now observed three phenotypically distinct clusters of $CD3^{-}CD7^{+}$ ILCs, one of which displayed features of ILC3/lymphoid tissue inducer cells (LTi; $CD3^{-}CD7^{+}CD117^{+}CD161^{+}CCR6^{+}CD127^{+}RORgt^{+}$). These results are in line with a recent study in which Elmentaite et al used single cell RNA sequencing to map the cell types in the human intestine[28]. They reported that LTi-like NCR^{+} and NCR^{-} ILC3s were particularly abundant in the fetal intestine compared to both pediatric and adult samples. Moreover, these were located in proximity to CXCL13-expressing lymphoid tissue organizer-like stromal cells, in line with their role in lymphoid tissue formation in the fetal gut[28]. It remains to be investigated how these observations match with the observed formation of lymphoid follicles in the fetal intestine in our current study. Remarkably, ILC3s in tissues from patients with Crohn's disease matched fetal NCR^{+} ILC3s with more than 60% probability, which suggests fetal lymphoid tissue development programs could be implicated in the Crohn's disease pathogenesis[28].

From 17 weeks onwards, B and T cells were the most abundant cell subsets and the composition of the fetal intestinal immune compartment remained relatively stable (Fig. 1 and 2). B cells were divided into two clusters. The most prominent of these clusters were composed of $CD20^{+}HLA\text{-}DR^{+}$ B cells that co-expressed CCR6 and CD1c. In humans, CD1c is expressed by mantle zone B-cells of the tonsil, lymph node and spleen, and marginal zone B (MZB) cells of the spleen[29]. Recently,

high expression of CD1c was described in a population of transitional B cells that migrate to the gut and later give rise to MZB cells[30]. MZB cells are strategically located at the interface between the circulation and the white pulp of the spleen, providing the first line of defense by rapidly producing IgM and IgG antibodies in response to infections[31]. They can also be found in the subepithelial dome of intestinal Peyer's patches and produce IgM, IgG and IgA antibodies to commensal antigens[31]. IMC analysis of human fetal intestines revealed the accumulation of fetal CD1c$^+$ B cells in lymphoid follicles, in close contact with CD3$^-$CD7$^+$ ILCs, T cells and HLA-DR$^+$ cells (Fig. 4 and Supplementary Fig. 5-6). As transitional B cells must migrate to the gut to give rise to mature clonally-diverse MZB[32], it is thus plausible that the fetal LFs are the maturation site of fetal MZB precursors where they are in close contact with T cells and HLA-DR$^+$ myeloid cells.

We previously described that substantial heterogeneity within the CD4$^+$ T cell compartment was already present at 17 weeks[14]. Moreover, substantial evidence has been presented indicating that the majority of fetal intestinal CD4$^+$ T cells display a memory phenotype[14, 15, 16]. Likewise, fetal intestinal CD8$^+$ T cells can display a memory phenotype. It has been speculated that this points to *in utero* exposure to foreign antigens. In agreement, Mishara *et al* recently provided evidence for the presence of bacterial species in fetal samples[33]. However, many have argued that the detection of microbial species in such samples is caused by contamination and this debate may not easily be settled. In any case, microbial presence in the fetus is sparse at best[33] and may not be sufficient to explain the abundance of memory T cells in the human fetal intestine samples. Alternatively, memory formation could be triggered by exposure to proteinous and non-proteinous antigens that gain access to the amniotic fluid, possibly derived from the maternal microbiota. Our previous results indicated that memory formation is associated with several signaling pathways, including that of the T cell receptor, supporting the notion that exposure to foreign antigens is at least partly responsible for the observed memory formation[14]. However, our current results indicate that the memory phenotype may also be associated with the expansion of adaptive immune cells, either in the developing fetal intestine or an intermediate tissue, perhaps analogous to the thymus where the majority of double-negative and single-positive thymocytes express CD45RO and display proliferative potential. Further research will be required to explore this option. Of note, fetal mesenteric lymph nodes at 20 gestational weeks contains T cells with both naïve and memory-like phenotype[34].

As observed before[14], a significant proportion of CD4$^+$ T cells expressed CD161

and lacked expression of CCR7, and a similar pattern was observed for CD3^{-}CD7^{+} ILCs, DN and CD8a^{+} T cells (Fig. 5), potentially reflecting the shared transcriptional program observed in adult human CD161^{+} circulatory CD4^{+}, CD8a^{+} (including MAIT cells) and TCRgd^{+} T cells[35]. Further analysis of the CD161^{+} cell subsets revealed that two clusters of CD117^{+}CCR6^{+}CD127^{+} cells were present that either lacked or expressed CD69 within CD3^{-}CD7^{+} ILCs, DN, CD4^{+} and CD8a^{+} T cells (Fig. 5a-d). Moreover, CD3^{-}CD7^{+} ILCs, DN, CD4^{+} and CD8a^{+} T cells displaying this CD69^{+}CD117^{+}CCR6^{+}CD127^{+} phenotype were identified in LFs by IMC (Fig. 5e), and pixel analysis confirmed the enrichment of CD161^{+}CD69^{+} pixels in areas where LFs were present (Fig. 5f). Together, the shared phenotype of the CD69^{+}CD117^{+}CD161^{+} CCR6^{+}CD127^{+} cells across subsets and their localization in the LF may indicate a common function in LF development, a matter that will be investigated in future studies. So far, CD161 has been associated with IFNg and IL-17A in adult CD4^{+} T cells[36], or IFNg production in adult CD4^{+}, CD8a^{+} and TCRgd^{+} T cells[35]. Interestingly, Cosmi *et al* revealed the presence of naïve CD161^{+}CD4^{+} T precursor cells in cord blood and postnatal thymus, that expressed RORgt and CCR6 and could differentiate into IL-17A/IFNg-producing cells[36]. Such committed thymus-derived naïve CD161^{+}CD4^{+} T cell precursors may enter the circulation during fetal development and home to the intestine.

While the presence of Ki-67^{+} in the human fetal intestine has been noted before, detailed analysis of fetal samples allowed us to identify stable pockets of Ki-67^{+} cells in all immune cell subsets throughout a major part of the second trimester. This result is compatible with sustained proliferation of immune-subset committed cells in time (Fig. 1-2 and Supplementary Fig. 1-4). Ki-67 is expressed at variable levels throughout the cell cycle, reaching its maximum during the S-M phases and decreasing via degradation in G1/G0[37]. High levels of Ki-67 expression, which would be detectable by IMC, suggest lack of quiescence and rapid progression through the cell cycle. This is supported by a re-analysis of our previously generated single cell RNA sequencing data[14] where a subset of the fetal intestinal CD4^{+} T cells were found to co-express *CCNB2*, *CDK1* and *MKI67* (Fig. 3b), genes associated with cell cycle. Moreover, spontaneous and IL-7-induced proliferation of fetal intestinal cells were observed *in vitro* and IMC confirmed the presence of Ki-67^{+} cells with different phenotypes both in LFs as well as scattered along the LP (Fig. 6). Of note, in the infant intestinal tract Ki-67^{+} staining was only detectable within isolated LFs and the epithelium, but not in the lamina propria[38]. Moreover, TREC analysis showed that T cells in the fetal intestine underwent an average of 3.5 (week 14) to 6.5 (week 22) divisions (Fig. 3a). Analysis of the expression of genes involved in TCR rearrangement (*RAG1*, *RAG2*, *DNTT* and *LIG4*) revealed

that only a few cells expressed *RAG1* and *LIG4*, while *RAG2* and *DNTT* were not expressed (Fig. 3d), arguing against extrathymic T cell development in the fetal intestine.

During the second trimester, the intestine not only doubles in length[39], but also villus and microvillus formation drive an even greater increase in the intestinal surface area[40]. Thus, immune cell colonization of the LFs and lamina propria requires an ever increasing number of immune cells. This can occur via continuous input from the fetal liver, thymus and bone marrow, and/or local proliferation. Given the constant proportion of Ki-67$^+$ cells in the fetal intestine and their presence in every immune subset throughout most of the second trimester, the most likely scenario is that fetal T cells develop in the thymus and then migrate to the periphery where they locally expand. Based on both Ki-67 expression and division history, we can envision two scenarios. In the first scenario, differentiated immune cells including T cells travel from the primary lymphoid organs to secondary lymphoid organs or intermediate tissues, where they undergo a few rounds of proliferation and then travel to the intestine. Given that Ki-67 is detectable at stable levels, the intestine would receive recently divided cells at a regular rate throughout the second trimester. In the second scenario, differentiated immune cells would reach the intestine at a regular rate during the second trimester, where they would receive local homeostatic proliferation signals and undergo a few rounds of division. In favor of the latter, we have detected local IL-7 production in the fetal intestine, both in the epithelium and the lamina propria (data not shown).

The situation of proliferating immune cells in a growing intestine could be paralleled to the filling of niches in a lymphopenic host through homeostatic proliferation, likely in the absence of antigen. It could be envisioned that as the organ grows, new stromal niches are generated that provide signals for proliferation. In support of this idea, it has been shown that the neonatal environment in mice is functionally lymphopenic, where transferred CD4$^+$ T cells undergo proliferation[41]. In immune-deficient hosts, lymphopenia-induced proliferation is driven by the increased availability of IL-7[41, 42, 43, 44]. We detected CD127 (IL-7Ra) on most fetal human lymphoid immune cells, except Tregs, B cells and some CD3$^-$CD7$^+$ ILC subsets (Fig. 1 and Supplementary Fig. 1-3). Unlike peripheral immune cells from healthy adults, fetal cells responded to IL-7 with vigorous proliferation after four days *in vitro*. This was accompanied by upregulation of CD40L and granzyme B in CD3$^-$CD7$^+$ ILCs, CD4$^+$ T cells, CD8ab$^+$ T cells and DN T cells, in the absence of concurrent cytokine production (Figure 7e, f, Supplementary Fig. 9). In healthy adults, IL-7-induced proliferation was found to be restricted to CD31$^+$ recent

thymic emigrants (RTEs)[45]. Fetal intestinal $CD4^+$ T cells may be RTEs, explaining their increased sensitivity towards IL-7. In mice, IL-7 is produced by stromal cells[46]. Further work will be required to elucidate the source of IL-7 in the human fetal intestine.

In summary, we identified a stable presence of Ki-67^+ cells in all major immune subsets of human fetal intestines during the second trimester, and IL-7-enhanced proliferation in *vitro*. Through IMC, we visualized the presence and development of fetal LFs throughout the second trimester and characterized the shared phenotype of $CD69^+CD117^+CD161^+CCR6^+CD127^+$ by fetal intestinal T cells and $CD3^-CD7^+$ ILCs frequently located within such LFs. Overall, these observations indicate the presence of immune subset-committed cells capable of local proliferation, contributing to the population size and development of an organized immune compartment throughout the 2nd trimester in the human fetal intestine.

Acknowledgements

We would like to thank the staff of the Center for Contraception, Abortion and Sexuality (Leiden and The Hague) for collection and provision of fetal material used in this work as well as the donors. We thank all operators in the Flow Cytometry Core Facility of the LUMC for technical assistance with measurements on Helios and Hyperion. We thank Marieke E. Ijsselsteijn for providing help and suggestions with IMC experiments. This research was supported by the China Scholarship Council (NG, NL and LJ). SMCSL was supported by Novo Nordisk Foundation (Renew NNF21CC0073729). FK was supported by BIOMAP (Bio-markers in Atopic Dermatitis and Psoriasis), a project funded by the Innovative Medicines Initiative 2 Joint Undertaking under grant agreement no. 821511 and by the collaboration project TIMID (LSHM18057-SGF) financed by the PPP allowance made available by Top Sector Life Sciences & Health to Samenwerkende Gezondheidsfondsen (SGF) to stimulate public-private partnerships and co-financing by health foundations that are part of the SGF.

Authorship Contributions

N.G., M.F.P. and F.K. conceived the study and wrote the manuscript. N.G. performed most experiments with the help of J.L., A. A. V and N.L.. Moreover, N.G., J.L., N.L., V.v.U., F.S., N.F.C.C.d.M. analyzed the data. S.M.C.d.S.L. collected and isolated the fetal intestine material. J.E. and B.L. set up the package of Cytosplore imaging for pixel analysis. All authors discussed the results and commented on

the manuscript.

Statistics

Results are shown as mean ± s.e.m. The statistics tests used were Wilcoxon matched-pairs signed-ranks test, and Mann-Whitney test for comparison. $P < 0.05$ was considered to be statistically significant. All statistics were analyzed using GraphPad Prism8 software.

Reporting Summary

Further information on research design is available in the Nature Research Reporting Summary linked to this article.

Data availability

Single-cell RNA-seq data is available via Gene Expression Omnibus accession code GSE122846. The flow cytometry data are available via Flow Repository (http://flowrepository.org/id/FR-FCM-Z5MB). Imaging mass cytometry data are deposited at Mendeley Data (https://data.mendeley.com/v1/datasets/m4vr79wsjs/draft?preview=1).

Software availability

The installer of Cytosplore Imaging and the PDF file of UserGuide are provided in https://sec.lumc.nl/mtg-viewer/imaging/win/se_3.3.2/Cytosplore_Imaging_SE_3.3.2.zip.

Reference

1. Park, J.-E., Jardine, L., Gottgens, B., Teichmann, S.A. & Haniffa, M. Prenatal development of human immunity. *Science* **368**, 600-603 (2020).
2. Holt, P.G. & Jones, C.A. The development of the immune system during pregnancy and early life. *Allergy* **55**, 688-697 (2000).
3. Thome, J.J.C. *et al.* Early-life compartmentalization of human T cell differentiation and regulatory function in mucosal and lymphoid tissues. *Nature Medicine* **22**, 72-77 (2016).
4. Howie, D. *et al.* Extrathymic T cell differentiation in the human intestine early in life. *J Immunol* **161**, 5862-5872 (1998).
5. Spencer, J., MacDonald, T., Finn, T. & Isaacson, P. The development of gut associated lymphoid tissue in the terminal ileum of fetal human intestine. *Clinical and experimental immunology* **64**, 536 (1986).
6. Golby, S. *et al.* B cell development and proliferation of mature B cells in human fetal intestine. *Journal of leukocyte biology* **72**, 279-284 (2002).
7. Fenton, T.M. *et al.* Immune Profiling of Human Gut-Associated Lymphoid Tissue Identifies a Role for Isolated Lymphoid Follicles in Priming of Region-Specific Immunity. *Immunity* **52**, 557-570. e556 (2020).
8. van de Pavert, S.A. & Mebius, R.E. New insights into the development of lymphoid tissues. *Nature Reviews Immunology* **10**, 664-674 (2010).
9. Shikhagaie, M.M. *et al.* Neuropilin-1 Is Expressed on Lymphoid Tissue Residing LTi-like Group 3 Innate Lymphoid Cells and Associated with Ectopic Lymphoid Aggregates. *Cell Reports* **18**, 1761-1773 (2017).
10. Fawkner-Corbett, D. *et al.* Spatiotemporal analysis of human intestinal development at single-cell resolution. *Cell* **184**, 810-826.e823 (2021).
11. Shen, P. & Fillatreau, S. Antibody-independent functions of B cells: a focus on cytokines. *Nature Reviews Immunology* **15**, 441-451 (2015).
12. Ruane, D.T. & Lavelle, E.C. The role of CD103+ dendritic cells in the intestinal mucosal immune system. *Frontiers in immunology* **2**, 25 (2011).
13. Bekiaris, V., Persson, E.K. & Agace, W.W. Intestinal dendritic cells in the regulation of mucosal immunity. *Immunol Rev* **260**, 86-101 (2014).
14. Li, N. *et al.* Memory CD4(+) T cells are generated in the human fetal intestine. *Nat Immunol* **20**, 301-312 (2019).
15. Schreurs, R.R.C.E. *et al.* Human Fetal TNF-α-Cytokine-Producing CD4+ Effector Memory T Cells Promote Intestinal Development and Mediate Inflammation Early in Life. *Immunity* **50**, 462-476. e468 (2019).
16. Stras, S.F. *et al.* Maturation of the Human Intestinal Immune System Occurs Early in Fetal Development. *Developmental Cell* **51**, 357-373.e355 (2019).
17. Giesen, C. *et al.* Highly multiplexed imaging of tumor tissues with subcellular resolution by mass cytometry. *Nature Methods* **11**, 417-422 (2014).
18. Guo, N. *et al.* A 34-Marker Panel for Imaging Mass Cytometric Analysis of Human Snap-Frozen Tissue. *Frontiers in Immunology* **11** (2020).
19. Li, N. *et al.* Mass cytometry reveals innate lymphoid cell differentiation pathways in the human fetal intestine. *J Exp Med* **215**, 1383-1396 (2018).
20. van Unen, V. *et al.* Visual analysis of mass cytometry data by hierarchical stochastic neighbour embedding reveals rare cell types. *Nature Communications* **8**, 1740 (2017).
21. van der Weerd, K. *et al.* Combined TCRG and TCRA TREC analysis reveals increased peripheral T-lymphocyte but constant intra-thymic proliferative history upon ageing. *Mol Immunol* **53**, 302-312 (2013).
22. Verstegen, R.H.J. *et al.* Quantification of T-Cell and B-Cell Replication History in Aging, Immunodeficiency, and Newborn Screening. *Front Immunol* **10**, 2084 (2019).
23. Faria, A.M. & Weiner, H.L. Oral tolerance. *Immunol Rev* **206**, 232-259 (2005).
24. Mestecky, J. & McGhee, J.R. Immunoglobulin A (IgA): molecular and cellular interactions involved in IgA biosynthesis and immune response. *Adv Immunol* **40**, 153-245 (1987).
25. van der Heijden, P.J., Stok, W. & Bianchi, A.T. Contribution of immunoglobulin-secreting cells in the murine small intestine to the total 'background' immunoglobulin production. *Immunology* **62**, 551-555 (1987).
26. Takiishi, T., Fenero, C.I.M. & Câmara, N.O.S. Intestinal barrier and gut microbiota: Shaping our immune responses throughout life. *Tissue Barriers* **5**, e1373208-e1373208 (2017).
27. Li, N. *et al.* Early-Life Compartmentalization of Immune Cells in Human Fetal Tissues Revealed by High-Dimensional Mass Cytometry. *Frontiers in Immunology* **10** (2019).
28. Elmentaite, R. *et al.* Cells of the human intestinal tract mapped across space and time. *Nature* **597**, 250-255 (2021).
29. Smith, M.E., Thomas, J.A. & Bodmer, W.F. CD1c antigens are present in normal and neoplastic B-cells. *J Pathol* **156**, 169-177 (1988).
30. Tull, T.J. *et al.* Human marginal zone B cell development from early T2 progenitors. *Journal of Experimental Medicine* **218** (2021).
31. Cerutti, A., Cols, M. & Puga, I. Marginal zone B cells: virtues of innate-like antibody-producing

lymphocytes. *Nat Rev Immunol* **13**, 118-132 (2013).
32. Zhao, Y. *et al.* Spatiotemporal segregation of human marginal zone and memory B cell populations in lymphoid tissue. *Nat Commun* **9**, 3857 (2018).
33. Mishra, A. *et al.* Microbial exposure during early human development primes fetal immune cells. *Cell* **184**, 3394-3409.e3320 (2021).
34. Mold, J.E. *et al.* Fetal and adult hematopoietic stem cells give rise to distinct T cell lineages in humans. *Science* **330**, 1695-1699 (2010).
35. Fergusson, J.R. *et al.* CD161 defines a transcriptional and functional phenotype across distinct human T cell lineages. *Cell Rep* **9**, 1075-1088 (2014).
36. Cosmi, L. *et al.* Human interleukin 17-producing cells originate from a CD161+CD4+ T cell precursor. *J Exp Med* **205**, 1903-1916 (2008).
37. Miller, I. *et al.* Ki67 is a Graded Rather than a Binary Marker of Proliferation versus Quiescence. *Cell Rep* **24**, 1105-1112.e1105 (2018).
38. Gustafson, C.E. *et al.* Limited expression of APRIL and its receptors prior to intestinal IgA plasma cell development during human infancy. *Mucosal Immunol* **7**, 467-477 (2014).
39. FitzSimmons, J., Chinn, A. & Shepard, T.H. Normal length of the human fetal gastrointestinal tract. *Pediatr Pathol* **8**, 633-641 (1988).
40. Neu, J. & Koldovsky, O. Nutrient absorption in the preterm neonate. *Clin Perinatol* **23**, 229-243 (1996).
41. Min, B. *et al.* Neonates support lymphopenia-induced proliferation. *Immunity* **18**, 131-140 (2003).
42. Surh, C.D. & Sprent, J. Homeostasis of naive and memory T cells. *Immunity* **29**, 848-862 (2008).
43. Fry, T.J. & Mackall, C.L. Interleukin-7: master regulator of peripheral T-cell homeostasis? *Trends Immunol* **22**, 564-571 (2001).
44. Guimond, M. *et al.* Interleukin 7 signaling in dendritic cells regulates the homeostatic proliferation and niche size of CD4+ T cells. *Nat Immunol* **10**, 149-157 (2009).
45. Silva, S.L. *et al.* IL-7-Induced Proliferation of Human Naive CD4 T-Cells Relies on Continued Thymic Activity. *Front Immunol* **8**, 20 (2017).
46. Martin, C.E. *et al.* Interleukin-7 Availability Is Maintained by a Hematopoietic Cytokine Sink Comprising Innate Lymphoid Cells and T Cells. *Immunity* **47**, 171-182.e174 (2017).

Supplementary information

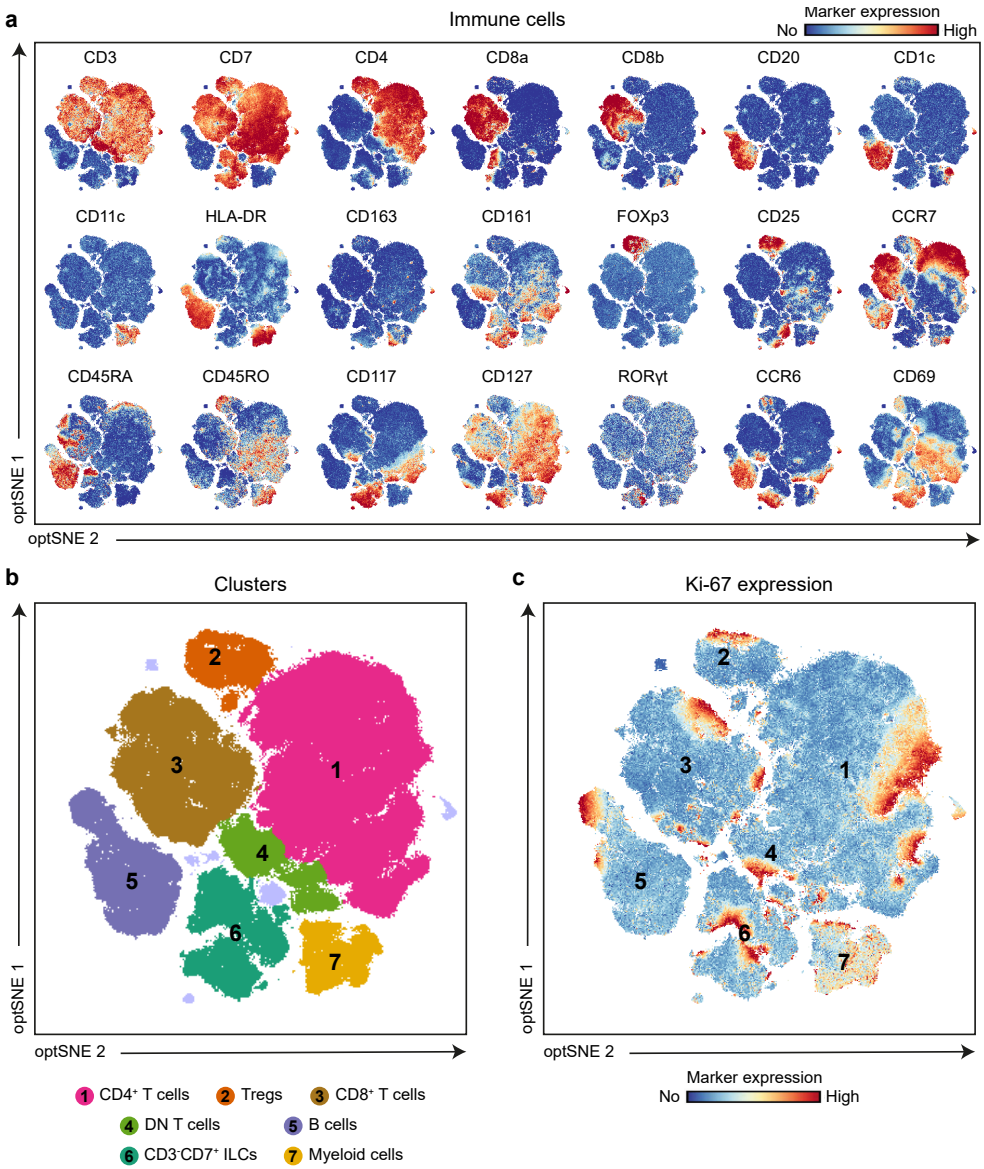

Supplementary Figure. 1 Identification of Ki-67$^+$ cells within all immune subsets in the human fetal intestine. (a) A collective optSNE was performed on CD45$^+$ immune cells from 7 human fetal intestinal samples in a second experiment. Each dot represents a single cell. In total, 5×10^5 CD45$^+$ immune cells were analyzed by OMIQ. Colors represent relative expression of indicated immune markers. **(b)** Based on the relative marker expression profile, each immune lineage was identified and color-coded. **(c)** Display of the Ki-67 expression within the CD45$^+$ immune cells. Colors represent relative expression of Ki-67.

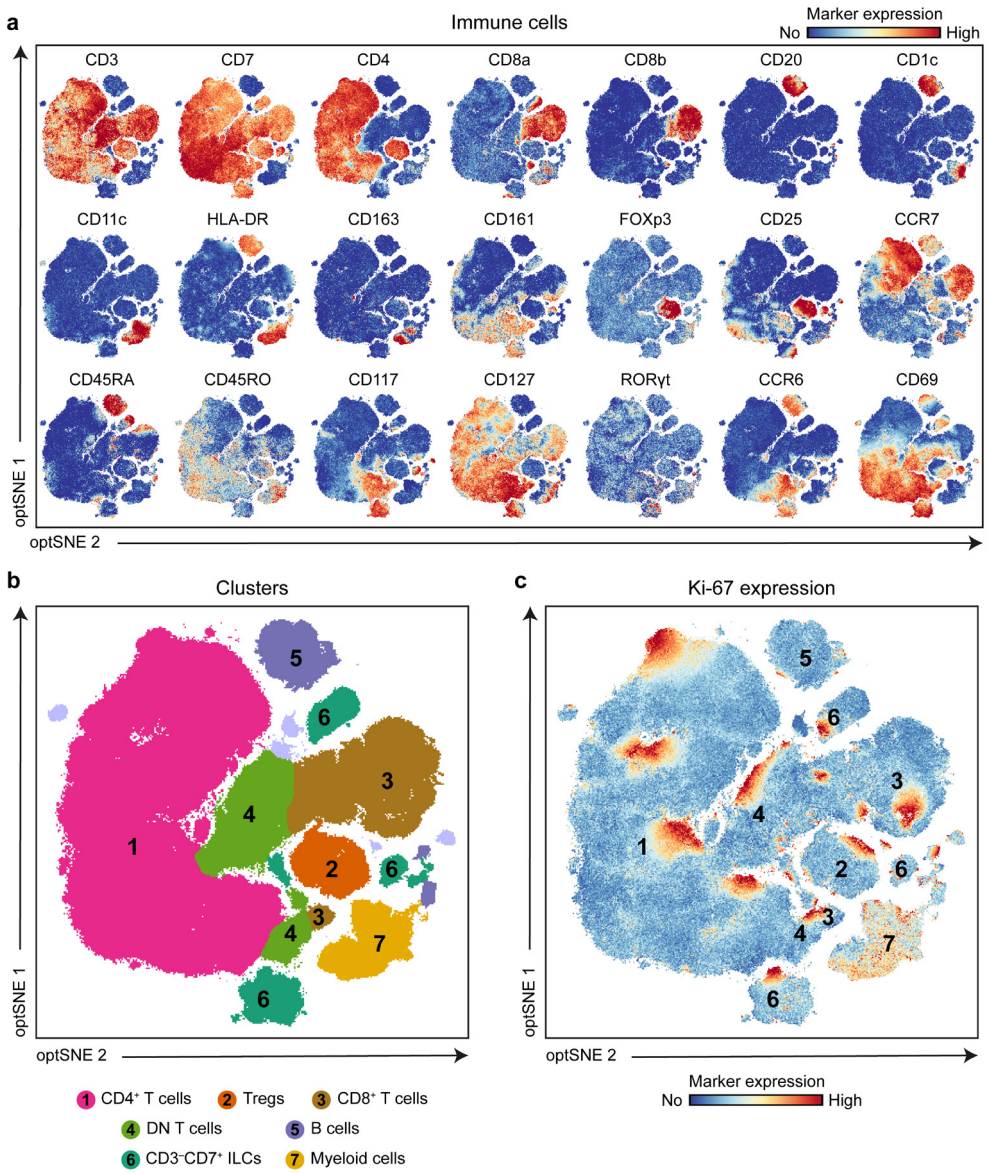

Supplementary Figure. 2 Identification of Ki-67⁺ cells within all immune subsets in the human fetal intestine. (a) A collective optSNE was performed on CD45⁺ immune cells from 12 human fetal intestinal samples in a third experiment. Each dot represents a single cell. In total, 1.02 × 10^6 CD45⁺ immune cells were analyzed by OMIQ. Colors represent relative expression of indicated immune markers. **(b)** Based on the relative marker expression profile, each immune lineage was identified and color-coded. **(c)** Display of the Ki-67 expression within the CD45⁺ immune cells. Colors represent relative expression of Ki-67.

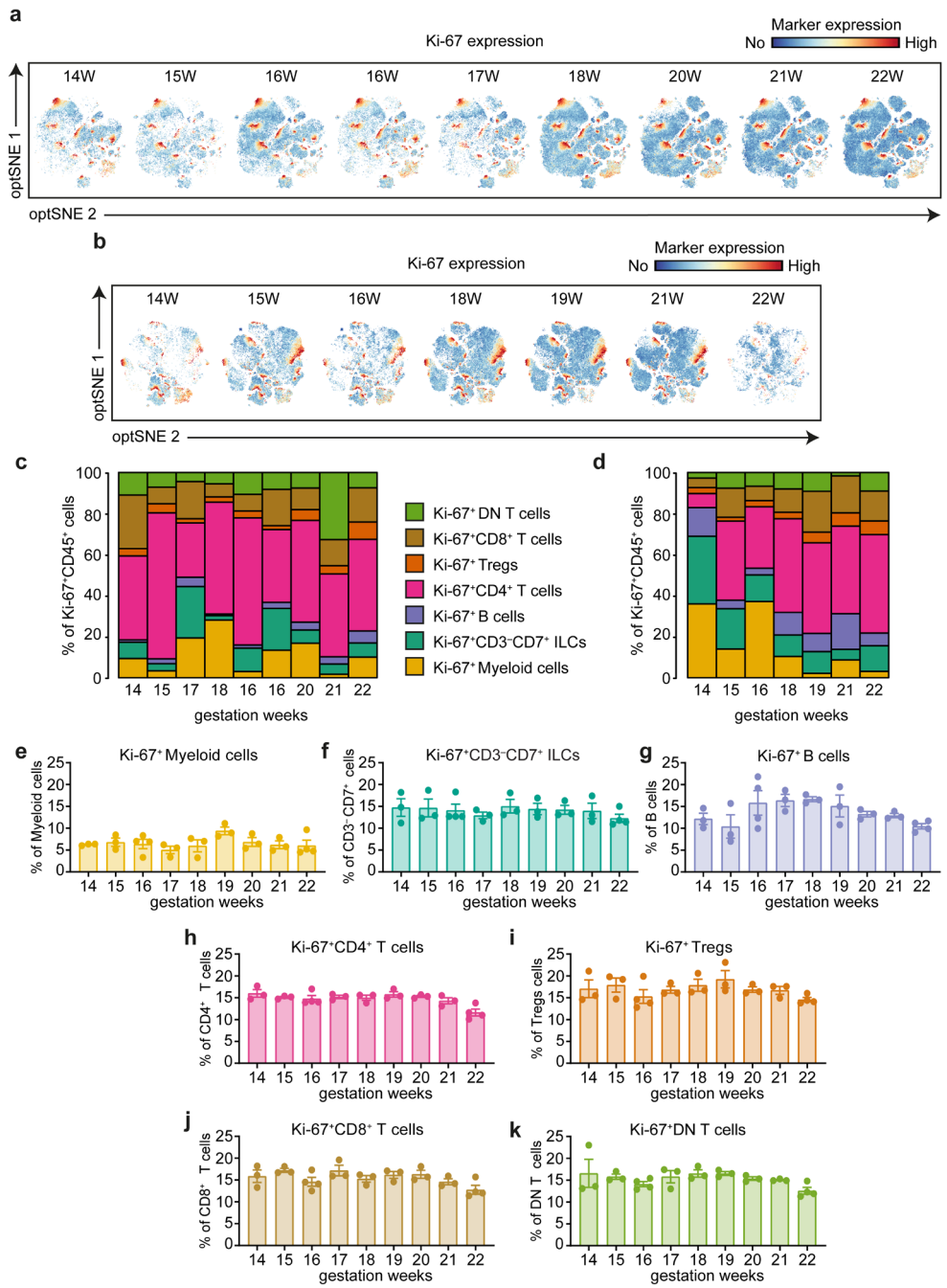

(Figure legend in next page)

Supplementary Figure. 3 Presence of Ki-67⁺ cells throughout gestational week 14 to 22. The presence of Ki-67⁺ cells in fetal intestinal samples from gestational week 14 through 22 was analyzed in two additional experiments. **(a)** Display of the Ki-67 expression in the optSNE plots of the individual fetal intestinal samples (n = 9) from gestational week 14 through 22 in a second experiment. Colors represent different level of Ki-67 expression. **(b)** Display of the Ki-67 expression in the optSNE plots of the individual fetal intestinal samples (n = 7) from gestational week 14 through 22 in a third experiment. Colors represent different level of Ki-67 expression. **(c-d)** Overview of the distribution of Ki-67⁺ cells in the indicated immune lineages from gestational week 14 through 22 in the additional two experiments. Colors indicate different immune subsets. **(e-k)** Overview of the percentages of Ki-67⁺ cells within each immune subset in all human fetal intestine samples analyzed (n = 28).

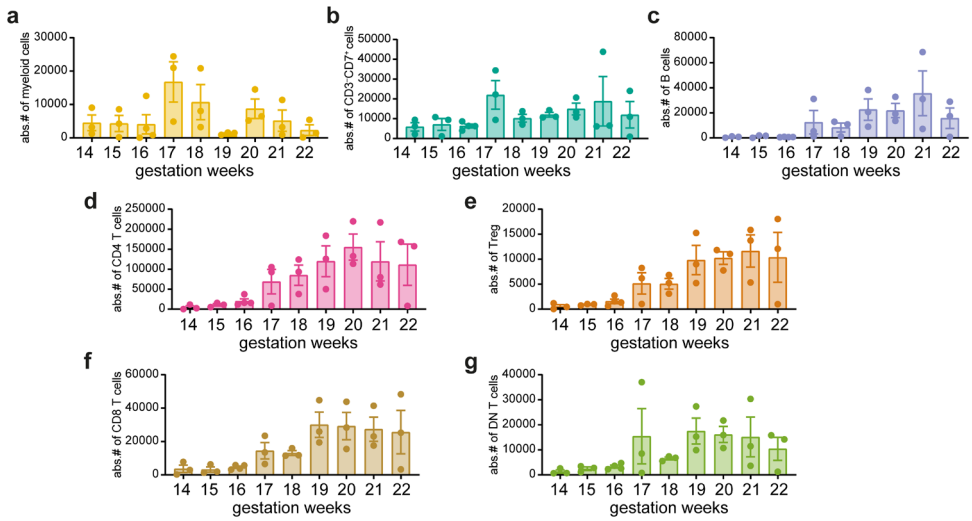

Supplementary Figure 4. Overview of the total cell count per indicated immune lineage from all human fetal intestine samples analyzed (n = 28).

Supplementary Figure. 5 Imaging mass cytometric analysis of immune subsets composition of LFs in human fetal intestine in time. (a) Visualization of lymphoid inducer cell-like cells (LTi-like: CD3⁻CD7⁺CD127⁺CD117⁺) within LFs. The white arrow indicates the expression of CD7, CD127 and CD117 in the absence of CD3. Scale bar, 40 µm. **(b)** Identification of CD20⁺ B cells (blue) within LFs. Scale bar, 200 µm. **(c)** Identification of CD20⁺CD1c⁺ B cells (magenta) within LFs. Scale bar, 40 µm. **(d)** Identification of HLA-DR⁺CD11c⁺ myeloid cells (white) within LFs. Scale bar, 40 µm. Data are from three independent experiments.

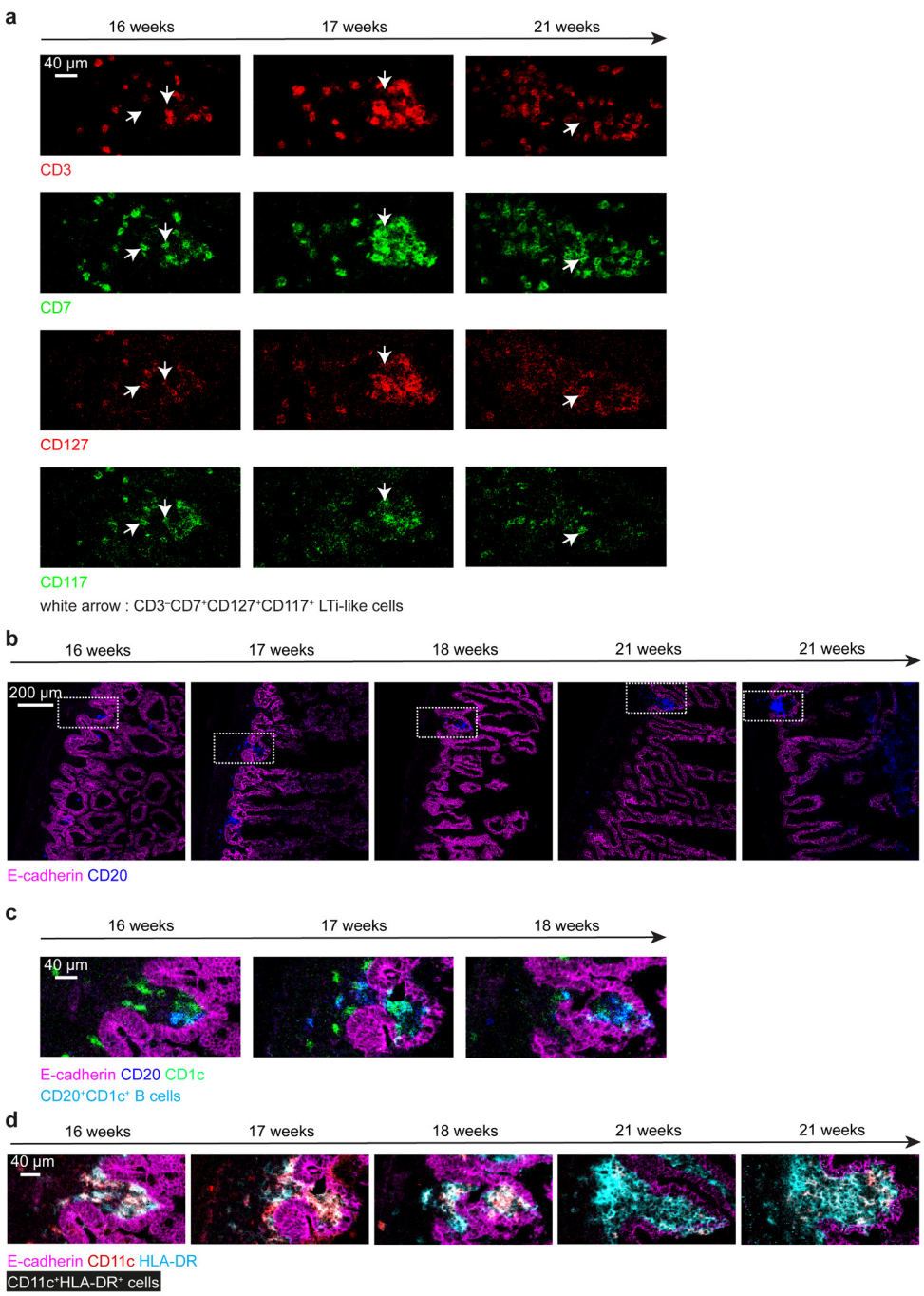

(Figure legend in previous page)

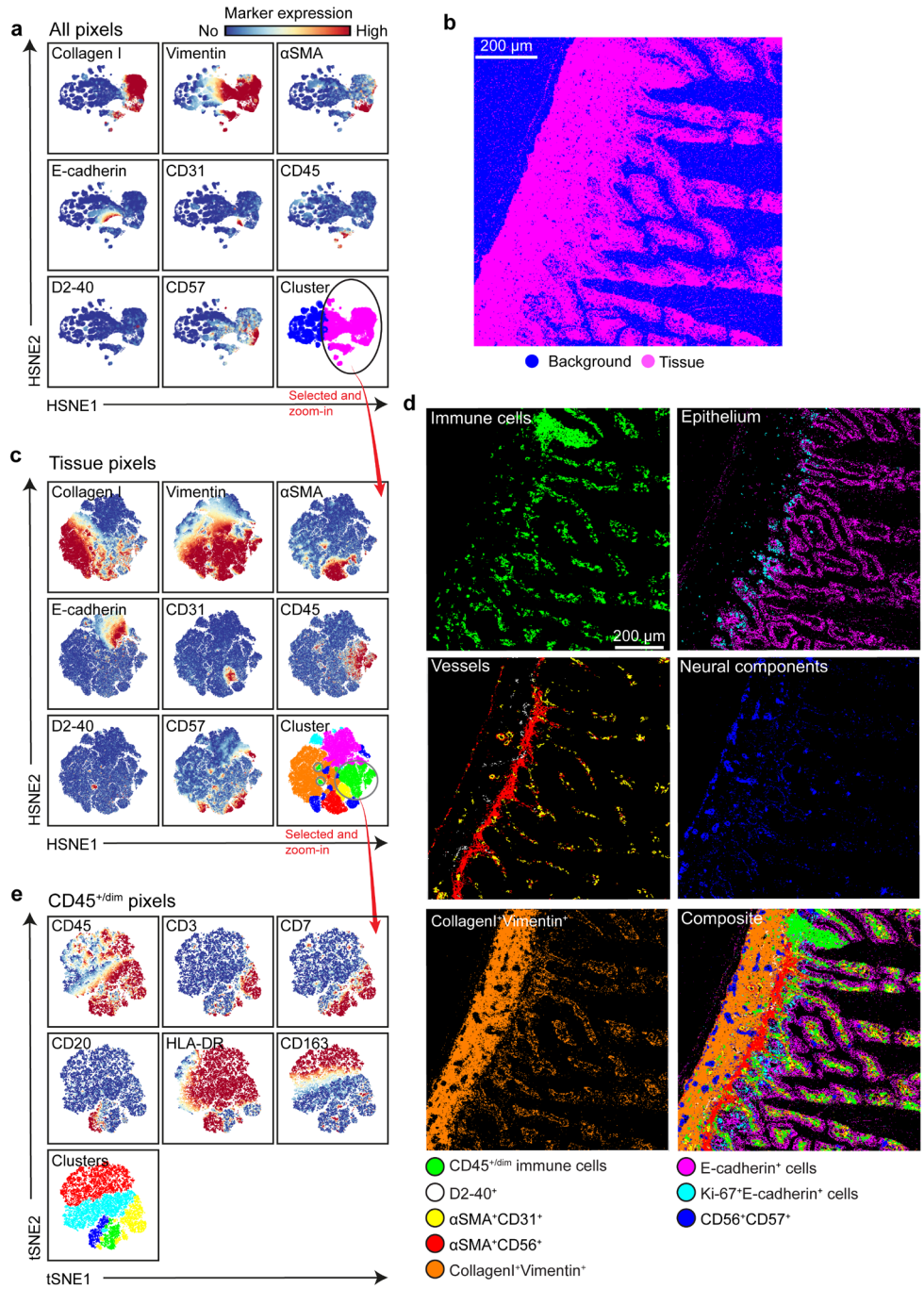

(Figure legend in next page)

Supplementary Figure. 6 The workflow of pixel analysis for IMC data by Cytosplore imaging. (a) An HSNE was performed on pixels from a ROI (1000 μm × 1000 μm) of a human fetal intestine sample. Each dot represents a pixel (1 μm2). Colors represent the relative expression of indicated markers. (b) Based on marker expression profile, the structural markers, CD45 (a) and DNA staining (not shown), the tissue pixels (colored pink) were distinguished from the non-tissue pixels (colored blue), and both were projected to the image viewer. (c) The tissue pixels were selected as indicated and a new higher resolution embedding was generated. Colors represent relative expression of indicated markers. (d) Based on marker expression profile (c), in this level, eight distinct clusters of pixels were identified and color coded. These clusters represented immune cells (CD45+/dim), 2 populations of epithelial cells (E-cadherin^{+}Ki-67^{+} and E-cadherin^{+}Ki-67^{-}), endothelial cells (αSMA^{+}CD31^{+}), smooth muscle cells (αSMA^{+}CD31^{-}), lymphatic endothelial cells (D2-40^{+}), neural components (CD57^{+}CD56$^{+/-}$) and extracellular matrix of the basement membrane (Collagen I^{+}Vimentin^{+}). (e) A further tSNE analysis of the CD45$^{+/dim}$ pixels identified the various immune cell clusters. Colors represent relative expression of indicated immune markers.

Supplementary Figure. 7 Visualization of Ki-67^{+} cells by IMC in human fetal intestine from gestational week 16. (a) Visualization of Ki-67^{+}CD45^{+} cells by staining of Ki-67 and CD45. Scale bar, 200 μm. **(b)** The combination of Ki-67 and immune lineage markers visualized **(a1)** Ki-67^{+}CD4^{+} T cells, **(a2)** Ki-67^{+}CD8^{+} T cells, **(a3)** Ki-67^{+}CD3^{-}CD7^{+} ILCs, **(a4)** Ki-67^{+}CD163^{+} macrophage, and **(a5)** Ki-67^{+}Lin^{-}HLA-DR^{+} myeloid cells in *situ*. White arrow indicated cells of interest. Scale bar, 20 μm**.**

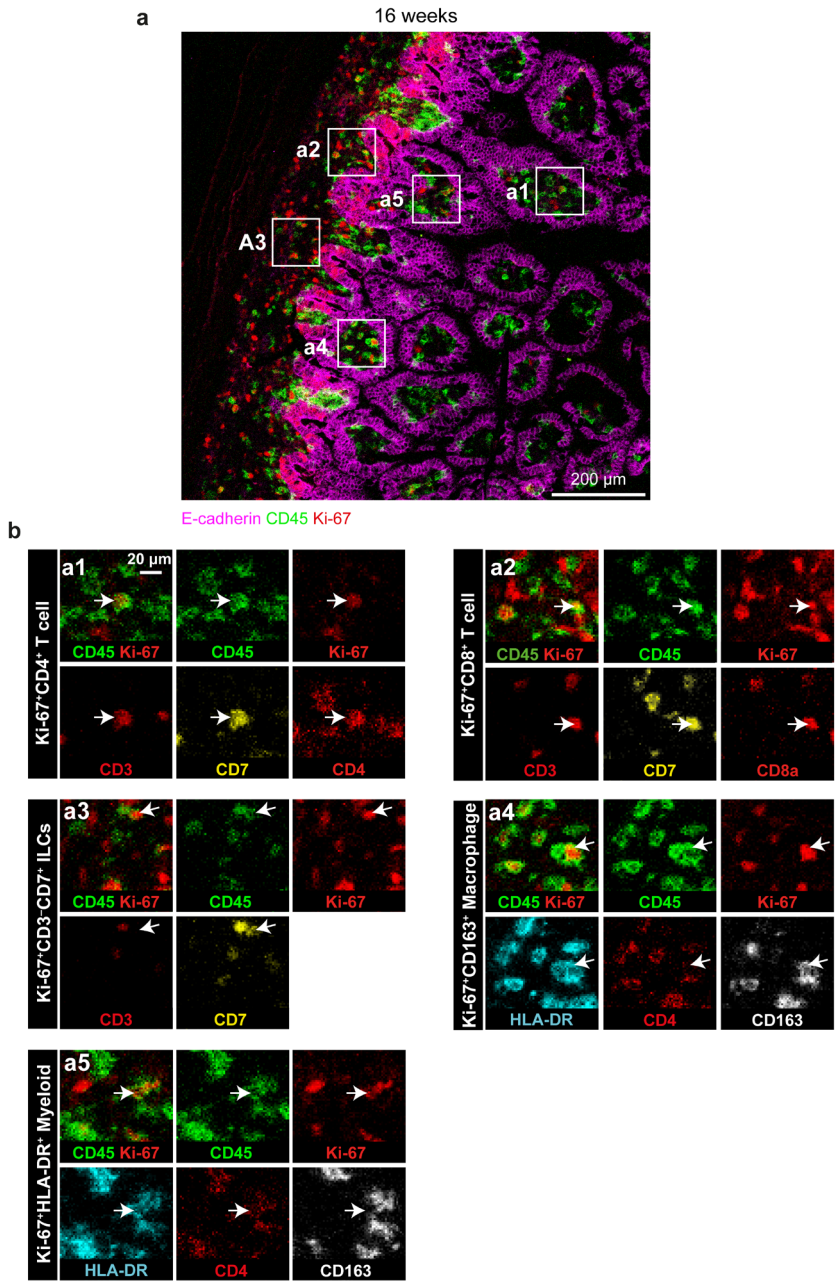

(Figure legend in previous page)

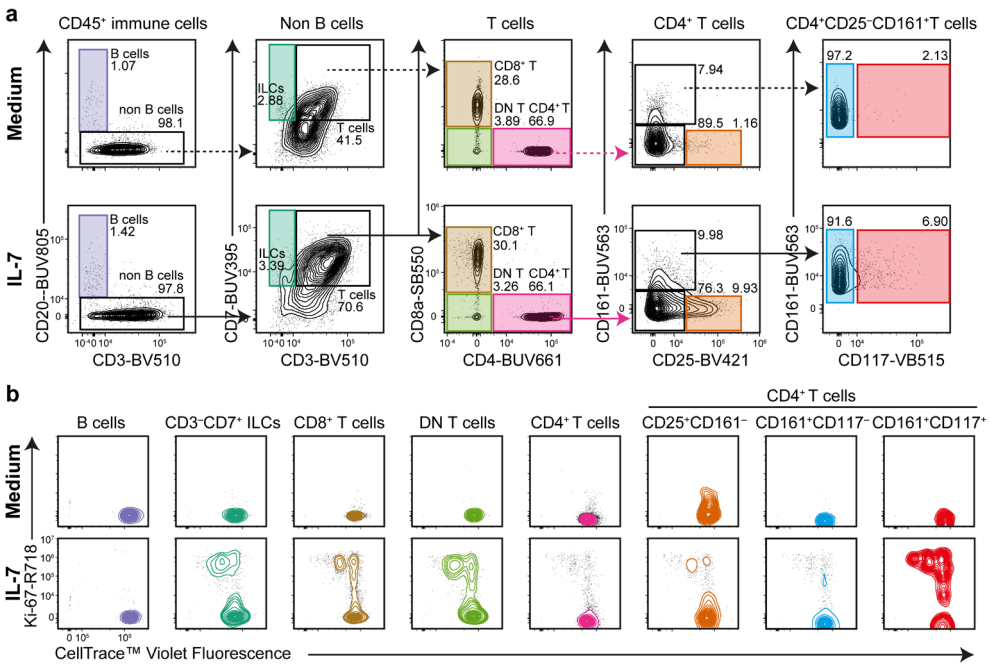

Supplementary Figure. 8 Proliferation assays of Ki-67⁺ cells in each immune subsets from the PBMCs sample. (a) Biaxial plots showing the identification of investigated immune subsets by Cytek Aurora flow cytometry in the PBMCs in medium and medium with IL-7. Colors indicate different immune subsets. **(b)** Biaxial plots showing expression of Ki-67 versus CellTrace™ Violet dye dilution on the indicated immune subsets in the PBMCs sample cultured in medium and medium with IL-7. Colors indicate different immune subsets.

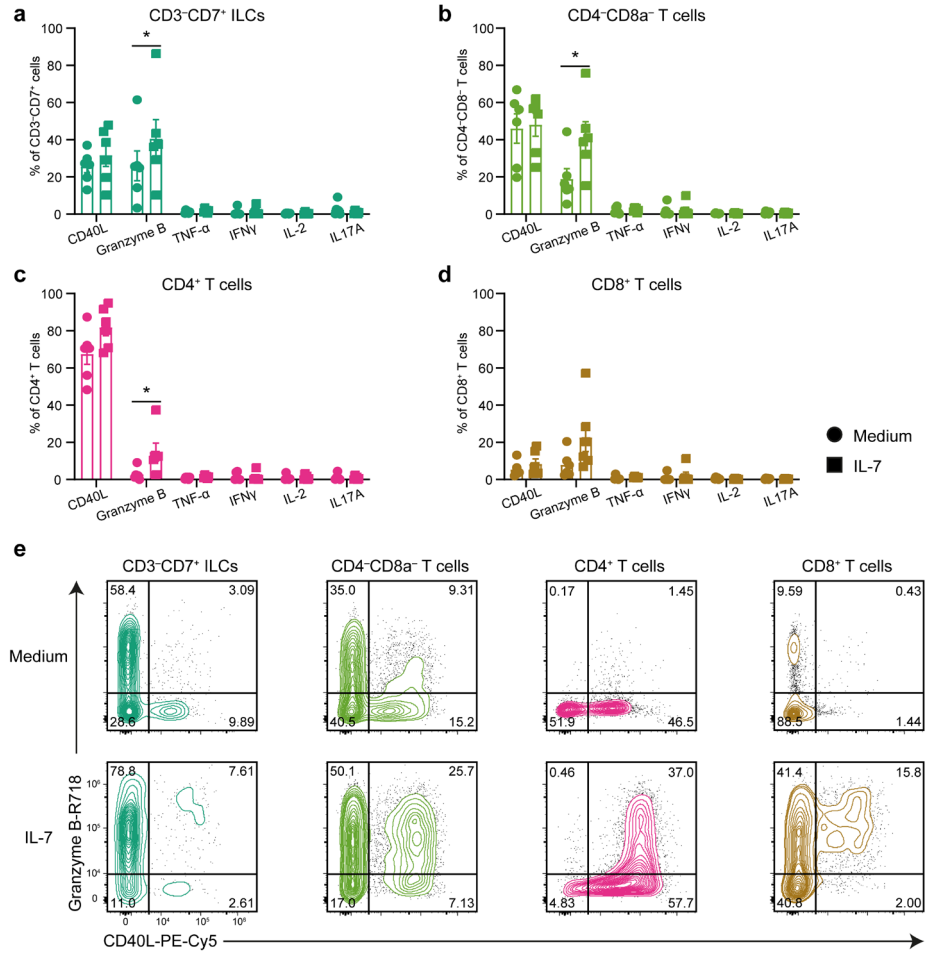

Supplementary Figure. 9 Functional profiling of fetal intestinal cells. (a-d) Fetal intestinal cells were cultured in the absence or presence IL-7 for 48 hours followed by flow cytometric analysis of the expression of CD40L, granzyme B, TNF-α, IFNγ , IL-2 , and IL-17A in $CD3^{-}CD7^{+}$ ILCs and T cells ($CD4^{-}CD8^{-}$ T, $CD4^{+}$ T and $CD8^{+}$ T). In total, four independent experiments were performed. **(e)** Intracellular expression of granzyme B and CD40L was determined for $CD3^{-}CD7^{+}$ ILCs and T cells ($CD4^{-}CD8^{-}$ T, $CD4^{+}$ T and $CD8^{+}$ T) by flow cytometry in both culture conditions. The biaxial plots show data from one representative experiment.

Supplementary Tables

Supplementary Table 1 Single-cell suspension spectral flow cytometry antibody panel.

	Antigen	Tag	Clone	Supplier	Cat.	Dilution
1	CCR6	BB700	11A9	BD	566478	40
2	CCR7	Spark NIR 685	G043H7	Biolegend	353257	25
3	CD117	VioBright 515	REA787	MACS	130-111-674	200
4	CD11c	PE/Cy7	3.9	Biolegend	301608	100
5	CD127	BV711	A019D5	Biolegend	351327	25
6	CD161	BUV563	HP-3G10	BD	749223	25
7	CD163	BV650	GHI/61	BD	563888	25
8	CD1c	SB436	L161	Invitrogen	62-0015-41	25
9	CD20	BV805	2H7	BD	612906	50
10	CD25	BV421	BC96	Biolegend	302630	50
11	CD3	BV510	UCHT1	Biolegend	300448	100
12	CD34	PE/CF594	581	BD	562383	50
13	CD4	CF568	SK3	CyTek	R7-20041	200
14	CD45	QD800	HI30	Invitrogen	Q10156	100
15	CD45R0	BV570	UCHL1	Biolegend	304225	200
16	CD45RA	PerCP	HI100	Biolegend	304155	200
17	CD69	APC/R700	FN50	BD	565155	50
18	CD7	BUV395	M-T701	BD	565979	100
19	CD8a	Spark Blue 550	SK1	Biolegend	344759	200
20	CD8b	BUV496	2ST8.5H7	BD	749837	200
21	FoxP3	APC	PCH101	Invitrogen	17-4776-42	25
22	HLA-DR	BV480	G46-6	BD	566154	200
23	Ki67	BV605	Ki-67	Biolegend	350521	25
24	RORgt	PE	Q21-559	BD	563081	25
25	Viability	L/D near IR	-	Invitrogen	L34976	1000
26	FC Block	-	-	Biolegend	422302	20

Supplementary Table 2 Imaging mass cytometry antibody panel on human fetal intestine from gestational week 21.

	Antigen	Tag	Clone	Supplier	Cat.	Dilution
1	CD45	89Y	HI30	FLM	3089003B	1/50
2	CD69	144Nd	FN50	FLM	3144018B	1/50
3	CD4	145Nd	RPA-T4	FLM	3145001B	1/50
4	CD8a	146Nd	RPA-T8	FLM	3146001B	1/50
5	Collagen I	147Sm	polyclonal	Millipore	AB758	1/100
6	α-SMA	148Nd	1A4	CST	CST 5685BF	1/200
7	E-cadherin	150Nd	24 E 10	CST	CST 3195BF	1/50
8	CD123	151Eu	6H6	FLM	3151001B	1/50
9	CD7	153Eu	CD7-6B7	FLM	3153014B	1/100
10	CD163	154Sm	GHI/61	FLM	3154007B	1/100
11	CD103	155Gd	EPR4166	Abcam	ab221210	1/50
12	CD122	158Gd	TU27	BioL	339015	1/25
13	CD68	159Tb	KP1	FLM	3159035D	1/100
14	CD5	160Gd	UCHT2	BioL	300627	1/25
15	CD20	161Dy	H1	FLM	3161029D	1/50
16	CD11c	162Dy	Bu15	FLM	3162005B	1/50
17	CD45	163Dy	D9M81	CST	13917BF	1/100
18	CD161	164Dy	HP-3G10	FLM	3164009B	1/50
19	Ki-67	166Er	D3B5	CST	CST 9129BF	1/200
20	CD27	167Er	O323	FLM	3167002B	1/50
21	HLA-DR	168Er	L243	BioL	307651	1/800
22	CD45RA	169Tm	HI100	FLM	3169008B	1/100
23	CD3	170Er	UCHT1	FLM	3170001B	1/100
24	CD28	171Yb	CD28.2	BioL	302937	1/50
25	CD38	172Yb	HIT2	FLM	3172007B	1/50
26	CD45RO	173Yb	UCHL1	BioL	304239	1/50
27	Vimentin	175Lu	D21H3	CST	CST 5741BF	1/200
28	CD56	176Yb	NCAM16.2	FLM	3176008B	1/100
Fluidigm (Flui), Cell Signaling Technology (CST) and Biolegend (BioL)						

Supplementary Table 3 Imaging mass cytometry antibody panel on human fetal intestine from gestational week 21.

	Antigen	Tag	Clone	Supplier	Cat.	Dilution
1	CD45	89Y	HI30	Flui	3089003B	1/50
2	D2-40	115In	D2-40	BioL	916606	1/50
3	FOXp3	142Nd	D608R	CST	12653BF	1/50
4	CD69	144Nd	FN50	Flui	3144018B	1/50
5	CD4	145Nd	RPA-T4	Flui	3145001B	1/50
6	CD8a	146Nd	RPA-T8	Flui	3146001B	1/50
7	Collagen I	147Sm	Polyclonal	Millipore	AB758	1/100
8	α-SMA	148Nd	1A4	CST	CST5685BF	1/200
9	CD31	149Sm	8 9C2	CST	CST3528BF	1/100
10	E-Cadherin	150Nd	24 E 10	CST	CST3195BF	1/50
11	CD123	151Eu	6H6	Flui	3151001B	1/50
12	CD7	153Eu	CD7-6B7	Flui	3153014B	1/100
13	CD163	154Sm	GHI/61	Flui	3154007B	1/100
14	CD103	155Gd	EPR4166	Abcam	ab221210	1/50
15	CD127	156Gd	R34.34	Beckman	18LIQ494	1/50
16	CD122	158Gd	TU27	BioL	339015	1/25
17	CD68	159Tb	KP1	Flui	3159035D	1/200
18	CD5	160Gd	UCHT2	BioL	300627	1/25
19	CD20	161Dy	H1	Flui	3161029D	1/50
20	CD11c	162Dy	Bu15	Flui	3162005B	1/50
21	CD45	163Dy	D9M81	CST	13917BF	1/200
22	CD161	164Dy	HP-3G10	Flui	3164009B	1/50
23	CD117	165Ho	104D2	BioL	313202	1/50
24	Ki-67	166Er	D3B5	CST	CST 9129BF	1/200
25	CD27	167Er	O323	Flui	3167002B	1/50
26	HLA-DR	168Er	L243	BioL	307651	1/800
27	CD45RA	169Tm	HI100	Flui	3169008B	1/100
28	CD3	170Er	UCHT1	Flui	3170001B	1/100
29	CD28	171Yb	CD28.2	BioL	302937	1/50
30	CD38	172Yb	HIT2	Flui	3172007B	1/100
31	CD45RO	173Yb	UCHL1	BioL	304239	1/50
32	CD57	174Yb	HNK-1/Leu-7	Abcam	Ab212403	1/100
33	Vimentin	175Lu	D21H3	CST	CST5741BF	1/200
34	CD56	176Yb	NCAM16.2	Flui	3176008B	1/50
Fluidigm (Flui), Cell Signaling Technology (CST) and Biolegend (BioL)						

Supplementary Table 4 Imaging mass cytometry antibody panel on human fetal intestine from gestational week 16 to 19.

	Antigen	Tag	Clone	Supplier	Cat.	Dilution
1	CD45	89Y	HI30	Flui	3089003B	50
2	D2-40	115In	D2-40	BioL	916606	50
3	FOXp3	142Nd	D608R	CST	12653BF	100
4	CD69	144Nd	FN50	Flui	3144018B	50
5	CD4	145Nd	RPA-T4	Flui	3145001B	50
6	CD8a	146Nd	RPA-T8	Flui	3146001B	50
7	Collagen I	147Sm	polyclonal	Millipore	AB758	100
8	CD34	148Nd	QBEND/10	Thermo	MA1-10202	50
9	CD31	149Sm	8 9C2	CST	CST3528BF	100
10	E-cadherin	150Nd	24 E 10	CST	CST 3195BF	50
11	CD123	151Eu	6H6	Flui	3151001B	50
12	CD141	152Sm	Phx-01	BioL	902102	50
13	CD7	153Eu	CD7-6B7	Flui	3153014B	100
14	CD163	154Sm	GHI/61	Flui	3154007B	100
15	CD103	155Gd	EPR4166	Abcam	ab221210	50
16	CD127	156Gd	R34.34	Beckman	18LIQ494	50
17	CD68	159Tb	KP1	Flui	3159035D	200
18	CD20	161Dy	H1	Flui	3161029D	50
19	CD11c	162Dy	Bu15	Flui	3162005B	50
20	CD11c	162Dy	S-HCL-3	BioL	125602	50
21	CD161	164Dy	HP-3G10	Flui	3164009B	50
22	CD117	165Ho	104D2	BioL	313202	50
23	Ki-67	166Er	D3B5	CST	CST 9129BF	200
24	CD27	167Er	O323	Flui	3167002B	50
25	HLA-DR	168Er	L243	BIoL	307651	800
26	CD45RA	169Tm	HI100	Flui	3169008B	100
27	CD3	170Er	UCHT1	Flui	3170001B	100
28	CD1c	171Yb	L161	BioL	331501	50
29	CD38	172Yb	HIT2	Flui	3172007B	100
30	CD45RO	173Yb	UCHL1	BioL	304239	50
31	CD57	174Yb	HNK-1/Leu-7	Abcam	Ab212403	100
32	CD25	175Lu	24204.0	Thermo	MA5-23714	50
33	CD56	176Yb	NCAM16.2	Thermo	MA1-06801	50
34	α-SMA	194Pt	1A4	CST	56856BF	100
35	Vimentin	198Pt	D21H3	CST	5741BF	100
Fluidigm (Flui), Cell Signaling Technology (CST) and Biolegend (BioL)						

Supplementary Table 5 The antibody panel of proliferation assays by spectrum flow cytometry.

	Antigen	Tag	Clone	Supplier	Cat.	Dilution
1	CD117	VioBright 515	REA787	MACS	130-111-674	200
2	CD11c	PE/Cy7	3.9	Biolegend	301608	100
3	CD127	BV711	A019D5	Biolegend	351327	25
4	CD161	BUV563	HP-3G10	BD Biosciences	749223	25
5	CD20	BUV805	2H7	BD Biosciences	612906	50
6	CD25	BV421	BC96	Biolegend	302630	50
7	CD3	BV510	UCHT1	Biolegend	300448	100
8	CD4	BUV661	SK3	BD Biosciences	612962	100
9	CD45	NovaBlue 610	2D1	Invitrogen	H005T02B05	50
10	CD7	BUV395	M-T701	BD Biosciences	565979	100
11	CD8a	SB550	SK1	Biolegend	344759	200
12	CD8b	BUV496	2ST8.5H7	BD Biosciences	749837	200
13	HLA-DR	BV750	L243	Biolegend	307671	50
14	Ki67	R718	B56	BD Biosciences	566963	100
15	Viability	L/D near IR	-	Invitrogen	L34976	1000
16	CellTrace™ Violet	CTV	-	Invitrogen	34557	4000
17	FC Block	-	-	Biolegend	422302	20

Supplementary Table 6 The antibody panel of functional profiles analysis by spectrum flow cytometry.

	Antigen	Tag	Clone	Supplier	Cat.	Dilution
1	CD117	VioBright 515	REA787	MACS	130-111-674	200
2	CCR7	Spark NIR 685	G043H7	Biolegend	353257	25
3	CD127	BV711	A019D5	Biolegend	351327	25
4	CD161	BUV563	HP-3G10	BD Biosciences	749223	25
5	CD20	BUV805	2H7	BD Biosciences	612906	50
6	CD25	BV421	BC96	Biolegend	302630	50
7	CD3	BV510	UCHT1	Biolegend	300448	100
8	CD4	BUV661	SK3	BD Biosciences	612962	100
9	CD45	NovaBlue 610	2D1	Invitrogen	H005T02B05	50
10	CD7	BUV395	M-T701	BD Biosciences	565979	100
11	CD8a	SB550	SK1	Biolegend	344759	200
12	CD8b	BUV496	2ST8.5H7	BD Biosciences	749837	200
13	CD45R0	BV570	UCHL1	Biolegend	304225	200
14	CD45RA	PerCP	HI100	Biolegend	304155	200
15	HLA-DR	BV750	L243	Biolegend	307671	50
16	Ki67	BV605	Ki-67	Biolegend	350521	25
17	Helios	PerCP/eFluor710	22F6	Thermo	46-9883-42	25
18	IL-17A	PE/Dazzle™ 594	BL168	Biolegend	512335	25
19	IFNg	BV750	RUO	BD Biosciences	566357	50
20	TNFa	PE/Cy7	MAb11	Thermo	25-7349-82	50
21	CD40L	PE/Cy5	24-31	Biolegend	310808	50
22	Granzyme B	R718	B56	BD Biosciences	566963	50
23	IL-2	PE	MQ1-17H12	BD Biosciences	560902	200
24	Viability	L/D near IR	-	Invitrogen	L34976	1000
25	CellTrace™ Violet	CTV	-	Invitrogen	34557	4000
26	FC Block	-	-	Biolegend	422302	20

Chapter 4

Mass Cytometric Analysis of Early Stage Mycosis Fungoides

Nannan Guo[1], Li Jia[1], Coby Out-Luiting[2], Noel F. C. C. de Miranda[3], Rein Willemze[2], Frits Koning[1], Maarten Vermeer[2], Koen Quint[2*]

[1]Department of Immunology, Leiden University Medical Center, Leiden, The Netherlands
[2]Department of Dermatology, Leiden University Medical Center, Leiden, The Netherlands
[3]Department of Pathology, Leiden University Medical Center, Leiden, The Netherlands

[*]**Correspondence**

Cells 2022, 11, 1062.

Abstract

Mycosis Fungoides (MF) is the most common subtype of cutaneous T-cell lymphoma. Early stage disease is characterized by superficial infiltrates of small to medium-sized atypical epidermotropic T-lymphocytes that are clonal related. Nevertheless, the percentage of atypical T cells is low with many admixed reactive immune cells. Despite earlier studies the composition and spatial characteristics of the cutaneous lymphocytic infiltrate has been incompletely characterized. Here, we applied mass cytometry to profile the immune system in skin biopsies of patients with early stage MF and in normal skin from healthy individuals. Single cell suspensions were prepared and labelled with a 43-antibody panel and data were acquired on a Helios mass cytometer. Unbiased hierarchical clustering of the data identified the major immune lineages and heterogeneity therein. This revealed patient-unique cell clusters in both the $CD4^+$ and myeloid cell compartment but also phenotypically distinct cell clusters that were shared by most patients. To characterize the immune compartment in the tissue context, we developed a 36-antibody panel and performed imaging mass cytometry on MF skin tissue. This visualized the structure of MF skin and the distribution of $CD4^+$ T cells, regulatory T-cells, $CD8^+$ T cells, malignant T cells, and various myeloid cell subsets. We observed clusters of $CD4^+$ T cells and multiple types of dendritic cells (DCs) identified through differential expression of CD11c, CD1a and CD1c in the dermis. These results indicate substantial heterogeneity in the composition of the local immune infiltrate but suggest a prominent role for clustered CD4-DC interactions in disease pathogenesis. Probably, the local inhibition of such interactions may constitute an efficient treatment modality.

Key terms: Mass cytometry; CyTOF; imaging mass cytometry; IMC; mycosis fungoides; Cutaneous T-cell Lymphoma; CTCL

Introduction

Mycosis fungoides (MF) is the most common variant of cutaneous T-cell lymphoma (CTCL), with a 5 years disease specific survival around 80% depending on the stage of the disease[1, 2]. The majority of MF patients have early stage disease (Stage IA/IB), with red scaly (sometimes itchy) patches and plaques on the skin with no extracutaneous involvement. Early stage MF can be extremely subtle, with skin lesions only present on a small body area. Those lesions are hard to recognize by untrained physicians and can be easily confused clinically as well as histologically with reactive dermatitis, leading to a diagnostic delay and mistreatment[3, 4]. Definite diagnosis is made by the clinicopathological correlation and sensitive for error. Therefore, the need of adjuvant diagnostic tools is desirable.

Histologically, early stage MF is characterized by small- to medium-sized pleomorphic T-cell lymphocytes with cerebriform nuclei infiltrating the basal layer of the epidermis (epidermotropism)[5]. However, the characteristic tumor cells in early stage MF can be scarce and hard to recognize. Immunophenotyping, to document loss of T cell antigens suggestive for a malignancy (CD3, CD5, CD7), and to determine the phenotype of the malignant cells (CD4, CD8, cytotoxic markers), can be of help. Still the diagnosis of early stage MF remains challenging, since early-stage MF lesions are characterized by a low number of tumor cells and an extensive inflammatory infiltrate with a relative abundance of $CD8^+$ T cells and dendritic cells (DCs). Multiple studies suggest that complex loops of cytokine and chemokine signaling between fibroblasts, keratinocytes and malignant T cells contribute to an inflammatory microenvironment that contribute to the progression of disease. These studies suggested that a decrease in $CD8^+$ T-cells and an increase in inhibitory M2 macrophages, combined with a shift from Th1 to Th2-dominated microenvironment, and alteration of the regulatory T-cell (Treg)/ Th17 balance lead to progression of MF. Furthermore the viability and growth of the malignant T-cells seemed partly dependent on interaction with immature dendritic cells, through contact between CD40 located on dendritic cells and CD40 ligand located on malignant T-cells[6]. Another in vitro study further supported previous observation, in which dendritic cells stimulates cultures of malignant T-cells and induces Treg cytokine production[7]. However, comprehensive studies investigating the different subsets of immune cells in tissue context are largely lacking, and little is known about cell-cell interactions between tumor cells and the reactive immune infiltrate.

Recently, single cell phenotyping platforms, such as single-cell RNA sequencing

and mass cytometry (cytometry by time-of-flight; CyTOF) have been utilized to investigate cellular heterogeneity[8, 9], to identify novel cellular subsets[10, 11], and to discover clinical relevant biomarkers with clinical value in human[12]. Mass cytometric techniques can characterize different immune cell populations in dissected skin cells and in the tissue contexture[13, 14]. Single cell mass cytometry allows an unbiased analysis of the complexity and heterogeneity of the human immune system as over 40 unique cellular markers can be measured simultaneously[15, 16]. In addition, imaging mass cytometry, which couples a laser ablation system with a mass cytometer, allows for the analysis of up to 40 markers in a single tissue section. With imaging mass cytometry, tissue structures can be visualized as well as the composition, distribution and spatial interactions of the stromal and immune cell subsets in the tissue context[17, 18].

In the current study, we applied single cell suspension and imaging mass cytometry to skin biopsies of early stage MF patients to gain deeper insight into the composition and organization of the immune compartment in the tissue context and the relation/interaction with malignant T-cells. We observed pronounced patient-specific characteristic features in the skin resident immune populations, and distinct clusters of lymphoid and myeloid cell populations in lesional skin that may drive the transformation and subsequent sustenance of the tumor cells in *situ*.

Material and methods

Patient selection

A total of 16 skin biopsies (4mm) with confirmed diagnoses of early stage MF (stage IA/IB; patches/plaques, no tumors) and 21 biopsies of normal skin (NS) were selected from the "Biobank Dermatology" of the Leiden University Medical Center. All biopsies were taken from the lesions of MF patients that were not previously treated with topical steroids, and the MF patients had not received any systemic medication yet at time of biopsy. All diagnoses had been confirmed by an expert panel of dermatologists and pathologists of the Dutch Cutaneous Lymphoma Group. An additional biopsy from the same lesion and photographic documentation were available for routine diagnostics and determination of the subtype of MF (i.e. Folliculotropic MF, $CD8^+$ MF). Approval by the medical ethical commission of the Leiden University Medical Center (protocol B19.005) was obtained in accordance with the local ethical guidelines and the Declaration of Helsinki. All patient provided written informed consent for biobanking. Baseline characteristics and disease course during follow-up are given in table S1, and the

sex and age characteristics of the NS donors are shown in table S2.

Skin biopsy processing

The fresh skin biopsies (MF, n=10; NS, n=17, for suspension mass cytometry) and the snap-frozen biopsies (MF, n=6; NS, n=4, for imaging mass cytometry) were retrieved from the biobank. Fresh skin punch biopsies were maintained in cold HBSS solution and brought to the laboratory within 10 - 30 mins. To obtain single cell suspensions, the skin biopsies were cut into small pieces and transferred to a gentleMACS C tube to incubate in 500 µl IMDM (Lonza, Basel, Switzerland) supplemented with 10% FCS, 1 mg/ml collagenase D (Roche Diagnostics), and 50 µg/ml DNase I (Roche Diagnostics, Basel, Switzerland), at 37°C for 2 hours, after which 500 µl of IMDM with 10% FCS was added to terminate digestion. Subsequently the gentleMACS program h_skin in gentleMACS™ Dissociator (Miltenyi Biotec, Bergisch Gladbach, Germany) was run after which the cells were spun down. Finally, cell suspensions were filtered through a 70-µm nylon cell strainer and immediately stained with the single-cell mass cytometry antibody panel. Snap-frozen skin tissues were obtained by embedding in optimal cutting temperature compound (O.C.T., VWR), frozen in cold isopentane (VWR) and store in -80° C for immunodetection staining by IMC.

Suspension mass cytometry antibody staining and data acquisition

Metal-conjugated antibodies used for single-cell mass cytometry are listed in Table S3. For self-conjugation of antibodies, BSA-free and carrier-free formulations of antibodies were purchased from different suppliers. Subsequently, conjugation of antibodies with lanthanide metals was performed using the MaxPar Antibody Labeling Kit (Fluidigm, San Francisco, CA, USA) following the manufacturer's instructions. Post-conjugation, all antibodies were eluted in 100 µl W-buffer (Fluidigm) and 100 µl antibody stabilizer buffer (Candor Bioscience) supplemented with 0.05% sodium azide. Procedures for mass cytometry antibody staining and data acquisition were performed as previously described[19]. In short, skin cells were incubated with 1 ml 250 µM Cell-ID™ intercalator-103Rh (Fluidigm) for 15 min at room temperature (RT) to distinguish live cells from dead cells in 5 ml microcentrifuge tubes. After washing once by by Maxpar® Cell Staining Buffer (Fluidigm), the skin cells were stained with metal-conjugated antibodies for 45 min at RT (Table S3). After staining and washing by Maxpar® Cell Staining Buffer (Fluidigm) for three times, cells were incubated with 1 ml 2000× diluted 250 µM Cell-ID™ intercalator-Ir (Fluidigm) in MaxPar Fix and Perm Buffer (Fluidigm) overnight at 4° C. The next day, skin cells were washed by Maxpar® Cell Staining Buffer (Fluidigm) for 3 times and spun down. Finally, cells were acquired on a

Helios time-of-flight mass cytometer (Fluidigm). Data were normalized by using EQ Four Element Calibration Beads (Fluidigm) with the reference EQ passport P13H2302 in each experiment.

Imaging mass cytometry staining and Data acquisition

Procedures for IMC antibody staining and data acquisition for snap-frozen tissue were carried out as previously described[20]. In short, snap-frozen human skin biopsies were sectioned at a thickness of 5 µm. All tissue sections were dried for 1 hour at RT after cutting, then were fixed by incubating with 1% paraformaldehyde (PFA) for 5 min at RT followed by 100% methanol for 5 min at -20° C. After fixation procedures, tissue sections were washed in Dulbecco's phosphate-buffered saline (DPBS, ThermoFisher Scientific, Waltham, MA, USA) with 1% bovine serum albumin (BSA, Sigma) and 0.05% Tween, rehydrated in additive-free DPBS. After washing, the tissue sections were blocked by Superblock Solution (ThermoFisher Scientific) for 30 min in a humid chamber at RT. Tissue sections were then stained with 36 antibodies mixture overnight at 4° C, all antibodies of IMC panel were listed in Table S4. After antibody mixture incubation, the tissue sections were washed and incubated with 125 nM Cell-ID^{Tm}Intercalator-Ir for 30 min at RT. After an additional wash, tissue sections were washed by Milli-Q water (Merck Millipore) for 1 min to remove additives and dried for 20 min at RT. The acquisition was performed by a UV-laser spot by-spot of Hyperion Imaging System at a resolution of 1 µm and a frequency of 200 Hz. Regions of interest (ROIs) with 1000 µm × 1000 µm or 1200 µm × 1000 µm were selected in skin tissue sections. We ablated the whole skin tissue section by 1 to 2 ROIs to cover the whole skin biopsy sections. After ablation by Hyperion (Fluidigm) as described in the Hyperion imaging system user guide, MCD files and txt files were generated for each sample for further analysis.

Data Analysis

Data for single, live CD45$^+$ cells were gated from each MF sample individually using Flowjo software as shown in Figure S1A. Subsequently, the data were sample tagged and hyperbolic arcsinh transformed with a cofactor of 5 and subjected to dimensionality reduction analysis in Cytosplore^{+HSNE}[15, 16]. We employed a 43-antibody panel for staining of single cell mass cytometry (Table S3). Major immune lineages were identified at the overview level of a hierarchical stochastic neighbor embedding (HSNE) analysis on CD45$^+$ cells data from all samples with default perplexity (30) and iterations (1000). All HSNE and t-SNE plots were generated in Cytosplore[15, 16]. The immune lineage population frequencies of CD45$^+$ cells were computed within the individual samples using the "prcomp" function, and the result was visualized using the "ggbiplot" function in R software. Hierarchical

clustering of the phenotype heatmap was created with Euclidean correction and average linkage clustering while the cell frequency heatmap with Spearman correction and average linkage clustering was generated in Matlab R2016b.

We utilized a 36-antibody panel for staining of IMC on snap-frozen skin tissue to visualize spatial data (Table S4). All IMC raw data were from three independent experiments and analyzed by using the Fluidigm MCD™ viewer (v1.0.560.2). The images of single marker within IMC panel are shown in Figure S5 to S14, to show the individual stains in each NS and MF sample. And the minimum and maximum threshold of each marker for all samples were provided as Table S5, in which the maximum threshold value reflects the staining density of the antibodies, while the minimum threshold value was used to reduce the background signal for each marker-channel. To combine related markers to visualize structure of skin tissue and distinct immune subsets, we utilized the Fluidigm MCD™ viewer to generate the images for a single ROI of skin tissue.

Results

Identification of Major Immune Lineages

We applied a 43-antibody panel to identify the major immune lineages ($CD4^+$ T cells, $CD8^+$ T cells, myeloid cells, B cells and innate lymphoid cells (ILCs)) in 10 early stage MF patients. This antibody panel contained markers for identification of the immune lineages, cellular differentiation, activation, trafficking, tissue residency and function (Table S3). Single, live $CD45^+$ cells were selected by means of DNA and CD45 staining, and commonly used mass cytometry parameters (Figure S1A). From the skin biopsies we acquired on average 1737 $CD45^+$ cells from normal skin (NS), and 16396 $CD45^+$ cells from MF skin by single-cell mass cytometry (Figure 1A). In agreement, IMC analysis revealed substantial immune cell infiltration in *situ* in MF patients in comparison with NS samples (Figure 1B). Due to much lower amount of immune cells detected on NS samples by both techniques, we next focused on MF patients for further analysis.

To analyze the composition of the immune cell infiltrate of MF patients, we integrated the data derived from 10 MF samples (3.6×10^5 $CD45^+$ cells), and performed a HSNE analysis in Cytosplore^{+HSNE} at the global level to identify the major immune lineages (Figure 2A). Based on the marker expression profiles (Figure 2B) and density features of the embedded cells (Figure S1B), we identified clusters of $CD3^+CD4^+$ T cells, $CD3^+CD8^+$ T cells, $CD11c^+/CD11b^+$ myeloid cells, $CD3^-CD20^-CD11c^-CD11b^-CD7^+$ innate lymphoid cells (ILCs), $CD20^+$ B cells and

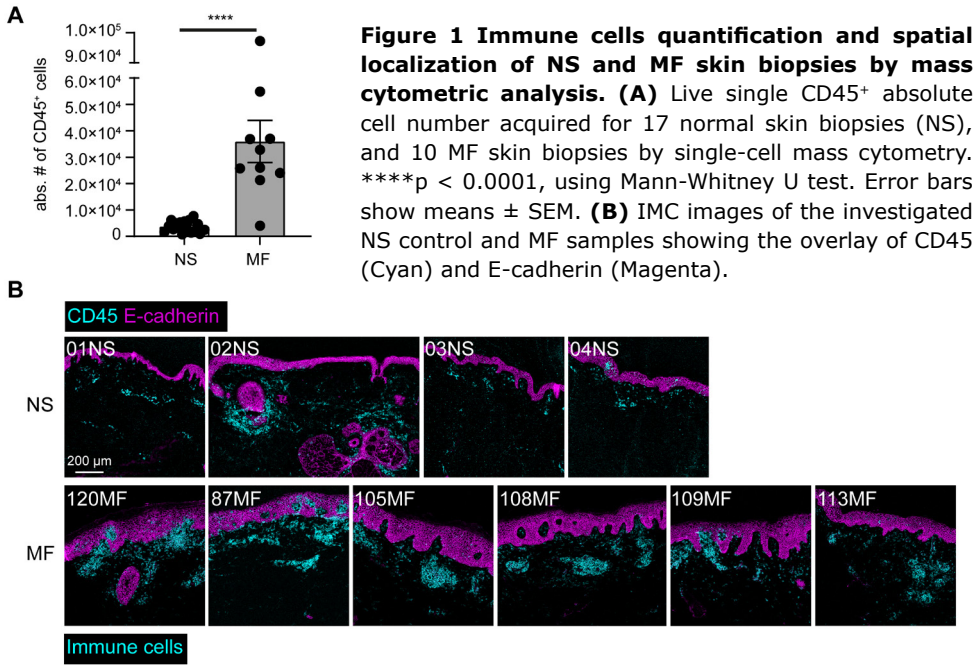

Figure 1 Immune cells quantification and spatial localization of NS and MF skin biopsies by mass cytometric analysis. (A) Live single CD45$^+$ absolute cell number acquired for 17 normal skin biopsies (NS), and 10 MF skin biopsies by single-cell mass cytometry. ****p < 0.0001, using Mann-Whitney U test. Error bars show means ± SEM. **(B)** IMC images of the investigated NS control and MF samples showing the overlay of CD45 (Cyan) and E-cadherin (Magenta).

abnormal CD3$^-$CD7$^-$CD8$^-$CD4$^+$ T cells (Figure 2A, S1B). Moreover, we quantified the relative frequencies of these major immune lineages within the CD45$^+$ cells of each MF patient (Figure 2C). We observed that CD3$^+$CD4$^+$ T cells were the dominant cell population in MF patients as they represented more than 50% of CD45$^+$ cells in eight out of ten MF patients. Both CD3$^+$CD8$^+$ T cells and myeloid cells were present in all patients, but their percentage varied significantly among patients. In five out of ten patients aberrant T cells with loss of CD3 and CD7 expression (CD3$^-$CD7$^-$CD8$^-$CD4$^+$ T cells) were observed. This aberrant phenotype was most prevalent in patient 79MF but lower in the other 4 patients (84MF, 82MF, 81MF, 62MF). Significant numbers of CD3$^-$CD20$^-$CD11c$^-$CD11b$^-$CD7$^+$ ILCs were only detected in three patients while only few B cells being present in all patient samples. Together, these global analyses revealed that all major immune lineages could be readily identified in MF patients, and that the composition of these immune cells differed among the evaluated patients.

Analysis of the CD4 T cell compartment reveals shared and patient-unique features

To define and compare the composition of the T cell immune compartment between MF samples, we next selected the T cell clusters individually and performed a tSNE analysis at the single-cell level. The embedding of the CD3$^{+/-}$CD4$^+$ T cells indicated

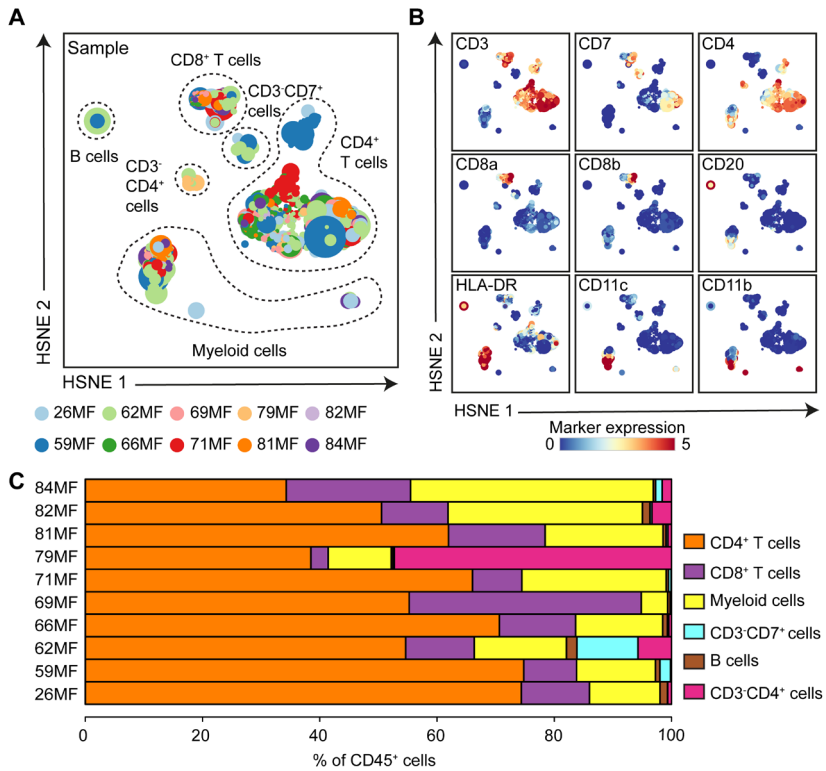

Figure 2 HSNE analysis reveals major immune lineages across MF patients. (A, B) HSNE embedding showing 6.9×10^4 landmarks representing all immune cells (3.6×10^5 cells) isolated from fresh skin biopsies of MF patients (n=10) at the overview level. Each dot represents a HSNE landmark and the size of the landmark indicates the number of cells that each landmark represents. Colors represent the individual MF patients (A) and the related expression level of indicated immune markers (B). **(C)** The composition of major immune lineage populations of $CD45^+$ cells in the individual MF patient is represented in horizontal bars where the colored segment lengths represent the proportion of cells as a percentage of $CD45^+$ cells in the sample. Colors represent the different major immune lineage population.

that next to shared features (encircled in gray, Figure 3A), distinct clusters of cells that were highly enriched in individual patients were also readily identified (encircled in black, Figure 3A). Based on the density features and related marker expression profiles of the t-SNE-embedded cells (Figure 3B, S2), we identified 27 distinct $CD4^+$ T cell clusters, each defined by a unique marker expression profile (Figure 3C). The associated cell frequency heatmap gave an overview of the relative abundance of those subsets in the patient samples (Figure 3D).

Unsupervised hierarchical clustering of the patient samples based on the cell frequency heatmap grouped 6 samples together while the other 4 samples were distinct (Figure 3D, top). Visual inspection of the heatmap indicated that the

clustering of the 6 samples was to a large extent due to the sharing of clusters CD4 T-2, CD4 T-6 and CD4 T-7, and to a lesser extent by CD4 T-1 and CD4 T-4 (Figure 3D, pink boxes), which was confirmed by the actual percentage of these subsets in the individual patient samples (Figure 3E). The actual percentage of these subsets in the individual patient samples support the notion that cluster CD4 T-1 and CD4 T-4 ($CD3^+CD5^+CD127^+CD45RO^+CCR7^-$ Effector memory) and CD4 T-2 ($CD3^+CD5^+CD127^-CD45RO^+CD25^+$ Treg-like) were the most important in this respect (Figure 3E). In contrast, the remaining 4 patient samples were distinguished by the presence of distinct clusters of CD4 T cells (Figure 3D, black boxes) that were either $CD3^+$ or $CD3^-$ and many of which display variable expression levels of CD30 and CLA (Figure 3C) and thus likely contain the abnormal cells in these patients. Here patient 62MF was typified by the presence of CD4 T-26 and T-27 ($CD3^-CD103^{+/-}CD26^+CD30^{low}CD5^+CD127^+PD1^+CD69^+CD45RO^+$), patient 71MF by cluster CD4 T-15, T-18 and T-28 ($CD3^+CD103^{+/-}CD30^{low}CLA^{low}CD5^+PD1^+CD69^+CCR4^+CCR7^+CD28^+CD45RO^+$), patient 79MF by cluster CD4 T-11 , T-14 ($CD3^{+/-}CD26^+CD30^+CLA^+CD25^{low}CD5^+CD127^{+/-}CD69^+CD28^+CD45RO^+$) and cluster CD4 T-16 ($CD3^-CD26^+CD5^-CD127^-CD69^+CD28^-CD45RO^+$), patient 59MF by cluster CD4 T-23 and T-24 ($CD3^-CD161^+CD26^+CD30^{+/-}CLA^{+/-}CD127^+CD103^{+/-}PD1^+CD69^+CCR6^+CD45RO^{+/-}$) and cluster CD4 T-21, CD4 T-22 ($CD3^+CD161^+CD103^{low/-}CD30^-CD127^{low}CLA^{+/-}CCR4^+CD28^-CCR7^+$) (Figure 3C). The actual percentages of these cell clusters in the individual patients underscores that these were the dominant cell type in the investigated biopsies (Figure 3F). In particular, the dominance of clusters in patients 71MF, 79MF and 59MF is striking where patient 79MF is distinct as it was the only one harboring a large population of $CD3^-CD30^+CD5^+CD4^+$ T cell (cluster CD4 T-11) (Figure 3D, 3F).

A similar analysis of the $CD8^+$ T cells showed that the distribution $CD8^+$ T cells was highly similar in nine out of ten patients (Figure S3A). Based on marker expression profiles and density feature, 25 $CD8^+$ T cell clusters were identified (Figure S3B-C). We observed that hierarchical clustering resulted in three patient groups (Figure S3D) while 71MF patient was separate, due to a high proportion of cluster CD8 T-26 and T-27 ($CD103^+CLA^+PD\text{-}1^+$) (Figure S3D).

In conclusion, hierarchical clustering of the T cell compartment revealed both shared and unique features of the MF patients, where the shared features may relate to an earlier disease state while the appearance of highly patient-specific cell clusters is probably related to evolution and the response of the tumor microenvironment.

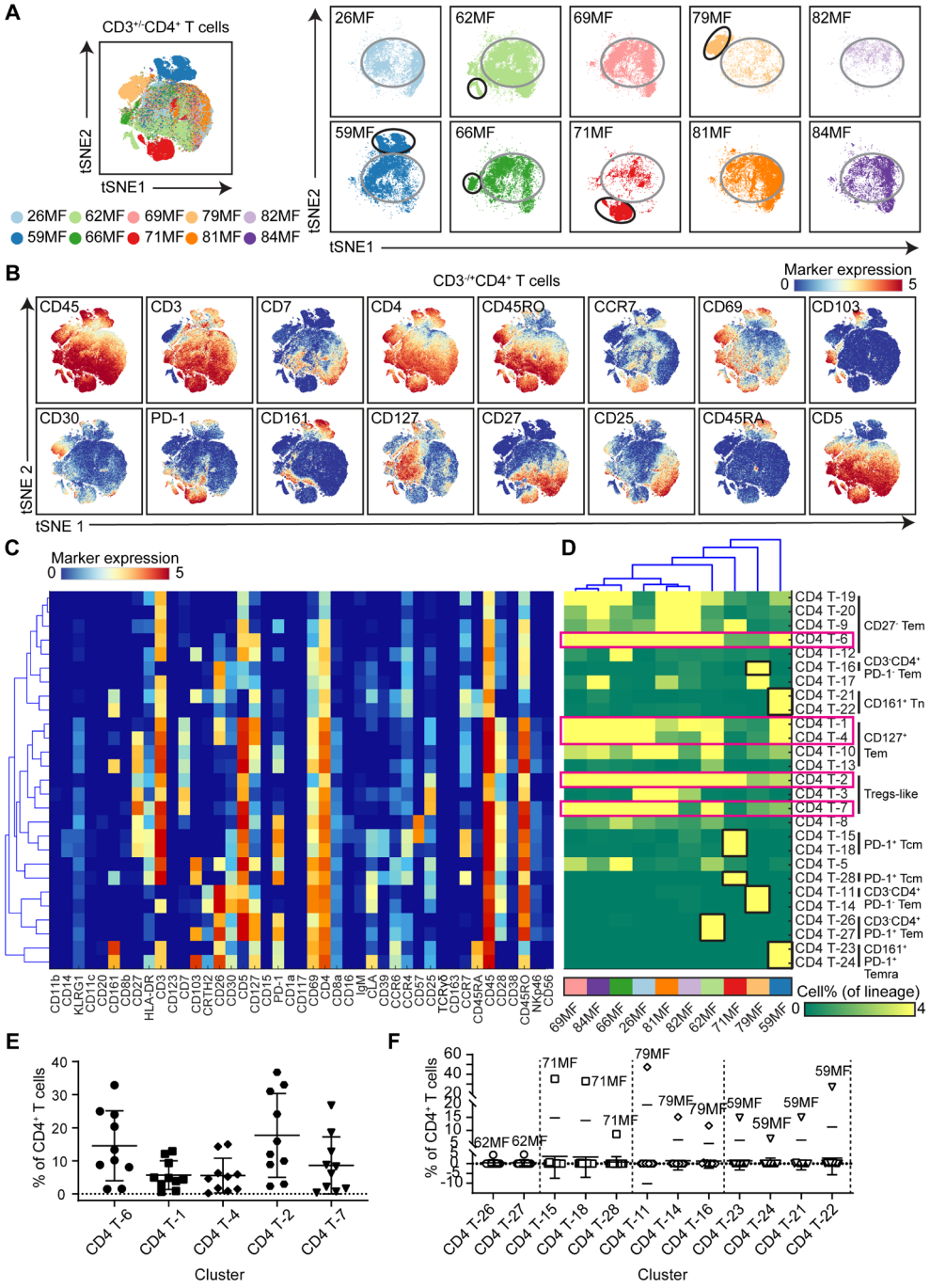

(Figure legend in next page)

Figure 3 Identification of phenotypically distinct clusters in the CD3$^{+/-}$CD4^{+} T cell compartment across MF samples. (A) A collective t-SNE was performed on CD4^{+} T cells (CD3^{+}CD4^{+} T cells and CD3^{-}CD4^{+} T cells) and stratified for samples (n = 10). In total, 2.3×10^{5} CD4^{+} T cells were analyzed in the plots. The large encircled cluster of cells (encircled in gray) harbors cells exhibiting a similar phenotype in all patients. The smaller cell clusters encircled in black are patient-unique and likely contain the abnormal cell populations in these patients. **(B)** Relative expression level of indicated immune markers. Colors represent different level of marker expression. **(C)** Heatmap showing the median of the marker expression values for the clusters identified and hierarchical clustering thereof. **(D)** Heatmap showing the corresponding cell frequencies of identified clusters of total CD4^{+} T cells in each sample. Colors represent different MF samples as indicated below the heatmap. The dendrogram shows the hierarchical clustering of samples. The clusters of CD4^{+} T cells highlighted by pink boxes are shared by the majority of MF patients. The clusters of cells highlighted by black boxes are unique for the individual patients. **(E)** Quantification of the shared CD4^{+} T cells clusters frequencies among samples in (C). Cluster IDs correspond to the ones in (C). **(F)** Quantification of the patient-unique CD4^{+} T cells clusters frequencies among samples in (C). Cluster IDs correspond to the ones in (C).

Analysis of the myeloid compartment reveals shared and patient-unique features

We next analyzed the myeloid compartment. Similar to the CD4^{+} T cells, the tSNE analysis revealed the presence of subsets that are overrepresented in particular MF patients (Figure 4A, patients 26MF, 62MF, 71MF and 84MF, encircled). Based on the distribution of the markers expression profiles (Figure 4B) and the density features of the t-SNE-embedded cells (Figure S4), 28 distinct myeloid cell clusters were identified that fall within 6 major clusters (CD11c^{dim}HLA-DR^{+} myeloid cells, CD11c^{-}HLA-DR^{+} cells, CD14^{+} monocytes, CD16^{+}CD15^{dim} monocytes, HLA-DR^{+}CD1a^{+}dendritic cells and CD163^{+} macrophages) (Figure 4C).

Figure 4 Identification of phenotypically distinct clusters in the myeloid cell compartment across MF samples. (A) A collective t-SNE was performed on myeloid cells and stratified for samples (N = 10). The plots are showing in total 6.1×10^{4} myeloid cells. The islands encircled in black are the unique-patient clusters of myeloid cells. **(B)** Relative expression level of indicated markers. Colors represent different level of marker expression. **(C)** Heatmap showing the median of the marker expression values for the clusters identified and hierarchical clustering thereof. **(D)** Heatmap showing the corresponding cell frequencies of the identified clusters as a percentage of total myeloid cells in each sample. Colors represent different samples as indicted below the heatmap. The dendrogram shows the hierarchical clustering of the samples. The clusters of myeloid cells highlighted in pink boxes are shared by the majority of MF patients. The clusters of myeloid cells highlighted in black boxes are patient-unique. **(E)** Quantification of the shared myeloid cells clusters frequencies among samples in (C). Cluster IDs correspond to the ones in (C). **(F)** Quantification of the patient-unique myeloid cells clusters frequencies in (C). Cluster IDs correspond to the ones in (C).

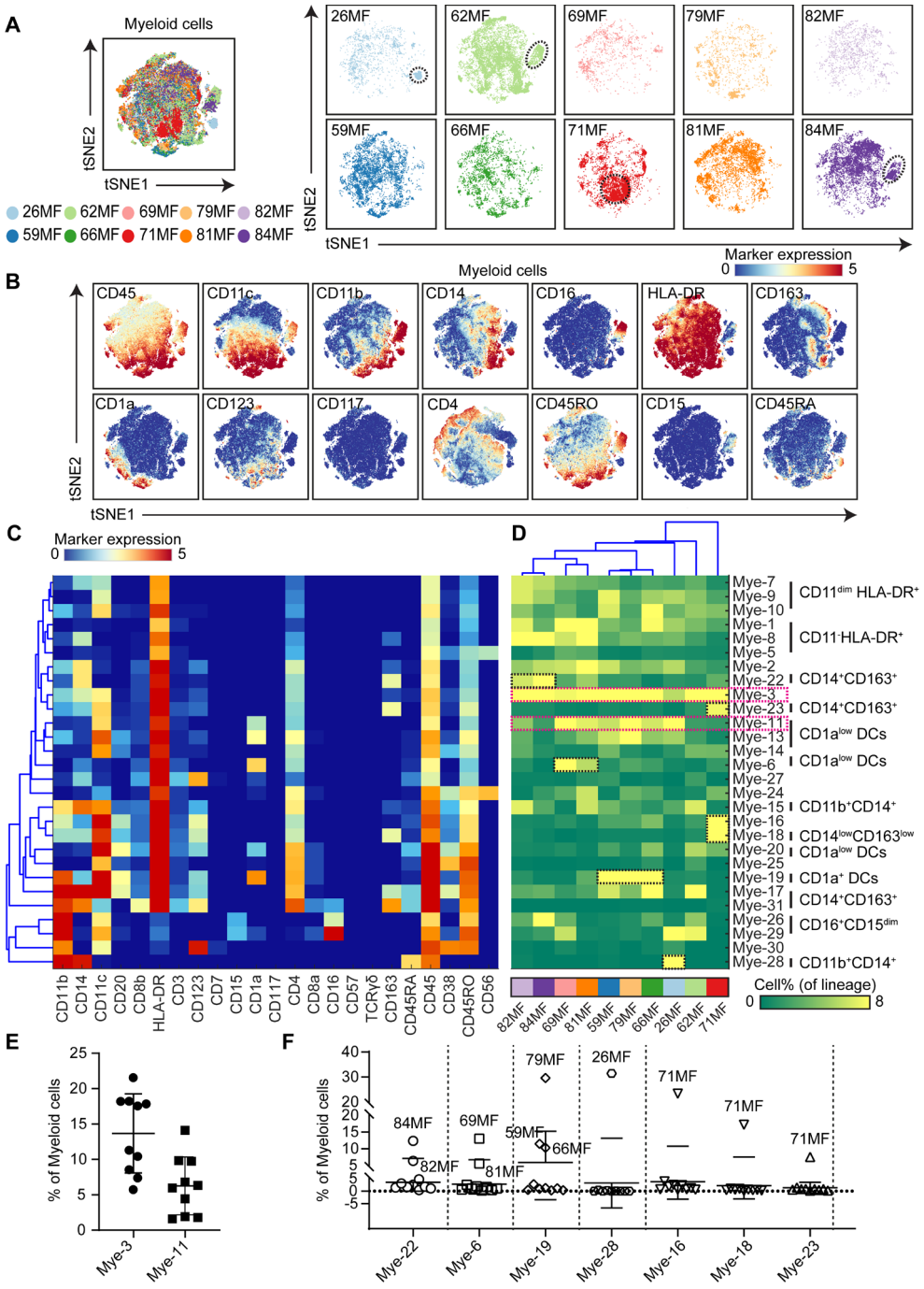

(Figure legend in previous page)

Compared to the $CD4^+$ T cells, the myeloid cell associated cell frequency heatmap was much more complex and indicative of much heterogeneity (Figure 4D). However, the subset Mye-3 ($CD11b^{low}CD11c^+CD14^{dim}$HLA-$DR^+CD4^{low}$) was present in all MF patients (Figure 4D, pink box), and cluster Mye-11 ($CD11b^-CD11c^+$HLA-$DR^+CD1a^{dim}CD4^{low}$) was also observed in the majority of MF patients (Figure 4D, pink box and 4E), while cluster Mye-19 ($CD1a^+CD11b^+CD11c^+$HLA-DR^+) marked patients 79F, 59MF and 66MF (Figure 4D, black box and 4F). In contrast, cluster Mye-28 ($CD11b^+CD11c^-CD14^+CD45RA^+CD163^-$HLA-$DR^-$) was essentially only present in patient 26MF and cluster Mye-16, 18 and 23 ($CD11b^{low/-}CD11c^+$HLA-$DR^+CD163^{+/-}$) only in 71MF (Figure 4D, black boxes and 4F). Finally, patient 82MF and 84MF shared cluster Mye-22 ($CD11b^-CD11c^-CD14^+$HLA-$DR^+CD163^+CD4^{low}$), and patient 69MF and 81MF shared cluster Mye-6 ($CD11b^-CD11c^-$HLA-$DR^+CD1a^+CD4^{low}$) (Figure 4D, black boxes and 4F). Thus, similar to the $CD4^+$ T cell compartment, the analysis of the myeloid compartment also revealed both shared and unique features of the MF patients that may relate to different stages of disease progression. Here it is important to note that in some patients (71MF, 79MF, and to a lesser extent 69MF and 59MF) both patient-unique $CD4^+$ T and myeloid cell populations were observed.

Imaging Mass Cytometry Reveals the Spatial Signatures in *situ*

To determine the spatial distribution of the immune and stromal cells in *situ* we applied an IMC panel comprising 36 antibodies to tissue sections of NS and MF skin biopsies. The antibody panel contained markers to visualize the overall tissue architecture such as E-Cadherin (epithelium), vimentin (intermediate filament), α-smooth muscle actin (αSMA) and collagen I (extracellular matrix), and markers to identify T cells (CD3, CD8, CD4, CD25, FOXP3, CD45RA, CD45RO), B cells (CD20), NK cells (CD7 and CD56), myeloid cells (CD11c), dendritic cells (CD1a, CD1c, CD123 and CD141), mast cells (CD117 and FcεRIα), monocytes and macrophages (CD14, CD68, CD163 and HLA-DR). In addition, CD31 was included to identify endothelial cells and Ki-67 to identify cell proliferation (Table S4). With this panel, snap-frozen tissue sections derived from four NS controls, and six early stage MF patients were stained after which data were acquired on a Hyperion imaging mass cytometer.

To obtain further information on the phenotype and localization of the immune cell subsets within the tissue context, we visualized the data by combinations of specific markers (Figure 5, 6). Here, the combination of E-cadherin and DNA as nuclear counterstain were used to distinguish the epidermis from the dermis on skin tissues from the NS control and the MF patient (Figure 5A), while more

proliferating keratinocytes (the basal cells in the epidermis) were visualized at the junction between the epidermis and dermis by staining with Ki-67 in the MF sample, compared with the NS control sample (Figure 5B). Finally, vimentin, collagen I and CD45 revealed the localization of the immune cells in the epidermis and dermis, in the latter mostly enriched nearby blood vessels identified by expression of CD31 and αSMA for both samples (Figure 5C-D). In addition, we found several subregions with more infiltrating immune cells in the MF sample compared with the NS control, based on CD45 staining (Figure 5D). To define the spatial organization of the immune cells in more detail for MF patient, we next focused on the analysis of lymphoid and myeloid cell populations in the MF tissue sections. Representative images are shown in Figure 5 in which we identified $CD3^+CD7^+$ T cells, abnormal $CD3^+CD7^-$ T cells and $CD3^-CD7^+$ ILCs (Figure 5E-01), $CD3^+CD4^+$ T cells and $CD3^+CD8^+$ T cells in the dermis, and $CD3^+CD4^-CD8^-$T cells in the epidermis (Figure 5E-02). In addition, analysis of the expression of CD45RA, FOXP3 and CD25, revealed that the large majority of T cells had a memory phenotype and allowed the distinction between $CD45RA^-$ memory $CD4^+$ T cells (Figure 5E-03) and $FOXP3^+CD25^+$ Tregs (Figure 5E-04). Moreover, various myeloid cells subsets were detected (Figure 5F), including $CD11c^+CD1a^+CD1c^+$ DCs, $CD11c^+CD1a^-CD1c^+$ DCs, and $CD11c^+CD1a^-CD1c^-$ myeloid cells in the dermis; and $CD11c^-CD1a^+CD1c^+$ Langerhans-like cells (LCs) in the epidermis (Figure 5F-01), while $HLA\text{-}DR^+CD163^+$ macrophages were present in the dermis (Figure 5F-02). Also, we observed lower expression levels of HLA-DR in the epidermal LCs compared to dermal DCs (Figure 5F-03). Few $HLA\text{-}DR^+CD123^+$ pDCs-like cells were detected in the dermis (Figure 5F-04). Importantly, we observed prominent co-localization of $CD4^+$ T cells with both $CD1a^+CD1c^+$ and $CD1a^-CD1c^+$ DCs in cellular aggregates just below the epidermis. Thus, by this approach, we were able to identify and visualize the presence and distribution of various lymphoid and myeloid immune cell subsets within a single tissue section simultaneously.

We next analyzed five additional early stage MF patients which revealed similar clusters of immune cells just below the epidermis in all MF patients (Figure 6). Figure S5 to S10 provide an overview of the individual markers stains for all MF patients. The substantial heterogeneity of immune cells were observed among MF patients. While $CD4^+$ T cells were the most abundant lymphoid cells in patients 105MF, 109MF and 113MF, $CD8^+$ T cells were more abundant in patient 87MF and $CD4^-CD8^-$ T cells in patient 108MF (Figure 6A). Also, myeloid cells were virtually absent from the lymphoid cell aggregate in patient 87MF (Figure 6B) while co-localization of lymphoid cells and myeloid cells, in particular $CD11c^+CD1a^+CD1c^+$ DCs, was observed in patients 105MF and 109MF and to a lesser extent in patients

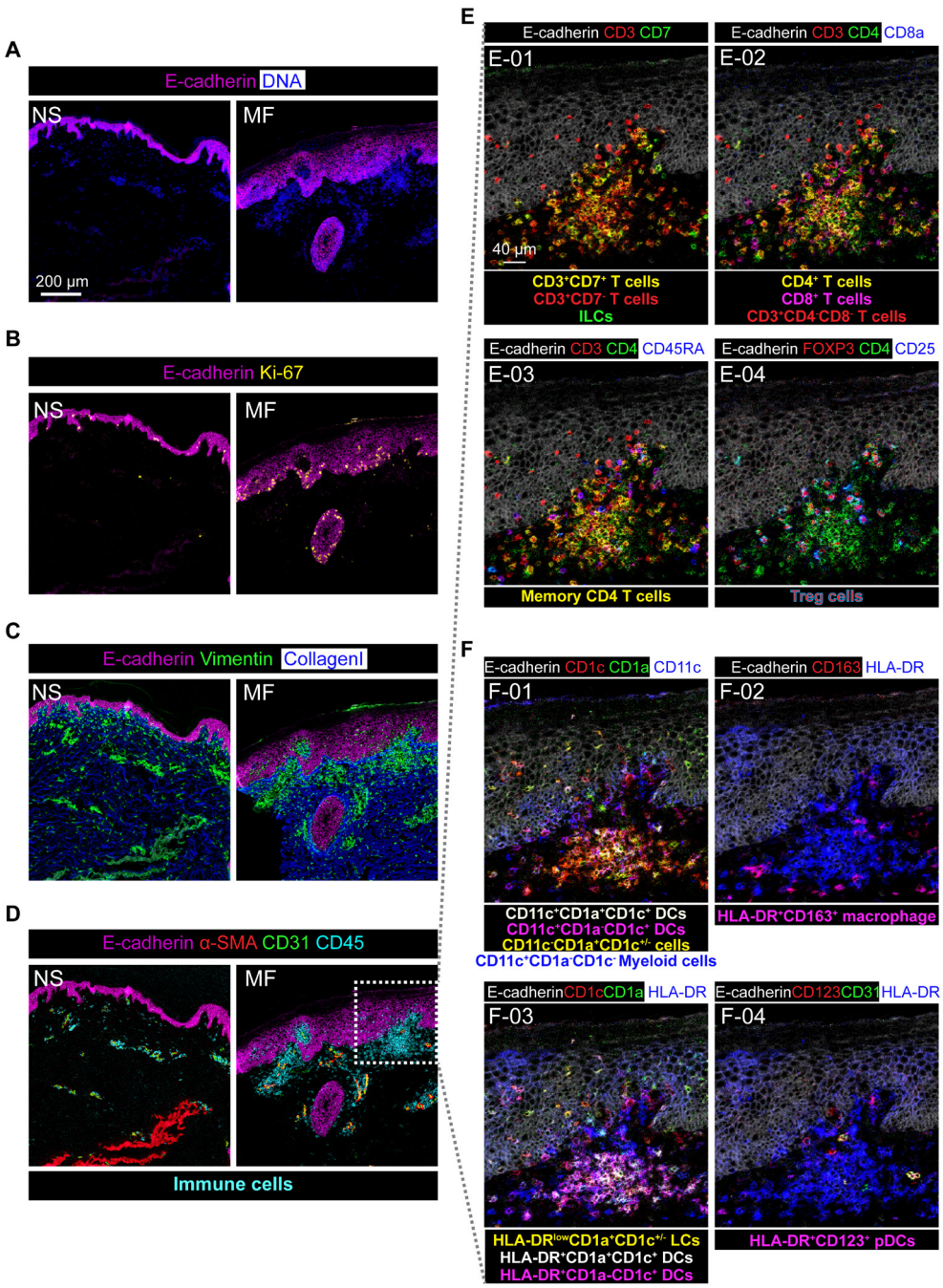

(Figure legend in next page)

Figure 5 Visualization of structure and the spatial distribution of the immune and stromal cell subsets in a single ROI in skin tissue by imaging mass cytometry. **(A-D)** Representative mass cytometry images of a NS and a MF skin sample showing the overlay of **(A)** E-Cadherin (colored in magenta) and DNA (colored in blue); **(B)** E-cadherin (colored in magenta) and Ki-67 (colored in yellow) to identify proliferating keratinocytes (E-Cadherin^{+}Ki-67^{+}); **(C)** E-cadherin (colored in magenta), Vimentin(colored in green) and Collagen I (colored in blue) to distinguish epidermis and dermis; **(D)** E-cadherin (colored in magenta), α-SMA (colored in red), CD31 (colored in green) and CD45 (colored in cyan) to show the location of CD45$^{+/dim}$ immune cells. **(E)** Identification of T cell and ILCs subsets for the MF sample : **(E-01)** CD3^{+}CD7^{+} T cells, CD3^{+}CD7^{-} T cells and ILCs (CD3^{-}CD7^{+}); **(E-02)** CD4^{+} T cells (CD3^{+}CD4^{+}), CD8^{+} T cells (CD3^{+}CD8^{+}) and CD4^{-}CD8^{-} T cells (CD3^{+}CD4^{-}CD8^{-}); **(E-03)** Memory CD4^{+} T cells (CD3^{+}CD4^{+}CD45RA^{-}); **(E-04)** Regulatory T cells (Tregs, CD3^{+}CD4^{+}CD25^{+}FOXP3^{+}). **(F)** Identification of myeloid cell, dendritic cells and macrophage subsets from the MF sample : **(F-01)** Different dendritic cells subsets based on different expression level of CD11c, CD1a and CD1c; **(F-02)** CD163^{+} macrophage (HLA-DR^{+}CD163^{+}); **(F-03)** Epidermal Langerhans cells (LCs, HLA-DR^{dim}CD1a^{+} CD1c^{+}), dendritic cells (DCs); **(F-04)** plasmacytoid dendritic cells-like cells (pDC-like, HLA-DR^{+}CD123^{+}).

108MF and 113MF (Figure 6C). Apart from patient 87MF, multiple types of antigen presenting cells were identified in all other patients based on differential expression of CD11c, CD1a and CD1c.

Together, this provides evidence that clusters of lymphoid and myeloid cells are found in the majority of early stage MF patients. Moreover, it reveals substantial heterogeneity in both the lymphoid and myeloid compartment within and among patients.

Discussion

In the current study we analyzed skin biopsies from early stage MF patients and healthy controls to characterize the complexity of the immune compartment using high-dimensional single-cell suspension mass cytometry and imaging mass cytometry. Compared with conventional flow cytometry and immunohistochemistry, these mass cytometry based techniques offer the opportunity to detect up to 40 cellular markers simultaneously, thus allowing a high resolution analysis of the immune compartment in the tissue context.

Figure 6 Detection of cell-cell interaction by combining T cell markers with myeloid cell markers in skin biopsies of five additional MF patients. **(A)** Visualization of CD4^{+} T cells, CD8^{+} T cells, and CD4^{-}CD8^{-} T cells. **(B)** Visualization of multiple types of antigen presenting cells (APCs) by the overlay of CD1c (colored in red), CD1a (colored in green), and CD11c (colored in blue). **(C)** The overlay of CD3 (colored in cyan), CD1c (colored in red), CD1a (colored in green), and CD11c (colored in blue) shows the distribution of the myeloid and T cell populations and complex interactions between those.

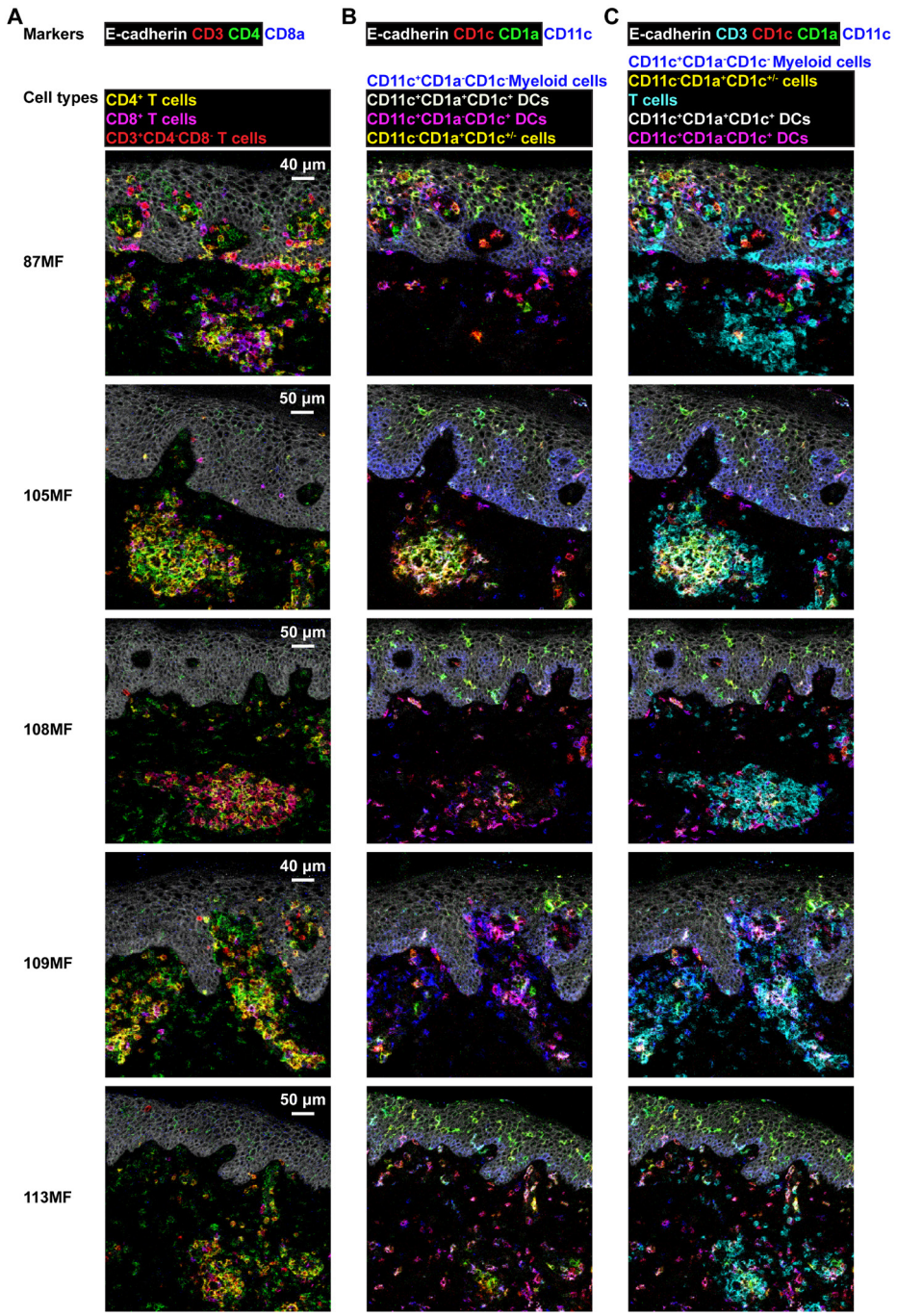

(Figure legend in previous page)

Previous studies found that early stages of MF were characterized by the presence of a small number of neoplastic cells together with an extensive inflammatory infiltrate composed of multiple types of immune cells[21, 22]. These observations have fueled the notion that this inflammatory response may contribute to the persistence and progression of MF lesions. In the present study we identified phenotypically distinct subsets in both the $CD4^+$ T cell and myeloid cell compartment that were shared by most patients. In addition, we found distinct $CD4^+$ T cell subsets that revealed an individual pattern, potentially representing a unique response of the tumor cells to the tumor microenvironment. In addition, substantial numbers of $CD4^+$ T cells co-localized with both $CD1a^+CD1c^+$HLA-DR^+ and $CD1a^-CD1c^+$HLA-DR^+ DCs in the dermis in *situ*. In this respect it is striking that the dominant presence of particular $CD4^+$ T cell clusters coincided with an elevated number of phenotypically distinct myeloid cells in some of the patients, suggesting that interactions between these $CD4^+$ T cells and myeloid cells may play a prominent role in disease control. Here it is of note that the composition, shape and organization of the lymphoid-myeloid cell aggregates differs substantially between patients. Future studies need to be performed to determine if this relates to disease progression and/or may have implications for therapy.

Previously, the studies focusing on Treg-like cells suggested that $FOXP3^+$ Tregs have a tumor suppressive role in the pathogenesis of MF/SS, but results have been discordant and conflicting[23, 24, 25]. In our single cell mass cytometry analysis clusters of Treg-like cells ($CD25^+CD45RO^+CD27^+$) were found in all patients. This observation was confirmed using imaging mass cytometry where $CD25^+FOXP3^+CD4^+$ T cells were found to be present in all investigated MF patients. Moreover, tumor-associated macrophages have been shown to generate an immunosuppressive tumor microenvironment by recruiting Tregs, myeloid cells and production of macrophage-related chemokines and angiogenic factors[26, 27, 28]. In patient 71MF, an increased number of $CD163^+$ macrophages were observed (Figure 4). Therefore, in future studies we will focus on the analysis of the interactions of the Tregs with myeloid and tumor cells in the tissue context. Here, future studies investigating the therapeutic effect of IFN-alpha and -gamma for immunomodulation of tumor associated macrophages might be of particular interest in such patients.

Finally, the PD-1/PD-L1 axis plays a central role in attenuating the immune response and antitumor immunity[29, 30] and has also emerged as a central tumor suppressor in T cell lymphomas[31]. We observed that PD-1 expression was higher in patients 71MF, 66MF and 59MF (Figure 3). However, due to the short follow-up time we could not observe a correlation between PD-1 expression and the disease

course. Future studies should investigate if the presence of PD-1^{+}CD4^{+} T cells correlates with progression to tumor stage disease. The therapeutic potential of PD-1 targeting therapy in these patients should be explored by investigating the factors driving PD-1 expression and functional consequences of PD-1 expression by CD4^{+} T cells as well.

In recent years, significant heterogeneity was observed between CTCL patients. Substantial clonotypic heterogeneity of skin- and blood-derived malignant T cells was observed by combining T-cell receptor clonotyping with cell surface marker profiling[32, 33, 34]. Moreover, genetic heterogeneity among and within CTCL patients was observed by TruSeq targeted RNA gene expression analysis[35]. These observations underscore the need to take into account the patients' individual malignant profiles for effective therapy of CTCL.

Moreover, among the various single cell techniques, cellular indexing of transcriptomes and epitopes by sequencing (CITE-seq) is a multimodal approach allowing simultaneous quantification of single-cell transcriptomes and surface proteins based on oligonucleotide-labeled antibodies of the same single cells[36]. Comparison of scRNA-seq, CyTOF and CITE-seq analyses, however, reveals discrepancies with the highest abundance of the T cell population in scRNA-seq analysis, followed by CyTOF and the lowest abundance in CITE-seq[37], pointing towards the need for further studies.

For future studies it would also be important to further optimize the antibody panels of single cell CyTOF for the detection of malignant T cells combined with detection of co-stimulatory signals (e.g. CD80)[38], immune modulatory signals (e.g. CD137, CD134 and CTLA4)[39, 40, 41], T cell exhaustion (e.g. ICOS)[42], and cytokine and chemokine receptors[43, 44], to further dissect the tumor microenvironment. In addition, while in the present study we have used the MCD™ viewer software to visualize the imaging mass cytometry data, this could be complemented with cell segmentation approaches based on the identification of nuclei to aid in the visualization of IMC data[45, 46]. Moreover, Imacyte[47] and Histocat[48], allow downstream imaging mass cytometry analysis to identify and quantify cell-cell interactions[49, 50]. Collectively, this allows for a further in-depth investigation of cellular interactions in skin tissues. Although the current study with a limited number MF patient needs to be expanded to confirm and extend the observations, we nonetheless demonstrate the ability to detect immune cell profile patterns in single cell suspensions of skin biopsies and visualize the spatial network in the tissue context. The identification of prominent cellular aggregates between CD4

T cells and myeloid cells in the dermis with a patient-unique cellular composition provides a framework for improving mycosis fungoides diagnosis and development of treatment tailored to the characteristic features of these aggregates in individual patients.

Supplementary Materials

The following supporting information can be downloaded at: https://www.mdpi.com/article/10.3390/cells11061062/s1, Figure S1: Gating strategy for single, live $CD45^+$ cells on MF samples (A), and identification of the overview level of $CD45^+$ cells by HSNE analysis (B). Figure S2: A collective t-SNE was performed on $CD3^-$ $CD4^+$ T cells and show the density map showing the local probability density of the embedded cells (left); Colors represent cluster partitions for per $CD4^+$ T cells subpopulation (right). Figure S3: Identification of phenotypically distinct clusters in the $CD3^+CD8^+$ T cell compartment across MF samples. Figure S4: A collective t-SNE was performed on myeloid cells. Figure S5-S14: Individual antibody stains for representative per skin sample by IMC. Table S1: Characteristics of patients with Mycosis fungoides diseases. Table S2: The sex and age characteristics of the NS healthy donors. Table S3: Single-cell suspension mass cytometry antibody panel. Table S4: Imaging mass cytometry antibody panel on frozen skin tissue. Table S5: The minimum and maximum threshold of each marker for per sample.

Author Contributions

N.G., M.V., F.K. and K.Q. conceived of the study and wrote the manuscript; N.G. performed most of the experiments with the help of L.J., C.O.-L. and N.F.C.C.d.M.; N.G. performed most of the analyses with the help of F.K., K.Q. and M.V.; K.Q., R.W. and M.V. obtained the fresh skin biopsies from the MF patients. All authors have read and agreed to the published version of the manuscript.

Funding

This research was supported by the China Scholarship Council (N.G. and L.J.). N.F.C.C.d.M. was funded by the European Research Council (ERC) under the European Union's Horizon 2020 Research and Innovation Programme (grant agreement no: 852832). F.K. was supported by BIOMAP (Bio-Markers in Atopic Dermatitis and Psoriasis), a project funded by the Innovative Medicines Initiative 2 Joint Undertaking (grant agreement no: 821511), and by the collaboration project TIMID (LSHM18057-SGF) financed by the PPP allowance made available by Top Sector Life Sciences & Health to Samenwerkende Gezondheidsfondsen (SGF) to stimulate public–private partnerships and co-financing by health foundations that are part of the SGF.

Institutional Review Board Statement

The study was conducted in accordance with the Declaration of Helsinki, and approved by the Medical Ethics Committee of Leiden University Medical Center (protocol: B19.005).

Informed Consent Statement

Informed consent was obtained from all subjects involved in the study.

Data Availability Statement

All data that support the findings of this study are available from the corresponding author upon reasonable request.

Acknowledgements

We thank the patients. We thank all operators in the Flow Cytometry Core Facility of the LUMC for technical assistance with measurements on Helios and Hyperion. We thank Marieke E. Ijsselsteijn from the Pathology department of the LUMC for providing help and suggestions in IMC experiments.

Conflicts of Interest

The authors declare no conflict of interest.

Reference

1. Willemze, R. *et al.* WHO-EORTC classification for cutaneous lymphomas. *Blood* **105**, 3768-3785 (2005).
2. Willemze, R. *et al.* The 2018 update of the WHO-EORTC classification for primary cutaneous lymphomas. *Blood* **133**, 1703-1714 (2019).
3. Reddy, K. & Bhawan, J. Histologic mimickers of mycosis fungoides: a review. *J Cutan Pathol* **34**, 519-525 (2007).
4. Chiba, T., Nagai, T., Osada, S.I. & Manabe, M. Diagnosis of Mycosis Fungoides Following Administration of Dupilumab for Misdiagnosed Atopic Dermatitis. *Acta Derm Venereol* **99**, 818-819 (2019).
5. Massone, C., Kodama, K., Kerl, H. & Cerroni, L. Histopathologic features of early (patch) lesions of mycosis fungoides: a morphologic study on 745 biopsy specimens from 427 patients. *Am J Surg Pathol* **29**, 550-560 (2005).
6. Berger, C. *et al.* The growth of cutaneous T-cell lymphoma is stimulated by immature dendritic cells. *Blood* **99**, 2929-2939 (2002).
7. Berger, C.L. *et al.* Cutaneous T-cell lymphoma: malignant proliferation of T-regulatory cells. *Blood* **105**, 1640-1647 (2005).
8. Gaydosik, A.M. *et al.* Single-Cell Lymphocyte Heterogeneity in Advanced Cutaneous T-cell Lymphoma Skin Tumors. *Clin Cancer Res* **25**, 4443-4454 (2019).
9. Li, N. *et al.* Early-Life Compartmentalization of Immune Cells in Human Fetal Tissues Revealed by High-Dimensional Mass Cytometry. *Frontiers in Immunology* **10** (2019).
10. Li, N. *et al.* Mass cytometry reveals innate lymphoid cell differentiation pathways in the human fetal intestine. *J Exp Med* **215**, 1383-1396 (2018).
11. de Vries, N.L. *et al.* High-dimensional cytometric analysis of colorectal cancer reveals novel mediators of antitumour immunity. *Gut* **69**, 691-703 (2020).
12. Havel, J.J., Chowell, D. & Chan, T.A. The evolving landscape of biomarkers for checkpoint inhibitor immunotherapy. *Nat Rev Cancer* **19**, 133-150 (2019).
13. Bandura, D.R. *et al.* Mass cytometry: technique for real time single cell multitarget immunoassay based on inductively coupled plasma time-of-flight mass spectrometry. *Anal Chem* **81**, 6813-6822 (2009).
14. Chang, Q. *et al.* Imaging Mass Cytometry. *Cytometry A* **91**, 160-169 (2017).
15. Hollt, T. *et al.* Cytosplore: Interactive Immune Cell Phenotyping for Large Single-Cell Datasets. *Comput Graph Forum* **35**, 171-180 (2016).
16. van Unen, V. *et al.* Visual analysis of mass cytometry data by hierarchical stochastic neighbour embedding reveals rare cell types. *Nat Commun* **8**, 1740 (2017).
17. Wang, Y.J. *et al.* Multiplexed In Situ Imaging Mass Cytometry Analysis of the Human Endocrine Pancreas and Immune System in Type 1 Diabetes. *Cell Metab* **29**, 769-783 e764 (2019).
18. Jackson, H.W. *et al.* The single-cell pathology landscape of breast cancer. *Nature* **578**, 615-620 (2020).
19. van Unen, V. *et al.* Mass Cytometry of the Human Mucosal Immune System Identifies Tissue- and Disease-Associated Immune Subsets. *Immunity* **44**, 1227-1239 (2016).
20. Guo, N. *et al.* A 34-Marker Panel for Imaging Mass Cytometric Analysis of Human Snap-Frozen Tissue. *Front Immunol* **11**, 1466 (2020).
21. Vermeer, M.H. *et al.* CD8+ T cells in cutaneous T-cell lymphoma: expression of cytotoxic proteins, Fas Ligand, and killing inhibitory receptors and their relationship with clinical behavior. *J Clin Oncol* **19**, 4322-4329 (2001).
22. Rubio Gonzalez, B., Zain, J., Rosen, S.T. & Querfeld, C. Tumor microenvironment in mycosis fungoides and Sézary syndrome. *Curr Opin Oncol* **28**, 88-96 (2016).
23. Gjerdrum, L.M. *et al.* FOXP3+ regulatory T cells in cutaneous T-cell lymphomas: association with disease stage and survival. *Leukemia* **21**, 2512-2518 (2007).
24. Tiemessen, M.M. *et al.* Lack of suppressive CD4+CD25+FOXP3+ T cells in advanced stages of primary cutaneous T-cell lymphoma. *J Invest Dermatol* **126**, 2217-2223 (2006).
25. Borcherding, N. *et al.* Single-Cell Profiling of Cutaneous T-Cell Lymphoma Reveals Underlying Heterogeneity Associated with Disease Progression. *Clin Cancer Res* **25**, 2996-3005 (2019).
26. Furudate, S. *et al.* Tumor-associated M2 macrophages in mycosis fungoides acquire immunomodulatory function by interferon alpha and interferon gamma. *J Dermatol Sci* **83**, 182-189 (2016).
27. Mendez-Enriquez, E. & García-Zepeda, E.A. The multiple faces of CCL13 in immunity and inflammation. *Inflammopharmacology* **21**, 397-406 (2013).
28. Tiemessen, M.M. *et al.* CD4+CD25+Foxp3+ regulatory T cells induce alternative activation of human monocytes/macrophages. *Proc Natl Acad Sci U S A* **104**, 19446-19451 (2007).
29. Francisco, L.M., Sage, P.T. & Sharpe, A.H. The PD-1 pathway in tolerance and autoimmunity. *Immunol Rev* **236**, 219-242 (2010).
30. Samimi, S. *et al.* Increased programmed death-1 expression on CD4+ T cells in cutaneous T-cell lymphoma: implications for immune suppression. *Arch Dermatol* **146**, 1382-1388 (2010).
31. Wartewig, T. & Ruland, J. PD-1 Tumor Suppressor Signaling in T Cell Lymphomas. *Trends Immunol* **40**, 403-414 (2019).

32. Iyer, A. *et al.* Clonotypic heterogeneity in cutaneous T-cell lymphoma (mycosis fungoides) revealed by comprehensive whole-exome sequencing. *Blood Adv* **3**, 1175-1184 (2019).
33. Hamrouni, A., Fogh, H., Zak, Z., Ødum, N. & Gniadecki, R. Clonotypic Diversity of the T-cell Receptor Corroborates the Immature Precursor Origin of Cutaneous T-cell Lymphoma. *Clin Cancer Res* **25**, 3104-3114 (2019).
34. Herrera, A. *et al.* Multimodal single-cell analysis of cutaneous T-cell lymphoma reveals distinct subclonal tissue-dependent signatures. *Blood* **138**, 1456-1464 (2021).
35. Litvinov, I.V. *et al.* Gene expression analysis in Cutaneous T-Cell Lymphomas (CTCL) highlights disease heterogeneity and potential diagnostic and prognostic indicators. *Oncoimmunology* **6**, e1306618 (2017).
36. Stoeckius, M. *et al.* Simultaneous epitope and transcriptome measurement in single cells. *Nature Methods* **14**, 865-868 (2017).
37. Yao, L. *et al.* Integrated Cytof, Scrna-Seq and Cite-Seq Analysis of Bone Marrow Immune Microenvironment in the Mmrf Commpass Study. *Blood* **136**, 28-29 (2020).
38. Zhang, Q. *et al.* Cutaneous T cell lymphoma expresses immunosuppressive CD80 (B7-1) cell surface protein in a STAT5-dependent manner. *J Immunol* **192**, 2913-2919 (2014).
39. Wong, H.K. *et al.* Increased expression of CTLA-4 in malignant T cells from patients with mycosis fungoides - Cutaneous T-cell lymphoma. *Journal of Investigative Dermatology* **126**, 212-219 (2006).
40. Kamijo, H. *et al.* Aberrant CD137 ligand expression induced by GATA6 overexpression promotes tumor progression in cutaneous T-cell lymphoma. *Blood* **132**, 1922-1935 (2018).
41. Jones, D., Fletcher, C.D., Pulford, K., Shahsafaei, A. & Dorfman, D.M. The T-cell activation markers CD30 and OX40/CD134 are expressed in nonoverlapping subsets of peripheral T-cell lymphoma. *Blood* **93**, 3487-3493 (1999).
42. Amatore, F. *et al.* ICOS is widely expressed in cutaneous T-cell lymphoma, and its targeting promotes potent killing of malignant cells. *Blood Adv* **4**, 5203-5214 (2020).
43. Lu, D. *et al.* The T-cell chemokine receptor CXCR3 is expressed highly in low-grade mycosis fungoides. *Am J Clin Pathol* **115**, 413-421 (2001).
44. Durgin, J.S., Weiner, D.M., Wysocka, M. & Rook, A.H. The immunopathogenesis and immunotherapy of cutaneous T cell lymphoma: Pathways and targets for immune restoration and tumor eradication. *J Am Acad Dermatol* **84**, 587-595 (2021).
45. Sommer, C., Straehle, C., Köthe, U. & Hamprecht, F.A. Ilastik: Interactive learning and segmentation toolkit. 2011 IEEE International Symposium on Biomedical Imaging: From Nano to Macro; 2011 30 March-2 April 2011; 2011. p. 230-233.
46. Jones, T.R. *et al.* CellProfiler Analyst: data exploration and analysis software for complex image-based screens. *BMC Bioinformatics* **9**, 482 (2008).
47. Somarakis, A., Van Unen, V., Koning, F., Lelieveldt, B. & Hollt, T. ImaCytE: Visual Exploration of Cellular Micro-Environments for Imaging Mass Cytometry Data. *IEEE Trans Vis Comput Graph* **27**, 98-110 (2021).
48. Schapiro, D. *et al.* histoCAT: analysis of cell phenotypes and interactions in multiplex image cytometry data. *Nature Methods* **14**, 873-876 (2017).
49. Ijsselsteijn, M.E., Somarakis, A., Lelieveldt, B.P.F., Hollt, T. & de Miranda, N.F.C.C. Semi-automated background removal limits loss of data and normalises the images for downstream analysis of imaging mass cytometry data. *bioRxiv*, 2020.2011.2026.399717 (2020).
50. Schulz, D. *et al.* Simultaneous Multiplexed Imaging of mRNA and Proteins with Subcellular Resolution in Breast Cancer Tissue Samples by Mass Cytometry. *Cell Systems* **6**, 25-36.e25 (2018).

Supplementary Information

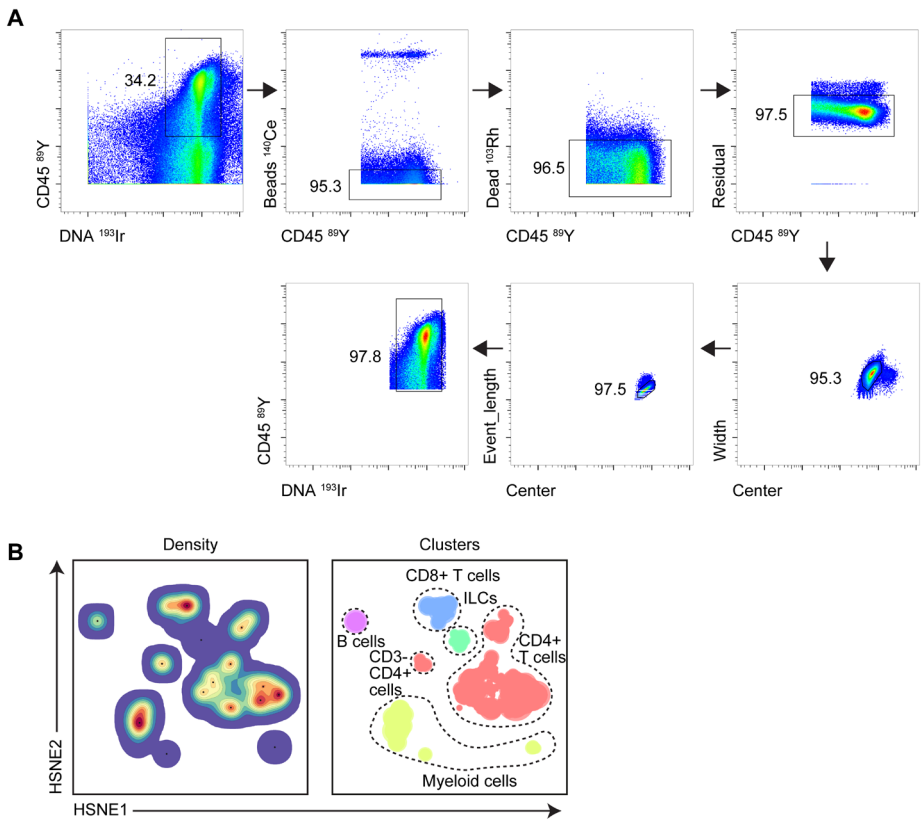

Figure S1 Gating strategy for single, live CD45⁺ cells on MF samples (A), and identification of the overview level of CD45⁺ cells by HSNE analysis (B).

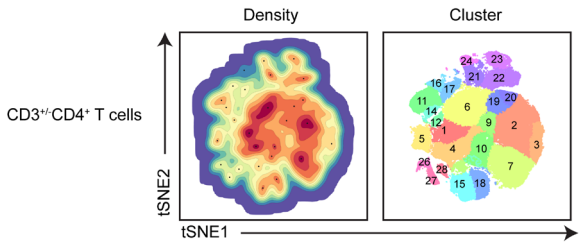

Figure S2 A collective t-SNE was performed on CD3⁻CD4⁺ T cells, and show the density map showing the local probability density of the embedded cells (left); Colors represent cluster partitions for per CD4⁺ T cells subpopulation (right).

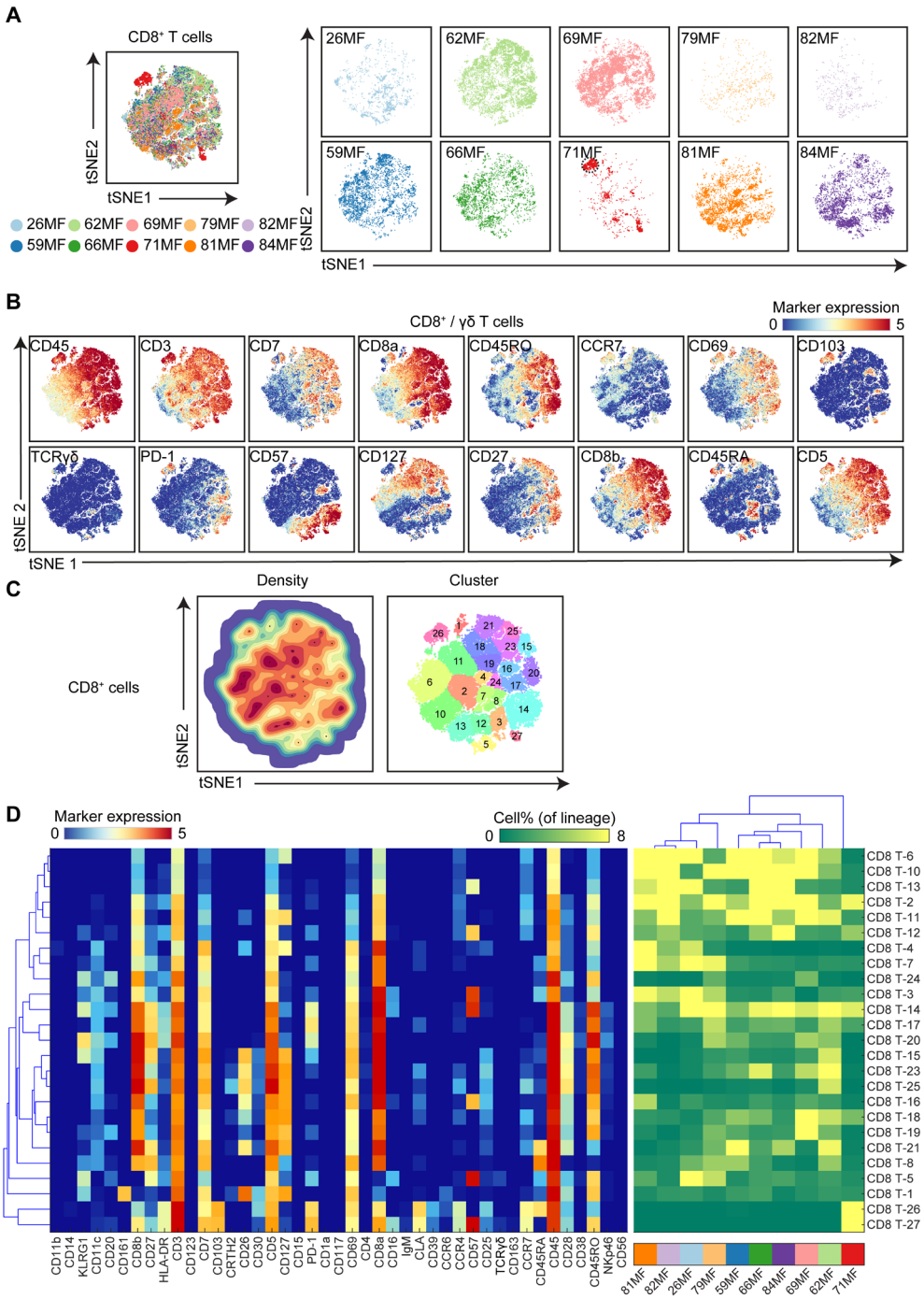

(Figure legend in next page)

Figure S3 Identification of phenotypically distinct clusters in the CD3⁺CD8⁺ T cell compartment across MF samples. (A) A collective t-SNE was performed on CD8⁺ T cells and stratified for samples (n = 10). In total, 5.1×104 CD8⁺ T cells were analyzed in the plots. **(B)** Relative expression level of indicated immune markers. Colors represent different level of marker expression. **(C)** The density map showing the local probability density of the embedded cells (left); Colors represent cluster partitions for per CD8⁺ T cells subpopulation (right). **(D)** Heatmap (blue-to-red scale) showing the median of marker expression values for the identified clusters and hierarchical clustering thereof; heatmap (green-to-yellow scale) showing the corresponding cell frequencies of identified clusters of total CD8⁺ T cells in each sample. The dendrogram shows the hierarchical clustering of samples. Colors represent different samples.

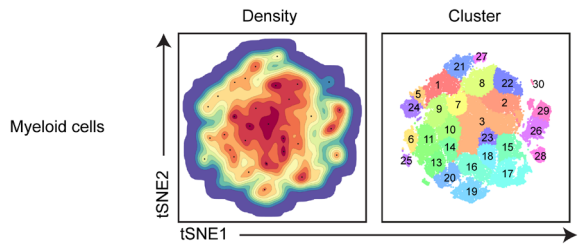

Figure S4 A collective t-SNE was performed on myeloid cells. The density map showing the local probability density of the embedded cells (left); Colors represent cluster partitions for per myeloid cells subpopulation (right).

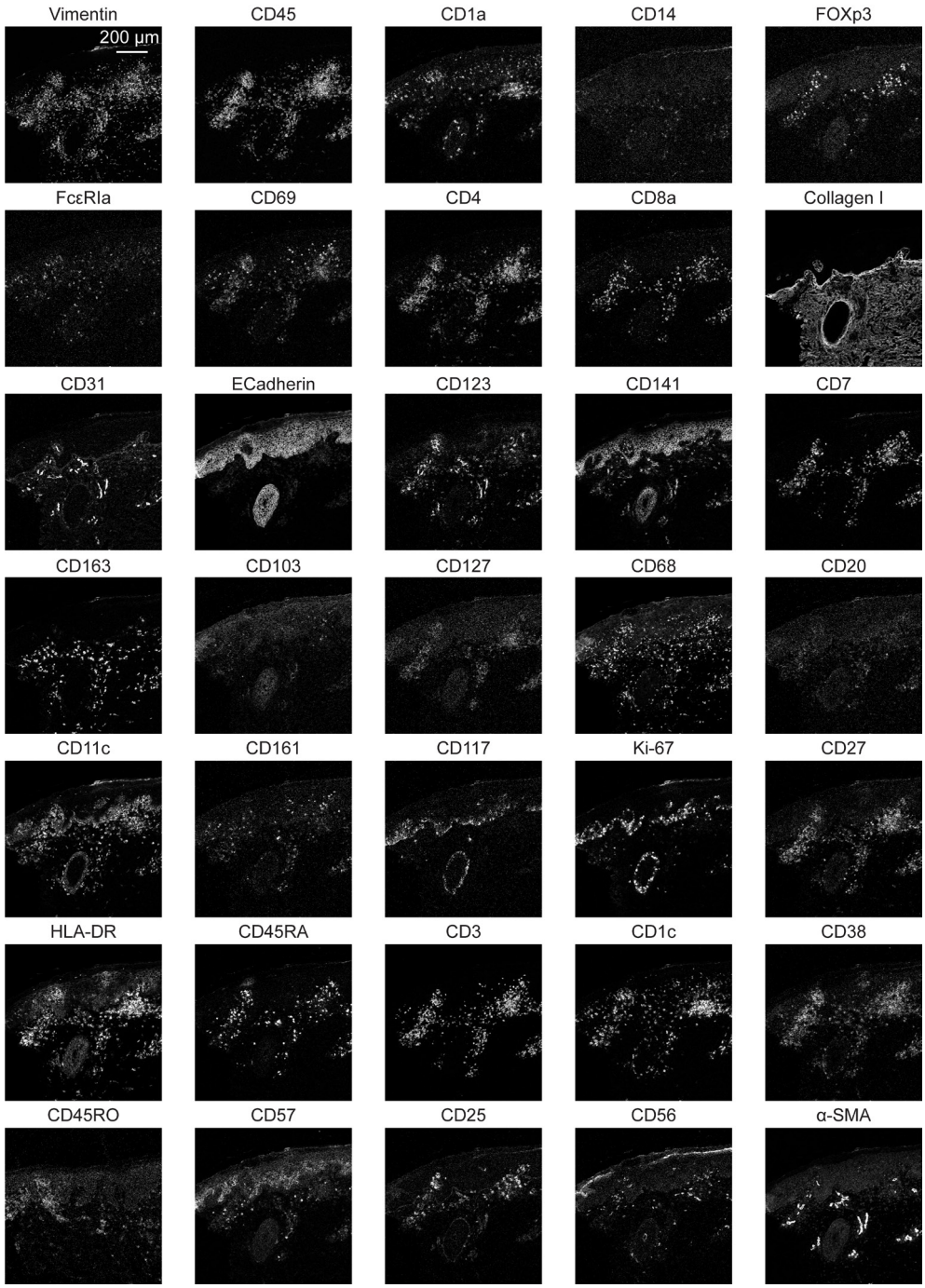

Figure S5 Individual antibody stains for representative MF patients (120MF) by IMC.

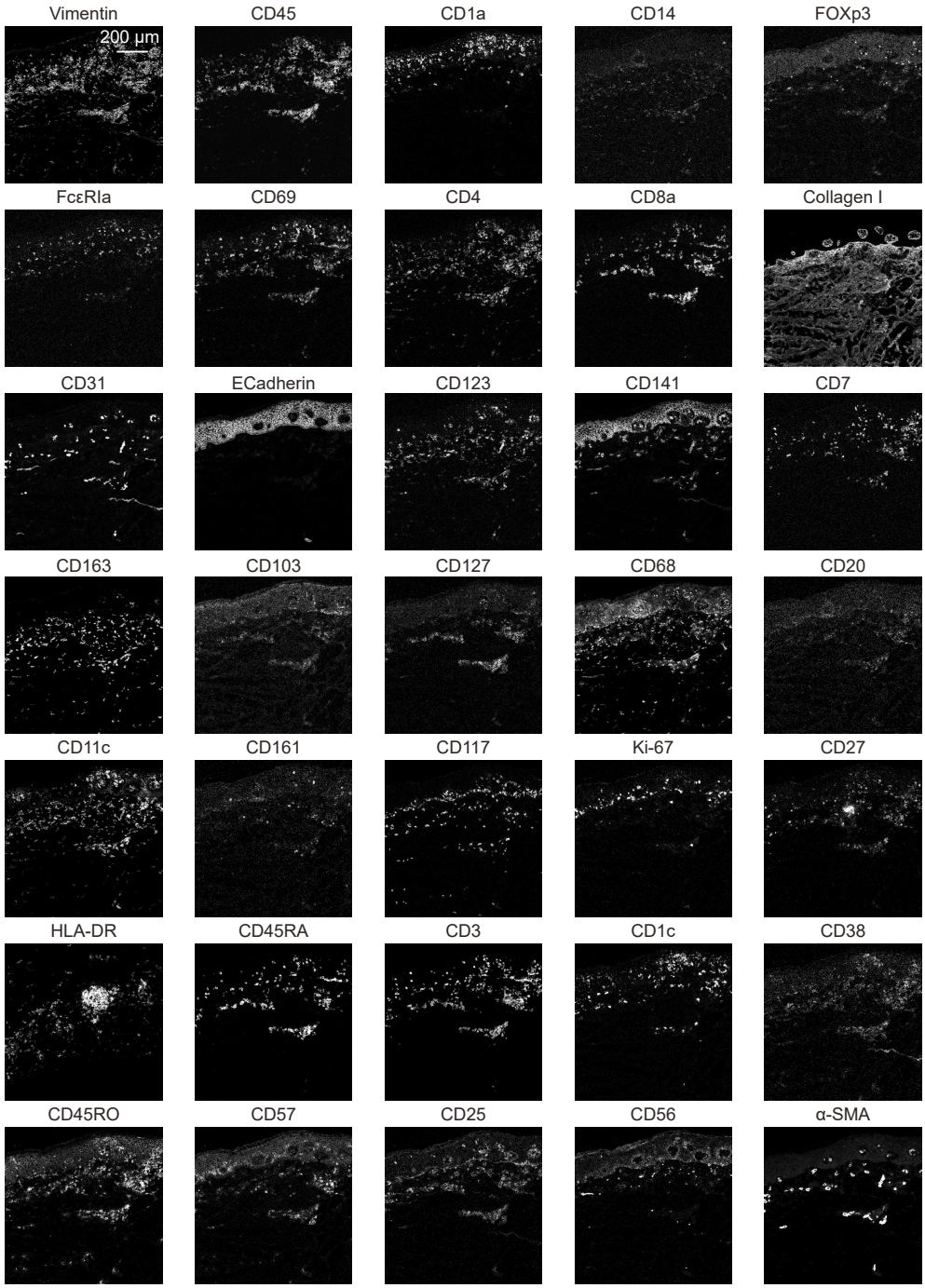

Figure S6 Individual antibody stains for 87MF patients by IMC.

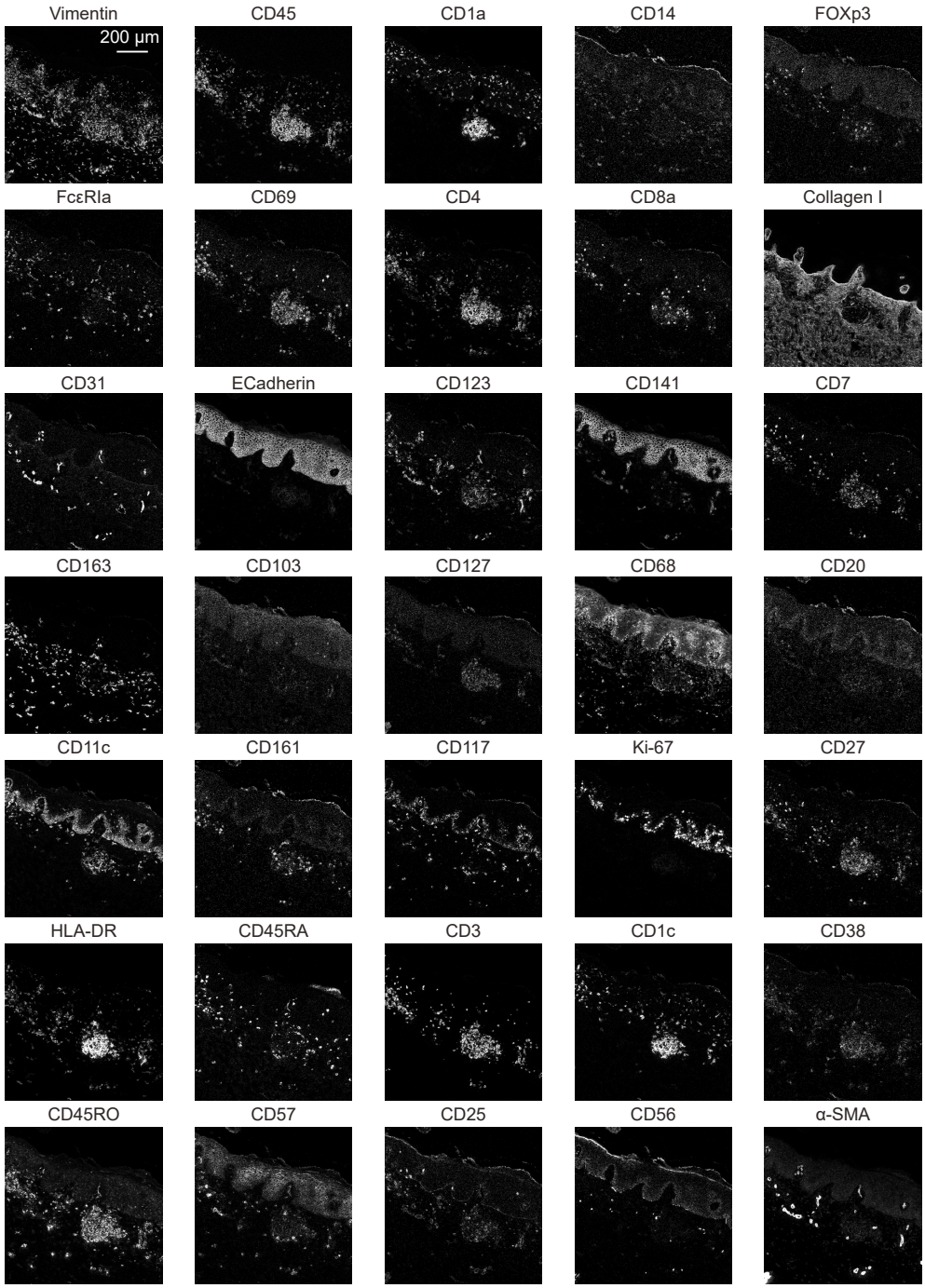

Figure S7 Individual antibody stains for 105MF patients by IMC.

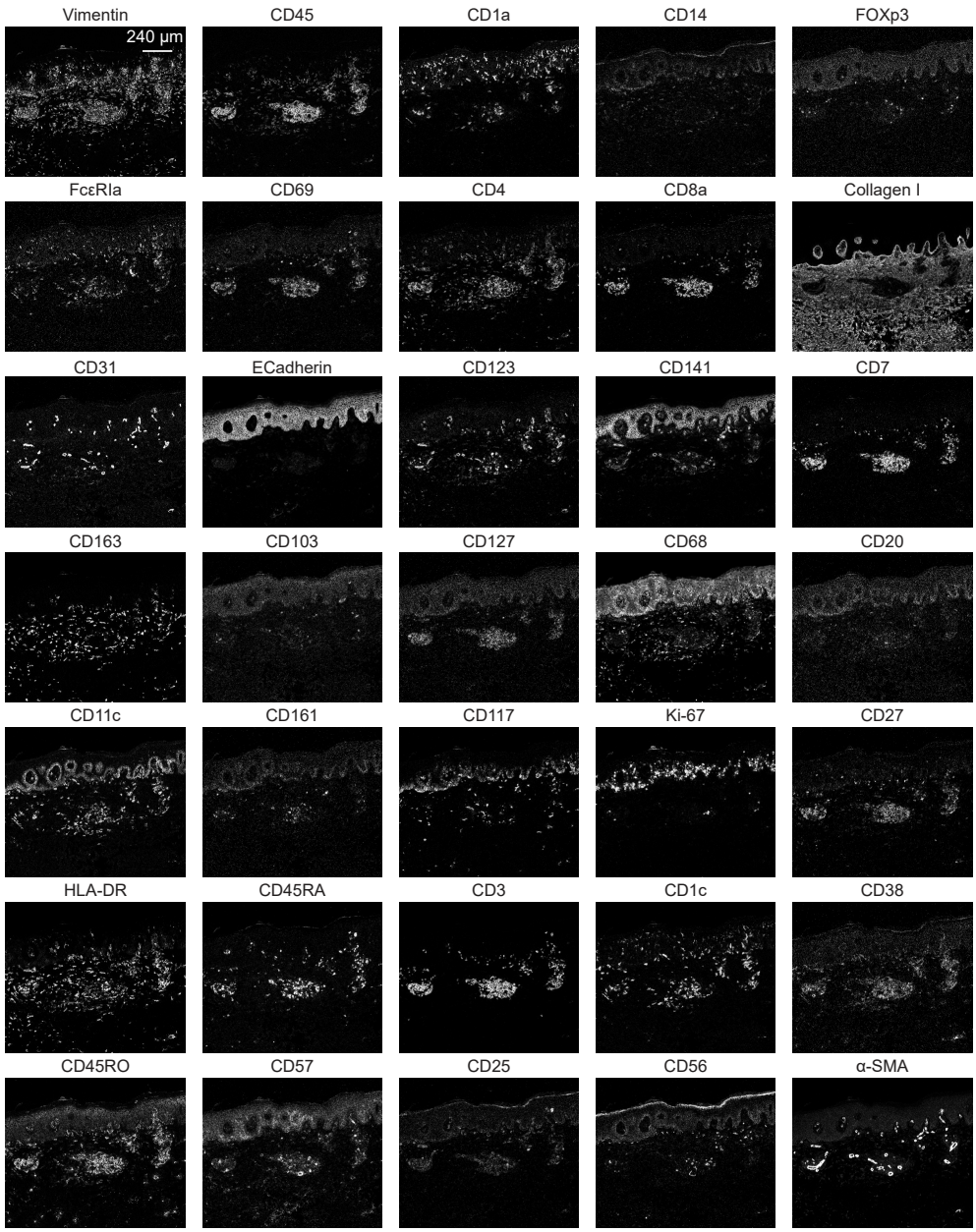

Figure S8 Individual antibody stains for 108MF patients by IMC.

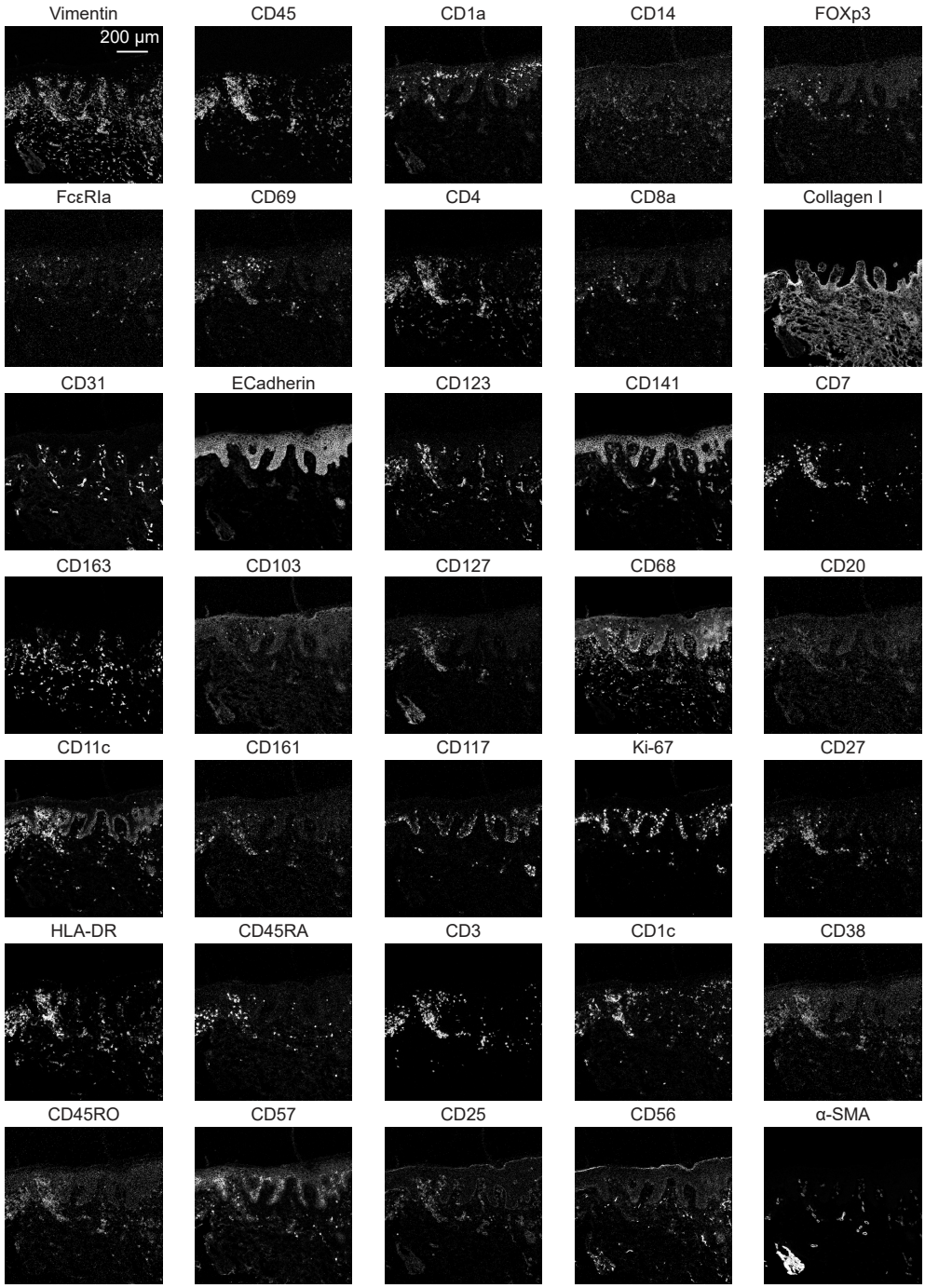

Figure S9 Individual antibody stains for 109MF patients by IMC.

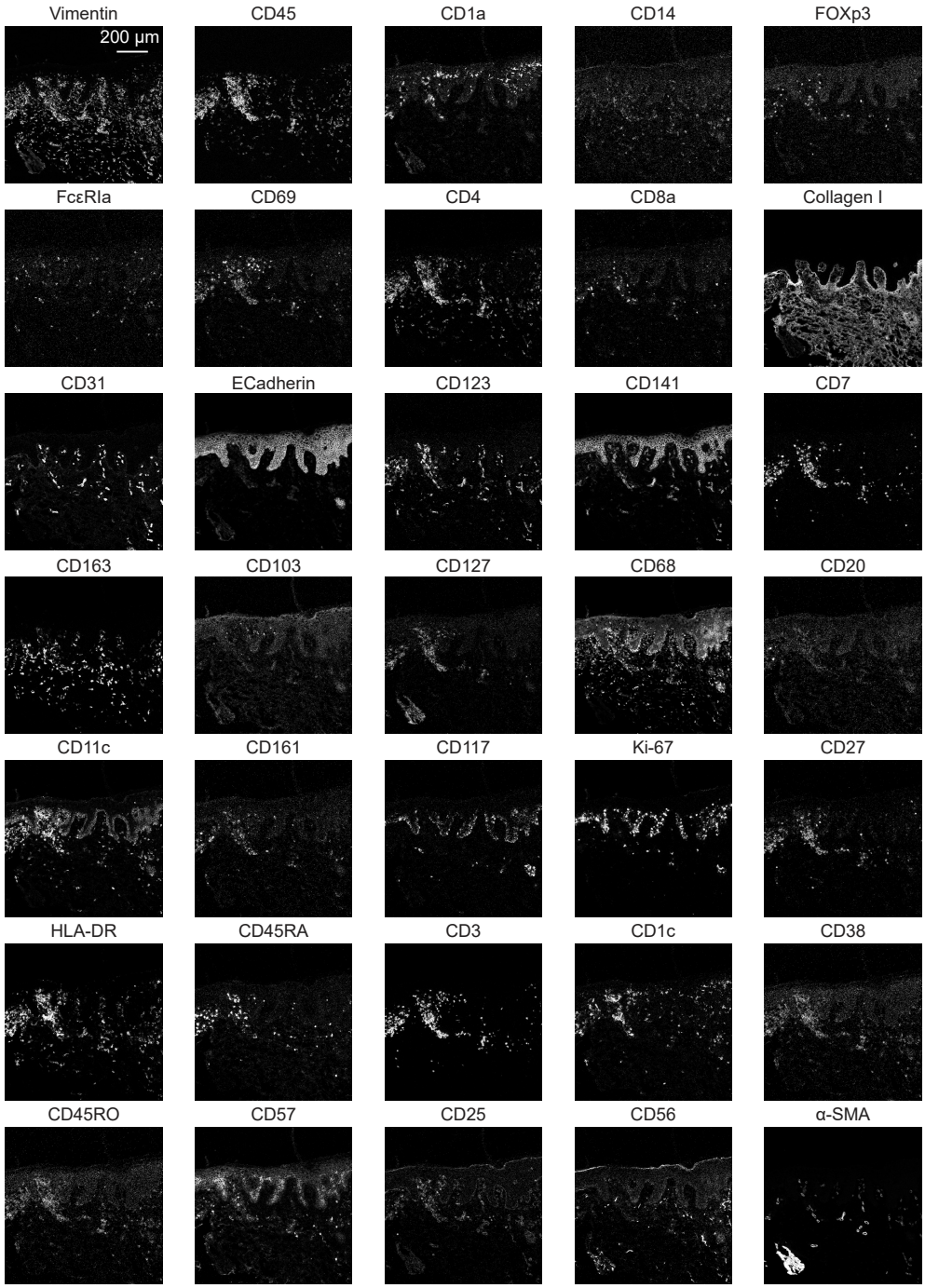

Figure S10 Individual antibody stains for 109MF patients by IMC.

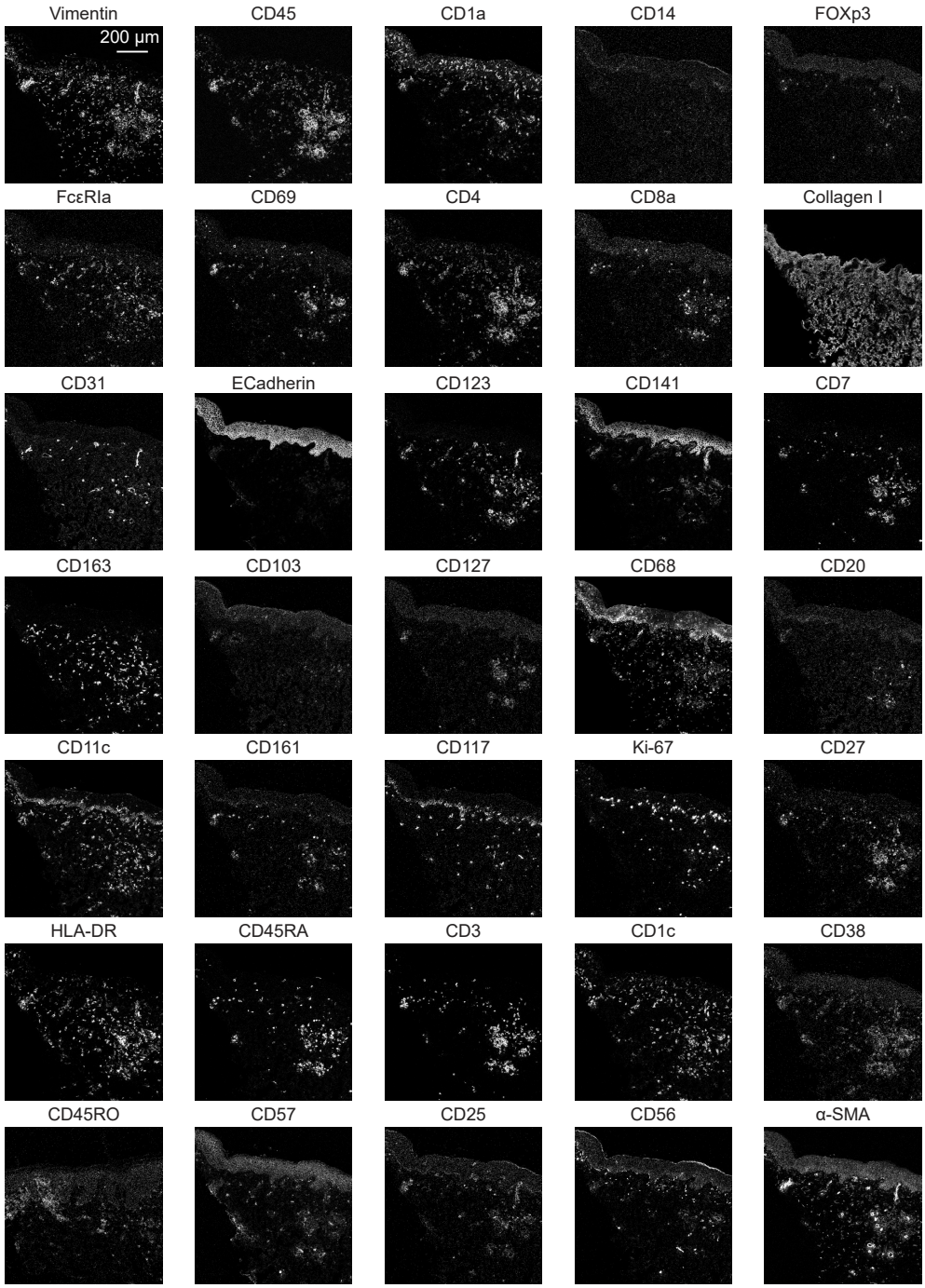

Figure S11 Individual antibody stains for 113MF patients by IMC.

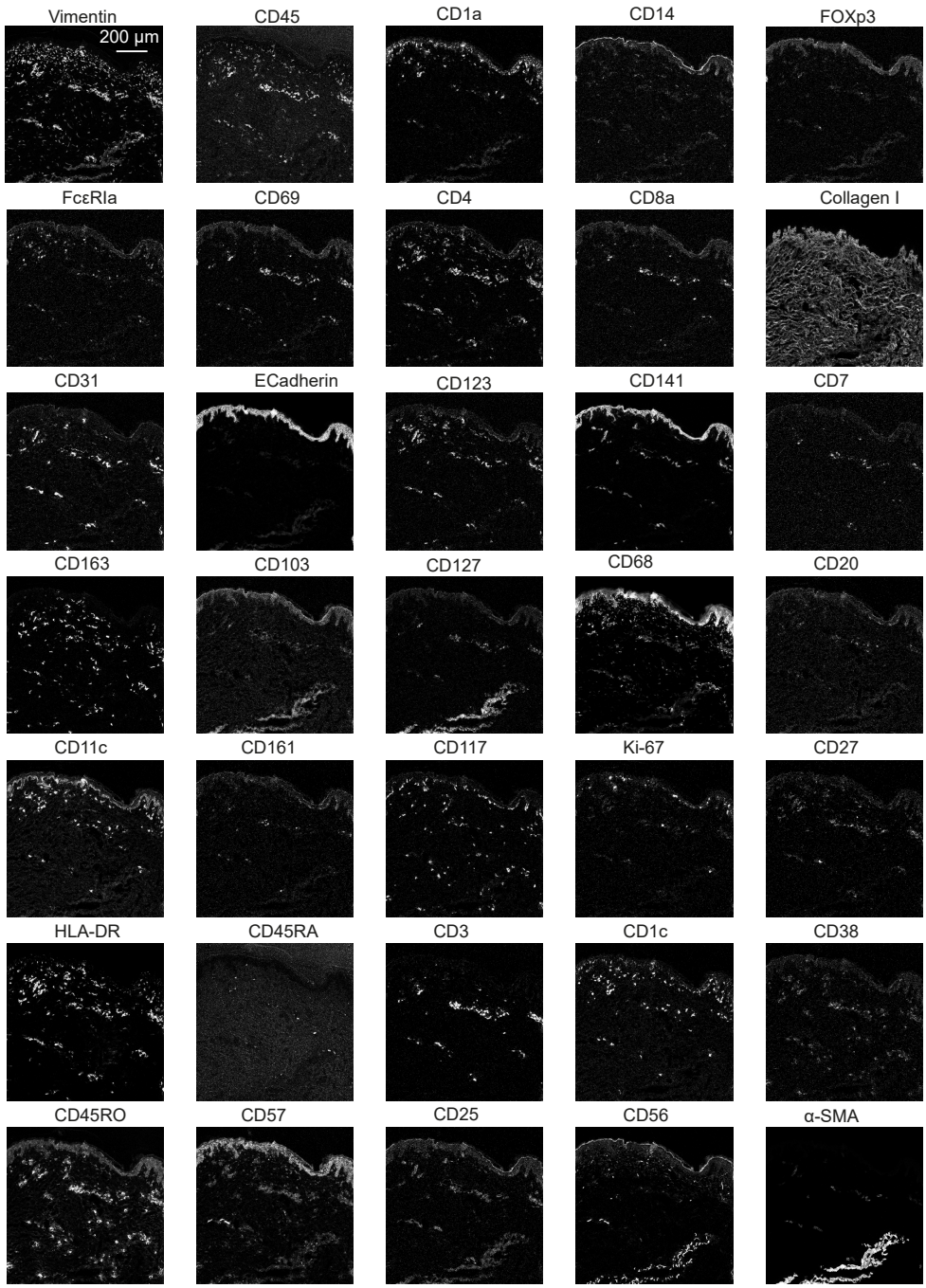

Figure S12 Individual antibody stains for 01NS patients by IMC.

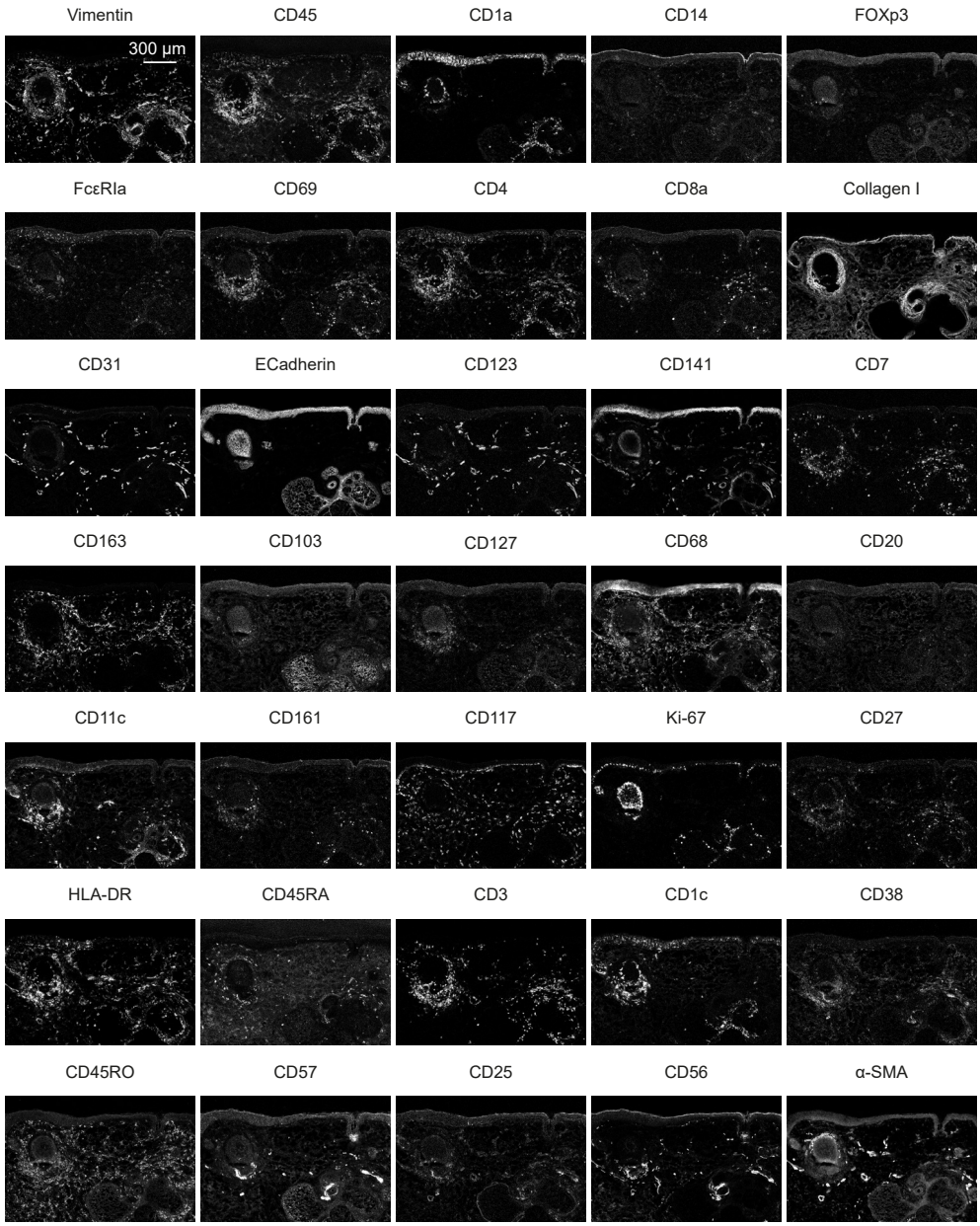

Figure S13 Individual antibody stains for 02NS patients by IMC.

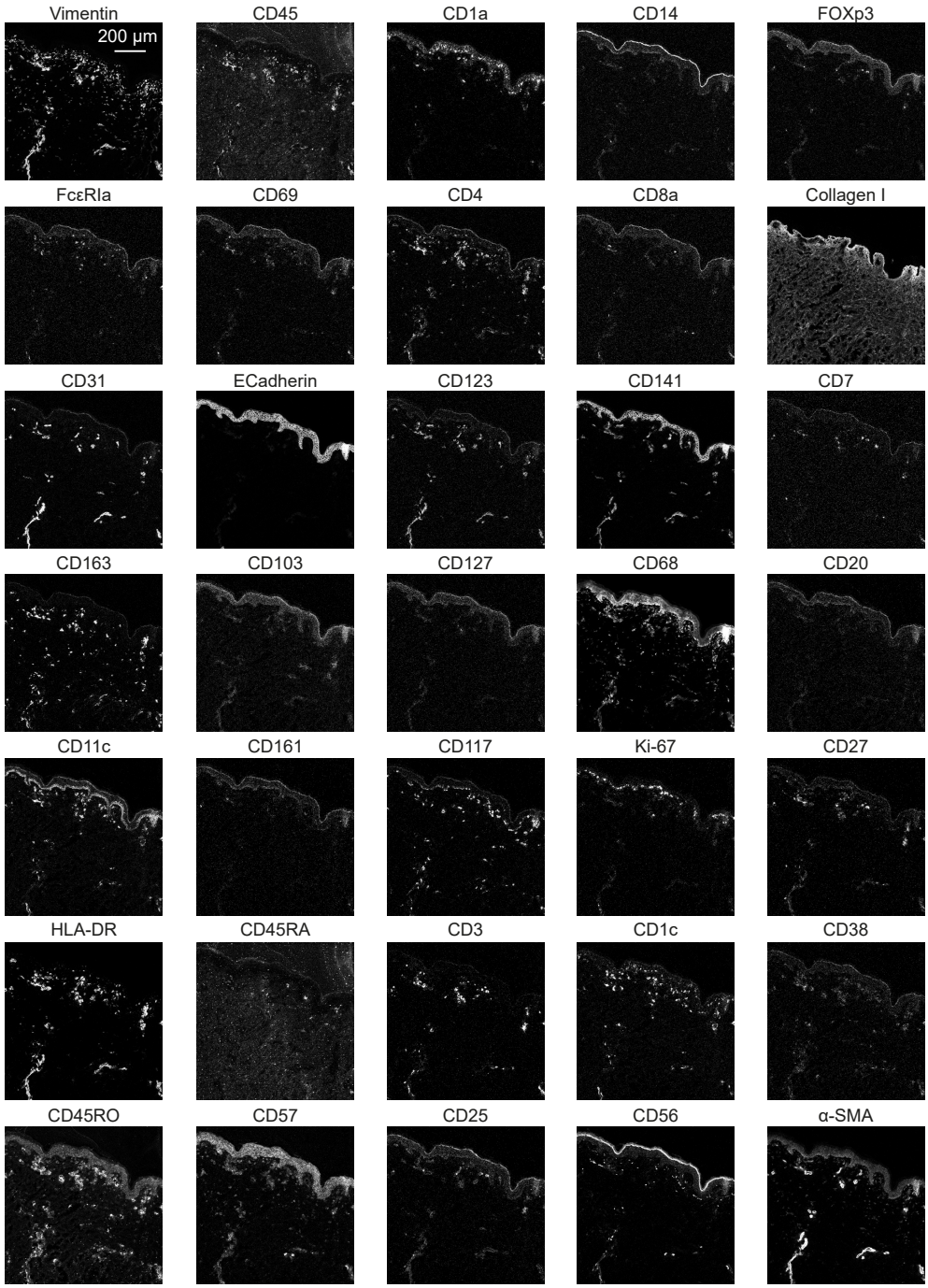

Figure S14 Individual antibody stains for 03NS patients by IMC.

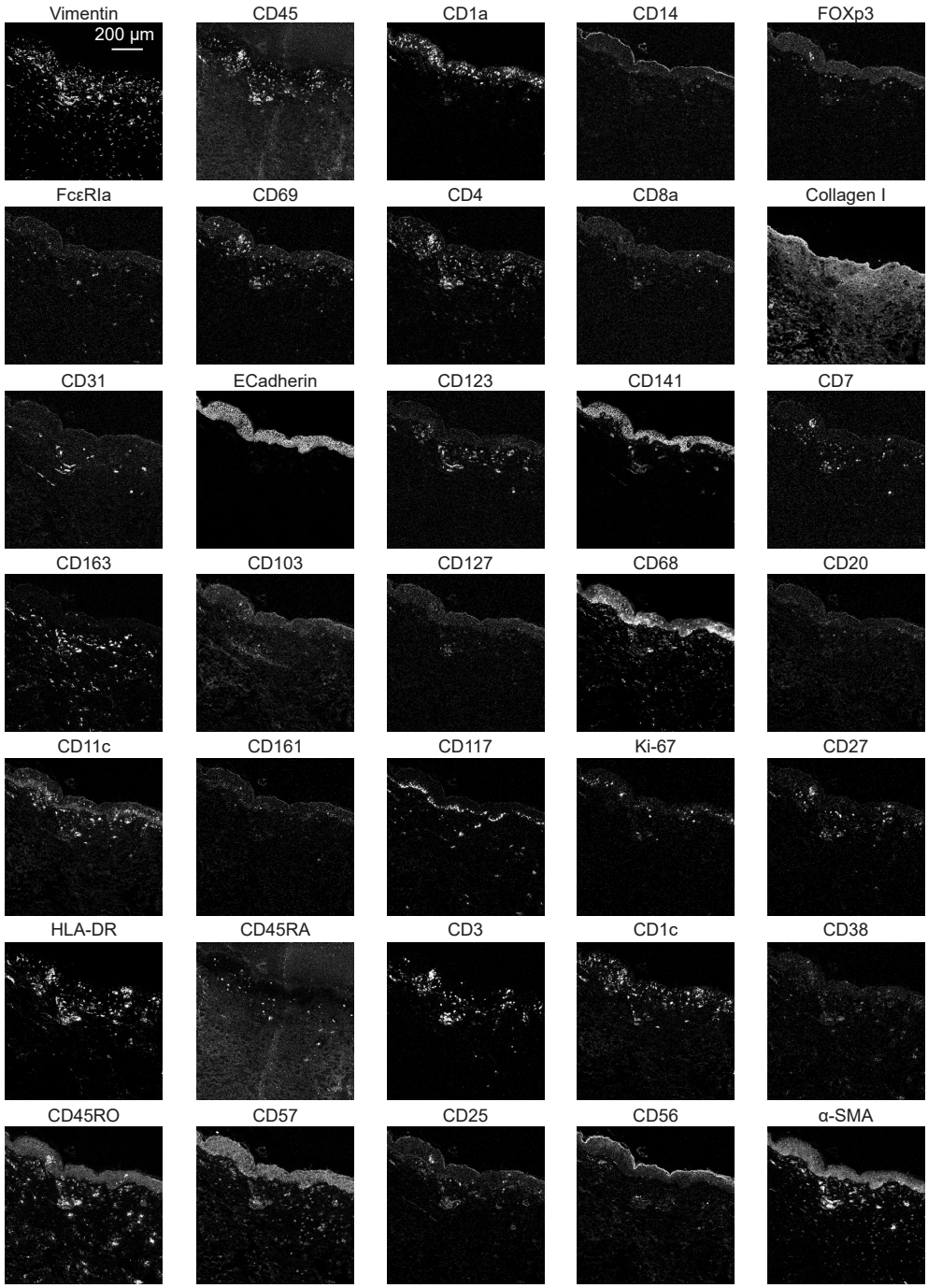

Figure S15 Individual antibody stains for 05NS patients by IMC.

Tables

Table S1 Characteristics of patients with Mycosis fungoides diseases.

Characteristics	MF patients by CyTOF (n=10)	MF Patients by IMC (n=6)
Sex (male:female)	6:4	4:2
Years of MF prior to biopsy		
Median	2	4
Range	0-21	2-8
Age at biopsy, years		
Median	54.5	62.5
Range	34-76	41-76
Stage at biopsy		
IA	0	1
IB	10	4
IIB	-	1
Follow-up, months		
Median	15	12
Range	12-20	8-20
Therapy after biopsy		
Topical corticosteroids	10	6
UV-therapy	5	-
Retinoids	2	-
Interferon-alpha	1	-
Radiotherapy	1	1
Disease course		
Progressive Disease	1	0
Stable disease	5	5
Partial Remission	2	1
Unknown	1	-

Table S2 The sex and age characteristics of the NS healthy donors.

Heathy Donors	IMC/CyTOF	Sex	Age
NS01	IMC	Female	78
NS02	IMC	Male	76
NS03	IMC	Male	41
NS04	IMC	Male	77
NS05	CyTOF	Male	62
NS06	CyTOF	Male	34
NS07	CyTOF	Male	78
NS08	CyTOF	Female	68
NS09	CyTOF	Male	52
NS10	CyTOF	Male	62
NS11	CyTOF	Female	73
NS12	CyTOF	Male	70
NS13	CyTOF	Male	70
NS14	CyTOF	Male	42
NS15	CyTOF	Male	70
NS16	CyTOF	Female	87
NS17	CyTOF	Male	74
NS18	CyTOF	Female	92
NS19	CyTOF	Male	86
NS20	CyTOF	Male	41
NS21	CyTOF	Male	81

Table S3 Single-cell suspension mass cytometry antibody panel.

	Antigen	Tag	Clone	Supplier	Cat.No	Dilution
1	CLA	104Pd	HECA-452	Biolegend	321302	1/50
2	CD39	108Pd	A1	Biolegend	328221	1/50
3	CD15	115In	W6D3	Biolegend	323035	1/50
4	CCR6	141Pr	G034E3	Fluidigm	31411003A	1/100
5	CD1a	142Nd	HI149	Sony	21100510	1/50
6	CD117	143Nd	104D2	Fluidigm	3143001B	1/100
7	CD69	144Nd	FN50	Fluidigm	3144018B	1/100
8	CD4	145Nd	RPA-T4	Fluidigm	3145001B	1/100
9	CD8a	146Nd	RPA-T8	Fluidigm	3146001B	1/200
10	CD57	147Sm	HNK-1	Biolegend	359602	1/200
11	CD16	148Nd	3G8	Fluidigm	3148004B	1/100
12	CD25	149Sm	2A3	Fluidigm	3149010B	1/100
13	IgM	150Nd	MHM88	Biolegend	314527	1/100
14	CD123	151Eu	6H6	Fluidigm	31511001B	1/100
15	TCRγδ	152Sm	11F2	Fluidigm	31512008B	1/50
16	CD7	153Eu	CD7-6B7	Fluidigm	3153014B	1/100
17	CD163	154Sm	GHI/61	Fluidigm	3154007B	1/100
18	CD103	155Gd	Ber-ACT8	Biolegend	350202	1/100
19	CRTH2	156Gd	BM16	Biolegend	350102	1/100
20	CD26	157Gd	BA5b	Biolegend	302702	1/100
21	CD30	158Gd	Ber-H2	Dako	M075101-2	1/50
22	CCR7	159Tb	G043H7	Fluidigm	3159003A	1/100
23	CD5	160Gd	UCHT2	Biolegend	300627	1/50
24	KLRG-1	161Dy	REA261	MACS	120-014-229	1/50
25	CD11c	162Dy	Bu15	Fluidigm	31612005B	1/200
26	CD20	163Dy	2H7	Biolegend	302343	1/200
27	CD161	164Dy	HP-3G10	Fluidigm	3164009B	1/100
28	CD127	165Ho	AO19D5	Fluidigm	3165008B	1/200
29	CD8b	166Er	SIDI8BEE	Ebio	15257407	1/50
30	CD27	167Er	O323	Fluidigm	3167002B	1/100
31	HLA-DR	168Er	L243	Biolegend	307651	1/300
32	CD45RA	169Tm	HI100	Fluidigm	3169008B	1/100
33	CD3	170Er	UCHT1	Fluidigm	3170001B	1/100
34	CD28	171Yb	CD28.2	Biolegend	302937	1/100
35	CD38	172Yb	HIT2	Fluidigm	31712007B	1/200
36	CD45RO	173Yb	UCHL1	Biolegend	304239	1/100
37	NKp46	174Yb	9E2	Biolegend	331902	1/40
38	PD-1	175Lu	EH 12.2H7	Fluidigm	3175008B	1/100
39	CD56	176Yb	NCAM16.2	Fluidigm	3176008B	1/100
40	CCR4	198Pt	205410	R & D	MAB1567-100	1/100
41	CD11b	209Bi	ICRF44	Fluidigm	3209003B	1/100
42	CD45	89Y	HI30	Fluidigm	3089003B	1/100
43	CD14	Qdot800	TüK4	ThermoFisher	Q10064	1/1000

Table S4 Imaging mass cytometry antibody panel on frozen skin tissue.

	Antigen	Tag	Clone	Supplier	Cat.	Dilution
1	CD1a	115In	010	Dako	M357101-2	1/50
2	CD14	141Pr	M5E2	BioL	301801	1/50
3	FOXp3	142Nd	236A/E7	eBioscience™	14-4777-82	1/100
4	FcεRIα	143Nd	AER-37 (CRA-1)	BioL	334602	1/50
5	CD69	144Nd	FN50	FLM	3144018B	1/50
6	CD4	145Nd	RPA-T4	FLM	3145001B	1/50
7	CD8a	146Nd	RPA-T8	FLM	3146001B	1/50
8	Collagen I	147Sm	polyclonal	Millipore	AB758	1/100
9	CD31	149Sm	89C2	CST	CST3528BF	1/100
10	E-cadherin	150Nd	24E10	CST	CST3195BF	1/50
11	CD123	151Eu	6H6	FLM	3151001B	1/50
12	CD141	152Sm	Phx-01	BioL	902102	1/50
13	CD7	153Eu	CD7-6B7	FLM	3153014B	1/100
14	CD163	154Sm	GHI/61	FLM	3154007B	1/100
15	CD103	155Gd	EPR4166	Abcam	ab221210	1/50
16	CD127	156Gd	R34.34	Beckman	18LIQ494	1/50
17	CD68	159Tb	KP1	FLM	3159035D	1/200
18	CD20	161Dy	H1	FLM	3161029D	1/50
19	CD11c	162Dy	S-HCL-3	BioL	125602	1/50
20	CD11c	162Dy	Bu15	FLM	3162005B	1/50
21	CD161	164Dy	HP-3G10	FLM	3164009B	1/50
22	CD117	165Ho	104D2	BioL	313202	1/50
23	Ki-67	166Er	D3B5	CST	CST9129BF	1/200
24	CD27	167Er	O323	FLM	3167002B	1/50
25	HLA-DR	168Er	L243	BioL	307651	1/800
26	CD45RA	169Tm	HI100	FLM	3169008B	1/100
27	CD3	170Er	UCHT1	FLM	3170001B	1/100
28	CD1c	171Yb	L161	BioL	331501	1/50
29	CD38	172Yb	HIT2	FLM	3172007B	1/100
30	CD45RO	173Yb	UCHL1	BioL	304239	1/50
31	CD57	174Yb	HNK-1/Leu-7	Abcam	Ab212403	1/100
32	CD25	175Lu	24204.0	Thermo	MA5-23714	1/50
33	CD56	176Yb	NCAM16.2	FLM	3176008B	1/50
34	αSMA	194Pt	1A4	CST	56856BF	1/100
35	Vimentin	198Pt	D21H3	CST	5741BF	1/100
36	CD45	89Y	HI30	FLM	3089003B	1/50
Fluidigm (Flui), Cell Signaling Technology (CST) and Biolegend (BioL)						

Table S5 The minimum and maximum threshold of each marker for per sample.

		NS01		NS02		NS03		NS04		87MF		105MF		106MF		109MF		113MF		120MF	
Channel	Marker	Min	Max	Min	Max	Min	Max	Min	Max	Min	Max	Min	Max	Min	Max	Min	Max	Min	Max	Min	Max
Y(89)	CD45	3	7.56	3	12.69	3	6.87	3	6.54	2	17.24	1	13.42	1	14.08	1	14.63	1	9.14	1	14.95
In(115)	CD1a	1	9.78	1	17.14	1	8.64	1	14.85	1	13.54	1	14.23	1	10.38	1	7.84	1	9.52	1	6.9
Pr(141)	CD14	1	4.22	1	4.13	1	5.2	1	3.5	1	3.23	0.5	3.8	1	3.51	1	3.34	1	2.83	1	3.03
Nd(142)	FOXP3	1	3.51	1	3.94	1	3.68	1	3.42	1	4.13	1	3.39	1	3.17	1	3.3	1	2.95	1.5	4.73
Nd(143)	FceRIα	1	3.64	1	3.52	1	3.17	1	3.06	1	4.64	1	5.73	1	4.61	1	3.48	1	5.2	1	3.59
Nd(144)	CD69	1	5.96	1	6.42	1	4.19	1	5.83	1	9.07	1	7.86	1	6.69	1	12.43	1	9	1	9.13
Nd(145)	CD4	1	8.12	1	9.3	1	6.28	1	6.87	1	8.82	1	11.11	1	8.22	1	10.87	1	7.79	1	7.61
Nd(146)	CD8a	1	5.12	1	4.98	1	3.33	1	3.1	1	10.82	1	10	1	10	1	10	1	8	1	10
Sm(147)	Collagen I	3	22.54	3	40.83	3	18.44	3	16.54	3	36.48	3	28.47	3	35.67	3	44.56	3	37.37	3	41.06
Sm(149)	CD31	3	23.58	3	29.34	3	22.96	1	5.42	3	27.81	3	17.62	3	23.52	3	34.06	3	14.84	3	23.49
Nd(150)	E-cadherin	3	44.14	3	55.93	3	37.57	3	32.67	3	27.2	3	28.28	3	30.02	3	28.08	3	26.68	3	24.93
Eu(151)	CD123	1	5.91	1.5	7.73	1	4.48	1	4.27	1	7.1	1	6.22	1	7.21	1	8.45	1	9.98	1	8.55
Sm(152)	CD141	1	22.26	3	27.95	3	17.13	3	16.54	3	15.22	3	21.35	3	17.98	3	19.68	2	15.44	3	13.94
Eu(153)	CD7	1	3.01	1	7.06	1	3.05	1	3.97	1	7.54	1	7.12	1	10.54	1	15.26	1	9.24	1	12.03
Sm(154)	CD163	3	30.43	1	20.83	1	16.89	2	15.73	2	54.73	3	32.38	3	36.23	2	41.86	1	20.47	1	23.33
Gd(155)	CD103	1	4.51	3	6.25	1	3.96	1	3.87	1	4.18	1	3.72	1	3.55	1	3.73	1	3.4	1	3.61
Gd(156)	CD127	1	6.4	1	4.11	1	3.29	0.5	3.13	1	4.58	1	3.84	1	3.8	1	4.75	1	3.51	1	3.68
Tb(159)	CD68	3	73.69	3	89.96	3	77.5	3	52.22	8	68.11	8	101.4	8	101.3	5	81.17	8	52.32	10	63.97
Dy(161)	CD20	1	3.44	2	3.63	1	3.4	1	3.14	1	3.47	1	3.34	1	3.16	1	3.2	1	3.64	1	3.23
Dy(162)	CD11c	3	9.55	3	13.65	3	8.46	3	7.06	3		3	14.13	3	12.33	3	14.89	2	13.34	3	16.88
Dy(164)	CD161	1	3.61	1	4.35	1	3.36	1	3.27	1	4.22	1	4.99	1	3.59	1	4.59	1	5.24	1	4.73
Ho(165)	CD117	1	13.62	1	13.62	1	11.85	1	15.73	1	15.46	1	10.99	1	13.61	1	9.14	1	9.16	1	6.33
Er(166)	Ki-67	1	8.35	1	19.62	1	13.21	1	5.79	1	13.6	1	25.18	1	21.68	1.5	25.96	1	15.77	1.5	16.44
Er(167)	CD27	1	4.55	0	5.45	1	6.43	1	7.31	1	10.76	1	7.14	1	6.5	1	7.57	1	6.67	1	6.73
Er(168)	HLA-DR	3	44.68	3	33.07	3	39.48	1	28.32	2	31.61	3	62.1	3	36.67	1	38.63	2	29.65	3	45.24
Tm(169)	CD45RA	3	8.84	3	8.64	3	9.55	3	7.76	3	70.32	2	21.36	2	20.26	3	21.42	2	25.68	2	25.35
Er(170)	CD3	1	25.74	1	20.68	1	16.74	1	17.71	1	29.95	1	20.8	1	25.46	1	27.53	1	18.94	1	22.41
Yb(171)	CD1c	1	10.98	1	10.54	1	9.62	1	9.47	1	13.22	1	17.29	1	12.87	1	9.8	1	13.53	1	16.51
Yb(172)	CD38	1	3.8	1	4.94	1	3.64	0.6	3.41	1	4.03	1	3.92	1	4.07	1	3.74	1	3.74	1	5.15
Yb(173)	CD45RO	3	28.42	3	51.66	3	21.86	3	20.36	3	26.56	3	26.05	3	23.51	3	27.58	3	23.54	3	26.98
Yb(174)	CD57	3	18.04	3	26.96	3	16.73	3	13.9	3	7.48	3	7.03	3	6.03	3	8.22	2	5.29	3	7.41
Lu(175)	CD25	1	4.17	1	4.35	1	4.32	1	4.24	1	5.21	1	4.32	1	3.97	1	3.99	0.5	3.67	1	6.28
Yb(176)	CD56	3	43.53	3	24.62	3	18.92	1	7.57	3	8.92	3	9.86	3	7.72	3	21.11	3	17.75	2	9.28
Pt(194)	αSMA	10	463.4	10	26.8	10	50.12	10	10.75	10	76.44	10	41.03	10	45.27	10	192.7	5	11.89	10	35.51
Pt(198)	Vimentin	5	129.4	5	175.8	5	117.4	5	95.46	5	175.5	5	113.5	5	117.7	5	116.3	3	116.5	5	117.8

Chapter 5

Immune Profiling of Psoriasis by Imaging Mass Cytometry

Nannan Guo[1], Mette Schreurs[1], Jeroen Eggermont[2], Elizabeth Kieras[3], David Eleuteri[3], Sharon Conder Niedecken[3], Christopher Ty[3], Boudewijn Lelieveldt[2], Noel F. C. C. de Miranda[4], Karen M. Page[3], Frits Koning[1] *

[1]Department of Immunology, Leiden University Medical Center, Leiden, The Netherlands
[2]Department of Radiology, Leiden University Medical Center, Leiden, The Netherlands
[3]Worldwide Research and Development, Pfizer Inc, Cambridge, Massachusetts, USA
[4]Department of Pathology, Leiden University Medical Center, Leiden, The Netherlands

*Correspondence

In preparation

Abstract

Psoriasis is a chronic inflammatory skin disorder characterized by keratinocyte hyperproliferation and differentiation combined with immune cell infiltration. Hereby, we applied imaging mass cytometry to profile the immune system in non-lesional and lesional skin biopsies from nine psoriasis patients. Snap-frozen skin sections were labelled with a 41-antibody panel followed by data acquisition on a Hyperion mass cytometer with 1 µm resolution. MCD™ Viewer was utilized to validate the staining quality of the IMC panel, and to visualize the tissue architecture. To characterize the immune compartment, we made use of HSNE-based pixel analysis in *Cytosplore Imaging* which allowed both the visualization of the structure of psoriatic skin, as well as the distribution and quantification of various T and myeloid cell subsets in the skin tissue samples. Moreover, we observed clusters of pixels harboring features of both T cells and myeloid cells (double feature pixels), presumably representing close contact between these two cell types. The results reveal a significant increase of the number of CD4 and CD8 T cells in lesional skin as well and an increase in the number of $CD206^+$ macrophages and $Fc\varepsilon RI^+$ mast cells. In contrast, no significant differences in the presence of dendritic cells (DCs) subsets were observed. However, double pixel analysis allowed the distinction of patients displaying frequent interactions between T cells and $CD207^+CD1c^+$ Langerhans-like DC in dermis. In addition, interactions between T cells and $CD207^-CD1c^+$ DC and between T cells and $CD206^+$ macrophages were observed in all patients but varied substantially. Thus, imaging mass cytometry in combination with pixel analysis allows classification of psoriasis patients based on differential presence of immune cell subtypes and interactions among those. Further work is needed to determine how this relates to disease severity and response to treatment.

Key terms: Imaging mass cytometry, IMC, CyTOF, Psoriasis

Introduction

Psoriasis (PS) is a common, chronic inflammatory skin disease with variations in severity depending on inheritance and environmental factors[1]. It is clinically characterized by the appearance of well-demarcated scaling erythematous plaques with thickened skin, and can affect joints and can be accompanied by a pro-inflammatory metabolic syndrome[2]. Psoriasis is an organ-specific autoimmune disease that is driven by the activated cellular immune system[3, 4], the pathophysiology of which is characterized by aberrant keratinocyte proliferation and immune cell infiltration in the dermis and epidermis in the lesional skin[5, 6, 7, 8]. Previous investigators have documented that macrophages and several populations of activated dendritic cells (DCs) were present in the inflamed skin[9, 10, 11, 12]. Immunofluorescence staining has shown that, compared to skin samples from healthy controls, psoriasis lesional skin has a higher level of tumor necrosis factor (TNF)-α producing $CD68^+$ macrophages - especially in early-phase psoriasis, while $CD68^+CD163^+$ macrophages are less abundant[13, 14]. In addition, IL-23 and IL-20 producing $CD11c^+$ DCs that express HLA-DR, CD40, and CD86, but lack the expression of the Langerhans cells (LCs) marker and the monocyte marker CD14 have the potential to activate T cells and keratinocytes to account for the progression of disease[15, 16, 17]. Moreover, patients with psoriasis showed increased presence of activated T-cells in skin lesions and PBMCs, the latter pointing to systemic activation[18, 19]. Flow cytometric analysis of blood showed the relationship between psoriasis disease severity (guttate, acute and chronic psoriasis) and different subsets of circulating CLA^+ T cells[20]. Single-cell RNA sequencing of rash-affected skin from psoriasis patients revealed active proliferative expansion of the regulatory T cells, tissue-resident memory T cells and exhausted $CD8^+$ T cells with a relative attenuation of antigen-presenting cells, suggesting involvement of these immune subsets in initiating and maintaining cutaneous inflammation[21, 22]. Moreover, the study in mice model system has clearly shown that locally activated and proliferating resident T cells are dependent on local TNF-α production, and are key players during the development of psoriatic lesions[23]. Infiltrating T cells in psoriasis lesions are mainly activated Type 1 T helper (Th1) and Th17 CD4 T cells[24, 25, 26].

The advances of high-dimensional imaging mass cytometry (IMC) approach offer new opportunities to simultaneously investigate diverse skin-resident immune cell populations of psoriasis with higher resolution than ever before in *situ*. Previously, we have developed an IMC-based approach which is able to detect more than 40 different heavy metal isotopes simultaneously, to profile and compare immune

systemic components and complexity in detail in the tissue context[27, 28, 29].

In this study, we applied IMC to skin biopsies from nine psoriasis patients to define the spatial orientation of the immune cells in the tissue context by a pixel-based analysis approach in *Cytosplore Imaging*. Firstly, we determined 16 separate clusters of skin immune population-associated pixels and calculated the percentage of each pixel-cluster in psoriasis. Here, we observed multiple clusters of pixels with features of both lymphoid and myeloid cells that were located in immune aggregates of lesional skin, pointing towards close cell-cell interactions related to the pro-inflammatory state in psoriatic lesions. Further analysis indicated the phenotype of the cells involved in these cell-cell interactions and revealed substantial patient heterogeneity, findings that might relate to psoriasis disease severity. Overall, our IMC data analysis at the pixel level provides a baseline for the identification of immune cell subsets, their distribution in *situ*, as well as their interactions, information that may be of relevance for the development of more targeted, patient-specific therapies.

Method

Tissue material

Both lesional and non-lesional skin samples from 9 psoriatic patients recruited by Pfizer Inc were included in this study. Patients were not receiving any conventional or biological systemic therapy at the time of sampling. The skin biopsies were embedded in optimal cutting temperature compound, snap-frozen in isopentane and stored at -80 °C. Baseline characteristics and disease course of these psoriatic patients were given in Table 1.

Mass cytometry antibodies preparation

Heavy metal isotope-labelled antibodies are listed in Table 2. Some antibodies were pre-conjugated (Fluidigm) while others were conjugated in-house with heavy metal isotopes using the Maxpar Antibody Labeling Kit and protocol (Fluidigm). The conjugation of antibodies against α-smooth muscle actin (αSMA) and collagen I with Cisplatin 194 and 198 were performed using a protocol adapted by Schulz et al[30]. CD31 was labelled with 209Bito using a protocol adapted by Spitzer et al[31].

Imaging Mass Cytometry staining

Imaging mass cytometry staining procedures on snap-frozen tissue were developed in our previous study[27]. Based on this the metal-tagged antibodies were used either for 2 hours at room temperature or overnight at 4°C as indicated in Table

2. IMC immunostaining was performed on all frozen skin samples from the nine patients in a single experiment. Tissue sections were dried at room temperature, followed by fixation with cold 1% paraformaldehyde (PFA) for 30 min at 4° C. Then, the skin sections were incubated with the first antibody mixture for 2 hours at room temperature (Table 2). After washing three times for 5 mins with staining buffer (0.5% BSA, 0.05% Tween in DPBS), the sections were incubated with the second antibody mixture overnight at 4°C (Table 2). Next, the sections were washed three times for 5 mins with staining buffer. Finally, the slides were washed one time for 2 mins with demineralized water, and dried under an air flow.

Imaging mass cytometry data acquisition

The entire skin sections were ablated at 200 Hz on a Helios time-of-flight mass cytometer coupled to a Hyperion Imaging System (Fluidigm). The Hyperion was autotuned using a 3-element tuning slide (Fluidigm) as described in the Hyperion imaging system user guide. The regions of interest (ROIs) per sample were selected based on hematoxylin and eosin (H&E) stains on consecutive slides. All raw data were analyzed for marker intensity based on the maximum signal threshold, defined at the 98th percentile of all pixels in a single ROI using Fluidigm MCD™ viewer (v1.0.560.2).

Imaging Mass Cytometry data analysis

Cytosplore Imaging facilitated the complete exploration pipeline in an integrated manner as described previously (Chapter 2). First, ome.TIFF files were exported from Fluidigm, and we applied the arcsin transformation with a cofactor of five upon loading the data sets to *Cytosplore imaging*. Next, we applied HSNE analysis[32] on all pixels from all ROIs which resulted in the clustering of pixels based on the marker expression profiles. Based on this tissue pixels were distinguished from background pixels followed by a second HSNE analysis of the tissue pixels to visualize the structural and cellular components in the skin tissue by projection of the resulting pixel clusters back onto the tissue section with the imaging viewer. Finally, we further refined the clustering by focusing on the $CD45^{+/dim}$ pixels and performed a t-SNE analysis for the immune markers. Using this approach, we could visualize T cells, $CD3^{-}CD7^{+}$ ILCs, B cells, DCs, macrophages and mast cells simultaneously in a single region. Strikingly, double features pixels were also identified and able to project onto skin tissue, to emphasize the interaction of myeloid cell subsets and lymphoid cells.

Results

Overview of the overall structure of lesional and non-lesional psoriatic skin by IMC

To survey the spatial distribution of the immune and non-immune compartments, IMC was performed on snap-frozen psoriatic skin sections using a 41-antibody panel. This panel contained structural (E-cadherin, Collagen I and α-smooth muscle actin (αSMA)), stromal (Vimentin and CD31), lymphocyte (CD3, CD20, CD7, CD4 and CD8a), and myeloid markers (CD11c, HLA-DR, CD207, CD1c, CD206, CD163) next to markers indicative of cellular differentiation, tissue residency, and cellular activation. Paired non-lesional and lesional skin samples from nine patients were included. Hematoxylin and eosin (H&E) staining of the skin samples (Figure 1A) yielded images that were highly similar to those obtained through of visualization DNA, Collagen I and αSMA staining by IMC; a representative patient sample is shown in Figure 1B. A further magnification of the image shows that the actual IMC image consists out of pixels (Figure 1B, lower images). We next employed *Cytosplore imaging* to analyze the expression patterns of all 41 markers simultaneously at the pixel level.

First we selected tissue-based pixels and performed an HSNE analysis based on the expression of E-cadherin, CD31, vimentin, Ki-67 and CD45 which yielded five major clusters of pixels representing the epidermis, vessels, stromal cells in the dermis, proliferating keratinocytes, and immune cells respectively (Figure 1C, D). Projection of these clusters back onto the tissue slide revealed the tissue architecture (Figure 1E), clearly demonstrating the thickening of the epidermis and an increase of Ki-67$^+$ keratinocytes in lesional skin compared to non-lesional skin. In addition, a significant increase and colocalization of CD31$^+$ endothelial and CD45$^+$ immune cells is evident in lesional skin (Figure 1E), while no apparent differences were observed between the presence of vimentin$^+$ stromal cells that were scattered throughout the dermis in both lesional and non-lesional skin (Figure 1E).

Thus, pixel-based analysis allows the visualization of the immune compartment within the tissue context.

Figure 1. The histologic analysis of psoriatic skin by H&E and IMC analysis. (A) H&E staining was performed on skin tissues of a psoriasis patient. **(B)** Overlay of DNA, Collagen I and αSMA to visualize the histology of skin by IMC analyzed in MCD™ Viewer. **(C-D)** Cellular pixels of skin were selected and clustered in *Cytosplore Imaging*. Colors represent the different cellular clusters in **(C)**. Colors represent relative expression of indicated markers in (**D**). **(E)** The main cellular components were projected back onto image in *Cytosplore imaging*. Colors represent indicated the various cellular components.

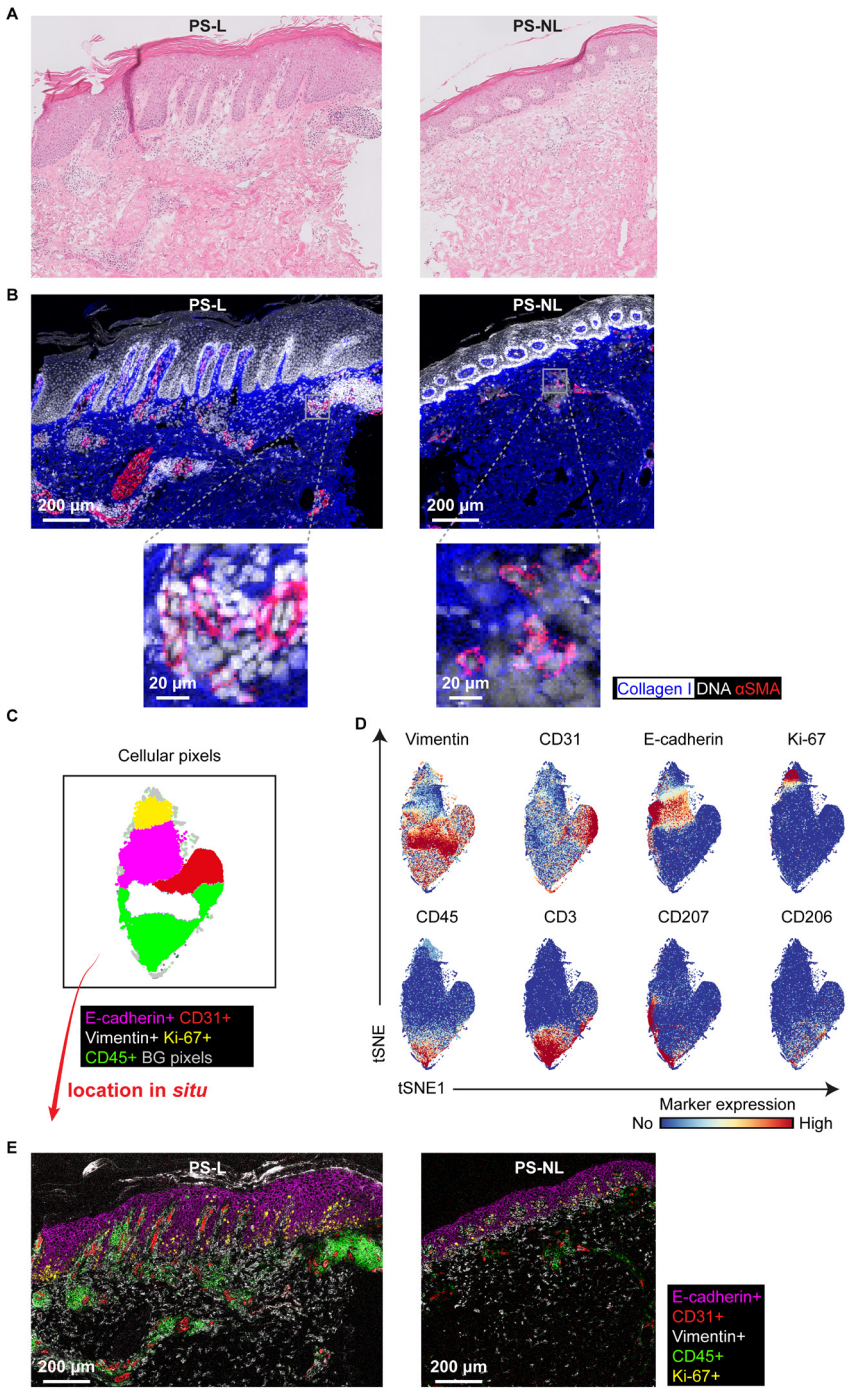

(Figure legend in previous page)

Immune cellular clusters of non-lesional and lesional psoriatic skin

To demonstrate the spatial organization of the immune cell subsets in *situ*, we performed an in-depth analysis of the $CD45^+$ immune cell-pixels, this identified 12 clusters of pixels in psoriatic skin, representing three T cell subsets ($CD3^+CD4^+$, $CD3^+CD8a^+$, $CD3^+CD4^-CD8a^-$), $CD3^-CD7^+$ innate lymphoid cells (ILCs), $CD20^+$HLA-DR^+ B cells, three DC subsets distinguished by differential expression of CD207 and CD1c, two subsets of macrophages ($CD206^+CD163^+$ and $CD206^+CD163^-$), and two mast cell sub-populations ($CD117^+$FceRIα^+ and $CD117^-$FceRIα^+) (Figure 2 and S1). Quantification of the number of pixels per immune cell subset demonstrates a significant increase of CD4 and CD8 T cells, macrophages and mast cells in lesional skin, while no significant differences were observed for the DC subsets (Figure 2B-E). The absence of CD45RA on the large majority of both CD4 and CD8 T cells indicates that these are predominantly memory T cells. Finally, $CD4^+$ T cells were more abundant as compared to $CD8^+$ T cells (Figure 2B). Visual inspection of the location of immune subset-specific pixels indicated that the majority of T cells, macrophages and mast cells were located in the dermis in both lesional and non-lesional skin samples (Figure 2F-I). Very few B cell and ILCs specific pixels were observed in both skin samples (Figure S1). As expected the majority of $CD207^+CD1c^-$ pixels, indicative of Langerhans cells, were located in the epidermis while the large majority dermal DC pixels were $CD207^-CD1c^+$ (Figure 2I).

Altogether, pixel analysis can be used to identify and visualize the spatial distribution of immune cell subsets. Moreover, it allows for unbiased pixel-based quantification of the presence of such subsets to facilitate the comparison of psoriatic non-lesional and lesional skin in *situ*.

Identification of pixel-clusters harboring features of both T and myeloid cells allow the quantification of immune interaction networks

As the generated images indicated substantial co-localization of T cells with myeloid cell types in the dermis of the lesional samples from psoriasis patients, we next aimed to further analyze and quantify such interactions in all patient samples.

Figure 2. Identification and quantification of immune subsets with pixel-based analysis of IMC images of lesional and non-lesional psoriatic skin samples. (A) A collective tSNE was performed on $CD45^{+/dim}$ pixels from the non-lesional and lesional skin of a representative psoriasis patient. Each dot represents a single pixel. Colors represent relative expression of the indicated immune markers. **(B-E)** Quantification of each immune subsets from nine psoriasis patients. **(F-I)** Display of spatial distribution of the identidied cell types in the non-lesional and lesional skin of a representative psoriasis patient. Error bars indicate mean ± s.e.m. *P < 0.05, ** P < 0.01, Wilcoxon signed-rank test for comparisons.

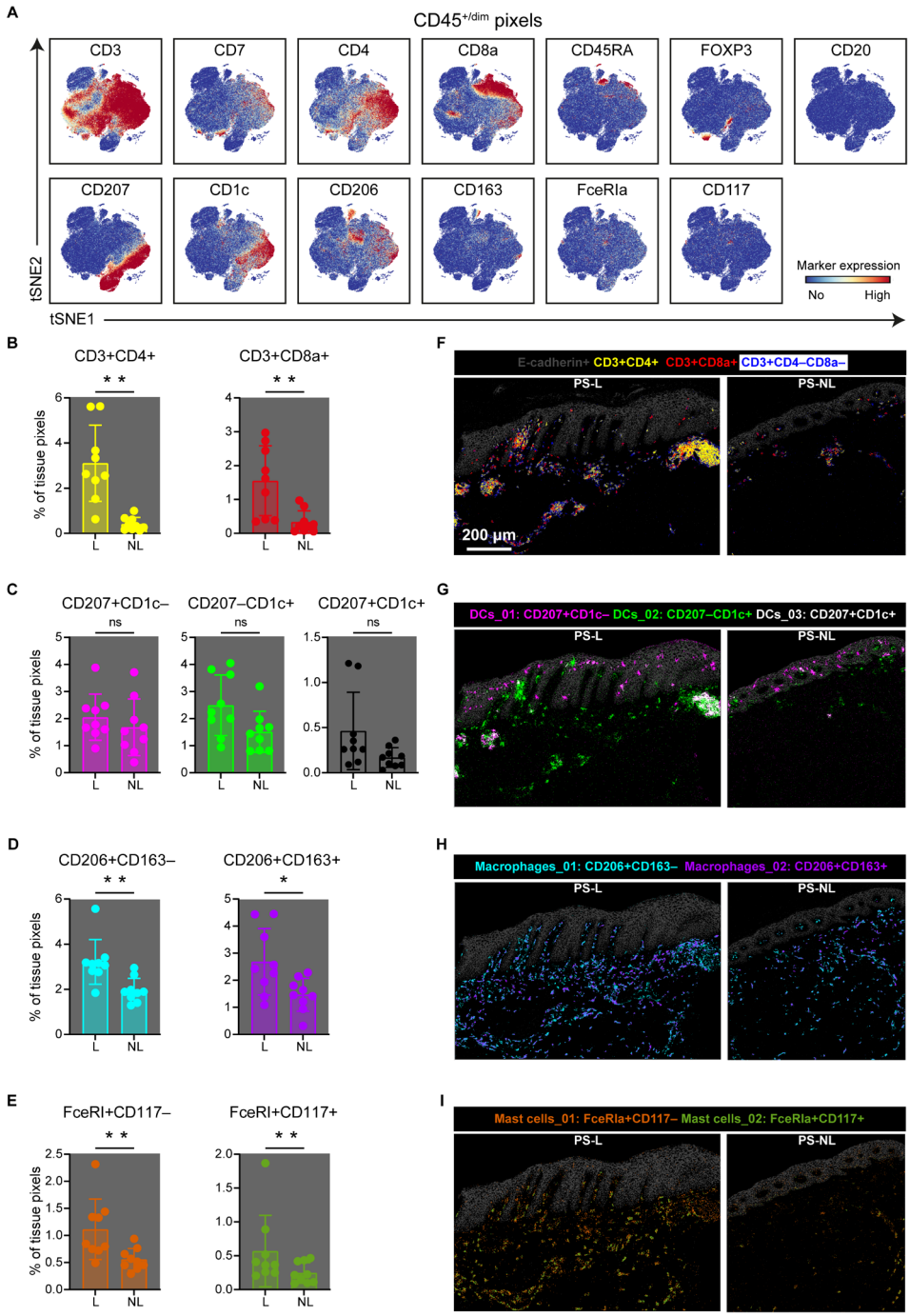

(Figure legend in previous page)

Here, we made use of clusters of pixels that harbored both T cell and myeloid markers, called double feature pixels hereafter. Figure 3 shows the distribution of $CD3^+$ pixels (red), $CD1c^+$ pixels (green), and $CD3^+CD1c^+$ double feature pixels (yellow) in a lesional skin section of a psoriatic patient, demonstrating the abundance of such double feature pixels in immune aggregates in the dermis. Further magnification of immune cell infiltrated area's indicates that these double feature pixels are predominantly found in between T cells and myeloid cells (Figure 3B) and thus likely represent close interactions between these two cell types.

Three types of double feature pixels could be readily identified in the HSNE-based pixel analysis pipeline, $CD3^+CD207^+CD1c^-$ (DCs_01&T), $CD3^+CD207^-CD1c^+$ (DCs_02&T), and $CD3^+CD207^+CD1c^+$ (DCs_03&T). We next quantified these double feature pixels in the lesional samples of the nine patients (Figure 4). For this we determined the total number of tissue pixels and the number of double feature pixels in each tissue sample and used this to calculate the percentage of double feature pixels (Figure 4A). Here, patients PS#08 and PS#09 had a high frequency of both DCs_02&T ($CD3^+CD207^-CD1c^+$) and DCs_03&T ($CD3^+CD207^+CD1c^+$) pixels, patients PS#4 and PS#6 had a high frequency of DCs_02&T pixels only, while the other patients exhibited a low frequency of both DCs_02&T and DCs_03&T (Figure 4A, B). Two pixel-clusters with features of T cells and macrophages were also identified in the lesional skin both of which were present in similar number sin patients samples (Figure 4C, S2). Interestingly, on patients PS#04, PS#08 and PS#09 a high proportion of pixels harboring features of T cells and macrophages were observed (Figure 4C).

Thus, pixel-based analysis of psoriasis skin samples allows the identification and quantification of cell-cell interactions that may underlie patients heterogeneity and disease severity.

Discussion

Psoriasis is an immune mediated inflammatory skin disease[33]. In our study, we analyzed non-lesional and lesional skin from patients with psoriasis to visualize the skin architecture and characterize the complexity of the innate and adaptive immune compartment in *situ* by IMC. Superior to conventional immunohistochemistry and immunofluorescence, IMC allows the detection of over 40 markers simultaneously. Therefore, the tissue context can be investigated with a higher resolution, for both the non-immune and immune compartments. Moreover, we used the in-house developed pixel-based approach, *Cytosplore*

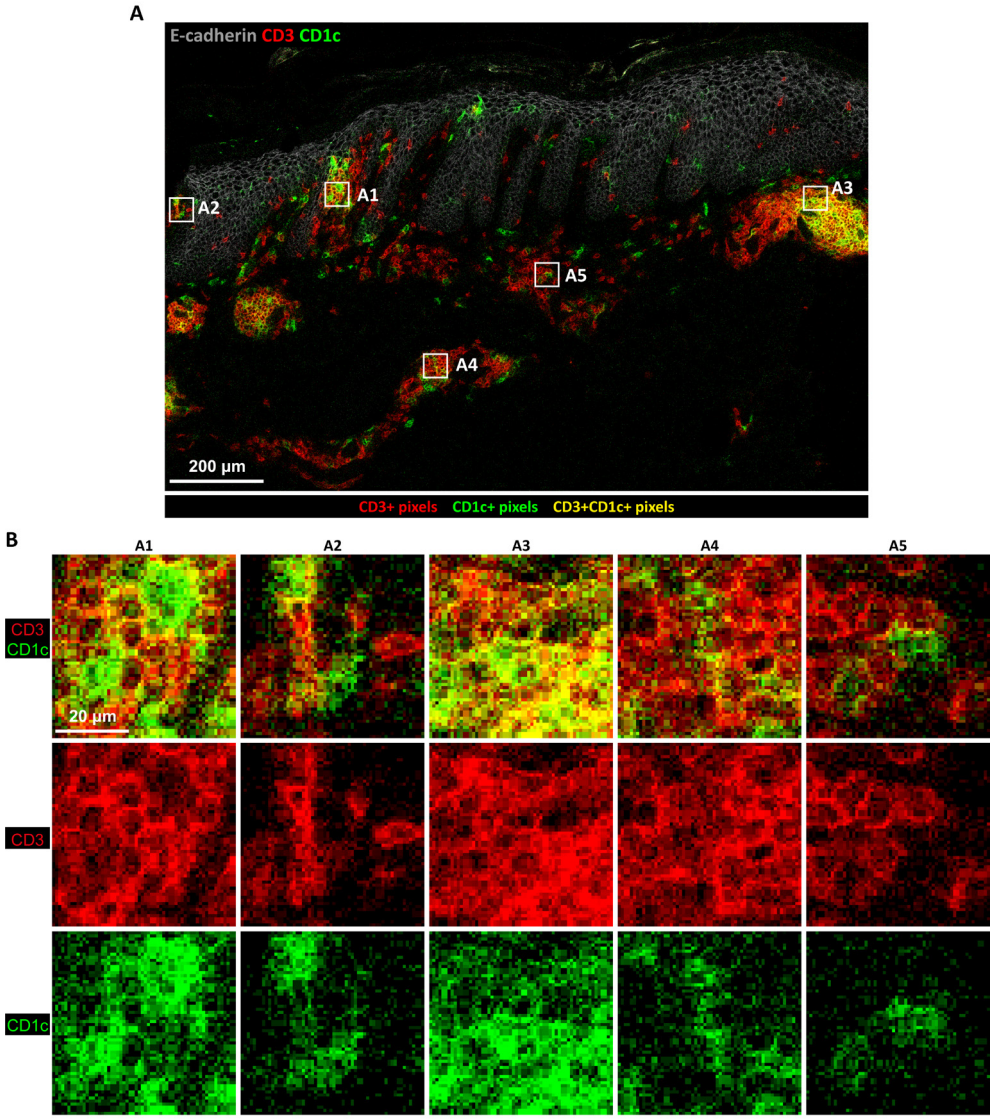

Figure 3. **Visualization of double feature pixels indicative of close proximity of T cells and DCs. (A)** Overlay by the staining of CD3 (red) and CD1c (green) in MCD™ Viewer visualize pixels that are CD3 and CD1c positive (yellow). **(B)** Magnification of the boxed areas in (A) with the individual markers as indicated.

Imaging, which was adapted from *Cytosplore*$^{+HSNE}$ [32], to visualize the composition and organization of immune cells for nine psoriasis patients. This allowed the identification of the various immune subsets in the skin samples. Moreover, the analysis of pixels harboring feature of both T cell and myeloid cells allowed the

identification, visualization and quantification of cell-cell interactions that may be related to disease severity.

Recently, the approaches based on cell segmentation analysis, like Imacyte[29] and Histocat[34] have been developed. Here, the creation of a single cell mask based on nuclei, cytoplasm/membrane, and background removal is necessary for each sample to allow for immunophenotyping within the spatial localization and subsequent neighborhood analysis[35]. However, due to differences in immune cell morphology and cell density variations in tissues, the true signal is frequently lost during the removal of background noise or cannot be exactly categorized into cells, particularly in areas where cells are densely packed. Here, pixel-based analysis provides an alternative that to identify cell subsets and quantify interactions between those.

Dendritic cells (DCs) are professional antigen presenting cells (APCs), and crucially involved in the initiation and propagation of adaptive immune responses to pathogens[36]. Langerhans cells (LCs) are unique as they are the only DC subset observed in the epidermis in normal skin[37]. During inflammation LCs become activated and transition through the dermis with differential expression of langerin, epithelial cell adhesion molecule (EpCam), CD11b and CD103[37]. Previous studies in mice models of skin infection identified three subset of skin DCs, LCs, Langerin $(CD207)^{+}$ dermal DCs, and classic dermal DCs. Here, LCs contribute to the generation of antigen-specific Th17 cells[38]. Recent studies have shown that IL-23 and IL-22 are important mediators in psoriasis skin inflammation[39, 40]. IL-23-producing macrophages and DCs are involved in the development of Th17 cells that have differentiated from naive T cells in the presence of IL-6 and TGF-β[41, 42]. Moreover, dermal macrophages are increased in psoriasis compared with normal skin[12], and have been shown to produce inflammatory TNF-α and inducible nitric oxide synthase (iNOS)[12, 43]. Moreover, many genes upregulated in activated macrophages have been found in psoriasis as well, including STAT1, CXCL9, Mx1, and HLA-DR[12]. Importantly, treatment with etanercept, a TNF receptor-immunoglobulin fusion protein, leads to a decrease in the presence of macrophages in psoriatic skin[44]. Altogether, the network of DCs and macrophages interacting with T cells in the skin lesion is a logical target for therapy of psoriasis.

According to the analysis of T and myeloid cells in psoriatic lesion, we identified three clusters of pixels of pixels harboring features of T cells and DCs based on the presence of CD3, langerin/CD207 and CD1c, suggesting crosstalk between T cells and various dermal DCs in the lesion. In addition, $CD206^{+}CD163^{+/-}$ macrophages

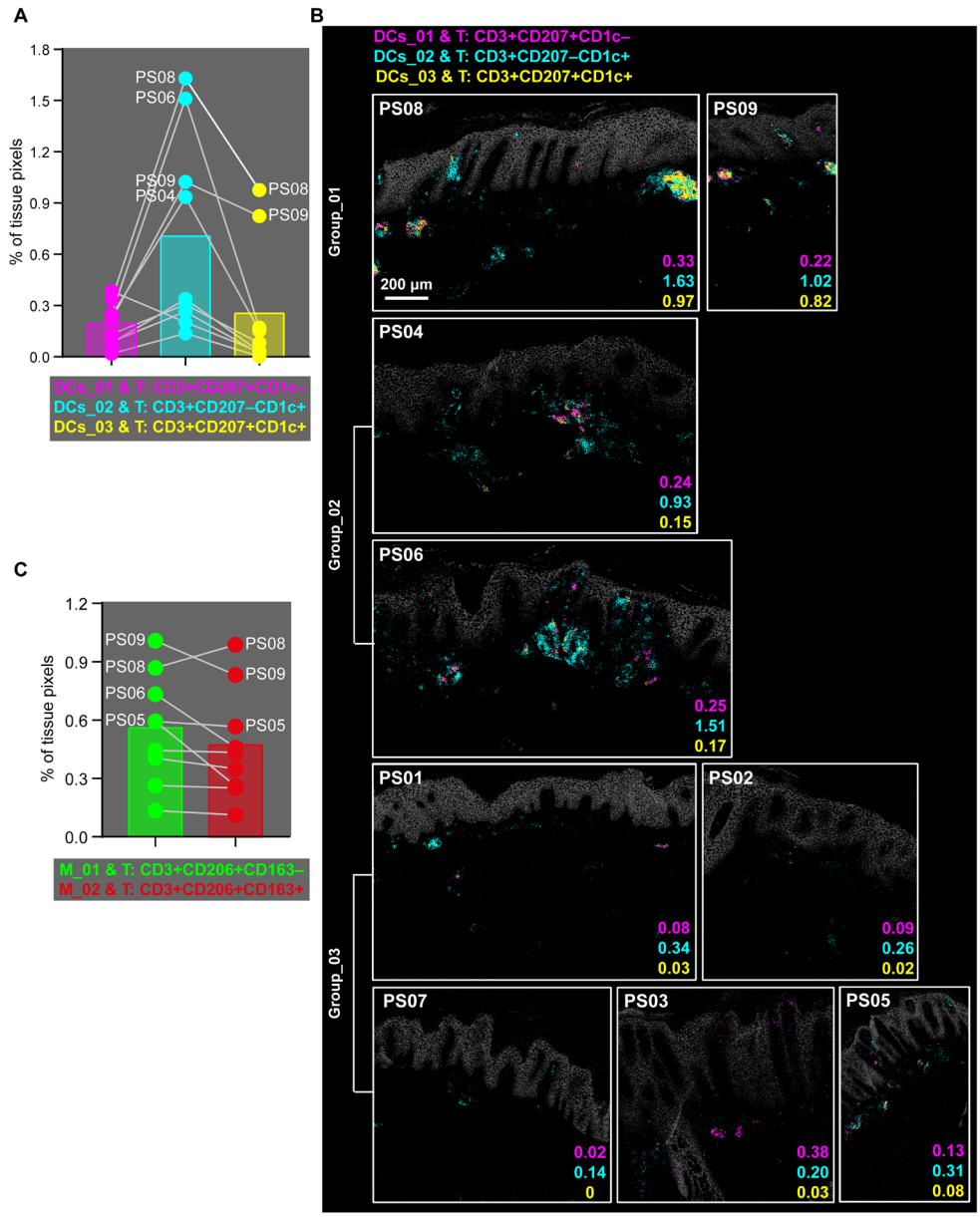

Figure 4. Identification and quantification of double feature pixelss in psoriatic lesions. (A-B) The quantification **(A)** and visualization **(B)** of three double feature pixel classes indicative of interaction between T and DCs in lesional skin samples. **(C)** The quantification of two double feature pixel classes indicative of interactions between T cells and macrophages in lesional skin samples. Colors represent different clusters as indicted.

were observed to colocalize with T cells in the lesion as well. Moreover, we observed substantial differences between the patients. A higher presence of pixels indicative of interaction between T cells and both DCs and macrophages were observed in patients PS#08 and PS#09, while much less evidence for such interactions was observed in other patients. However, at present we did not find a correlation between the clinical scores and our observations (Table 1). Possibly, this could be due to the fact that the Psoriasis Area and Severity Index (PASI) score is related to the overall assessment of the patient and may not reflect the actual severity in the skin lesion region investigated. However, our results indicate that substantial differences can be detected between patients. Further studies with larger sample sizes will be needed to explore the possible correlation with disease severity. Future work will be also required to elucidate the functional profile of the cell subsets with more advanced IMC antibody panels, mRNA analysis and functional studies.

Collectively, the current study provides an alternative, pixel-based analysis method for IMC datasets, especially suitable for tissue samples with densely packed cells. Moreover, we showed the composition and distribution of immune subsets *in situ* for psoriasis patients, and different patterns of colocalization of T cells and myeloid cells. Our work provided a reference basis to better understand immune profiling of psoriasis, and may potentially facilitate improved prognosis and treatment of psoriasis.

Funding

This research was supported by BIOMAP (Bio-markers in Atopic Dermatitis and Psoriasis), a project funded by the Innovative Medicines Initiative 2 Joint Undertaking under grant agreement no. 821511 (NG and FK). N.F.C.C.d.M. is funded by the European Research Council (ERC) under the European Union's Horizon 2020 Research and Innovation Programme (grant agreement no. 852832).

Acknowledgements

We thank the patients. We thank all operators in the Flow Cytometry Core Facility of the LUMC for technical assistance with measurements on Helios and Hyperion.

Authorship Contributions

NG and FK conceived the study and wrote the manuscript. NG performed most experiments with the help of MS and NFCCdM. NG performed most of the analyses with the help of FK, JE and BL. EK, DE, SCN, CT and KMP collected skin biopsies from psoriasis patients. All authors discussed the results and commented on the manuscript.

Reference

1. Green, M.S., Prystowsky, J.H., Cohen, S.R., Cohen, J.I. & Lebwohl, M.G. Infectious complications of erythrodermic psoriasis. *J Am Acad Dermatol* **34**, 911-914 (1996).
2. Griffiths, C.E. & Barker, J.N. Pathogenesis and clinical features of psoriasis. *Lancet* **370**, 263-271 (2007).
3. Lebwohl, M. Psoriasis. *Lancet* **361**, 1197-1204 (2003).
4. Lowes, M.A., Bowcock, A.M. & Krueger, J.G. Pathogenesis and therapy of psoriasis. *Nature* **445**, 866-873 (2007).
5. Bowcock, A.M. & Krueger, J.G. Getting under the skin: the immunogenetics of psoriasis. *Nat Rev Immunol* **5**, 699-711 (2005).
6. Boyman, O. *et al.* Activation of dendritic antigen-presenting cells expressing common heat shock protein receptor CD91 during induction of psoriasis. *Br J Dermatol* **152**, 1211-1218 (2005).
7. Lew, W., Bowcock, A.M. & Krueger, J.G. Psoriasis vulgaris: cutaneous lymphoid tissue supports T-cell activation and "Type 1" inflammatory gene expression. *Trends Immunol* **25**, 295-305 (2004).
8. Krueger, J.G. The immunologic basis for the treatment of psoriasis with new biologic agents. *J Am Acad Dermatol* **46**, 1-23; quiz 23-26 (2002).
9. Nestle , F.O. *et al.* Plasmacytoid predendritic cells initiate psoriasis through interferon-α production. *Journal of Experimental Medicine* **202**, 135-143 (2005).
10. Lowes, M.A. *et al.* Increase in TNF-α and inducible nitric oxide synthase-expressing dendritic cells in psoriasis and reduction with efalizumab (anti-CD11a). *Proceedings of the National Academy of Sciences* **102**, 19057-19062 (2005).
11. Krueger, J.G. The immunologic basis for the treatment of psoriasis with new biologic agents. *Journal of the American Academy of Dermatology* **46**, 1-26 (2002).
12. Fuentes-Duculan, J. *et al.* A subpopulation of CD163-positive macrophages is classically activated in psoriasis. *J Invest Dermatol* **130**, 2412-2422 (2010).
13. Leite Dantas, R. *et al.* Macrophage-mediated psoriasis can be suppressed by regulatory T lymphocytes. *J Pathol* **240**, 366-377 (2016).
14. Kamata, M. & Tada, Y. Dendritic Cells and Macrophages in the Pathogenesis of Psoriasis. *Front Immunol* **13**, 941071 (2022).
15. Lee , E. *et al.* Increased Expression of Interleukin 23 p19 and p40 in Lesional Skin of Patients with Psoriasis Vulgaris. *Journal of Experimental Medicine* **199**, 125-130 (2004).
16. Wang, F. *et al.* Prominent Production of IL-20 by CD68+/CD11c+ Myeloid-Derived Cells in Psoriasis: Gene Regulation and Cellular Effects. *Journal of Investigative Dermatology* **126**, 1590-1599 (2006).
17. Lowes, M.A. *et al.* Increase in TNF-alpha and inducible nitric oxide synthase-expressing dendritic cells in psoriasis and reduction with efalizumab (anti-CD11a). *Proc Natl Acad Sci U S A* **102**, 19057-19062 (2005).
18. Czarnowicki, T. *et al.* Skin-homing and systemic T-cell subsets show higher activation in atopic dermatitis versus psoriasis. *J Allergy Clin Immunol* **136**, 208-211 (2015).
19. Guttman-Yassky, E. & Krueger, J.G. Atopic dermatitis and psoriasis: two different immune diseases or one spectrum? *Current Opinion in Immunology* **48**, 68-73 (2017).
20. Ferran, M., Giménez-Arnau, A.M., Bellosillo, B., Pujol, R.M. & Santamaria-Babi, L.F. Circulating CLA+ T cell subsets inversely correlate with disease severity and extension in acute psoriasis but not in chronic plaque psoriasis. *Eur J Dermatol* **18**, 647-650 (2008).
21. Liu, J. *et al.* Single-cell RNA sequencing of psoriatic skin identifies pathogenic Tc17 cell subsets and reveals distinctions between CD8(+) T cells in autoimmunity and cancer. *J Allergy Clin Immunol* **147**, 2370-2380 (2021).
22. Liu, Y. *et al.* Classification of human chronic inflammatory skin disease based on single-cell immune profiling. *Sci Immunol* **7**, eabl9165 (2022).
23. Boyman, O. *et al.* Spontaneous development of psoriasis in a new animal model shows an essential role for resident T cells and tumor necrosis factor-alpha. *J Exp Med* **199**, 731-736 (2004).
24. Austin, L.M., Ozawa, M., Kikuchi, T., Walters, I.B. & Krueger, J.G. The Majority of Epidermal T Cells in Psoriasis Vulgaris Lesions can Produce Type 1 Cytokines, Interferon-γ, Interleukin-2, and Tumor Necrosis Factor-α, Defining TC1 (Cytotoxic T Lymphocyte) and TH1 Effector Populations:1 a Type 1 Differentiation Bias is also Measured in Circulating Blood T Cells in Psoriatic Patients. *Journal of Investigative Dermatology* **113**, 752-759 (1999).
25. Kim, J. & Krueger, J.G. Highly Effective New Treatments for Psoriasis Target the IL-23/Type 17 T Cell Autoimmune Axis. *Annual Review of Medicine* **68**, 255-269 (2017).
26. Noda, S. *et al.* The Asian atopic dermatitis phenotype combines features of atopic dermatitis and psoriasis with increased TH17 polarization. *Journal of Allergy and Clinical Immunology* **136**, 1254-1264 (2015).
27. Guo, N. *et al.* A 34-Marker Panel for Imaging Mass Cytometric Analysis of Human Snap-Frozen Tissue. *Frontiers in Immunology* **11** (2020).
28. Ijsselsteijn, M.E., Somarakis, A., Lelieveldt, B.P.F., Höllt, T. & de Miranda, N.F.C.C. Semi-automated background removal limits data loss and normalizes imaging mass cytometry data. *Cytometry*

Part A **99**, 1187-1197 (2021).
29. Somarakis, A., Van Unen, V., Koning, F., Lelieveldt, B. & Hollt, T. ImaCytE: Visual Exploration of Cellular Micro-Environments for Imaging Mass Cytometry Data. *IEEE Trans Vis Comput Graph* **27**, 98-110 (2021).
30. Schulz, A.R. & Mei, H.E. Surface Barcoding of Live PBMC for Multiplexed Mass Cytometry. *Methods Mol Biol* **1989**, 93-108 (2019).
31. Spitzer, M.H. *et al.* Systemic Immunity Is Required for Effective Cancer Immunotherapy. *Cell* **168**, 487-502.e415 (2017).
32. van Unen, V. *et al.* Visual analysis of mass cytometry data by hierarchical stochastic neighbour embedding reveals rare cell types. *Nature Communications* **8**, 1740 (2017).
33. Liang, Y., Sarkar, M.K., Tsoi, L.C. & Gudjonsson, J.E. Psoriasis: a mixed autoimmune and autoinflammatory disease. *Curr Opin Immunol* **49**, 1-8 (2017).
34. Schapiro, D. *et al.* histoCAT: analysis of cell phenotypes and interactions in multiplex image cytometry data. *Nat Methods* **14**, 873-876 (2017).
35. Ijsselsteijn, M.E., Somarakis, A., Lelieveldt, B.P.F., Höllt, T. & de Miranda, N. Semi-automated background removal limits data loss and normalizes imaging mass cytometry data. *Cytometry A* **99**, 1187-1197 (2021).
36. Banchereau, J. *et al.* Immunobiology of Dendritic Cells. *Annual Review of Immunology* **18**, 767-811 (2000).
37. Kaplan, D.H. In vivo function of Langerhans cells and dermal dendritic cells. *Trends in Immunology* **31**, 446-451 (2010).
38. Igyártó, B.Z. *et al.* Skin-resident murine dendritic cell subsets promote distinct and opposing antigen-specific T helper cell responses. *Immunity* **35**, 260-272 (2011).
39. Ma, H.L. *et al.* IL-22 is required for Th17 cell-mediated pathology in a mouse model of psoriasis-like skin inflammation. *J Clin Invest* **118**, 597-607 (2008).
40. Lowes, M.A. *et al.* Psoriasis vulgaris lesions contain discrete populations of Th1 and Th17 T cells. *J Invest Dermatol* **128**, 1207-1211 (2008).
41. Zheng, Y. *et al.* Interleukin-22, a T(H)17 cytokine, mediates IL-23-induced dermal inflammation and acanthosis. *Nature* **445**, 648-651 (2007).
42. McKenzie, B.S., Kastelein, R.A. & Cua, D.J. Understanding the IL-23-IL-17 immune pathway. *Trends Immunol* **27**, 17-23 (2006).
43. Verma, D. *et al.* Enhanced Inflammasome Activity in Patients with Psoriasis Promotes Systemic Inflammation. *J Invest Dermatol* **141**, 586-595.e585 (2021).
44. Zaba, L.C. *et al.* Amelioration of epidermal hyperplasia by TNF inhibition is associated with reduced Th17 responses. *J Exp Med* **204**, 3183-3194 (2007).

Supplementary information

Tables

Table 1 The clinical characteristics for psoriasis patients/skin lesional samples.

Patient No.	Sex	Age	BSA[1]	PASI[2]
PS#01	Male	45	6	8.2
PS#02	Female	23	4	7.2
PS#03	Male	34	4	6.3
PS#04	Male	61	7	8.2
PS#05	Male	55	4	5.8
PS#06	Male	69	3	4.2
PS#07	Female	56	5	3.6
PS#08	Male	54	6	9
PS#09	Female	56	5	6.4

[1]Score of Body Surface Area (BSA) with Psoriasis

[2]Higher PASI scores representing increasing severity of psoriasis

Table 2 Imaging mass cytometry antibody panel on the skin samples from psoriasis patients.

	Antigen	Tag	Clone	Supplier	Dilution	Incubation
1	CD94	141 Pr	DX22	Biolegend	50	RT
2	CD94	141 Pr	HP-3D9	BD Biosciences	50	RT
3	CXCR1	152Sm	5A12	BD Biosciences	50	RT
4	CD127	158 Gd	R34.34	Beckman	50	RT
5	PD-L1	150Nd	SP142	Fluidigm	50	RT
6	CD66b	163Dy	6/40c	Biolegend	50	RT
7	PD-1	165Ho	EH12.2H7	Fluidigm	50	RT
8	CD45RO	173Yb	UCHL1	Biolegend	50	RT
9	CD56	176Yb	NCAM16.2	Fluidigm	50	RT
10	CD207	148 Nd	4C7	Biolegend	100	RT
11	CD206	172Yb	19.2	BD Biosciences	100	RT
12	CD45	89Y	HI30	Fluidigm	50	4 °C
13	CD103	155Gd	Ber-ACT8	Biolegend	50	4 °C
14	CD1a	115In	010	Dako	50	4 °C
15	FcεRIα	143Nd	AER-37 (CRA-1)	Biolegend	50	4 °C
16	CD69	144Nd	FN50	Fluidigm	50	4 °C
17	CD4	145Nd	RPA-T4	Fluidigm	50	4 °C
18	CD8a	146Nd	RPA-T8	Fluidigm	50	4 °C
19	CD117	147Sm	104D2	Biolegend	50	4 °C
20	CD27	149Sm	O323	Biolegend	50	4 °C
21	CD123	151Eu	6H6	Fluidigm	50	4 °C
22	CD86	156Gd	IT2.2	Fluidigm	50	4 °C
23	E-cadherin	159Tb	67A4	Biolegend	50	4 °C
24	CD172a	160 Gd	15-414	Biolegend	50	4 °C
25	CD20	161Dy	H1	Fluidigm	50	4 °C
26	CD11c	162Dy	S-HCL-3	Biolegend	50	4 °C
27	CD11c	162Dy	Bu15	Fluidigm	50	4 °C
28	CD161	164Dy	HP-3G10	Fluidigm	50	4 °C
29	Granzyme B	167Er	GB11	Fluidigm	50	4 °C
30	CD1c	171Yb	L161	Biolegend	50	4 °C
31	CD25	175Lu	24204	Thermo Fisher	50	4 °C
32	FOXP3	142Nd	236A/E7	Thermo Fisher	100	4 °C
33	CD7	153Eu	CD7-6B7	Fluidigm	100	4 °C
34	CD163	154Sm	GHI/61	Fluidigm	100	4 °C
35	CD45RA	169Tm	HI100	Fluidigm	100	4 °C
36	CD3	170Er	UCHT1	Fluidigm	100	4 °C
37	CD57	174Yb	HNK-1	Biolegend	100	4 °C
38	αSMA	194Pt	1A4	CST	100	4 °C
39	Collagen I	196Pt	Polyclonal	Millipore	100	4 °C
40	Vimentin	198Pt	WM59	Biolegend	100	4 °C
41	CD31	209Bi	WM59	Biolegend	100	4 °C
42	Ki-67	166Er	D3B5	CST	200	4 °C
43	HLA-DR	168Er	L243	Biolegend	800	4 °C
Cell Signaling Technology (CST)						

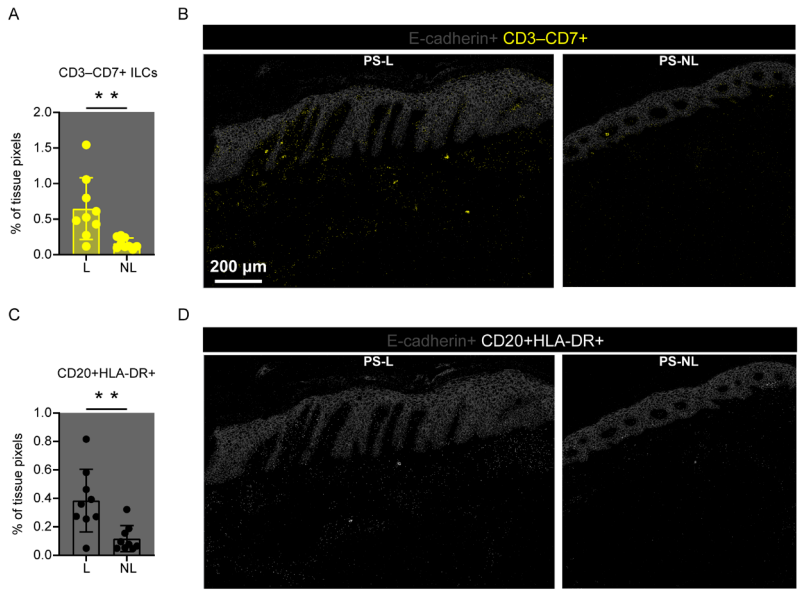

Figure S1. Quantification of pixels of CD3^{-}CD7^{+} ILCs and B cells from nine psoriasis patients and display of spatial distribution on the non-lesional and lesional skin of a representative psoriasis patient. Error bars indicate mean ± s.e.m. ** P < 0.01, Wilcoxon signed-rank test for comparisons.

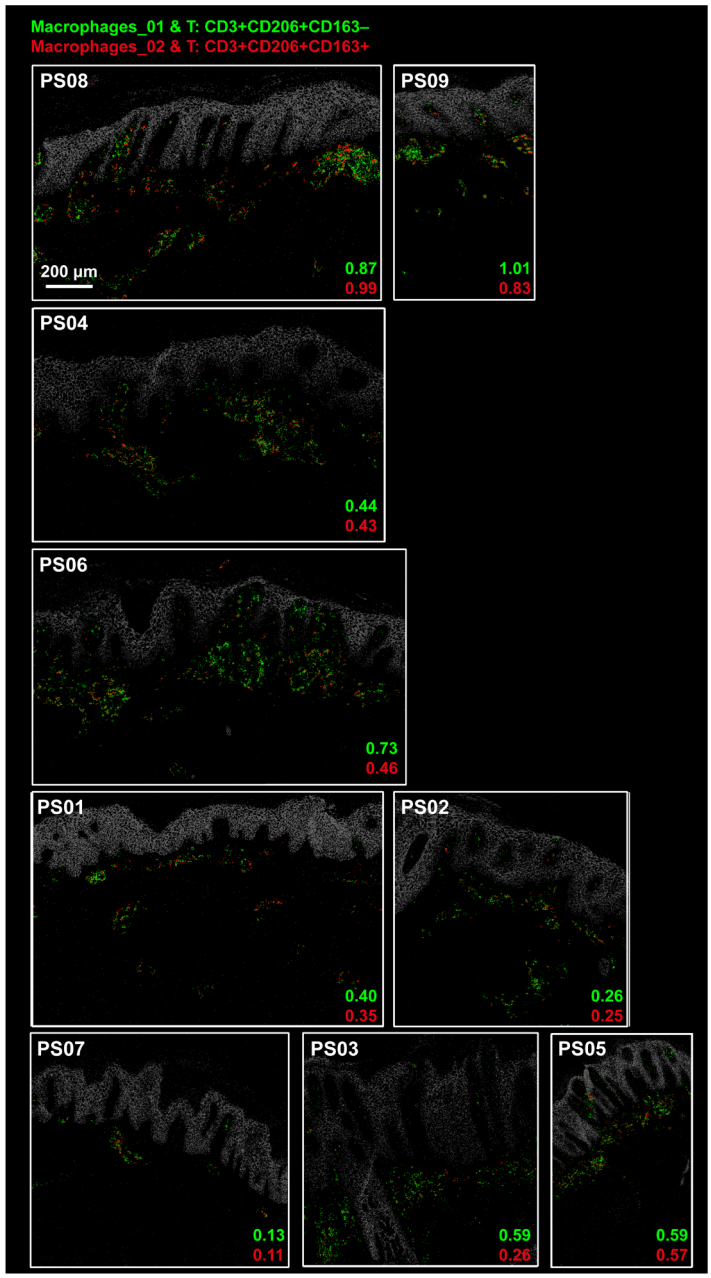

Figure S2. Visualization of two pixel-clusters harboring features of T cells and macrophages in lesional skin samples from psoriasis patients.

Chapter 6

Summarizing discussion

In recent years, single-cell mass cytometry (CyTOF) has been used to simultaneously examine the expression of surface and intracellular proteins on single cell suspensions isolated from blood and tissue samples, to reveal disease-associated immune characteristics and identify functional biomarkers and therapeutic targets of disease[1, 2, 3, 4]. In addition, imaging mass cytometry (IMC) has been developed to enable multiplexed detection of proteins to delineate spatial cellular interactions and immune system heterogeneity in the tissue context[5, 6]. In this thesis, we have introduced the adoption of IMC on snap-frozen tissues. For this we developed a dedicated antibody panel, optimized the staining procedure, validated staining quality, and performed basic analysis of datasets by MCD™ Viewer, followed by downstream analysis based on pixels. IMC with a 36-marker panel was applied on human fetal intestine to investigate immune system development during the second trimester. Moreover, to investigate disease-associated immune subsets, IMC with a dedicated antibody panel was performed on skin biopsies from patients suffering from mycosis fungoides or psoriasis. Here, we aimed to determine whether there is a correlation between clinical parameters and IMC findings.

Imaging mass cytometry and data analysis

To enable IMC on snap-frozen tissues, we optimized the staining protocol for a 34-marker panel to obtain a high signal/noise ratio while preserving the morphology of the tissue samples. For this, we used immunohistochemistry for the primary selection of suitable antibodies. In addition, we determined the optimal drying time of the freshly cut tissue sections, compared fixation procedures, and investigated the optimal incubation condition for each of the antibodies in the panel (**Chapter 2**). Guided by the DNA (Intercalator-Ir) signal and the signal/noise ratio of each marker in MCD™ Viewer software, we determined on the optimal staining methods for the full IMC antibody panel for analysis of snap-frozen human fetal intestinal samples. In addition, this protocol was adapted for optimal performance when applied to skin tissue samples.

Multiplexed imaging data can be analyzed by visualization of the individual markers and overlays of several markers with different colors to reveal the tissue architecture and the spatial distribution and interactions between different cell types (**Chapter 2-5**). Moreover, several computational approaches have been developed to analyze all markers in the panel simultaneously, such as HistoCAT[7] and ImaCytE[8]. To extract single-cell data from the images, single cells are generated by using cell segmentation masks Ilastik and CellProfiler. To normalize variations in signal intensity and background between samples, a normalization strategy

for the processing of IMC data is applied prior to analysis by high-dimensional reduction tools[9]. Once imaging data have been segmented, downstream analysis by several approaches/algorithms can be used to identify immune and non-immune cells, the abundance of cell subsets, and the cellular neighborhoods in which these cells are present in health and disease[10, 11, 12].

We also have applied the optimized segmentation workflow to process the IMC datasets on skin biopsies of patients with psoriasis in **Chapter 5**. By comparing the DNA staining with the cell segmentation we observed that this approach is unable to accurately segment regions with a high cellular density, impacting on the cell phenotype identification and cell-cell interaction analysis (**Figure 1**). However, as such areas with dense immune infiltrates are likely to reflect disease-related cellular interactions it is important to gain more information on the composition of these immune infiltrates. For this we developed *Cytosplore imaging* to analyze the IMC data at the pixel level, by which we were able to identify and quantify individual cell types within these aggregates (**Chapter 2 and 5**). Moreover, pixel analysis enables the identification of so-called double-feature pixels, pixels containing markers of two cell types, like T cells and APCs, and thus most likely reflecting co-localization of T cells and APCs (**Chapter 5**), both potential diagnostic/therapeutic targets in both intestinal and skin diseases. Moreover, this feature of the pixel-based analysis provides semi-quantitative data on cell-cell interactions, which can be further explored by texture-aware dimensionality reduction methods to analyze spatial pixel neighborhoods by distance measures in future work[13].

The human fetal intestine

To study the development of the human fetal intestine, we applied spectral flow cytometry together with IMC to human fetal intestinal samples from week 14 through week 22 of gestation. With spectral flow cytometry, we identified distinct populations of Ki-67 expressing cells within all major immune subsets present in the samples. Moreover, the percentage of Ki-67$^+$ cells in these immune subsets remained constant throughout the second trimester of gestation, suggesting that there is a continuous pool of proliferating cells to populate the growing fetal intestine. Since the majority of the immune cells in the fetal intestine expressed CD127 (IL-7 receptor, IL-7R), IL-7 was used to stimulate the fetal immune cells to investigate the proliferative potential *in vitro*. Here we observed proliferation of fetal immune cells that was enhanced by the presence of IL-7 and accompanied by upregulation of CD40L and granzyme B expression, providing evidence that the observed Ki-67 expression reflected proliferative potential of fetal intestinal

immune cells. In addition, we performed RNAscope analysis which allows the visualization of selected RNA molecules with high sensitivity *in situ*[14]. Here, we observed the presence of IL-7 transcripts in both the lamina propria and epithelium of a human fetal intestinal sample from gestational week 14 (**Figure 2A-C**), suggesting that fetal intestinal cells can produce IL-7 during fetal development supporting immune cell proliferation. Future elucidation of the cell types producing IL-7 in the human fetal intestine would require a combination of RNAscope and IMC. This combination of techniques has been successfully applied to chemokine expression analysis in tumor samples[15] and should be feasible to be used for analysis of the human fetal intestine as well. This will be the subject of further studies.

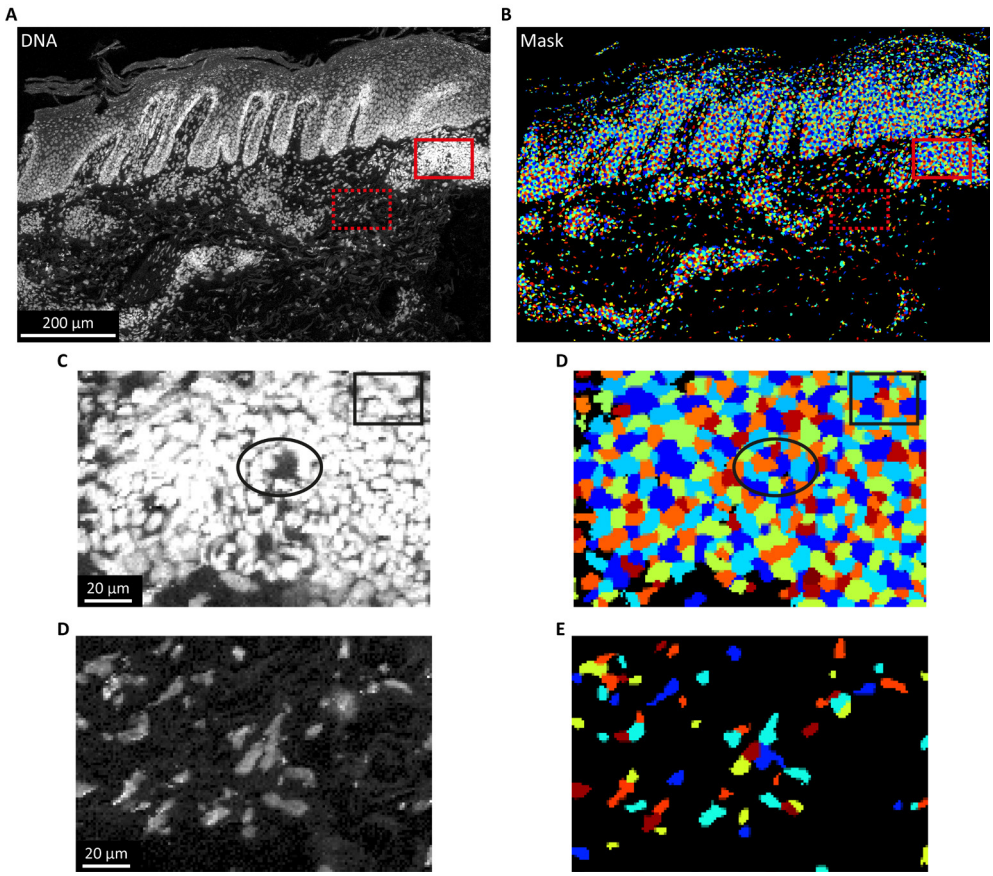

Figure 1 Generation of single cell masks in a representative ROI from a psoriatic lesion. (A) DNA staining performance colored by white in MCD™ viewer. A region with high-density cells is boxed by the solid line, while a region with low-density cells boxed by a dashed line. **(B)** Single cell masks by Ilastic and CellProfiler. Colors are used for visualization of individual cells. **(C-D)** DNA staining and cell mask for the region with high cellular density. **(E-F)** DNA staining and cell mask for the region with low cellular density.

IMC identified formation of lymphoid follicles (LFs) in the developing intestine just below the epithelium from week 16 onwards, harboring B cells, T cells, ILCs and myeloid cells. Also, Ki-67 positive cells were detected in all major immune subsets both in the LF and in the lamina propria. As described previously, the chemokine CXCL13 has an important role in the formation of secondary lymphoid organs by mediating the influx of mature lymphocytes into the newly forming follicles and regulating the recruitment of LTi cells[16]. CXCL13 expression has also been detected in lymphoid follicles present in inflamed tissue sites, for example ulcerative colitis[17]. RNAscope analysis of the human fetal intestine revealed the presence of CXCL13 in the lamina propria of a human fetal intestinal sample from gestational week 14 (**Figure 2D**), where the location and distribution of the CXCL13 signal fits with the location and distribution of lymphoid follicles identified by IMC. Further investigations are needed to explore the role of CXCL13 in the formation of lymphoid follicles in the developing fetal intestine.

Moreover, our IMC data revealed abundant expression of CD161 and CD69 in the LF of human fetal intestines (**Chapter 3**). In addition, further analysis by spectral flow cytometry showed that $CD161^{+}CD69^{+}$ T and $CD3^{-}CD7^{+}$ ILCs cells co-expressed CD117, CD127 and CCR6 (**Chapter 3**). These data fit with the observation that in the murine small and large intestinal mucosa a large fraction of closely packed lymphocytes in cryptopatches expressed CD117 and CD127, pointing to the presence of T and/or B lympho-hemopoietic progenitors[18]. Moreover, our data indicate that a subset of $CD161^{+}CD69^{+}CD117^{+}CD127^{+}CCR6^{+}$ cells expressed Ki-67, compatible with cellular proliferation. Additional work is needed to determine whether these Ki-67^{+} cells represent a stable subset or a transitional phenotype in the human fetal intestine.

Formation of $CD4^{+}$ T cell memory in the human fetal intestine

Previously, we revealed the presence of memory $CD4^{+}$ and $CD8^{+}$ T cells in human fetal intestine[19], suggesting *in utero* exposure to foreign antigens. Additional observations showed that memory formation was associated with several signaling pathways, including that of the T cell receptor. However, whether fetal T cells are exposed to foreign antigens is still a matter of debate. In this thesis we have expanded on our initial observations by studying the proliferative capacities of the fetal intestinal immune compartment across the second gestational trimester. We have also described for the first time the formation of organized lymphoid structures in the fetal intestine (**Chapter 3**).

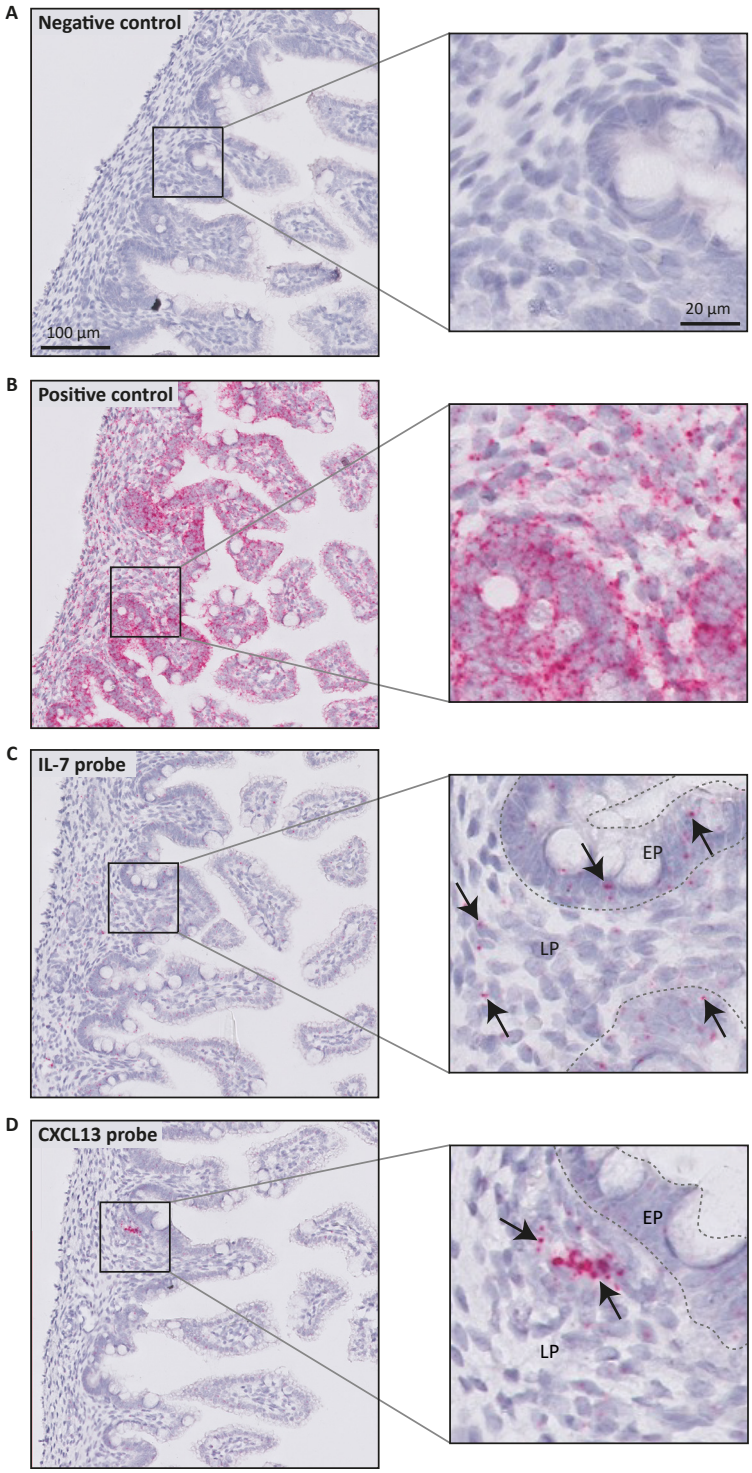

Figure 3 RNAscope detection of RNA in a FFPE human fetal intestinal sample from gastational week 14.
(A) Negative control *PPIB* probe.
(B) Positive control *DapB* probe.
(C) IL-7 probe.
(D)CXCL13 probe.
Nuclei were counterstained with hematoxylin.
EP, epithelium;
LP, lamina propria.

With these new data in mind, we can envision two scenarios for the *in utero* formation of CD4⁺ T cell memory (**Figure 3**):

1) Naive CD4⁺ T cells migrate from the thymus to mucosal inductive sites (Mesenteric lymph nodes or LFs in the lamina propria), where they encounter antigen-presenting DCs and differentiate into mucosal-imprinted memory T cells, as has been described for adult intestinal mucosa[20, 21, 22]. Then they migrate to effector sites in the fetal intestine.
2) Naive CD4⁺ T cells migrate directly from the thymus to the fetal intestinal lamina propria, where they encounter abundant proliferation signals that lead to their expansion and acquisition of a memory-like phenotype, as has been described for lymphopenia-induced proliferation[23, 24, 25].

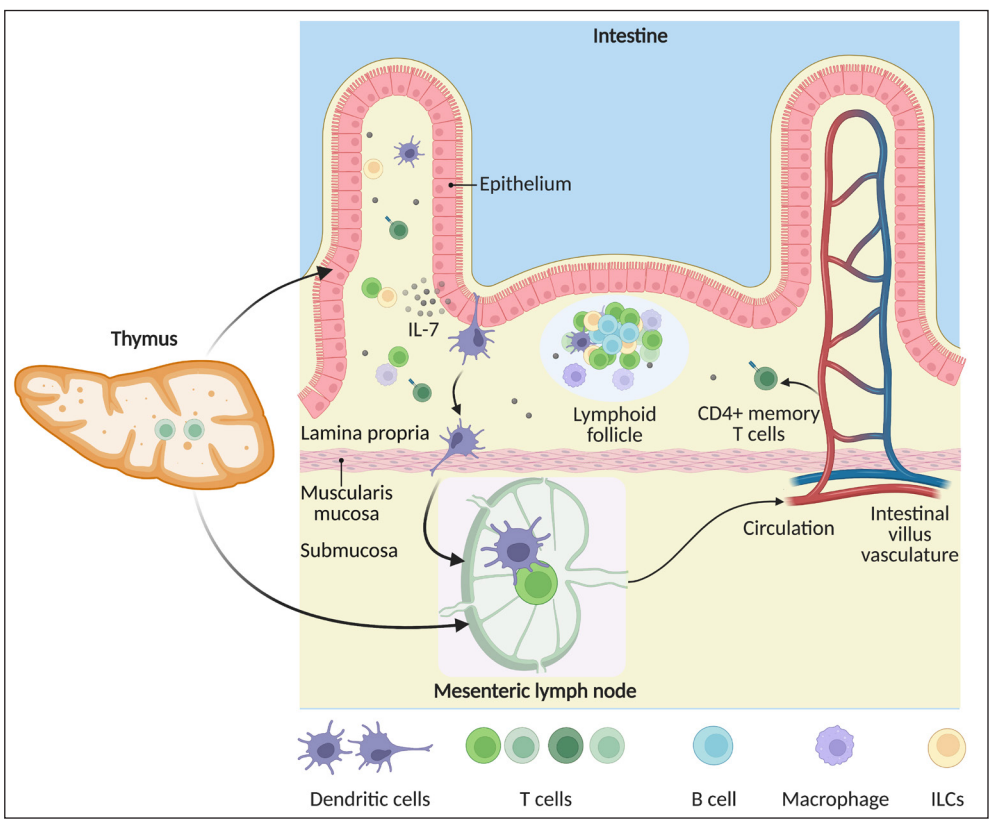

Figure 3. Depiction of memory formation in human fetal intestines. Created in Biorender.com.

Scenario 1: Memory formation at induction sites

For the first scenario to be plausible, two conditions have to be met. First, mature

inductive sites where DCs and naïve T cells can meet have to be present. Second, foreign antigen has to be available for the DCs to present.
Mesenteric lymph nodes (MLNs) are key sites for the generation of memory T cells with mucosal imprinting[26, 27]. What do we know about the timeline of human MLN development? In the human fetus, T lymphocyte differentiation is initiated in the thymus at 7-9 post-gestational weeks (PGW), and the first TCRab T cells leave the thymus by 12PGW[28]. The first lymphoid cells can be found in the lymph node (LN) primordium at 12 PGW, while monocytes and macrophages can be found from 13 PGW onwards[29]. In the 14 PGW, lymphoid cells with features of immature precursor-type thymocytes gradually fill in the cortex of the LNs[30], indicating that these cells migrate directly from the thymus to LNs. In the human fetus, MLNs can be detected as early as 13 PGW[31]. Although not determined yet for MLNs, in axillary LNs at 14 PGW, $CD4^+$ T cells are distributed throughout the anlage[32]. Meanwhile, B cells are found mainly in the outer cortex, although not yet organized in follicles, and during subsequent weeks, loosely aggregated primary follicles emerge[32, 33]. This timeline coincides with the gradual filling of LFs in the fetal intestine described in **Chapter 3**, and suggests that mucosal inductive sites develop throughout the entire second gestational trimester, and points to a plausible interaction between T cells and DCs. In support of this, in **Chapter 2**, T cells were detected in close proximity to $CD11c^+$ myeloid cells and $CD163^+$ macrophages in the lamina propria of human fetal intestines, supporting antigen uptake and presentation by myeloid cells. In **Chapter 3**, we identified proliferating naïve and memory T cells, as well as $CD1c^+$ B cells and lymphoid tissue inducer cells by suspension flow cytometry from 14 PGW onwards. Moreover, IMC analysis of human fetal intestines showed the presence of locally proliferating cells within lymphoid follicles and lamina propria as early as 16 PGW. Although the nature of the antigen is yet to be determined, the spatial distribution of T cells and APCs in the LFs supports the hypothesis of LFs as mucosal inductive sites.

Scenario 2: Lymphopenia-like expansion of naïve T cells, with acquisition of a memory-like phenotype

T cell survival and proliferation depend on availability of cytokines provided by other cell types (e.g. epithelial cells, stromal cells). Gamma-chain cytokines (including IL-2, IL-4, IL-7, IL-9 and IL-15), which share the common gamma chain cytokine receptor subunit, play an essential role in maintaining T cell memory[34], especially IL-7[35]. In LNs, the expression of IL-7 together with the CCR7 ligands (CCL19 and CCL21) by fibroblastic reticular cells attracts $CCR7^+$ T cells and provides signals for their survival[36]. Our data reveals that IL-7 can induce proliferation of naïve and memory T cells of human fetal intestine in vitro. Moreover, IL-7 transcript can

be found in both the epithelium and lamina propria in the human fetal intestine (Figure 3C). Thus, the formation of T cells with a memory phenotype in the fetal intestine can also be due to cytokine-driven expansion to populate the growing organ.

In summary, at the moment we could find evidence supporting both scenarios. Future studies are needed to further elucidate the contribution of APCs in LFs and IL-7 to the generation of memory-like $CD4^+$ T cells in the human fetal intestine.

Possible improvements of diagnostic process for Mycosis Fungoides

Currently, the diagnosis of mycosis fungoides (MF) is based on immunopathological criteria, that helps with determining the atypical lymphocytes suggestive for "cancer cells". Besides an atypical form, atypical lymphocytes show loss of immunophenotypic markers like CD2, CD3, CD5 and/or CD7 (**Table 1**)[37]. Nevertheless, some reactive dermatitis may have an atypical reactive infiltrate with marker loss like CD7, making it difficult to diagnose MF at an early stage. In those cases T-cell clonality might help, but is not entirely conclusive. For improvement of the current diagnostic process, it may be helpful if we understand the tumor microenvironment in more detail, to help in differentiating a tumor microenvironment from a reactive microenvironment. New techniques including single-cell suspension mass cytometry (CyTOF) and imaging mass cytometry (IMC) can facilitate the understanding of this microenvironment in more detail.

Table 1 Immunopathologic algorithm for diagnosis of early MF. (Table adapted from Pimpinelli et al. 2005)

Immunopathologic Criteria	**Scoring system**
1) < 50% $CD2^+$, $CD3^+$, and/or $CD5^+$ T cells	1 point for one or more criteria
2) < 10% $CD7^+$ T cells	
3) Epidermal/dermal discordance of CD2, CD3, CD5, or CD7	

In **Chapter 4**, we used CyTOF and IMC to profile the tissue resident immune cells of 10 patients with early stage of mycosis fungoides. Based on single-cell suspension data in **Chapter 4**, the shared clusters of $CD5^+CD127^+$ effector memory T cells and $CD5^+CD127^-CD25^+$ Treg-like cells were identified among these early stage MF patients. Furthermore, $CD11c^+CD14^+$ myeloid cells and $HLA\text{-}DR^+CD1a^+$ DCs were observed in the majority of MF patients. In addition, IMC revealed the co-localization of T cells with phenotypically distinct subsets of dendritic cells

(DCs) in immune aggregates in the dermis of MF patients. Altogether, these new insights might provide a basis for further studies aiming to distinguish the MF microenvironment from that in reactive dermatitis. Furthermore, a study with larger sample sizes and healthy controls will be needed to elucidate the possible prognostic value of interfering T-DCs interactions in MF.

In addition, several reports have shown that up to 15% of early-stage patients experience disease progression to advanced stage MF with an estimated 5-year survival of 24%[38, 39]. In early stage of MF, CXCR3 as interferon (IFN)-inducible chemokine receptor, induced by the IFN-γ, was up-regulated in malignant lymphocytes[40, 41]. In the advanced stage of MF, however, malignant T cells expressed more CCR4 than CXCR3[42]. As CCR4 has been described as the receptor for CCL22, primarily produced by DCs in dermis, it is likely that the interaction between CCR4 and CCL22 is involved in DCs-T stimulation[43]. Recently, scRNAseq analysis for skin tumor cells from patient with advanced stage MF revealed that malignant tumor infiltrating T lymphocytes highly expressed genes related to cell cycle progression and proliferation, and checkpoint molecules including TIM3, PD1, LAG3 and CTLA-4[44]. Moreover, gene expression profiling corroborated positive correlations between increased expression of checkpoint inhibitors and higher tumor stage of disease[45]. So it might be very useful to use CyTOF and IMC to evaluate the expression patters of these chemokine receptors and ligands, and markers indicative of cell regulation and proliferation in future experiments as well to gain better insight into the factors that play a role in the progression of early stage MF to advanced stage MF, results that may be useful for the development of better prognostics and targeted therapeutics in the future.

Future perspectives of psoriasis

Psoriasis is a chronic inflammatory skin disorder characterized by keratinocyte hyperproliferation and differentiation combined with immune cell infiltration. It is known that in the psoriatic dermis mature myeloid dendritic cells (DCs) aggregate with skin infiltrating T cells[46, 47]. Here, IL-23/IL-20-producing DCs have the potential to activate Th17 cells in psoriasis[48], causing the proliferation seen within psoriatic lesions[49]. Moreover, pathogenic Th17 cells are sustained by IL-23 within the dermis[50, 51]. In addition, keratinocytes produce additional cytokines, such as IFN-α, IL-6, and IL-10, resulting in epidermal hyperplasia[52, 53].

In **Chapter 5**, we applied imaging mass cytometry to compare lesional skin with non-lesional skin from patients with psoriasis in a proof of principle study

to determine if it would be useful to apply this technique to gain further insight into the cellular interactions that underlie psoriasis. We observed that psoriatic lesions contained prominent immune aggregates with many T cells and DCs in the dermis. Moreover, multiple types DCs subsets were observed. For more detailed analysis of the results we made use of pixel-based which allowed the visualization of the structure of psoriatic skin and the distribution and quantification of T and myeloid cell subsets. Moreover, this approach identified clusters of pixels presenting with features of both T cells and myeloid cells, likely representing direct contact between T cells and myeloid cells. This identified patients displaying frequent interactions between T cells and $CD207^{+}CD1c^{+}$ LC-like DCs in the dermis. In addition, interactions between T cells and $CD207^{-}CD1c^{+}$ DCs and between T cells and $CD206^{+}$ macrophages were observed but these varied substantially between patients. This allowed a preliminary classification of patients based on the presence of particular cell subtypes and interactions between those cell subtypes. However, further work is required determine if this relates to disease severity. It will be particularly rewarding to investigate if such differences between patients correlate to response to treatment and as such may be useful to distinguish potential responders to treatment. Moreover, it may provide leads for the development of novel therapeutic strategies.

Concluding remarks

In conclusion, the work described in this thesis demonstrates that imaging mass cytometry can provide novel information on the nature and organization of the immune system within the tissue context at barrier sites like the human intestine and skin. Our work on the human fetal intestine shows that in combination with single cell technologies this revealed a prominent role for IL-7-driven local immune cells proliferation to allow for the formation of complex organized lymphoid follicles and to fill up the immune system in the rapidly growing organ. Our work on mycosis fungoides and psoriasis indicates that imaging mass cytometry can be used to identify both disease-specific and patient-specific patterns in the composition and local organization of the immune system. Further work is needed to determine if this will be useful for patient classification and to predict response to treatment.

Reference

1. Hartmann, F.J. *et al.* High-dimensional single-cell analysis reveals the immune signature of narcolepsy. *Journal of Experimental Medicine* **213**, 2621-2633 (2016).
2. Irish, J.M. *et al.* Single Cell Profiling of Potentiated Phospho-Protein Networks in Cancer Cells. *Cell* **118**, 217-228 (2004).
3. Bruggner, R.V., Bodenmiller, B., Dill, D.L., Tibshirani, R.J. & Nolan, G.P. Automated identification of stratifying signatures in cellular subpopulations. *Proceedings of the National Academy of Sciences* **111**, E2770-E2777 (2014).
4. de Vries, N.L. *et al.* High-dimensional cytometric analysis of colorectal cancer reveals novel mediators of antitumour immunity. *Gut* **69**, 691-703 (2020).
5. Schulz, D. *et al.* Simultaneous Multiplexed Imaging of mRNA and Proteins with Subcellular Resolution in Breast Cancer Tissue Samples by Mass Cytometry. *Cell Syst* **6**, 25-36.e25 (2018).
6. Giesen, C. *et al.* Highly multiplexed imaging of tumor tissues with subcellular resolution by mass cytometry. *Nature Methods* **11**, 417-422 (2014).
7. Schapiro, D. *et al.* histoCAT: analysis of cell phenotypes and interactions in multiplex image cytometry data. *Nature Methods* **14**, 873-876 (2017).
8. Somarakis, A., Unen, V.V., Koning, F., Lelieveldt, B. & Höllt, T. ImaCytE: Visual Exploration of Cellular Micro-Environments for Imaging Mass Cytometry Data. *IEEE Transactions on Visualization and Computer Graphics* **27**, 98-110 (2021).
9. Ijsselsteijn, M.E., Somarakis, A., Lelieveldt, B.P.F., Höllt, T. & de Miranda, N. Semi-automated background removal limits data loss and normalizes imaging mass cytometry data. *Cytometry A* **99**, 1187-1197 (2021).
10. Damond, N. *et al.* A Map of Human Type 1 Diabetes Progression by Imaging Mass Cytometry. *Cell Metab* **29**, 755-768.e755 (2019).
11. Keren, L. *et al.* A Structured Tumor-Immune Microenvironment in Triple Negative Breast Cancer Revealed by Multiplexed Ion Beam Imaging. *Cell* **174**, 1373-1387.e1319 (2018).
12. Krop, J. *et al.* Imaging mass cytometry reveals the prominent role of myeloid cells at the maternal-fetal interface. *iScience* **25**, 104648 (2022).
13. Vieth, A., Vilanova, A., Lelieveldt, B., Eisemann, E. & Höllt, T. Incorporating Texture Information into Dimensionality Reduction for High-Dimensional Images. 2022 IEEE 15th Pacific Visualization Symposium (PacificVis); 2022: IEEE; 2022. p. 11-20.
14. Wang, F. *et al.* RNAscope: a novel in situ RNA analysis platform for formalin-fixed, paraffin-embedded tissues. *J Mol Diagn* **14**, 22-29 (2012).
15. Hoch, T. *et al.* Multiplexed imaging mass cytometry of the chemokine milieus in melanoma characterizes features of the response to immunotherapy. *Sci Immunol* **7**, eabk1692 (2022).
16. Marchesi, F. *et al.* CXCL13 expression in the gut promotes accumulation of IL-22-producing lymphoid tissue-inducer cells, and formation of isolated lymphoid follicles. *Mucosal Immunol* **2**, 486-494 (2009).
17. Carlsen, H.S., Baekkevold, E.S., Johansen, F.E., Haraldsen, G. & Brandtzaeg, P. B cell attracting chemokine 1 (CXCL13) and its receptor CXCR5 are expressed in normal and aberrant gut associated lymphoid tissue. *Gut* **51**, 364-371 (2002).
18. Kanamori, Y. *et al.* Identification of novel lymphoid tissues in murine intestinal mucosa where clusters of c-kit+ IL-7R+ Thy1+ lympho-hemopoietic progenitors develop. *J Exp Med* **184**, 1449-1459 (1996).
19. Li, N. *et al.* Memory CD4(+) T cells are generated in the human fetal intestine. *Nat Immunol* **20**, 301-312 (2019).
20. Buettner, M. & Bode, U. Lymph node dissection--understanding the immunological function of lymph nodes. *Clin Exp Immunol* **169**, 205-212 (2012).
21. Houston, S.A. *et al.* The lymph nodes draining the small intestine and colon are anatomically separate and immunologically distinct. *Mucosal Immunol* **9**, 468-478 (2016).
22. Iwata, M. *et al.* Retinoic acid imprints gut-homing specificity on T cells. *Immunity* **21**, 527-538 (2004).
23. Min, B. *et al.* Neonates support lymphopenia-induced proliferation. *Immunity* **18**, 131-140 (2003).
24. Guimond, M. *et al.* Interleukin 7 signaling in dendritic cells regulates the homeostatic proliferation and niche size of CD4+ T cells. *Nat Immunol* **10**, 149-157 (2009).
25. Surh, C.D. & Sprent, J. Homeostasis of naive and memory T cells. *Immunity* **29**, 848-862 (2008).
26. Huang, F.P. *et al.* A discrete subpopulation of dendritic cells transports apoptotic intestinal epithelial cells to T cell areas of mesenteric lymph nodes. *J Exp Med* **191**, 435-444 (2000).
27. Sheridan, B.S. & Lefrançois, L. Regional and mucosal memory T cells. *Nat Immunol* **12**, 485-491 (2011).
28. Lobach, D.F. & Haynes, B.F. Ontogeny of the human thymus during fetal development. *J Clin Immunol* **7**, 81-97 (1987).
29. Markgraf, R., von Gaudecker, B. & Müller-Hermelink, H.K. The development of the human lymph node. *Cell and Tissue Research* **225**, 387-413 (1982).
30. von Gaudecker, B. & Müller-Hermelink, H.K. The development of the human tonsilla palatina. *Cell Tissue Res* **224**, 579-600 (1982).

31. Cupedo, T., Nagasawa, M., Weijer, K., Blom, B. & Spits, H. Development and activation of regulatory T cells in the human fetus. *Eur J Immunol* **35**, 383-390 (2005).
32. Asano, S. *et al.* Immunohistologic detection of the primary follicle (PF) in human fetal and newborn lymph node anlages. *Pathol Res Pract* **189**, 921-927 (1993).
33. Westerga, J. & Timens, W. Immunohistological analysis of human fetal lymph nodes. *Scand J Immunol* **29**, 103-112 (1989).
34. Lantz, O., Grandjean, I., Matzinger, P. & Di Santo, J.P. Gamma chain required for naïve CD4+ T cell survival but not for antigen proliferation. *Nat Immunol* **1**, 54-58 (2000).
35. Tan, J.T. *et al.* IL-7 is critical for homeostatic proliferation and survival of naive T cells. *Proc Natl Acad Sci U S A* **98**, 8732-8737 (2001).
36. Link, A. *et al.* Fibroblastic reticular cells in lymph nodes regulate the homeostasis of naive T cells. *Nature Immunology* **8**, 1255-1265 (2007).
37. Pimpinelli, N. *et al.* Defining early mycosis fungoides. *J Am Acad Dermatol* **53**, 1053-1063 (2005).
38. Talpur, R. *et al.* Long-term outcomes of 1,263 patients with mycosis fungoides and Sézary syndrome from 1982 to 2009. *Clin Cancer Res* **18**, 5051-5060 (2012).
39. Scarisbrick, J.J. *et al.* Cutaneous Lymphoma International Consortium Study of Outcome in Advanced Stages of Mycosis Fungoides and Sézary Syndrome: Effect of Specific Prognostic Markers on Survival and Development of a Prognostic Model. *J Clin Oncol* **33**, 3766-3773 (2015).
40. Lu, D. *et al.* The T-cell chemokine receptor CXCR3 is expressed highly in low-grade mycosis fungoides. *Am J Clin Pathol* **115**, 413-421 (2001).
41. Kuo, P.T. *et al.* The Role of CXCR3 and Its Chemokine Ligands in Skin Disease and Cancer. *Front Med (Lausanne)* **5**, 271 (2018).
42. Sugaya, M. Chemokines and cutaneous lymphoma. *J Dermatol Sci* **59**, 81-85 (2010).
43. Wu, M., Fang, H. & Hwang, S.T. Cutting edge: CCR4 mediates antigen-primed T cell binding to activated dendritic cells. *J Immunol* **167**, 4791-4795 (2001).
44. Gaydosik, A.M. *et al.* Single-Cell Lymphocyte Heterogeneity in Advanced Cutaneous T-cell Lymphoma Skin Tumors. *Clin Cancer Res* **25**, 4443-4454 (2019).
45. Querfeld, C. *et al.* Primary T Cells from Cutaneous T-cell Lymphoma Skin Explants Display an Exhausted Immune Checkpoint Profile. *Cancer Immunol Res* **6**, 900-909 (2018).
46. Zaba, L.C. *et al.* Amelioration of epidermal hyperplasia by TNF inhibition is associated with reduced Th17 responses. *J Exp Med* **204**, 3183-3194 (2007).
47. Kim, T.-G. *et al.* Dermal Clusters of Mature Dendritic Cells and T Cells Are Associated with the CCL20/CCR6 Chemokine System in Chronic Psoriasis. *Journal of Investigative Dermatology* **134**, 1462-1465 (2014).
48. Wang, F. *et al.* Prominent production of IL-20 by CD68+/CD11c+ myeloid-derived cells in psoriasis: Gene regulation and cellular effects. *J Invest Dermatol* **126**, 1590-1599 (2006).
49. Schön, M.P. & Boehncke, W.-H. Psoriasis. *New England Journal of Medicine* **352**, 1899-1912 (2005).
50. Lee, Y. *et al.* Induction and molecular signature of pathogenic TH17 cells. *Nature Immunology* **13**, 991-999 (2012).
51. Lowes, M.A., Russell, C.B., Martin, D.A., Towne, J.E. & Krueger, J.G. The IL-23/T17 pathogenic axis in psoriasis is amplified by keratinocyte responses. *Trends in Immunology* **34**, 174-181 (2013).
52. Page, K.M. *et al.* Molecular and Cellular Responses to the TYK2/JAK1 Inhibitor PF-06700841 Reveal Reduction of Skin Inflammation in Plaque Psoriasis. *J Invest Dermatol* **140**, 1546-1555. e1544 (2020).
53. Sohn, S.J. *et al.* A restricted role for TYK2 catalytic activity in human cytokine responses revealed by novel TYK2-selective inhibitors. *J Immunol* **191**, 2205-2216 (2013).

Appendices

Summary in English

Imaging mass cytometry

Imaging mass cytometry (IMC) is an extension of CyTOF technology with a laser ablation system, which can be applied on snap-frozen tissue slides and archived paraffin slides. Like in single cell mass cytometry, the technique makes use of metal-labelled antibodies to allow the incorporation of a high number of antibodies simultaneously.

In **Chapter 2**, the optimal staining procedures for IMC on snap-frozen tissue slides from fetal and adult intestinal samples were developed to visualize the tissue architecture and the spatial distribution of the stromal and immune cells. Moreover, in **Chapter 3**, we built up the *Cytosplore Imaging* platform to analyze dense immune infiltrates identified within the IMC images. This allowed for the identification and detailed characterization of lymphoid follicles in the fetal intestine that are composed of B cells, T cells, $CD3^{-}CD7^{+}$ ILCs and myeloid cells and found just below the epithelium in the developing intestine. Moreover, there was abundant co-expression of CD69 and CD161 in lymphoid follicles of the human fetal intestine.

In **Chapter 4**, an IMC dataset on normal skin samples and skin samples from patients with mycosis fungoides were acquired and analyzed to obtain a global overview of the distribution of $CD4^{+}$ T cells, Tregs, $CD8^{+}$ T cells, malignant T cells, and various myeloid cell subsets. Here we observed distinct clusters of $CD4^{+}$ T cells and multiple types of dendritic cells identified through differential expression of CD11c, CD1a and CD1c in the dermis of MF skin.

In **Chapter 5**, IMC was used to compare major immune compartments in non-lesional and lesinal skin from psoriasis patients. The analysis based on pixels in *Cytosplore Imaging* quantified the number of pixels per immune cell subset (the area of per immune cell subset) and demonstrated a significant increase of $CD4^{+}$ and $CD8^{+}$ T cells, macrophages and mast cells in lesional skin, while no significant differences were observed for the dendritic cell subsets. Moreover, the analysis of the IMC dataset at the pixel level revealed the presence of pixels harboring expression of both T and myeloid cell markers, so-called double feature pixels, most likely representing close interactions between these cell subsets.

Development of the human fetal intestinal immune system

In **Chapter 3**, we have used a combination of spectral flow cytometry, imaging mass cytometry and RNAscope to obtain detailed insight into the composition and spatial organization of the developing fetal intestinal immune system throughout the second trimester of gestation.

The spectral flow cytometry analysis readily identified all major immune subsets and heterogeneity therein in the developing human fetal intestines in time. Moreover, this identified stable clusters of Ki-67 expressing cells within all identified immune subsets that remained present in time. Also, imaging mass cytometry identified the formation of lymphoid follicles just below the epithelium in the developing intestine from week 16 onwards, harboring B cells, T cells, $CD3^{-}CD7^{+}$ ILCs and myeloid cells and confirmed the presence of Ki-67^{+} cells in the various immune subsets *in situ*. This also identified the presence of $CD1c^{+}$ B cells and $ROR\gamma t^{+}CD117^{+}CD127^{+}$ LTi- like cells, compatible with the formation of lymphoid follicles the human fetal intestine. Moreover, the presence of CXCL13 mRNA transcripts *in situ* provided further evidence for the formation of such follicles in the developing human fetal intestine.

Finally, we observed that a $CD69^{+}CD117^{+}CD161^{+}CCR6^{+}CD127^{+}$ phenotype was shared by subsets of fetal intestinal $CD3^{-}CD7^{+}$ ILCs and T cells and that these cells preferentially reside in the LFs, and harbor Ki-67^{+} cells, indicating a role in the development of these follicles. *In vitro*, Ki-67^{+} cells in these major immune subsets were capable of spontaneous proliferation, and IL-7 stimulation enhanced the proliferation of these cells. Together with the demonstration of the presence of IL-7 mRNA transcripts in both the lamina propria and epithelium of the human fetal intestine this supports the hypothesis that IL-7 plays an important role in the development of the human fetal intestinal immune system.

These observations indicate the presence of immune subset-committed cells capable of local proliferation, contributing to the development and growth of organized immune structures throughout the 2^{nd} trimester in the human fetal intestine, presumably preparing the infant for the microbial colonization right after birth.

The immune system in skin diseases

Mycosis Fungoides

In **Chapter 4**, we aimed to gain a better understanding of the immune microenvironment in early stage mycosis fungoides (MF). We applied both single-cell and imaging mass cytometry to characterize the immune composition in individual patients. We observed shared $CD4^+$ T cell and myeloid cell subsets in all patients while unique subsets to particular patients were identified as well imaging mass cytometry revealed dense aggregates of T cells with various dendritic cell types in the dermis, likely implied in the disease pathogenesis and representing a potential target for treatment. These results might be helpful for improved diagnosis and personalized treatment of patients with mycosis fungoides.

Psoriasis

In **Chapter 5,** we applied imaging mass cytometry to investigate immune infiltration in patients with mild to moderate psoriasis. The *Cytosplore Imaging* pixel analysis of the IMC dataset identified distinct composition and organization of the immune compartment lesional skin biopsies as compared to non-lesional skin biopsies. In addition, we identified several clusters of "double feature pixels", indicative of close interactions between T cells and various myeloid/DC cell subsets, and likely linked to disease pathogenesis. Finally, preliminary evidence indicates that the quantity of the "double feature pixels" in a given sample may correlate with the severity of psoriasis, an issue that should be explored in a larger number of patient samples.

Overall, the work described in this thesis demonstrates show that the novel high-dimensional technologies provide unprecedented insight into the composition and spatial organization the barrier immune system in health and diseases.

Nederlandse Samenvatting

Imaging mass cytometry

"Imaging mass cytometry" (IMC) in een uitbreiding op de CyTOF technologie, gekoppeld met een laser ablatie systeem, die gebruikt kan worden voor gevroren en gefixeerde weefselcoupes. Net zoals bij "single cell mass cytometry" wordt er gebruik gemaakt van metaal gelabelde antilichamen, waardoor er met een hoog aantal antilichamen gelijktijdig gekleurd kan worden.

In **hoofdstuk 2** werd het IMC kleuringsprotocol, voor het visualiseren van de weefselarchitectuur en het lokaliseren van stromale en immuun cellen in gevroren weefsel van foetale en volwassen darmsamples ontwikkeld. In **hoofdstuk 3** werd het Cytosplore Imaging-platform opgebouwd om immuun infiltraties te visualiseren die met de IMC-technologie werden gevisualiseerd. Dit maakte het mogelijk om lymfoide structuren, samengesteld uit B-cellen, T-cellen, $CD3^{-}CD7^{+}$ ILC's en myeloïde cellen, te identificeren die zich net onder het epitheel van de foetale darm bevonden. Tevens werd frequent co-expressie van CD69 en CD161 in de lymfoïde structuren gevonden.

In **hoofdstuk 4** werd een IMC-dataset van huidbiopten van gezonde controles en patiënten met mycosis fungoides verkregen en geanalyseerd om een globaal overzicht te verkrijgen van de distributie van de kwaadaardige T-cellen en de heterogeniteit van het immuunsysteem in deze patiënten en controles. We hebben verschillende clusters van $CD4^{+}$ T-cellen en meerdere soorten dendritische cellen kunnen waarnemen door differentiële expressie van CD11c, CD1a en CD1c in de dermis van de MF-huid.

In **hoofdstuk 5** werd IMC gebruikt om de samenstelling van het immuun compartiment in aangedane en niet-aangedane huid van psoriasispatiënten met elkaar te vergelijken. Cytosplore Imaging analyse werd gebruikt voor kwantificering van het aantal pixels per immuun cel populatie en dit toonde een significante toename van $CD4^{+}$ en $CD8^{+}$ T-cellen, macrofagen en mestcellen in de aangedane huid, terwijl er geen significant verschil werd waargenomen voor de dendritische cel populaties. De analyse onthulde ook de aanwezigheid van zogenaamde "double feature pixels" die op pixelniveau kenmerken van zowel T-cellen markers en myeloïde cel markers herbergen, en als zodanig hoogstwaarschijnlijk nauwe interacties tussen deze cel populaties vertegenwoordigen.

Ontwikkeling van het menselijke foetale intestinale immuun systeem

In **hoofdstuk 3** werd een combinatie van spectrale flowcytometrie, IMC en RNAscope gebruikt om een gedetailleerd inzicht te krijgen in de samenstelling en ruimtelijke organisatie van de ontwikkeling van het foetale intestinale immuunsysteem gedurende het tweede trimester van de zwangerschap.

Met de spectrale flowcytometrie analyse konden alle belangrijke immuun celpopulaties, en de heterogeniteit daarin geïdentificeerd worden. Bovendien visualiseerde dit clusters van Ki-67+ cellen binnen alle geïdentificeerde immuun cel populaties, die tijdens het tweede trimester aanwezig bleven, wat duidt op lokale proliferatie van alle immuunpopulaties in de zich ontwikkelende darm.

IMC liet vanaf week 16 de vorming van lymfoïde structuren zien, net onder het epitheel, met daarin B-cellen, T-cellen, $CD3^{-}CD7^{+}$ ILC's en myeloïde cellen, en bevestigde de aanwezigheid van Ki-67^{+} cellen in de verschillende immuunpopulaties *in situ*. Hier werd ook de aanwezigheid van $CD1c^{+}$ B-cellen en $ROR\gamma t^{+}CD117^{+}CD127^{+}$ LTi-achtige cellen, compatibel met de vorming van lymfoïde structuren, geïdentificeerd. Bovendien leverde de aanwezigheid van CXCL13-mRNA-transcripten *in situ* verder bewijs voor de vorming van follikels in de menselijke foetale darm.

Ten slotte werd een $CD69^{+}CD117^{+}CD161^{+}CCR6^{+}CD127^{+}$ fenotype waargenomen die gedeeld werd door populaties van foetale intestinale $CD3^{-}CD7^{+}$ ILC's en T-cellen. Deze cellen werden met name in de lymphoide structuren waargenomen en hebben co-expressie met Ki-67^{+}-cellen, wat wijst op een rol in de ontwikkeling van deze structuren. *In vitro* waren de Ki-67^{+}-cellen in staat tot spontane proliferatie en dit werd versterkt door IL-7-stimulatie. Samen met de aanwezigheid van IL-7 mRNA-transcripten in zowel de lamina propria als het epitheel van de menselijke foetale darm, ondersteunt dit de hypothese dat IL-7 een belangrijke rol speelt in de ontwikkeling van het menselijke foetale intestinale immuunsysteem.

Deze waarnemingen wijzen op de aanwezigheid van gecommitteerde immuuncellen die in staat zijn tot lokale proliferatie, wat bijdraagt aan de ontwikkeling en groei van georganiseerde immuunstructuren gedurende het 2e trimester in de menselijke foetale darm. Vermoedelijk bereidt dit de foetus voor op de microbiële kolonisatie direct na de geboorte.

Het immuun systeem bij huidziekten

Mycosis Fungoides

In **hoofdstuk 4** wilden wij een beter beeld krijgen van de immuun-micro-omgeving in een vroeg stadium van mycosis fungoides (MF). Met behulp van massa cytometrie werd de samenstelling van het immuunsysteem bij individuele patiënten gekarakteriseerd. We observeerden $CD4^+$ T-cellen myeloïde celpopulaties die bij alle patiënten aanwezig waren maar tevens celpopulaties die slecht in sommige patiënten aantoonbaar waren. IMC visualiseerde aggregaten van T-cellen met verschillende soorten dendritische cellen in de dermis, waarschijnlijk betrokken bij de pathogenese van de ziekte en een potentieel doelwit voor behandeling. Deze resultaten kunnen nuttig zijn voor een betere diagnose en gepersonaliseerde behandeling van patiënten met mycosis fungoides.

Psoriasis

In **hoofdstuk 5** hebben we IMC toegepast om immuun infiltratie te onderzoeken bij patiënten met milde tot matige psoriasis. De Cytosplore Imaging pixel analyse van de IMC-dataset identificeerde een verschillende samenstelling en organisatie in het immuun compartiment van de aangedane huidbiopten in vergelijking met de niet-aangedane huidbiopten. Daarnaast hebben we verschillende clusters van "double feature pixels" geïdentificeerd, wat indicatief is voor een interacties tussen T-cellen en verschillende populaties van myeloïde/DC-cellen, en waarschijnlijk gekoppeld aan de pathogenese. Ten slotte werd er preliminair bewijs gevonden dat de kwantiteit van deze "double feature pixels" kan correleren met de ernst van de ziekte. Dit moet in een vervolgstudie nader worden onderzocht.

Al met al toont het werk beschreven in dit proefschrift aan dat de nieuwe hoog-dimensionale technologieën een ongekend inzicht verschaffen in de samenstelling en ruimtelijke organisatie van het immuunsysteem bij gezondheid en ziekte.

Curriculum vitae

Nannan Guo was born on the 25th of June in 1992 in Changchun, China, where she grew up. In 2010, She started her studies Biotechnology at Jilin University in Changchun, and obtained her Bachelor's degree in 2014. She then attended the Biochemistry and Molecular Biology at Jilin University as a master under the supervision of Prof. Ouyang Hongsheng. In 2017, she obtained her master degree with research project on "Screening of the paired heavy chain-light chain gene sequences from a single cell secreting neutralizing antibody of swine fever virus". After obtaining funding for a four-year PhD study abroad from the Chinese scholarship, thereby, she started her PhD study in January 2018 at the department of Immunology (IMMU) at Leiden University Medical Center (LUMC) under the supervision of Prof. Frits Koning.

As described in this thesis, her research focused on investigate immune compartmentalization in the developing human intestine, and lesional/healthy skin tissue from patients with mycosis fungoides and psoriasis by single-cell spectral flow cytometry, suspension mass cytometry, single-cell RNA-sequencing, functional assays, RNAscope and imaging mass cytometry during her PhD study. Since 2021, Nannan collaborated with the group of Prof. Dr. Stephan Weidinger from University Hospital Schleswig-Holstein for clinical trial of Atopic Dermatitis by IL-13 antibody treatment. During her PhD studies, she visited seven conferences related to Immunology, of which she attended four with an oral presentation.

List of publications

Guo N, Li N, Li J, Jiang Q, Schreurs M, van Unen V, Chuva de Sousa Lopes SM, Vloemans SA, Eggermont J, Lelieveldt BPF, Staal FJT, de Miranda NFCC, Pascutti MF, Koning F. Immune subset-committed proliferating cells populate the human foetal intestine throughout the second trimester of gestation.
Nature Communications 2023, 10;14(1):1318

Guo N, Jia L, Out-Luiting C, Miranda N, Willemze R, Koning F, Vermeer M, Quint K. Mass Cytometric Analysis of Early-Stage Mycosis Fungoides.
Cells 2022, 11(7), 1062.

Guo N, van Unen V, Ijsselsteijn ME, Ouboter LF, van der Meulen AE, Chuva de Sousa Lopes SM, de Miranda N, Koning F, Li N. A 34-Marker Panel for Imaging Mass Cytometric Analysis of Human Snap-Frozen Tissue.
Frontiers in Immunology 2020, 11:1466.

Li N, van Unen V, **Guo N**, Abdelaal T, Somarakis A, Eggermont J, Mahfouz A, Chuva de Sousa Lopes SM, Lelieveldt BPF, Koning F. Early-Life Compartmentalization of Immune Cells in Human Fetal Tissues Revealed by High-Dimensional Mass Cytometry.
Frontiers in Immunology 2019, 10:1932.

Li N, van Unen V, Abdelaal T, **Guo N**, Kasatskaya SA, Ladell K, McLaren JE, Egorov ES, Izraelson M, Chuva de Sousa Lopes SM, Höllt T, Britanova OV, Eggermont J, de Miranda NFCC, Chudakov DM, Price DA, Lelieveldt BPF, Koning F. Memory CD4+ T cells are generated in the human fetal intestine.
Nature Immunology 2019, 20:301-312.

Raeber ME, Caspar D, Zurbuchen Y, **Guo N**, Schmid J, Michler J, Steiner UC, Moor AE, Koning F, Boyman O. Interleukin-2 immunotherapy reveals human regulatory T cell subsets with distinct functional and gatekeeper features.
Submitted

Guo N, Schreurs M, Eggermont J, Kieras E, Eleuteri D, Niedecken SC, Ty C, Leieveldt BPF, de Miranda NFCC, Page KM, Koning F. Immune Profiling of Psoriasis by Imaging Mass Cytometry.
In preparation

Acknowledgments

After impressive PhD journey, I would like to express my gratitude to many people for their support and encouragement during my PhD and writing this thesis.

First and foremost, I would like to express my sincere gratitude to my promotor Frits Koning, who gives me the opportunity to perform research in our group at LUMC. You stimulate me to obtain a deeper understanding of human Immunology, and many thanks for your (timely) support and guidance not only in my research within these years, but also in improving my language, dealing with cultural differences, listening to my difficulties encountered in life and always encouraging me a lot with patience.

And my co-promotor M. Fernanda Pascutti, I greatly appreciated your positive attitudes and support towards my research during my PhD study, especially for your expertise in intestinal immune system development. Also my co-promotor Koen Quint, many thanks for your patient guidance and all your supports over the years for the studies of inflammatory skin diseases. I always feel that the dark clouds above my head went away after our meetings; my research questions and confusions were well resolved by receiving your help.

I would like to thanks my collaborators, Noel F. C. C. de Miranda, Bouderwjn Lelieveldt, Frank J. T. Staal, Susana M. Chuva de Sousa Lopes, Maarten Vermeer, Andrea E. van der Meulen, and Karen M Page for sharing your knowledge and insights, which improve my research during this challenging time.

Many thanks to my sweet colleagues, LiNa, JiaLi (my paranymph), Mette (my paranymph), Vincent, Tessa, Laura, Qinyue, Natasja, Yvonne, Munisha, Juliette, Veerle, Emma, Sanne and Ciska in our group. All of you always give me help and encourage me, which makes me feel at home. I am so happy of working together with you, enjoyable for discussion during our weekly data meeting, and chatting during lunch and dinner.

Thanks Marieke, Jeroen, Antonis, Coby, Sandra, Els, Kees and Janine for your selfless experience sharing and kindly help in my research. Thanks Paul for helping with all the problems of my computer and software. I would like to express my sincere thanks to colleagues in the department of Immunology. You help me to get used to the working environment in Netherlands. And many thanks to all operators in FCF. You are always patient to help me solve practical issues when I

measure samples.

In addition, I would like to thank my dear Chinese friends in Leiden, Gangqi, Yan, Zhuang, Jiaxin, Jing, Wenjun, Hongxia, Junling, Ying, Enchen, Wensen, Shengnan, Yufeng, Jin and all my friends. I enjoyed sharing experiences, drinking, having dinner and playing games together with you. Thank you for your friendship that always helped me to get back to work with full of energy. I also want to thank my dearest friends in China, Min and Yuning, who always listen to my difficulties and give me support anytime.

Last but not the least, I would like to express the depth of my gratitude to my families. Dear my dad and mom, thanks a lot for your unconditional love and support within these years. You contribute a lot to me and support me to achieve my goals in each stage of my study. Dear sister and brother in law, thanks for being there with me.

The journey comes to an end, but memories last forever.